

LOW-ENERGY NUCLEAR REACTIONS USING TIME-DEPENDENT DENSITY
FUNCTIONAL THEORY

By

Kyle Godbey

Dissertation

Submitted to the Faculty of the
Graduate School of Vanderbilt University
in partial fulfillment of the requirements
for the degree of

DOCTOR OF PHILOSOPHY
in
Physics

May 8th, 2020

Nashville, Tennessee

Approved:

Date:

Victoria Greene, Ph.D.

Kelly Holley-Bockelmann, Ph.D.

Norman Tolk, Ph.D.

Sait A. Umar, Ph.D.

Kalman Varga, Ph.D.

Dedication

I dedicate this thesis to

Dedication right here

and

Another dedication!

Acknowledgment

First and foremost, ...

TABLE OF CONTENTS

	Page
DEDICATION	ii
ACKNOWLEDGMENTS	iii
LIST OF TABLES	vi
LIST OF FIGURES	vii
CHAPTERS	
1 Introduction	1
1.1 Section 1	1
2 Dependence of fusion on isospin dynamics	2
2.1 Introduction	2
2.2 Formalism	4
2.3 Results	10
2.4 Conclusion	16
3 How the Pauli exclusion principle affects fusion of atomic nuclei	17
3.1 Introduction	17
3.2 Formalism	19
3.3 Results	21
3.4 Conclusion	30
4 The influence of tensor force on the microscopic heavy-ion interaction potential	31
4.1 Introduction	32
4.2 Theoretical framework	35
4.3 results	39
4.4 Summary	47
4.5 Acknowledgments	48

5	Influence of the tensor interaction on heavy-ion fusion cross sections	50
5.1	Introduction	51
5.2	Theoretical framework	53
5.3	Results	59
5.4	Conclusions	69
6	Absence of hindrance in microscopic $^{12}\text{C} + ^{12}\text{C}$ fusion study	71
6.1	Introduction	72
6.2	Formalism	75
6.3	Results	84
6.4	Conclusion	88
7	Deformed shell effects in $^{48}\text{Ca} + ^{249}\text{Bk}$ quasifission fragments	91
7.1	Introduction	91
7.2	Method	94
7.3	Results	100
7.4	Conclusions	115
8	Microscopic predictions for production of neutron rich nuclei in the reaction $^{176}\text{Yb} + ^{176}\text{Yb}$	117
8.1	Introduction	118
8.2	Formalism: TDHF and TDRPA	120
8.3	Results	126
8.4	Summary and Discussion	137
9	Future Work	139
9.1	Work in Progress	139
9.2	Conclusion	139
REFERENCES		140
A	Appendix A	196

LIST OF TABLES

Table	Page
4.1 Isoscalar and isovector spin-current coupling constants in units of MeV fm ⁵ .	46

LIST OF FIGURES

	Figure	Page
2.1	For the $^{40}\text{Ca}+^{48}\text{Ca}$ system; Total and isoscalar DC-TDHF potentials. The shaded region corresponds to the reduction originating from the isovector contribution to the energy density. The insert shows the isoscalar and isovector contributions to the interaction barrier without the Coulomb potential. The TDHF collision energy was $E_{\text{c.m.}} = 55 \text{ MeV}$	6
2.2	For the $^{16}\text{O}+^{208}\text{Pb}$ system; (a) Total and isoscalar DC-TDHF potentials at $E_{\text{c.m.}} = 75 \text{ MeV}$. The shaded region corresponds to the reduction originating from the isovector contribution to the energy density. (b) Same as in (a) except for $E_{\text{c.m.}} = 90 \text{ MeV}$. (c) Same as in (a) except for $E_{\text{c.m.}} = 120 \text{ MeV}$	8
2.3	Isoscalar and isovector breakdown of the potential barrier for two systems at the same $E_{\text{c.m.}}/V_B = 1.065$; (a) $^{48}\text{Ca}+^{208}\text{Pb}$. The shaded region corresponds to the increase originating from the isovector contribution to the energy density. (b) Same as in (a) except $^{50}\text{Ti}+^{208}\text{Pb}$. The shaded region corresponds to the decrease originating from the isovector contribution to the energy density.	9
2.4	For (a) $^{40}\text{Ca}+^{132}\text{Sn}$, (b) $^{48}\text{Ca}+^{132}\text{Sn}$ systems; Total and isoscalar DC-TDHF potentials. In (a) the blue shaded region corresponds to the reduction originating from the isovector contribution. In (b) we see no isovector effect. (c) the isovector effect is reversed causing hindrance as shown by the red shaded region. The inserts show the isoscalar and isovector contributions to the interaction barrier without the Coulomb potential. The TDHF collision energy was $E_{\text{c.m.}} = 120 \text{ MeV}$	11
2.5	Neutron and proton current vectors in $^{40,48}\text{Ca}+^{132}\text{Sn}$ at $E_{\text{c.m.}} = 120 \text{ MeV}$ and at a separation $R = 11.5 \text{ fm}$ between the fragments.	12
2.6	Fusion cross-section in $^{40}\text{Ca}+^{132}\text{Sn}$ calculated with (black line) and without (red line) isovector reduction, using the potentials of Fig. 2.4a.	15

3.1	(a-c) Nucleus-nucleus potential without (FHF) and with (DCFHF) Pauli exclusion principle between nucleons of different nuclei. Potentials from a Gram-Schmidt antisymmetrization (dotted-dashed line) and from DCFHF without rearrangement of the spin-orbit density (thin dashed line) are shown in panel (a). M3Y (dotted line) and M3Y+rep (dotted-dashed line) phenomenological potentials (Henning Esbensen and Şerban Mişcu, 2007) are shown in panel (c). (d-f) Experimental, (Morton et al., 1999; Dasgupta et al., 2007; Montagnoli et al., 2012; Stefanini et al., 2009) and theoretical (coupled-channels calculations with couplings to low-lying collective 2^+ and/or 3^- states) fusion cross-sections $\sigma_{fus.}$ versus centre of mass energy $E_{c.m.}$. (g-i) Logarithmic slopes of $\sigma_{fus.} E_{c.m.}$ versus $E_{c.m.} - V_B$ where V_B is the barrier energy. In (g-i), FHF and DCFHF cross-sections are obtained without couplings, the latter being included via a shift in $E_{c.m.}$ (see text).	22
3.2	$^{16}\text{O} + ^{16}\text{O}$ nucleus-nucleus potential without (FHF) and with (DCFHF) Pauli exclusion principle between nucleons of different nuclei.	23
3.3	Same as Fig. 3.2 for $^{48}\text{Ca} + ^{208}\text{Pb}$	24
3.4	Same as Fig. 3.2 for $^{40}\text{Ca} + ^{48}\text{Ca}$. DCFHF potentials of the other $^A\text{Ca} + ^A\text{Ca}$ are also reported.	26
4.1	Internuclear potential obtained from DC-TDHF approach shown for the evolution of the systems (a) $^{12}\text{C} + ^{12}\text{C}$ at $E_{c.m.} = 8$ MeV and (b) $^{16}\text{O} + ^{16}\text{O}$ at $E_{c.m.} = 12$ MeV with SLy5 (open circle) and SLy5t (solid circle) forces.	42
4.2	Internuclear potential obtained from FHF and DC-TDHF approaches for the Ca+Ca, Ca+Ni, and Ni+Ni reactions with tensor (SLy5t) and without tensor (SLy5) forces.	43
4.3	Internuclear potential obtained from DC-TDHF approach for the reaction $^{48}\text{Ca} + ^{48}\text{Ca}$ with SLy5, SLy5t, T22, T26, T44, and T62 forces.	45
4.4	Internuclear potential obtained from DC-TDHF approach for the Ca+Sn systems with SLy5 (open circle) and SLy5t (solid circle) forces.	49
5.1	Fusion cross sections obtained from the DC-TDHF approach for (a) $^{12}\text{C} + ^{12}\text{C}$ at $E_{c.m.} = 8$ MeV and (b) $^{12}\text{C} + ^{13}\text{C}$ at $E_{c.m.} = 8$ MeV with SLy5 (black solid line) and SLy5t (red dashed line) forces.	60

5.2	S factors obtained from the DC-TDHF approach for (a) $^{12}\text{C} + ^{12}\text{C}$ at $E_{\text{c.m.}} = 8$ MeV and (b) $^{12}\text{C} + ^{13}\text{C}$ at $E_{\text{c.m.}} = 8$ MeV with SLy5 (black solid line) and SLy5t (red dashed line) forces.	61
5.3	Fusion cross sections obtained from the DC-TDHF approach for (a) $^{40}\text{Ca} + ^{40}\text{Ca}$ at $E_{\text{c.m.}} = 55$ MeV, (b) $^{40}\text{Ca} + ^{48}\text{Ca}$ at $E_{\text{c.m.}} = 55$ MeV, and (c) $^{48}\text{Ca} + ^{48}\text{Ca}$ at $E_{\text{c.m.}} = 55$ MeV with SLy5 (black solid line) and SLy5t (red dashed line) forces.	63
5.4	Fusion cross sections obtained from the DC-TDHF approach and experimental data from (Stefanini et al., 2009) for $^{48}\text{Ca} + ^{48}\text{Ca}$ at $E_{\text{c.m.}} = 55$ MeV with (a) SLy5 (black solid line) and SLy5t (red dashed line) forces and (b) T22 (purple dotted line), T26 (green dash-dotted line), T44 (blue dash-dot-dotted line), and T62 (orange dashed line) forces.	65
5.5	Fusion cross sections obtained from the DC-TDHF approach for (a) $^{48}\text{Ca} + ^{100}\text{Sn}$ at $E_{\text{c.m.}} = 125$ MeV, (b) $^{48}\text{Ca} + ^{116}\text{Sn}$ at $E_{\text{c.m.}} = 125$ MeV, and (c) $^{48}\text{Ca} + ^{120}\text{Sn}$ at $E_{\text{c.m.}} = 125$ MeV with SLy5 (black solid line) and SLy5t (red dashed line) forces.	67
5.6	Fusion cross sections obtained from the DC-TDHF approach for $^{16}\text{O} + ^{208}\text{Pb}$ at $E_{\text{c.m.}} = 75$ MeV with SLy5 (black solid line) and SLy5t (red dashed line) forces.	68
6.1	Ion-Ion fusion potentials from DC-TDHF, FHF, and DCFHF using the UNEDF1 force.	77
6.2	3D contour plot over projected pseudocolor density plot at distance of the barrier peak at $R = 8.06$ fm. Solid red contour surface is drawn for $\rho = 0.08$ fm $^{-3}$ and opaque gray shading is drawn for $\rho = 0.008$ fm $^{-3}$ to show the value and location of interacting densities.	78
6.3	Density profile along the collision axis of the $^{12}\text{C} + ^{12}\text{C}$ system at the barrier peak for densities from the static FHF method and dynamic DC-TDHF method.	79
6.4	Comparison of $^{12}\text{C} + ^{12}\text{C}$ fusion cross sections from DC-TDHF, FHF, and DCFHF using the UNEDF1 force and experimental data from (Aguilera et al., 2006; Spillane et al., 2007; Zickefoose, 2011; Barrón-Palos et al., 2006; High and Čujec, 1977; Jiang et al., 2018; Mazarakis and Stephens, 1973; Patterson et al., 1969) in (a) logarithmic and (b) linear scales. The hindrance model is from Ref. (Jiang et al., 2007).	80

6.5	Comparison of $^{12}\text{C}+^{12}\text{C}$ fusion S factors from DC-TDHF, FHF, and DCFHF using the UNEDF1 force, DC-TDHF using the SLy4d force, the hindrance model from (Jiang et al., 2007), and experimental data from (Aguilera et al., 2006; Spillane et al., 2007; Zickefoose, 2011; Barrón-Palos et al., 2006; High and Čujec, 1977; Jiang et al., 2018; Mazarakis and Stephens, 1973; Patterson et al., 1969).	85
6.6	Comparison of $^{12}\text{C}+^{12}\text{C}$ fusion S factors from DC-TDHF at (a) differing TDHF energies and (b) using different functionals.	88
7.1	Schematic representation of the initial configuration for an impact parameter b and a velocity vector \mathbf{v}_∞ defining the collision plane and the collision axis. The orientation of the target is defined by the angles β (rotation around the axis perpendicular to the reaction plane) and α (rotation around the collision axis).	96
7.2	Isodensity surfaces at $\rho = 0.145, 0.1$, and 0.02 fm^{-3} in blue, green, and pink, respectively, shown at times $t \approx 0$ (a), 2.1 (b), 5.8 (c), and 6.4 zs (d) for an initial orientation $\beta = 135^\circ$ and an angular momentum $L = 60\hbar$. For visualization purposes, the reaction plane is 37° off the plane of the page.	98
7.3	Total kinetic energy of the fragments as a function of their mass ratio. The curve corresponds to the Viola systematics (Viola et al., 1985; Hinde et al., 1987).	101
7.4	Mass ratio M_R as a function of orientation angle β for central collisions. Fusion is indicated by the shaded area.	102
7.5	(a) Distribution of scattering angle $\theta_{c.m.}$ versus mass ratio M_R (MAD). The colors correspond to different ranges of angular momenta. (b) Fragment mass yield (histogram). The solid line gives a smooth representation of the histogram using the kernel density estimation with bandwidth 0.012 . (c) Mass yields obtained for different ranges of angular momenta.	105
7.6	(a) Distribution of scattering angle $\theta_{c.m.}$ versus proton number Z (ZAD). (b) Fragment proton number yield without (lighter shade) and with angular cut $\theta_{c.m.} > 70$ degrees (darker shade). The vertical line represents potential proton shell gap.	109
7.7	(a) Distribution of scattering angle $\theta_{c.m.}$ versus neutron number N (NAD). (b) Fragment neutron number yield without (lighter shade) and with angular cut $\theta_{c.m.} > 70$ degrees (darker shade). The vertical lines represent potential neutron shell gaps.	110

7.8	Distribution of proton number Z versus neutron number N of the fragments. The dashed line represents the N/Z ratio of the compound nucleus. The inset is a zoom around the light fragment. Thin dashed lines indicate the positions of ^{94}Sr ($Z = 38, N = 56$) and ^{100}Zr ($Z = 40, N = 60$).	113
7.9	Isodensity surfaces at $\rho = 0.1 \text{ fm}^{-3}$ for $L = 90\hbar$ and $\beta = 120^\circ$ (top), and $L = 60\hbar$ and $\beta = 135^\circ$ (bottom), just after the breaking of the neck. The light fragment (right) in the top is a ^{94}Sr ($Z = 38, N = 56$) and a ^{100}Zr ($Z = 40, N = 60$) in the bottom. The contour line in the bottom represents the same density as in the top.	114
8.1	Static nuclear potentials for $^{176}\text{Yb} + ^{176}\text{Yb}$ in the side-side (blue (dark) lines) and tip-tip (green (light) lines) orientations from FHF and DCFHF.	124
8.2	Scattering angles for $^{176}\text{Yb} + ^{176}\text{Yb}$ collisions at center of mass energies (a) $E_{\text{c.m.}} = 660 \text{ MeV}$ and (b) $E_{\text{c.m.}} = 880 \text{ MeV}$ in the side-side (circles) and tip-tip (squares) orientations. The dotted (dashed) line plots the Rutherford scattering angle for $E_{\text{c.m.}} = 660 \text{ MeV}$ (880 MeV).	128
8.3	Total kinetic energies of the outgoing fragments in $^{176}\text{Yb} + ^{176}\text{Yb}$ collisions at center of mass energies $E_{\text{c.m.}} = 660 \text{ MeV}$ (blue circles) and $E_{\text{c.m.}} = 880 \text{ MeV}$ (red squares) in the side-side orientation.	129
8.4	TDRPA predictions of correlations σ_{NZ} (a) and fluctuations σ_{NN} (b) and σ_{ZZ} (c) for $^{176}\text{Yb} + ^{176}\text{Yb}$ collisions for four initial configurations over a range of impact parameters.	130
8.5	Mass angle distributions for $^{176}\text{Yb} + ^{176}\text{Yb}$ collisions at (a) $E_{\text{c.m.}} = 660 \text{ MeV}$ in the side-side orientation, (b) $E_{\text{c.m.}} = 660 \text{ MeV}$ in the tip-tip orientation, (c) $E_{\text{c.m.}} = 880 \text{ MeV}$ in the side-side orientation, and (d) $E_{\text{c.m.}} = 880 \text{ MeV}$ in the tip-tip orientation. The colorbar represents cross sections in millibarns per bin of mass ratio and degree.	132
8.6	Mass energy distributions for $^{176}\text{Yb} + ^{176}\text{Yb}$ collisions at (a) $E_{\text{c.m.}} = 660 \text{ MeV}$ in the side-side orientation, (b) $E_{\text{c.m.}} = 660 \text{ MeV}$ in the tip-tip orientation, (c) $E_{\text{c.m.}} = 880 \text{ MeV}$ in the side-side orientation, and (d) $E_{\text{c.m.}} = 880 \text{ MeV}$ in the tip-tip orientation. The colorbar represents cross sections in millibarns per bin of mass ratio and MeV.	133

- 8.7 Primary fragments production cross sections for $^{176}\text{Yb} + ^{176}\text{Yb}$ collisions at $E_{\text{c.m.}} = 660$ MeV in the side-side orientation overlaid onto the chart of nuclides. The innermost contour corresponds to a cross section of 1 millibarn, with subsequent contours drawn every 0.2 mb. Finally, we also plot a boundary contour drawn at the microbarn level. Chart from (Edward Simpson, 2019). 135

Chapter 1

Introduction

1.1 Section 1

1.1.1 Subsection 1

Chapter 2

Dependence of fusion on isospin dynamics

Abstract

We introduce a new microscopic approach to calculate the dependence of fusion barriers and cross-sections on isospin dynamics. The method is based on the time-dependent Hartree-Fock theory and the isoscalar and isovector properties of the energy density functional (EDF). The contribution to the fusion barriers originating from the isoscalar and isovector parts of the EDF is calculated. It is shown that for non-symmetric systems the isovector dynamics influence the sub-barrier fusion cross-sections. For most systems this results in an enhancement of the sub-barrier cross-sections, while for others we observe differing degrees of hindrance. We use this approach to provide an explanation of recently measured fusion cross sections which show a enhancement at low $E_{\text{c.m.}}$ energies for the system $^{40}\text{Ca}+^{132}\text{Sn}$ as compared to the more neutron-rich system $^{48}\text{Ca}+^{132}\text{Sn}$, and discuss the dependence of sub-barrier fusion cross-sections on transfer.

2.1 Introduction

One of the major open questions in fusion reactions of exotic neutron-rich nuclei is the dependence of the fusion cross section on the neutron excess, or equivalently on the total isospin quantum number $T_z = (Z - N)/2$. This is a timely subject given the expected availability of increasingly exotic beams at rare isotope facilities ([Balantekin et al., 2014b](#)). The influence of isospin dynamics on fusion is also one of the key questions pertaining to the production of superheavy elements using neutron rich nuclei ([Loveland, 2007](#)). Besides being a fundamental nuclear structure and reaction question, the answer to this inquiry is also vital to our understanding of the nuclear equation of state (EOS) and symmetry energy ([Li et al., 2014](#)). The EOS plays a key role in elucidating the structure of exotic nuclei ([Chen and Piekarewicz, 2015](#)), the dynamics of heavy ion collisions ([Danielewicz et al., 2002; Tsang et al., 2009](#)), the composition of neutron stars ([Haensel and Zdunik, 1990; Chamel](#)

and Haensel, 2008; Horowitz et al., 2004; Utama et al., 2016), and the mechanism of core-collapse supernovae (Bonche and Vautherin, 1981; Watanabe et al., 2009; Shen et al., 2011). The influence of isospin flow during heavy-ion reaction is usually discussed in term of the (N/Z) asymmetry of the target and projectile or the Q -values for nucleon transfer.

The presence of positive Q -value transfer channels has been shown to enhance sub-barrier fusion in various systems (Jiang et al., 2014a). However, what affects the magnitude of this enhancement is still actively debated (Kohley et al., 2011, 2013; Kolata et al., 2012; Jiang et al., 2015a; Liang et al., 2016). In particular, recent experiments carried out with radioactive ^{132}Sn beams and with stable ^{124}Sn beams on $^{40,48}\text{Ca}$ (Kolata et al., 2012) and $^{58,64}\text{Ni}$ (Kohley et al., 2011) targets have shown that the enhancement is observed at much lower cross-sections in the heavier (Ni+Sn) systems (Jiang et al., 2015a) than in the lighter (Ca+Sn) ones. Various possible effects have been invoked to explain these observations (Liang et al., 2016), such as a larger role of dissipation due to the increase of the charge product Z_1Z_2 of the collision partners (Wolfs, 1987; Evers et al., 2011; Rafferty et al., 2016). It is also known that for systems with $Z_1Z_2 \gtrsim 1600$, the so-called quasifission, where the nuclei re-separate after a significant mass transfer, strongly hinders fusion (Tőke et al., 1985).

The effect of neutron transfer on fusion is traditionally described within the coupled-channels (CC) method (Rowley et al., 1992; Esbensen et al., 1998; Kouichi Hagino and Noboru Takigawa, 2012) and models incorporating intermediate neutron rearrangements (Zagrebaev, 2003; Zagrebaev et al., 2007; Karpov et al., 2015). These approaches, however, model the transfer process on a schematic way and they require nuclear data which are often unknown for exotic nuclei. New approaches are then needed to describe realistically the effect of both proton and neutron transfers on fusion of stable and exotic nuclei. In particular, dissipation induced by transfer should be properly accounted for.

Here, we take a first step toward this ambitious theoretical program by investigating the overall effect of isospin dynamics induced mostly by neutron and/or proton transfer

in collisions of asymmetric systems (Dasso et al., 1985; Ph. Chomaz et al., 1993; Baran et al., 1996, 2001; Simenel et al., 2001; Baran et al., 2005; Simenel et al., 2007; Baran et al., 2009; Oberacker et al., 2012; Umar et al., 2008b). In particular, we address the impact of isospin dynamics on fusion barriers and cross-sections using the microscopic time-dependent Hartree-Fock (TDHF) theory (Negele, 1982; Simenel, 2012b) together with the density-constrained TDHF (DC-TDHF) method for calculating fusion barriers (Umar and Oberacker, 2006f). This choice is motivated by the fact that the TDHF approach has been used to successfully describe multinucleon transfer (Simenel, 2010b; Simenel et al., 2012; Kazuyuki Sekizawa and Kazuhiro Yabana, 2013b; Scamps and Lacroix, 2013b; Bourgin et al., 2016), as well as strongly damped reactions such as deep-inelastic collisions (Koonin et al., 1977; Simenel, 2011b) and quasi-fission (Wakhle et al., 2014; Umar et al., 2015b, 2016b), without relying on an *a priori* knowledge of the structure of the reactants. Therefore, these microscopic dynamical calculations incorporate the fundamental mechanisms which are relevant for a realistic description of the effect of transfer on fusion, including with exotic beams. As a first application, various systems from Ca+Ca to Ca+Sn are considered.

2.2 Formalism

In the TDHF approximation the many-body wavefunction is replaced by a single Slater determinant and this form is preserved at all times, implying that two-body correlations are neglected. In this limit, the variation of the time-dependent action with respect to the single-particle states, ϕ_λ^* , yields the most probable time-dependent path in the multi-dimensional space-time phase space represented as a set of coupled, nonlinear, self-consistent initial value equations for the single-particle states

$$h(\{\phi_\mu\}) \phi_\lambda(r, t) = i\hbar \frac{\partial}{\partial t} \phi_\lambda(r, t) \quad (\lambda = 1, \dots, A), \quad (2.1)$$

where h is the HF single-particle Hamiltonian. These are the fully microscopic time-dependent Hartree-Fock equations.

Almost all TDHF calculations employ the Skyrme EDF, which allows the total energy of the system to be represented as an integral of the energy density $\mathcal{H}(\mathbf{r})$ (Engel et al., 1975)

$$E = \int d^3\mathbf{r} \mathcal{H}(\mathbf{r}), \quad (2.2)$$

which includes the kinetic, isoscalar, isovector, and Coulomb terms (Dobaczewski and Dudek, 1995):

$$\mathcal{H}(\mathbf{r}) = \frac{\hbar^2}{2m} \tau_0 + \mathcal{H}_0(\mathbf{r}) + \mathcal{H}_1(\mathbf{r}) + \mathcal{H}_C(\mathbf{r}). \quad (2.3)$$

In particular,

$$\mathcal{H}_I(\mathbf{r}) = C_I^\rho \rho_I^2 + C_I^s \mathbf{s}_I^2 + C_I^{\Delta\rho} \rho_I \Delta \rho_I + C_I^{\Delta s} \mathbf{s}_I \cdot \Delta \mathbf{s}_I + C_I^\tau (\rho_I \tau_I - \mathbf{j}_I^2) + C_I^T (\mathbf{s}_I \cdot \mathbf{T}_I - \mathbf{j}_I^2) + C_I^{\nabla J} (\rho_I \nabla \cdot \mathbf{J}_I + \mathbf{s}_I \cdot (\nabla \times \mathbf{j}_I)), \quad (2.4)$$

where we have used the gauge invariant form suitable for time-dependent calculations. The isospin index $I = 0, 1$ for isoscalar and isovector energy densities, respectively. The most common choice of Skyrme EDF restricts the density dependence of the coupling constants to the C_I^ρ and C_I^s terms only. These density dependent coefficients contribute to the coupling of isoscalar and isovector fields in the Hartree-Fock Hamiltonian. The isoscalar (isovector) energy density, $\mathcal{H}_0(\mathbf{r})$ ($\mathcal{H}_1(\mathbf{r})$), depends on the isoscalar (isovector) particle density, $\rho_0 = \rho_n + \rho_p$ ($\rho_1 = \rho_n - \rho_p$), with analogous expressions for other densities and currents. Values of the coupling coefficients as well as their relation to the alternative parametrizations of the Skyrme EDF can be found in (Dobaczewski and Dudek, 1995).

The above form of the EDF is more suitable for studying the isospin dependence of nuclear properties and have been employed in nuclear structure studies (Dobaczewski and Dudek, 1995). In the same spirit we can utilize this approach to study isospin dependent effects in nuclear reactions microscopically. In particular, the density-constrained time-

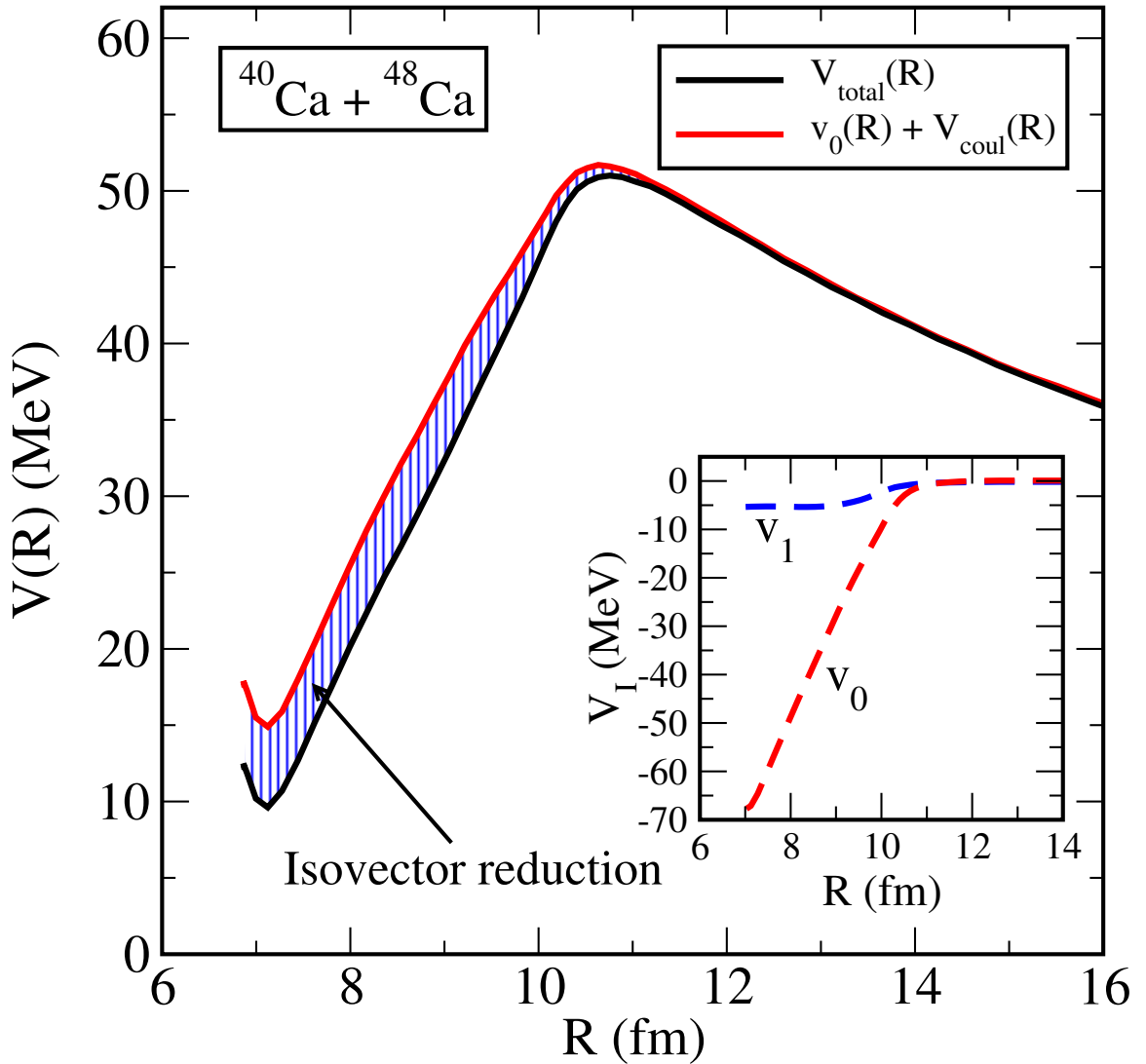


Figure 2.1: For the $^{40}\text{Ca} + ^{48}\text{Ca}$ system; Total and isoscalar DC-TDHF potentials. The shaded region corresponds to the reduction originating from the isovector contribution to the energy density. The insert shows the isoscalar and isovector contributions to the interaction barrier without the Coulomb potential. The TDHF collision energy was $E_{\text{c.m.}} = 55$ MeV.

dependent Hartree-Fock (DC-TDHF) method (Umar and Oberacker, 2006f) can be employed to study isospin effects on fusion barriers and fusion cross-sections. The DC-TDHF approach calculates the nucleus-nucleus potentials $V(R)$ directly from TDHF dynamics and has been used to calculate fusion cross-sections for a wide range of reactions (Umar et al., 2014b; Simenel et al., 2013d; Umar et al., 2012b; Umar and Oberacker, 2006e; Oberacker et al., 2010b; Umar et al., 2009b; Jiang et al., 2015b). The basic idea of this approach is the following: At certain times t or, equivalently, at certain internuclear distances $R(t)$, a static energy minimization is performed while constraining the proton and neutron densities to be equal to the instantaneous TDHF densities. We refer to the minimized energy as the “density constrained energy” $E_{\text{DC}}(R)$. The ion-ion interaction potential $V(R)$ is obtained by subtracting the constant binding energies E_{A_1} and E_{A_2} of the two individual nuclei

$$V(R) = E_{\text{DC}}(R) - E_{A_1} - E_{A_2}. \quad (2.5)$$

The calculated ion-ion interaction barriers contain all of the dynamical changes in the nuclear density during the TDHF time-evolution in a self-consistent manner. As a consequence of the dynamics the DC-TDHF potential is energy dependent (Umar et al., 2014b). Using the decomposition of the Skyrme EDF into isoscalar and isovector parts [Eq. (2.4)], we can re-write this potential as

$$V(R) = \sum_{I=0,1} v_I(R) + V_C(R), \quad (2.6)$$

where $v_I(R)$ denotes the potential computed by using the isoscalar and isovector parts of the Skyrme EDF given in Eq. (2.3) in Eq. (2.5). The Coulomb potential is also calculated via Eq. (2.5) using the Coulomb energy density.

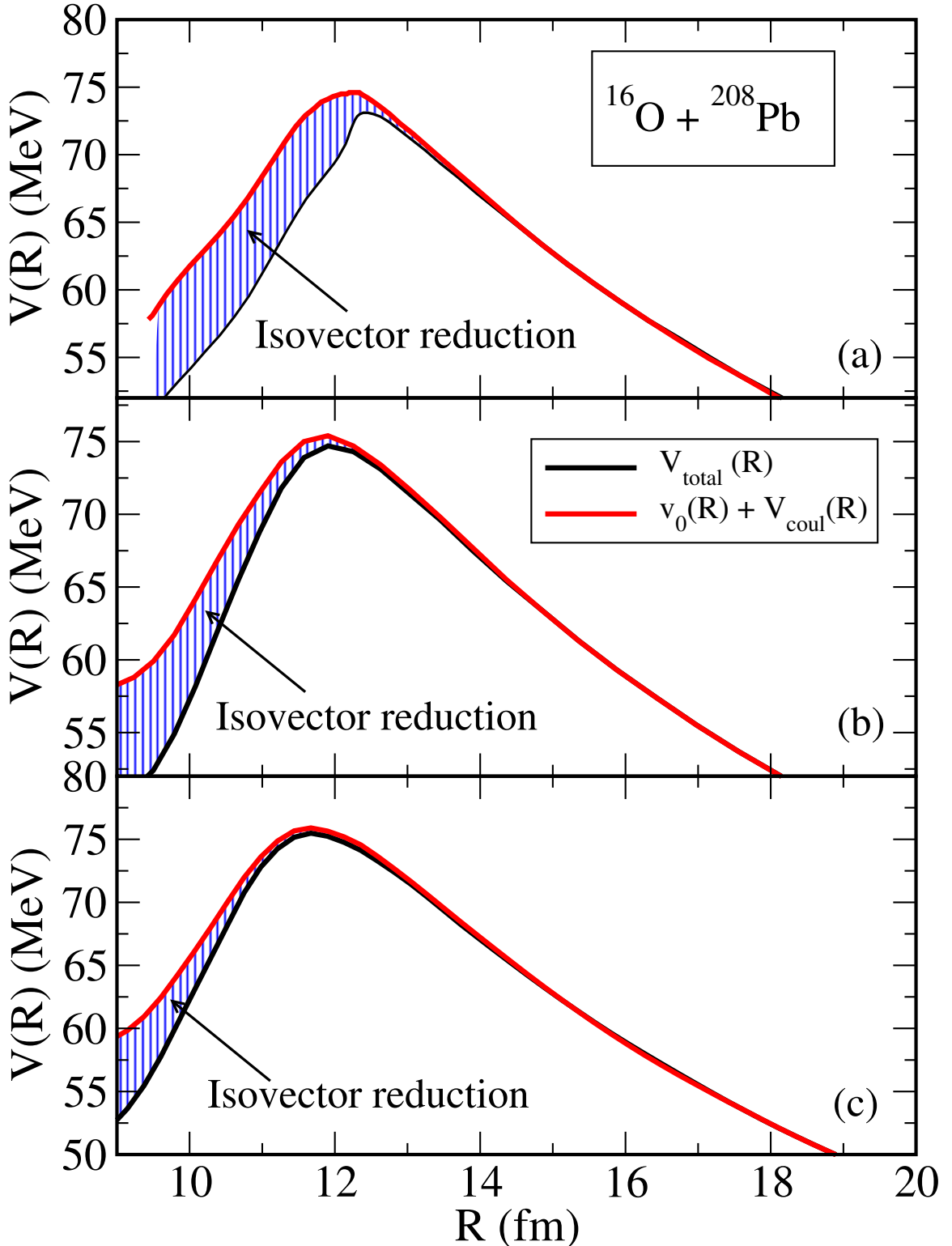


Figure 2.2: For the $^{16}\text{O} + ^{208}\text{Pb}$ system; (a) Total and isoscalar DC-TDHF potentials at $E_{\text{c.m.}} = 75$ MeV. The shaded region corresponds to the reduction originating from the isovector contribution to the energy density. (b) Same as in (a) except for $E_{\text{c.m.}} = 90$ MeV. (c) Same as in (a) except for $E_{\text{c.m.}} = 120$ MeV.

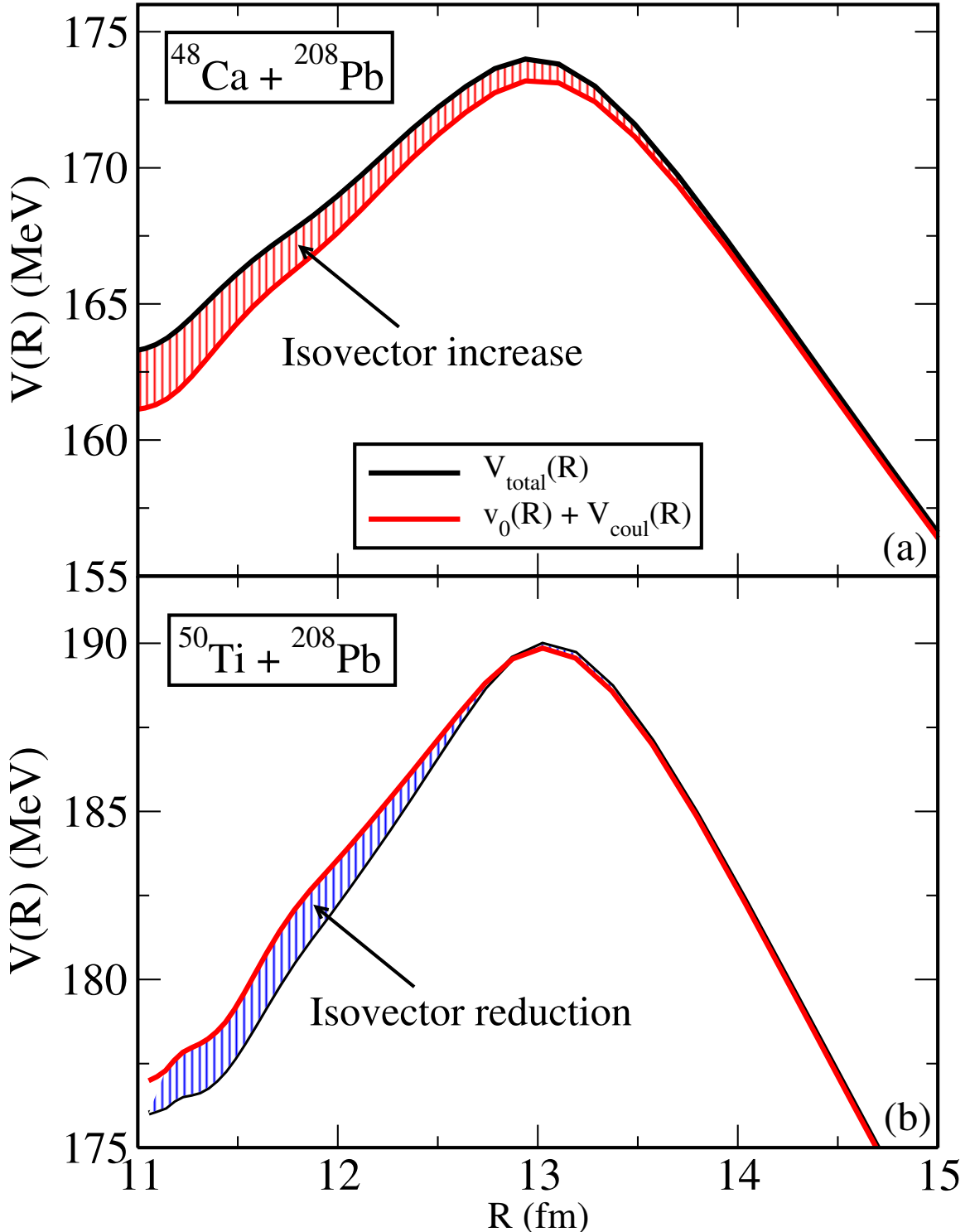


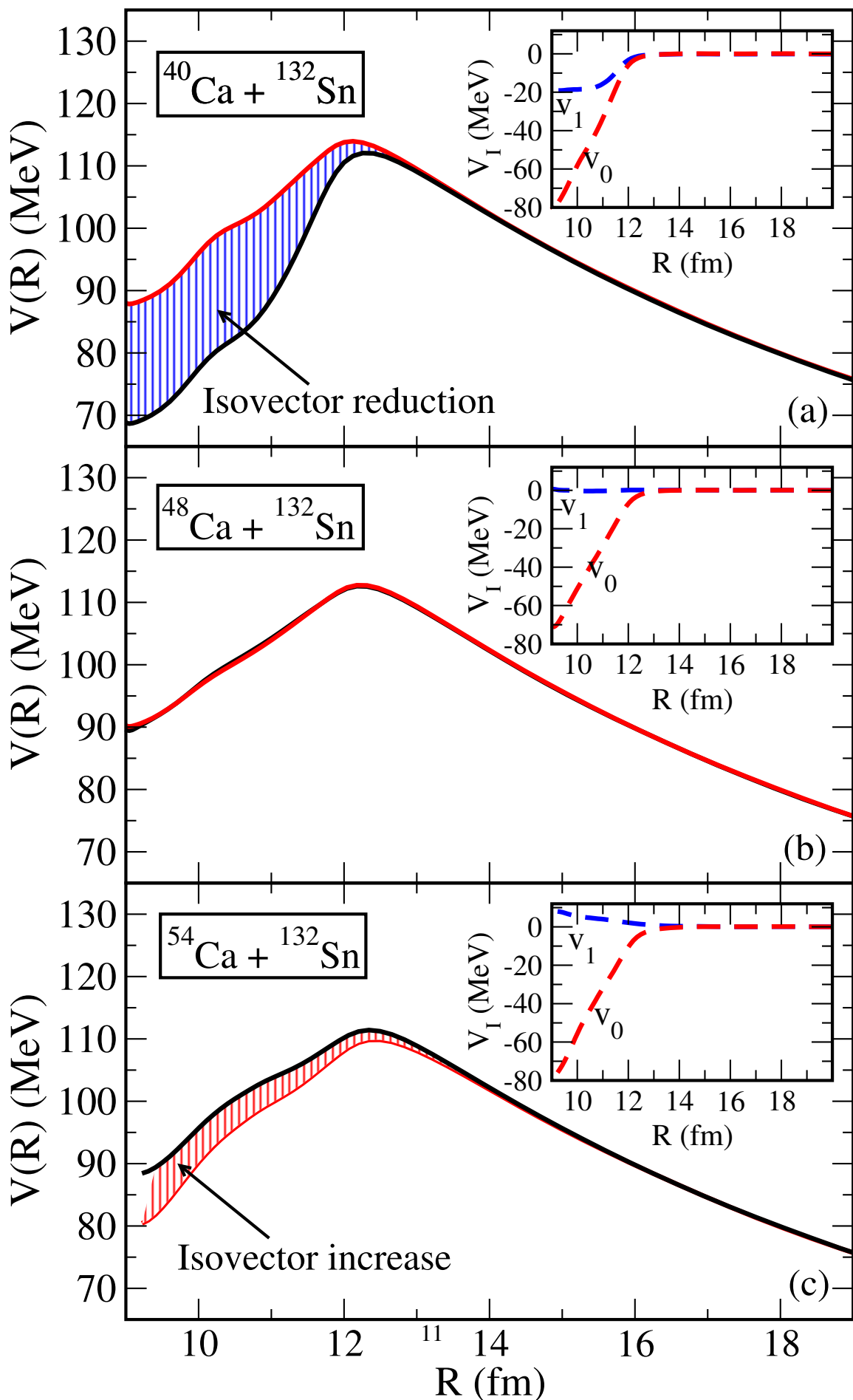
Figure 2.3: Isoscalar and isovector breakdown of the potential barrier for two systems at the same $E_{\text{c.m.}}/V_B = 1.065$; (a) $^{48}\text{Ca} + ^{208}\text{Pb}$. The shaded region corresponds to the increase originating from the isovector contribution to the energy density. (b) Same as in (a) except $^{50}\text{Ti} + ^{208}\text{Pb}$. The shaded region corresponds to the decrease originating from the isovector contribution to the energy density.

2.3 Results

We have used the DC-TDHF approach to study fusion barriers for a number of systems. Calculations were done in a three-dimensional Cartesian geometry with no symmetry assumptions ([Umar and Oberacker, 2006g](#)) and using the Skyrme SLy4 EDF ([Chabanat et al., 1998](#)). The three-dimensional Poisson equation for the Coulomb potential is solved by using Fast-Fourier Transform techniques and the Slater approximation is used for the Coulomb exchange term. The box size used for all the calculations was chosen to be $60 \times 30 \times 30 \text{ fm}^3$, with a mesh spacing of 1.0 fm in all directions. These values provide very accurate results due to the employment of sophisticated discretization techniques ([Umar et al., 1991a](#)).

In Fig. 2.1 we show the total and isoscalar fusion barriers (both including the Coulomb contribution) for the $^{40}\text{Ca}+^{48}\text{Ca}$ system at $E_{\text{c.m.}} = 55$ MeV. For the Ca+Ca systems the energy dependence is relatively weak ([Keser et al., 2012b; Umar et al., 2014b; Kouhei Washiyama and Denis Lacroix, 2008](#)). The reduction of the isoscalar barrier is due to the isovector contribution. It is evident that the isovector dynamics results in the narrowing of the fusion barrier, thus resulting in an enhancement of the sub-barrier fusion cross-sections. The insert in Fig. 2.1 shows the isovector and isoscalar components without the Coulomb contribution. We have also calculated fusion barriers for the $^{40}\text{Ca}+^{40}\text{Ca}$ and $^{48}\text{Ca}+^{48}\text{Ca}$ systems, where the isovector contribution is zero as expected from symmetry. Irrespective of its isovector/isoscalar nature, the DC-TDHF potential is a way to represent the potential felt by the system at a given time. The relation between time and distance between the fragments then allow to represent the potential in the traditional manner, i.e., as a function of the internuclear distance. The fact that the isovector reduction occurs essentially inside the barrier indicates that the proton and neutron flows become larger for stronger overlap occurring in the later stage of fusion.

As an example of a more asymmetric system we performed calculations for the $^{16}\text{O}+^{208}\text{Pb}$ system at $E_{\text{c.m.}} = 75$ MeV. Results are shown in Fig. 2.2(a). Here we see a substantial



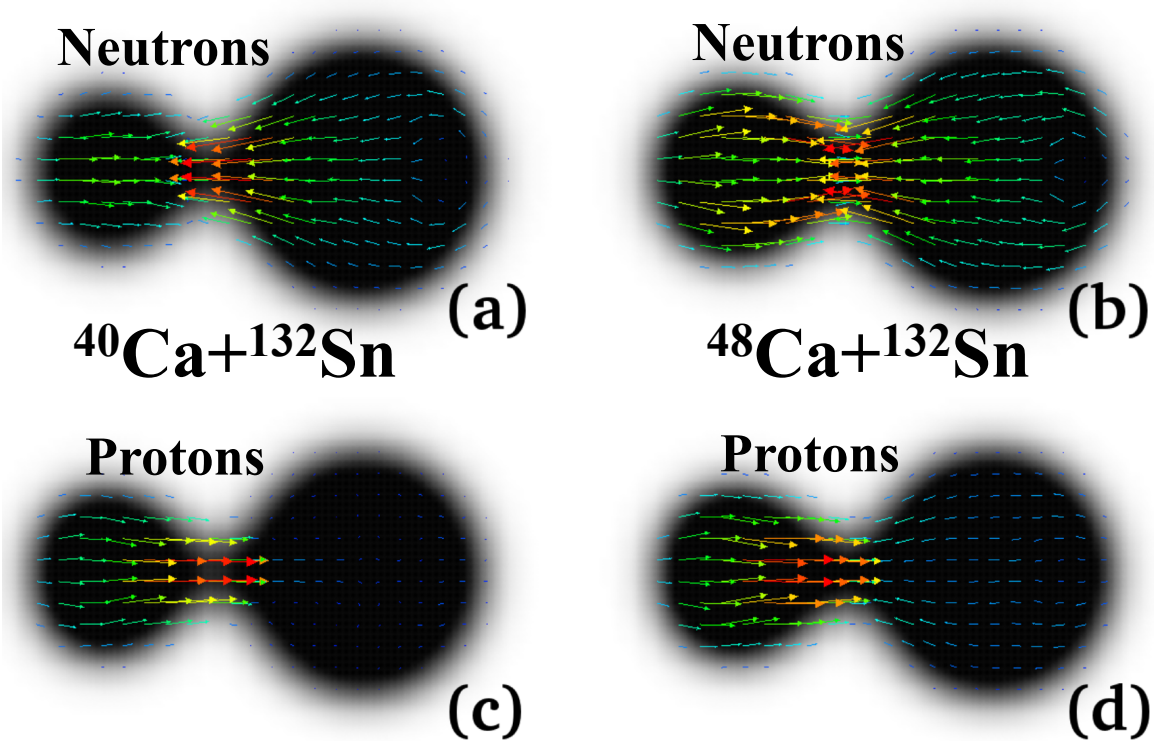


Figure 2.5: Neutron and proton current vectors in $^{40,48}\text{Ca} + ^{132}\text{Sn}$ at $E_{\text{c.m.}} = 120 \text{ MeV}$ and at a separation $R = 11.5 \text{ fm}$ between the fragments.

enhancement of sub-barrier fusion due to the isovector dynamics. For this system we have performed further calculations at c.m. energies of 90 MeV and 120 MeV shown in Fig. 2.2(b-c). As the beam energy increases, the relative contribution from the isovector component to the total barrier decreases, while the overall barrier height increases with increasing energy. At TDHF energies much higher than the barrier height the total barriers approaches the frozen density barrier ([Kouhei Washiyama and Denis Lacroix, 2008](#); [Umar et al., 2014b](#)) due to the inability of the system to rearrange at that time-scale at which time the isovector contribution vanishes as well. Next, we have calculated isoscalar and isovector breakdown of the potential barrier for two systems at the same $E_{\text{c.m.}}/V_B = 1.065$ as shown in Fig. 2.3(a,b) for; $^{48}\text{Ca} + ^{208}\text{Pb}$ system where the shaded region corresponds to the increase in the barrier originating from the isovector contribution to the energy density, and for the $^{50}\text{Ti} + ^{208}\text{Pb}$ system where the shaded region corresponds to the decrease in the barrier originating from the isovector contribution to the energy density. The above results

demonstrate the influence of isovector dynamics on typical fusion barriers.

We next look at Ca+Sn reactions. The experimental observation of a sub-barrier fusion enhancement in the system $^{40}\text{Ca}+^{132}\text{Sn}$ as compared to more neutron-rich system $^{48}\text{Ca}+^{132}\text{Sn}$ was the subject of a previous DC-TDHF study ([Oberacker and Umar, 2013](#)), where it was shown that the fusion barriers for the two systems have essentially the same height but the fusion barrier for the $^{48}\text{Ca}+^{132}\text{Sn}$ system was much wider than that for the $^{40}\text{Ca}+^{132}\text{Sn}$ system. We see in Fig. 2.4(a) a strong reduction of the isoscalar barrier due to the isovector contribution. This behavior is similar to that of the previous two systems albeit the isovector reduction is somewhat larger as shown in the insert of Fig. 2.4(a). We then performed the same calculation for the $^{48}\text{Ca}+^{132}\text{Sn}$ system as shown in Fig. 2.4(b). The startling result is the vanishing of the isovector contribution. With no isovector reduction the fusion barrier for this system is much wider than that for the $^{40}\text{Ca}+^{132}\text{Sn}$ system for which substantial reduction occurs. The absence of the isovector component for the $^{48}\text{Ca}+^{132}\text{Sn}$ system could be a reflection of the negative Q -values for neutron pickup. This is the first direct observation of this phenomena in microscopic calculations.

This may also explain why for the $^{48}\text{Ca}+^{132}\text{Sn}$ system simply considering the 2^+ and 3^- excitations of the target and projectile in coupled-channel calculations is able to reproduce the sub-barrier fusion cross-sections, whereas doing the same for the $^{40}\text{Ca}+^{132}\text{Sn}$ system grossly under-predicts the cross-sections. In Ref. ([Kolata et al., 2012](#)), this was attributed to transfer which manifests itself in the isovector dynamics. In Fig. 2.4(c) we have also calculated the potential barriers for the theoretical $^{54}\text{Ca}+^{132}\text{Sn}$ reaction. Here, we see that the influence of the isovector component is reversed, as indicated by the shaded region. This reversal leads to the widening of the potential barrier, further hindering sub-barrier fusion.

In all the studied systems, we observe an isovector reduction in the presence of positive Q -values for transfer channels. This can be understood from the $C_I^\rho \rho_I^2$ term in Eq. (2.3) which quantitatively dominates. When an isospin equilibration occurs (driven by positive

Q -values), the $I = 1$ contribution gets reduced as $(\rho_p - \rho_n)^2$ decreases in each fragment and C_1^ρ is positive. This also explains why, in systems with only negative Q -values, the isovector contribution to the potential vanishes. In very few cases, such as for the theoretical $^{54}\text{Ca} + ^{132}\text{Sn}$ reaction, we even found an increase of the potential which is attributed to more complex density dependencies of H_1 in Eq. (2.3).

In order to investigate the role of transfer in more detail we have plotted in Fig. 2.5 the microscopic TDHF neutron and proton currents for $^{40,48}\text{Ca} + ^{132}\text{Sn}$ at $E_{\text{c.m.}} = 120$ MeV and at the nuclear separation $R = 11.5$ fm, which is slightly inside the barrier but still corresponds to an early stage of the reaction. In $^{40}\text{Ca} + ^{132}\text{Sn}$, neutrons flow from Sn to Ca (Fig. 2.5a) and protons from Ca to Sn (Fig. 2.5c), compatible with the fact that there are many positive Q -value channels for these transfers to occur. For $^{48}\text{Ca} + ^{132}\text{Sn}$, which has no positive Q -value transfer channel, we observe a convergence of neutrons towards the neck (Fig. 2.5b), which is what we would expect in the fusion process. This is also what is observed for protons in (Fig. 2.5d), although there is a larger displacement of protons from Ca towards the neutron-rich neck. As a result, the isovector current density in the neck region is an order of magnitude lower for the $^{48}\text{Ca} + ^{132}\text{Sn}$ system in comparison to the $^{40}\text{Ca} + ^{132}\text{Sn}$. This is the primary cause for the disappearance of the isovector contribution to the barrier.

Finally, the impact of the isovector contribution to the fusion dynamics is shown in Fig. 2.6, where fusion cross-sections have been computed from the DC-TDHF potentials of Fig. 2.4a. The effect of the isovector reduction is particularly visible at sub-barrier energies where an enhancement of the fusion cross-sections by about an order of magnitude is observed. To our knowledge, this is the first microscopic evidence of the enhancement of fusion due to coupling to transfer channels.

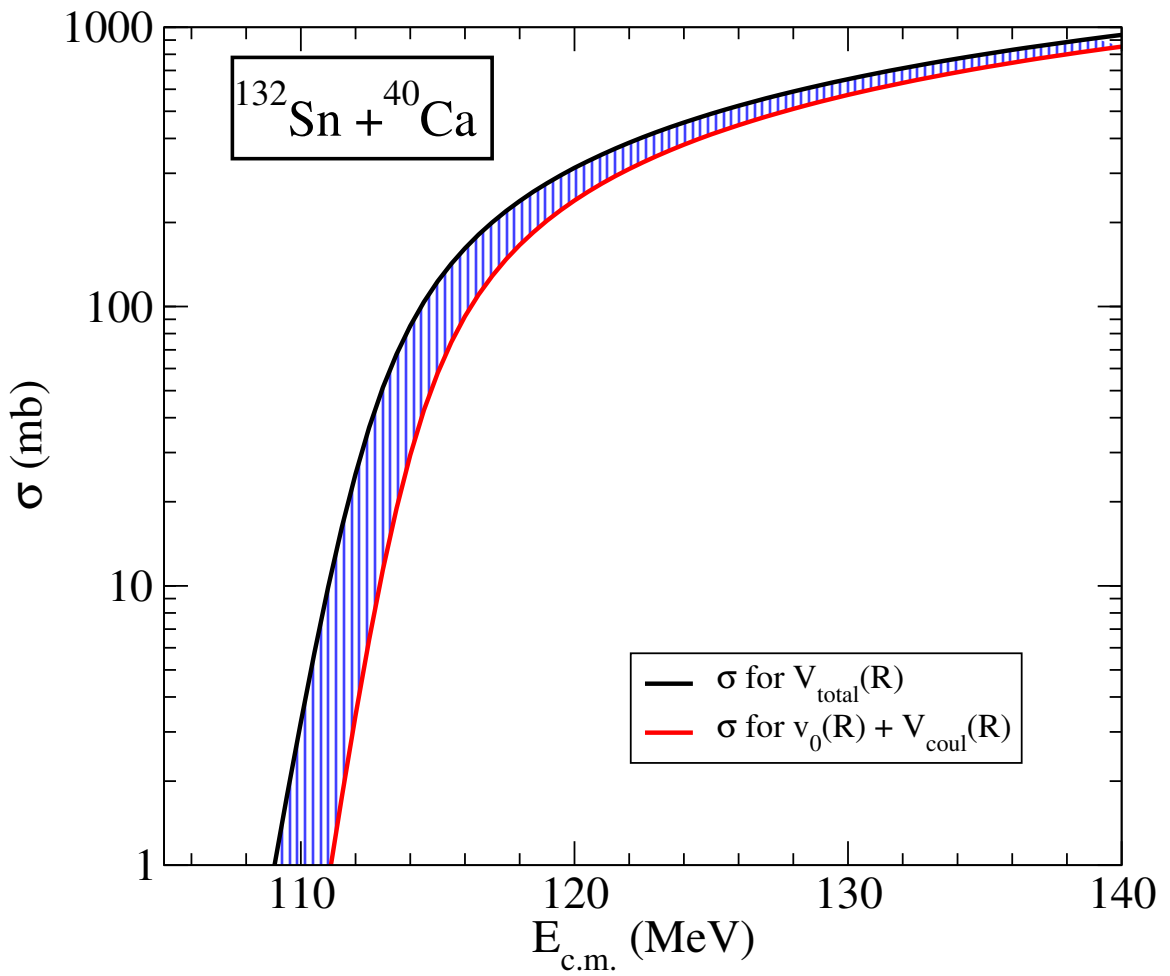


Figure 2.6: Fusion cross-section in $^{40}\text{Ca}+^{132}\text{Sn}$ calculated with (black line) and without (red line) isovector reduction, using the potentials of Fig. 2.4a.

2.4 Conclusion

In summary, we have developed a microscopic approach to study the effect of isospin dynamics on fusion barriers. We have shown that for most systems isovector dynamics results in the thinning of the barrier thus enhancing the sub-barrier fusion cross-sections. The isovector reduction effect vanishes for symmetric systems as well as the $^{48}\text{Ca}+^{132}\text{Sn}$ system for which neutron pickup Q -values are all negative. These results provide a quantitative measure for the importance of transfer for sub-barrier fusion reactions. Furthermore, they elucidate the non-trivial dependence of sub-barrier fusion for neutron-rich systems and illustrate the importance of dynamical microscopic models that incorporate the nuclear structure and reactions on the same footing.

We thank K. Vo-Phuoc for useful discussions regarding the Ca+Sn systems. This work has been supported by the U.S. Department of Energy under grant No. DE-SC0013847 with Vanderbilt University and by the Australian Research Council Grant No. FT120100760.

Chapter 3

How the Pauli exclusion principle affects fusion of atomic nuclei

Abstract

The Pauli exclusion principle induces a repulsion between composite systems of identical fermions such as colliding atomic nuclei. Our goal is to study how heavy-ion fusion is impacted by this “Pauli repulsion”. We propose a new microscopic approach, the density-constrained frozen Hartree-Fock method, to compute the bare potential including the Pauli exclusion principle exactly. Pauli repulsion is shown to be important inside the barrier radius and increases with the charge product of the nuclei. Its main effect is to reduce tunnelling probability. Pauli repulsion is part of the solution to the long-standing deep sub-barrier fusion hindrance problem.

3.1 Introduction

The idea that identical fermions cannot occupy the same quantum state was proposed by Stoner ([Stoner, 1924](#)) and generalized by Pauli ([Pauli, 1925](#)). Known as the Pauli exclusion principle, it was at first empirical, but is now explained by the spin-statistic theorem in quantum field theory ([Fierz, 1939](#); [Pauli, 1940](#)). The importance of the “Pauli exclusion principle” cannot be overstated. For instance, it is largely responsible for the stability of matter against collapse, as demonstrated by the existence of white dwarfs. It is also expected to play a crucial role in the dynamics of systems of identical fermions. For instance, it could impact quantum tunnelling of complex systems which remains one of the greatest challenges of the quantum many-body problem. This work addresses the question of the effect of the Pauli exclusion principle on tunnelling of complex systems in the specific framework of nuclear physics which offers an ideal ground to test concepts of the quantum many-body problem.

The Pauli exclusion principle generates a repulsion between composite systems of identical fermions at short distance. For example, it repels atomic electron clouds in ionic

molecules due to the fermionic nature of the electron. Another example is the hard-core repulsion between two nucleons induced by identical quarks of the same color present in both nucleons. Naturally, a similar effect is expected to occur between atomic nuclei which are composite systems of nucleons. Indeed, it has been predicted that the Pauli exclusion principle should induce a repulsion (called “Pauli repulsion” hereafter) between strongly overlapping nuclei ([Fliessbach, 1971](#)).

The Pauli repulsion should then be included in the nucleus-nucleus potentials used to model reactions such as (in)elastic scattering, (multi)nucleon transfer, and fusion. However, Pauli repulsion is usually neglected in these models: it has been argued that the outcome of a collision between nuclei is mostly determined at a distance where the nuclei do not overlap much and thus the effects of the Pauli exclusion principle are minimized. This argument is based on the assumption that nuclei do not necessarily probe the inner part of the fusion barrier. However, at energies well above the barrier, the system could reach more compact shapes where one cannot neglect the effect of the Pauli principle anymore, as was shown by several authors in the 1970’s ([Fliessbach, 1971](#); [Brink and Stancu, 1975](#); [Zint and Mosel, 1975](#); [Beck et al., 1978](#); [Sinha and Moszkowski, 1979](#)). Similarly, for deep sub-barrier energies the inner turning-point of the fusion barrier entails significant overlap between the two nuclei ([Dasso and Pollarolo, 2003](#); [Umar et al., 2012b](#)).

Using a realistic microscopic approach to compute nucleus-nucleus bare potentials, we show that, in fact, the Pauli repulsion plays an important role on fusion at deep sub-barrier energies. In particular, it provides a natural (though only partial) explanation for the experimentally observed deep sub-barrier fusion hindrance ([Jiang et al., 2002](#); [Dasgupta et al., 2007](#); [Stefanini et al., 2010](#)) (see Ref. ([Back et al., 2014b](#)) for a review) which has led to various theoretical interpretations ([Ş. Mişcu and Esbensen, 2006b](#); [Mişcu and Esbensen, 2007](#); [Dasgupta et al., 2007](#); [Diaz-Torres et al., 2008](#); [Diaz-Torres, 2010](#); [Takatoshi Ichikawa et al., 2009](#); [Ichikawa, 2015](#)), although none of them directly consider Pauli repulsion as a possible mechanism.

3.2 Formalism

In order to investigate the effect of Pauli repulsion on heavy-ion fusion, we introduce a novel microscopic method called density-constrained frozen Hartree-Fock (DCFHF) to compute the interaction between nuclei while accounting exactly for the Pauli exclusion principle between nucleons. The microscopically derived bare nucleus-nucleus potential including Pauli repulsion is then used to study deep sub-barrier fusion. For simplicity, we focus on systems with doubly-magic nuclei which are spherical and non-superfluid. As an example, $^{16}\text{O}+^{16}\text{O}$, $^{40,48}\text{Ca}+^{40,48}\text{Ca}$, $^{16}\text{O}, ^{48}\text{Ca}+^{208}\text{Pb}$ reactions are studied theoretically and compared with experimental data.

To avoid the introduction of new parameters, we adopt the idea of Brueckner *et al.* ([Brueckner et al., 1968b](#)) to derive the bare potential from an energy density functional (EDF) $E[\rho]$ written as an integral of an energy density $\mathcal{H}[\rho(\mathbf{r})]$, i.e.,

$$E[\rho] = \int d\mathbf{r} \mathcal{H}[\rho(\mathbf{r})]. \quad (3.1)$$

The bare potential is obtained by requiring frozen ground-state densities ρ_i of each nucleus ($i = 1, 2$) which we compute using the Hartree-Fock (HF) mean-field approximation ([Hartree, 1928; Fock, 1930](#)). The Skyrme EDF ([Skyrme, 1956b](#)) is used both in HF calculations and to compute the bare potential. It accounts for the bulk properties of nuclear matter such as its incompressibility which is crucial at short distances ([Brueckner et al., 1968b; S. Mišicu and Esbensen, 2006b; Hossain et al., 2015](#)). Neglecting the Pauli exclusion principle between nucleons in different nuclei leads to the usual frozen Hartree-Fock (FHF) potential ([V. Yu. Denisov and Nörenberg, 2002; Kouhei Washiyama and Denis Lacroix, 2008; Cédric Simenel and Benoit Avez, 2008; Simenel, 2012b](#))

$$V_{FHF}(\mathbf{R}) = \int d\mathbf{r} \mathcal{H}[\rho_1(\mathbf{r}) + \rho_2(\mathbf{r} - \mathbf{R})] - E[\rho_1] - E[\rho_2], \quad (3.2)$$

where \mathbf{R} is the distance vector between the centres of mass of the nuclei. The FHF potential,

assumed to be central, can then directly be used to compute fusion cross-sections ([Simenel et al., 2013b](#); [Bourgin et al., 2016](#); [Vo-Phuoc et al., 2016](#)).

Our new DCFHF method is the static counter-part of the density-constrained time-dependent Hartree-Fock approach developed to extract the nucleus-nucleus potential of dynamically evolving systems ([Umar and Oberacker, 2006f](#)). In particular, this approach shows that the Pauli exclusion principle splits orbitals such that some states contribute attractively (bounding) and some repulsively (antibounding) to the potential ([Umar et al., 2012c](#)). In order to disentangle effects of the Pauli exclusion principle from the dynamics, we need to investigate the bare potential without polarisation effects. The dynamics can be included in a second step via, e.g., coupled-channels ([Simenel et al., 2013b](#)) or TDHF ([Kouhei Washiyama and Denis Lacroix, 2008](#); [Simenel et al., 2013d](#); [Umar et al., 2014b](#)) calculations. A discussion about the use of DCFHF potentials in coupled-channels calculations can be found in supplemental material [URL].

In the present method, it is important that the nuclear densities remain frozen as the densities of the HF ground-states of the collision partners. Consequently, the DCFHF approach facilitates the computation of the bare potential by using the self-consistent HF mean-field with exact frozen densities. The Pauli exclusion principle is included exactly by allowing the single-particle states, comprising the combined nuclear density, to reorganize to attain their minimum energy configuration and be properly antisymmetrized as the many-body state is a Slater determinant of all the occupied single-particle wave-functions. The HF minimization of the combined system is thus performed subject to the constraint that the local proton (p) and neutron (n) densities do not change:

$$\delta \langle H - \sum_{q=p,n} \int d\mathbf{r} \lambda_q(\mathbf{r}) [\rho_{1q}(\mathbf{r}) + \rho_{2q}(\mathbf{r} - \mathbf{R})] \rangle = 0, \quad (3.3)$$

where the $\lambda_{n,p}(\mathbf{r})$ are Lagrange parameters at each point of space constraining the neutron and proton densities. See Supplemental Material [URL] for details of the implementation

of the DCFHF method. This equation determines the state vector (Slater determinant) $|\Phi(\mathbf{R})\rangle$. The DCFHF potential, assumed to be central, is then defined as

$$V_{\text{DCFHF}}(R) = \langle \Phi(\mathbf{R}) | H | \Phi(\mathbf{R}) \rangle - E[\rho_1] - E[\rho_2]. \quad (3.4)$$

FHF and DCFHF calculations of bare nucleus-nucleus potentials were done in a three-dimensional Cartesian geometry with no symmetry assumptions using a static version of the code of Ref. ([Umar and Oberacker, 2006g](#)) and using the Skyrme SLy4d interaction ([Ka-Hae Kim et al., 1997](#)) which has been successful in describing various types of nuclear reactions ([Simenel, 2012b](#)). The three-dimensional Poisson equation for the Coulomb potential is solved by using Fast-Fourier Transform techniques and the Slater approximation is used for the Coulomb exchange term. The static HF equations and the DCFHF minimizations are implemented using the damped gradient iteration method. The box size used for all the calculations was chosen to be $60 \times 30 \times 30 \text{ fm}^3$, with a mesh spacing of 1.0 fm in all directions. These values provide very accurate results due to the employment of sophisticated discretization techniques ([Umar et al., 1991a,b](#)).

3.3 Results

The FHF (solid line) and DCFHF (dashed line) potentials are shown in Figs. 3.1(a-c) for $^{40}\text{Ca}+^{40}\text{Ca}$, $^{48}\text{Ca}+^{48}\text{Ca}$, and $^{16}\text{O}+^{208}\text{Pb}$ systems, respectively. We observe that the Pauli exclusion principle (present only in DCFHF) induces a repulsion at short distance in the three systems. The resulting effects are negligible outside the barrier and relatively modest near the barrier. However, the impact is more important in the inner barrier region, with the production of a potential pocket at short distance. Interestingly, the most important effect of Pauli repulsion is to increase the barrier width. It is then expected to reduce the sub-barrier tunneling probability as the latter decreases exponentially with the barrier width.

The impact of Pauli repulsion on the nucleus-nucleus potential varies with the systems. In $^{16}\text{O}+^{16}\text{O}$ (see Fig. 3.2), the pocket height is negative and Pauli repulsion is expected

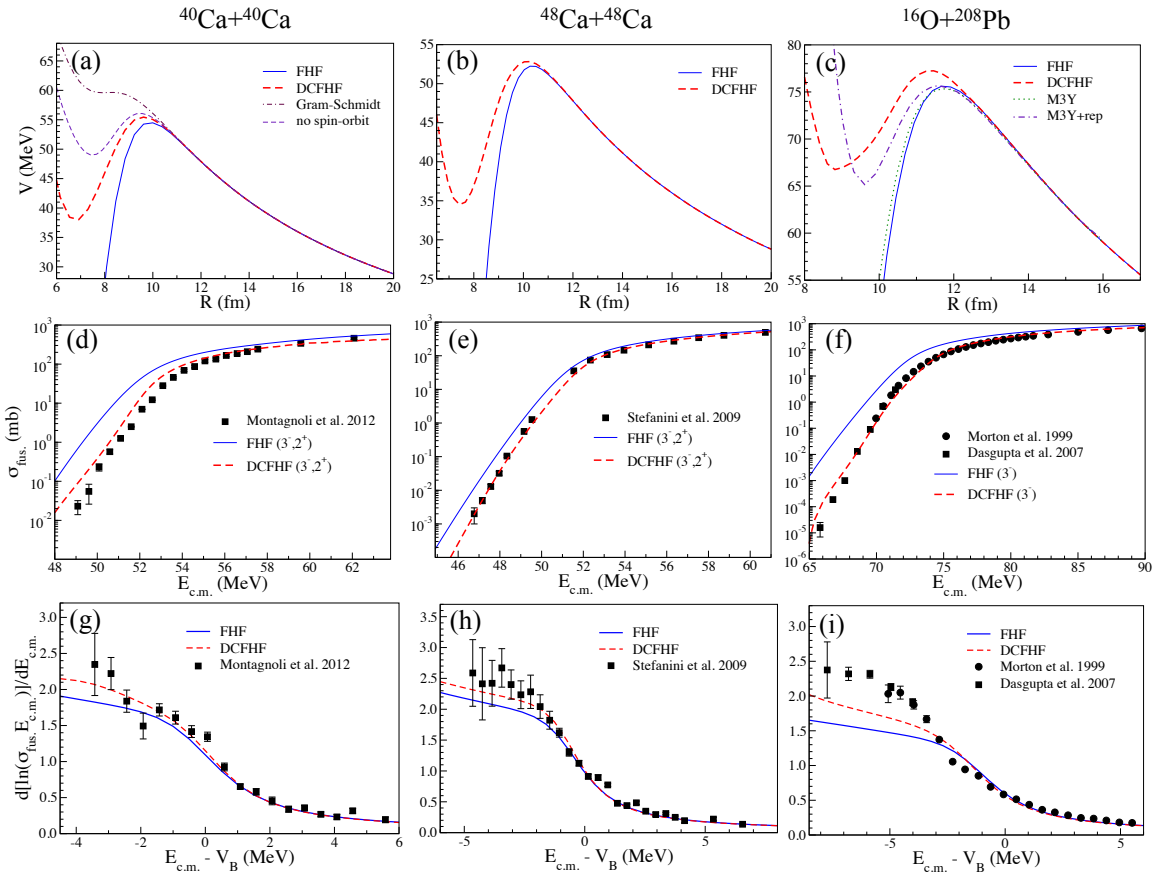


Figure 3.1: (a-c) Nucleus-nucleus potential without (FHF) and with (DCFHF) Pauli exclusion principle between nucleons of different nuclei. Potentials from a Gram-Schmidt anti-symmetrization (dotted-dashed line) and from DCFHF without rearrangement of the spin-orbit density (thin dashed line) are shown in panel (a). M3Y (dotted line) and M3Y+rep (dotted-dashed line) phenomenological potentials (Henning Esbensen and Şerban Mişcu, 2007) are shown in panel (c). (d-f) Experimental, (Morton et al., 1999; Dasgupta et al., 2007; Montagnoli et al., 2012; Stefanini et al., 2009) and theoretical (coupled-channels calculations with couplings to low-lying collective 2⁺ and/or 3⁻ states) fusion cross-sections $\sigma_{\text{fus.}}$ versus centre of mass energy $E_{\text{c.m.}}$. (g-i) Logarithmic slopes of $\sigma_{\text{fus.}} E_{\text{c.m.}}$ versus $E_{\text{c.m.}} - V_B$ where V_B is the barrier energy. In (g-i), FHF and DCFHF cross-sections are obtained without couplings, the latter being included via a shift in $E_{\text{c.m.}}$ (see text).

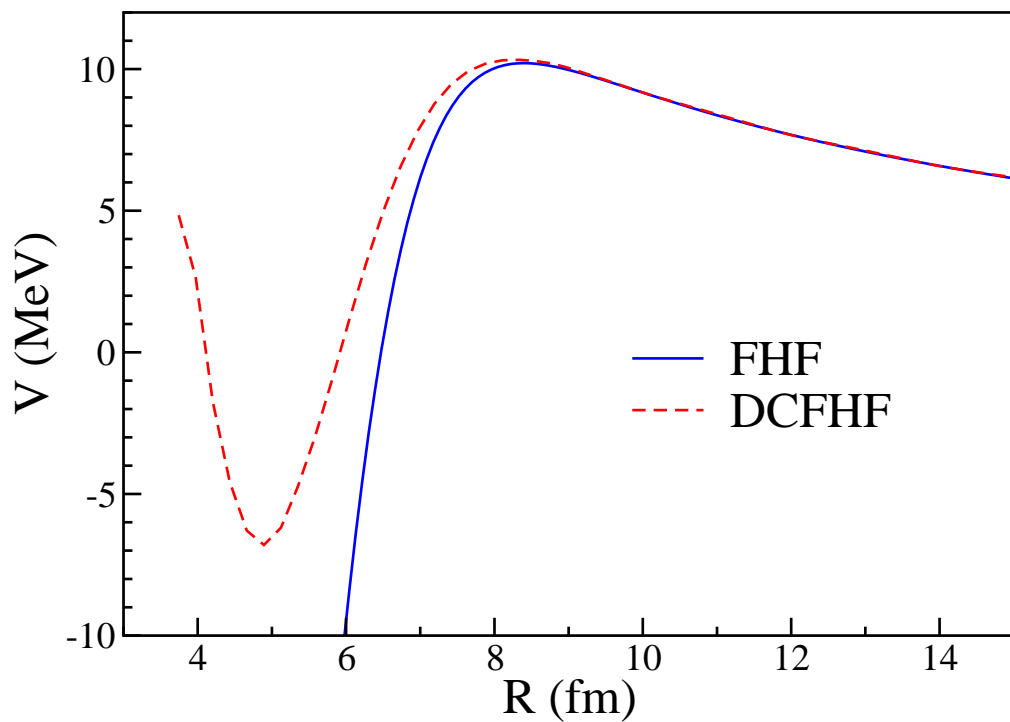
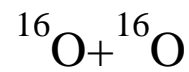


Figure 3.2: $^{16}\text{O} + ^{16}\text{O}$ nucleus-nucleus potential without (FHF) and with (DCFHF) Pauli exclusion principle between nucleons of different nuclei.

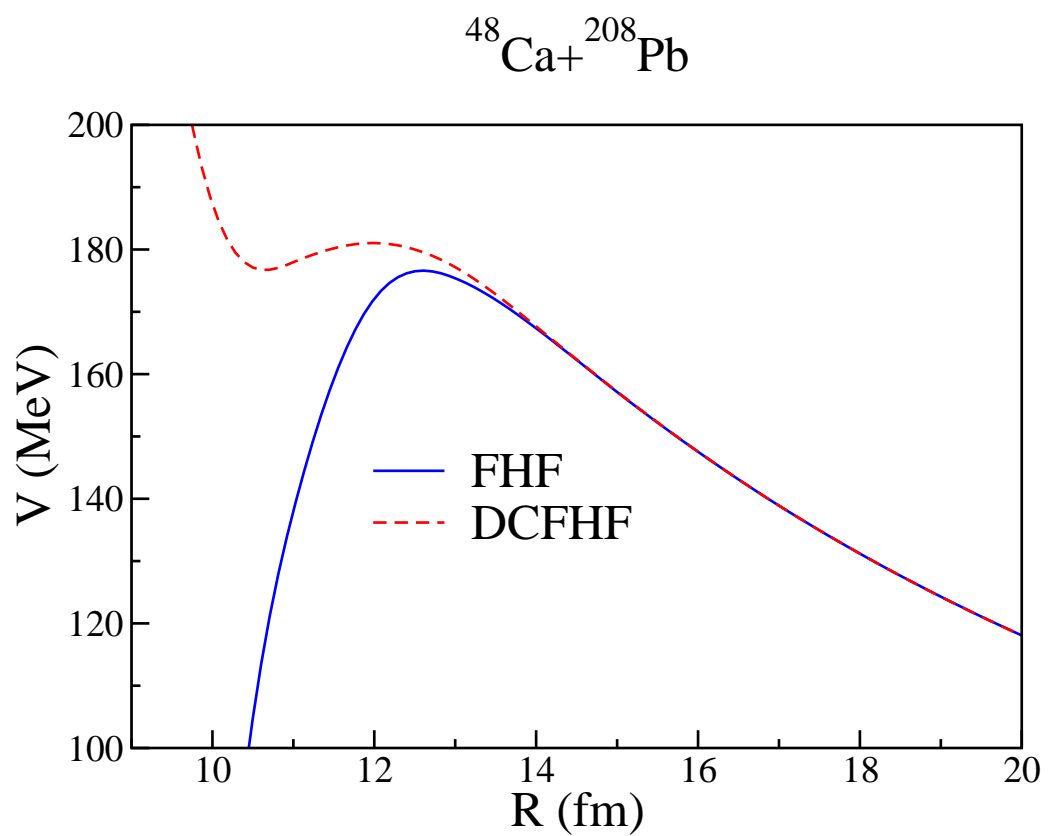


Figure 3.3: Same as Fig. 3.2 for $^{48}\text{Ca} + ^{208}\text{Pb}$.

to have a small impact on fusion in this system, except potentially at astrophysical energies. However, the pocket becomes shallower with increasing charge product Z_1Z_2 and almost disappears in $^{48}\text{Ca}+^{208}\text{Pb}$ (see Fig. 3.3). This is consistent with the fact that more nuclear overlap (and thus a larger Pauli repulsion) is required to compensate the larger Coulomb repulsion between the fragments. However, the two-body picture for such heavy systems is questionable. Fig. 3.3 shows indeed an extreme case where the DCFHF calculation predicts that fusion is impossible at 3% below the barrier. In fact, a smooth transition toward an adiabatic potential for the compound system is expected ([Takatoshi Ichikawa et al., 2009](#)) which would allow fusion to occur at lower energies. Finally, the Pauli repulsion not only depends on Z_1Z_2 , but also on the number of neutrons. This is illustrated in Fig. 3.4 which compares the DCFHF potentials for the three $^{40,48}\text{Ca}+^{40,48}\text{Ca}$ systems. At touching distance, additional neutrons increase the barrier radius (due to the neutron skin) and thus decrease its height. For this reason, $^{48}\text{Ca}+^{48}\text{Ca}$ has the lowest barrier and $^{40}\text{Ca}+^{40}\text{Ca}$ the largest one. However, $^{48}\text{Ca}+^{48}\text{Ca}$ also exhibits the strongest Pauli repulsion of the three systems. This is interpreted as an effect of the larger number of neutrons overlapping at short distance, thus increasing the Pauli repulsion. Note also that, once dynamics is included, fusion in these systems may behave differently and static effects on the bare potential could be washed out by the dynamics ([Vo-Phuoc et al., 2016](#)). In particular, fusion in the $^{40}\text{Ca}+^{48}\text{Ca}$ system is expected to be strongly affected by transfer channels ([Jiang et al., 2010; Montagnoli et al., 2012](#)), a feature which has only recently been studied in microscopic approach ([Godbey et al., 2017b](#)).

In principle, the Pauli repulsion is expected to be energy dependent. One source of energy dependence is the diminishing of the overlap between wave functions with relative kinetic momentum at higher energies reducing the Pauli repulsion ([Fliessbach, 1971; Brink and Stancu, 1975; Göritz and Mosel, 1976; Beck et al., 1978](#)). Other sources are the dependence of the EDF on the current density (needed for Galilean invariance) ([Brink and Stancu, 1975](#)) and non-local effects of the Pauli exclusion principle leading to an energy

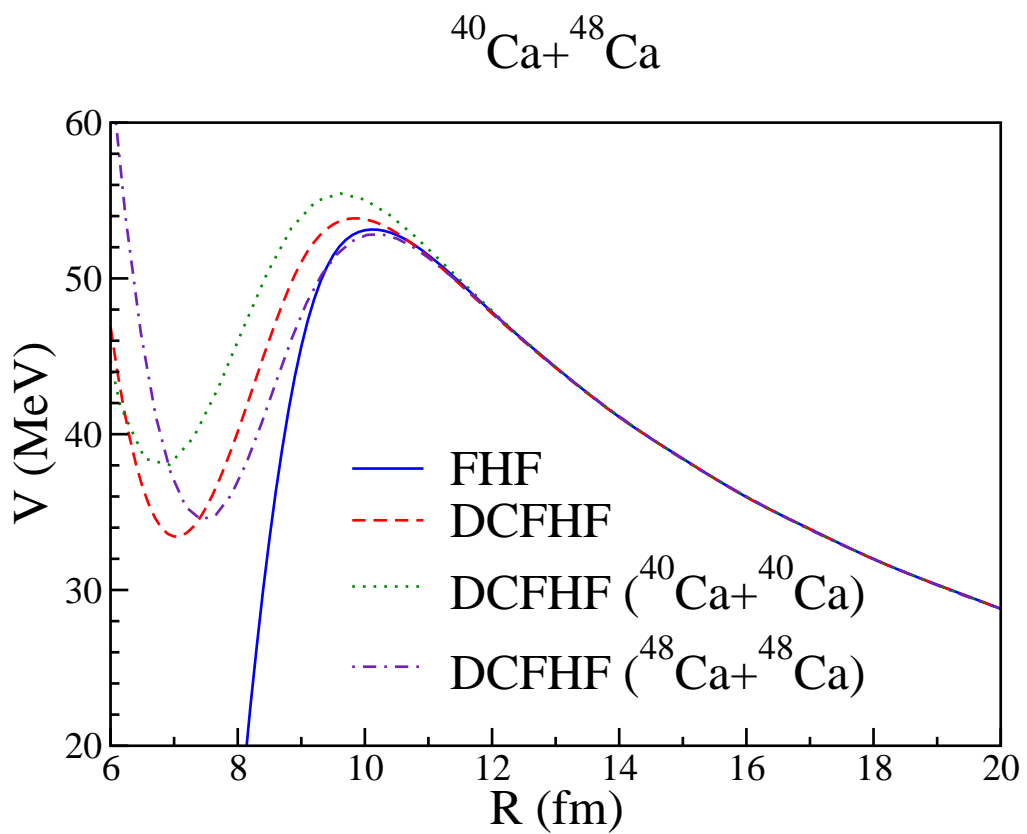


Figure 3.4: Same as Fig. 3.2 for $^{40}\text{Ca} + ^{48}\text{Ca}$. DCFHF potentials of the other $^A\text{Ca} + ^A\text{Ca}$ are also reported.

dependence of the local equivalent potential (Schmid et al., 1982; Chamon et al., 2002). These effects, however, are expected to impact the Pauli repulsion at energies much higher than the barrier (at least twice the barrier energy in $^{16}\text{O}+^{16}\text{O}$ (Fliessbach, 1971; Brink and Stancu, 1975)), and can then be neglected in near barrier fusion studies.

We have also tested other methods to account for Pauli repulsion in the bare potential. For instance, antisymmetrizing overlapping ground-state wave-functions (Fliessbach, 1971; Brink and Stancu, 1975; Zint and Mosel, 1975) can be done with a Gram-Schmidt procedure. Although the resulting potential properly accounts for the Pauli exclusion principle, it leads to much higher repulsion as illustrated in Fig. 3.1(a) (dotted-dashed line) for the $^{40}\text{Ca}+^{40}\text{Ca}$ system in which the potential pocket, and therefore the fusion barrier, simply disappear. Let us use a simple model to explain the origin of this large repulsion. Consider two single-particle wave functions $\varphi_{1,2}$ belonging to the HF ground-states of the two different nuclei and which have a small overlap in the neck region at \mathbf{r}_0 only: $\varphi_1^*(\mathbf{r})\varphi_2(\mathbf{r}) \simeq \alpha\delta(\mathbf{r} - \mathbf{r}_0)$. By definition, the total frozen density of these two nucleons is $\rho_F = |\varphi_1|^2 + |\varphi_2|^2$. The evaluation of observables, however, requires antisymmetrized wave-functions such as $\tilde{\varphi}_{\pm} = \mathcal{N}_{\pm}(\varphi_1 \pm \varphi_2)$ with normalization coefficients $\mathcal{N}_{\pm} = (2 \pm \alpha \pm \alpha^*)^{-1/2}$ and overlaps $\langle \tilde{\varphi}_- | \tilde{\varphi}_+ \rangle = 0$. The corresponding density reads

$$\tilde{\rho} = |\tilde{\varphi}_+|^2 + |\tilde{\varphi}_-|^2 \simeq \rho_F - \frac{1}{2}(\alpha + \alpha^*)^2\delta(\mathbf{r} - \mathbf{r}_0).$$

It is reduced in the neck compared to the frozen density and thus leads to a smaller nuclear attraction between the nuclei or, equivalently, to a spurious repulsion between the fragments as seen in Fig. 3.1(a). Naive antisymmetrization procedures are then not compatible with the frozen density picture. This was also recognized in the earlier work concerning α -nucleus scattering studies (Fliessbach, 1975), where specialized normalization operators were developed to reconstruct the states following a Gram-Schmidt orthogonalization. However, these methods could only be applied using semi-analytic methods. The DCFHF

achieves this without any approximation. These methods have also been subsequently criticized by groups performing resonating group method (RGM) calculations ([Aoki and Horiuchi, 1983](#); [Wada and Horiuchi, 1987](#); [Tohsaki et al., 1975](#); [Tang et al., 1978](#)). In principle, RGM does provide a theoretical approach to construct inter nuclear potentials with full antisymmetrization. However, such calculations have thus far been limited to light systems and direct reactions due to their complexity.

Let us now discuss another traditional method which is to account for Pauli repulsion simply by increasing the kinetic energy density $\tau(\mathbf{r})$ (e.g., via the Thomas-Fermi model) ([Brink and Stancu, 1975](#); [Zint and Mosel, 1975](#); [Beck et al., 1978](#); [V. Yu. Denisov and Nesterov, 2010](#); [Nesterov, 2013](#)). This method would be valid if the effect of the Pauli exclusion principle was only to rearrange the kinetic energy term $\frac{\hbar^2}{2m}\tau$ without impacting other terms of the functional. In fact, the EDF also depends on τ via the “ $t_{1,2}$ ” momentum dependent terms of the Skyrme effective interaction ([Skyrme, 1956b](#)) and, then, a variation of $\tau(\mathbf{r})$ also affects the nuclear part of the potential ([Brink and Stancu, 1975](#); [V. Yu. Denisov and Nesterov, 2010](#)). At the same time, we have also observed that including the Pauli exclusion principle has a strong impact on the spin-orbit energy. This is illustrated in Fig. 3.1(a) for the $^{40}\text{Ca}+^{40}\text{Ca}$ system. For this system, removing the spin-orbit interaction in the FHF potential (not shown in the figure) has little effect, but strongly increases the repulsion between the fragments in the DCFHF potential (thin dashed line). This shows that the spin-orbit energy absorbs a large part of the Pauli repulsion. Thus, the Pauli exclusion principle has a more complicated effect than just increasing the kinetic energy.

Coupled-channels calculations of fusion cross-sections were performed with the cc-FULL code ([Hagino et al., 1999](#)) using Woods-Saxon fits of the FHF and DCFHF potentials. By default, the incoming wave boundary condition (IWBC) was used. For shallow pocket potentials, however, the IWBC should be replaced by an imaginary potential at the potential pocket to avoid numerical instabilities. This is done for calculations with the $^{16}\text{O}+^{208}\text{Pb}$ DCFHF potential using a modified version of ccFULL with Woods-Saxon pa-

rameters $\{V_I = 30 \text{ MeV}, a_I = 1 \text{ fm}, r_I = 0.3 \text{ fm}\}$ for the imaginary potential. Couplings to the low-lying collective 2^+ (in calcium isotopes) and 3^- states are included with standard values of the coupling constants (Morton et al., 1999; Rowley and Hagino, 2010). In `CCFULL`, one (two) vibrational mode(s) can be included in the projectile (target). For the 2^+ states, we then use the fact that, for symmetric systems, the mutual excitation of one-phonon states in both nuclei can be approximated by one phonon with a coupling constant scaled by $\sqrt{2}$ (Esbensen and Landowne, 1987). Here, the CC calculations are kept simple and include only the most relevant couplings. Improvements could be obtained, e.g., by including anharmonicity of the multi-phonon states (Yao and Hagino, 2016). The resulting fusion cross-sections are plotted in Figs. 3.1(d-f). Calculations with the FHF potential systematically overestimate the data while the DCFHF potential leads to a much better agreement with experiment at all energies, and ranging over eight orders of magnitude in cross-sections. This shows the importance of taking into account Pauli repulsion in the bare potential for fusion calculations. We emphasise that these calculations are performed without adjustable parameters.

The behaviour of fusion at deep sub-barrier energies is often studied using the logarithmic slope $d \ln(\sigma_{fus.} E_{c.m.}) / dE_{c.m.}$. Large logarithmic slopes are a signature of a rapid decrease of $\sigma_{fus.}$ with decreasing energy. Deep-sub-barrier fusion hindrance is characterised by the failure of theoretical models to reproduce large logarithmic slopes observed experimentally at low energy. To avoid numerical instabilities due to shallow potentials in the calculations of logarithmic slopes, couplings to internal excitations of the nuclei have been removed in the calculations of barrier transmission and accounted for via an overall lowering of V_B by less than 5% depending on the structure of the reactants (Dasgupta et al., 2007). Indeed, it has been shown that couplings have little effects on the logarithmic slope at these energies (Dasgupta et al., 2007). We see in Fig. 3.1(g-i) that the inclusion of Pauli repulsion in DCFHF indeed increases the logarithmic slope at low energy.

3.4 Conclusion

Although Pauli repulsion is shown to play a crucial role, it is not yet sufficient to reproduce experimental data at deep sub-barrier energies. Other contributions are expected to come from dissipative effects (Dasgupta et al., 2007) and from the transition between the nucleus-nucleus potential to the one-nucleus adiabatic potential (Takatoshi Ichikawa et al., 2009). However, repulsive effects from the incompressibility of nuclear matter invoked in (Ş. Mişicu and Esbensen, 2006b) are not observed in our microscopic calculations. Both the FHF and DCFHF calculations use the same Skyrme functional (SLy4d) with a realistic compression modulus of the symmetric nuclear matter $K_\infty \simeq 230$ MeV. Although the FHF potential properly takes into account effects due to incompressibility, it is very close to standard phenomenological potentials. We illustrate this with the example of the M3Y potential (Ş. Mişicu and Esbensen, 2006b) in Fig. 3.1(c). The addition of a repulsive component at short distance [M3Y+rep parametrisation shown with a dotted-dashed line Fig. 3.1(c)], introduced phenomenologically in (Ş. Mişicu and Esbensen, 2006b) to explain experimental fusion data at deep sub-barrier energies, then cannot be justified by an effect of incompressibility. It is more likely that it simulates other effects such as Pauli repulsion.

C.S. thanks E. Simpson for useful discussions. This work has been supported by the Australian Research Council Grant No. FT120100760, and by the U.S. Department of Energy under grant No. DE-SC0013847 with Vanderbilt University.

Chapter 4

The influence of tensor force on the microscopic heavy-ion interaction potential abstract

[Background] The tensor interaction is known to play an important role in the nuclear structure studies of exotic nuclei. However, most microscopic studies of low-energy nuclear reactions neglect the tensor force, resulting in a lack of knowledge concerning the effect of the tensor force on heavy-ion collisions. An accurate description of the heavy-ion interaction potential is crucial for understanding the microscopic mechanisms of heavy-ion fusion dynamics. Furthermore, the building blocks of the heavy-ion interaction potential in terms of the ingredients of the effective nucleon-nucleon interaction provides the physical underpinnings for connecting the theoretical results with experiment. The tensor force has never been incorporated for calculating the nucleus-nucleus interaction potential.

[Purpose] The theoretical study of the influence of the tensor force on heavy-ion interaction potentials is required to further our understanding of the microscopic mechanisms entailed in fusion dynamics.

[Method] The full Skyrme tensor force is implemented into the static Hartree-Fock and dynamic density-constrained time-dependent Hartree-Fock (DC-TDHF) theory to calculate both static (frozen density) and dynamic microscopic interaction potentials for reactions involving exotic and stable nuclei.

[Results] The static potentials are found to be systematically higher than the dynamical results, which are attributed to the microscopic dynamical effects included in TDHF. We also show that the dynamical potential barriers vary more significantly by the inclusion of tensor force than the static barriers. The influence of isoscalar and isovector tensor terms is also investigated with the TIJ set of forces. For light systems, the tensor force is found to have an imperceptible effect on the nucleus-nucleus potential. However, for medium and heavy spin-unsaturated reactions, the potentials may change from a fraction of an MeV to

almost 2 MeV by the inclusion of tensor force, indicating a strong impact of the tensor force on sub-barrier fusion.

[Conclusions] The tensor force could indeed play a large role in the fusion of nuclei, with spin-unsaturated systems seeing a systematic increase in ion-ion barrier height and width. This fusion hindrance is partly due to static, ground state effects from the inclusion of the tensor force, though additional hindrance appears when studying nuclear dynamics.

4.1 Introduction

With the increasing availability of radioactive ion beams, the study of structure and reactions of exotic nuclei is one of the most fascinating research areas in nuclear physics ([Balantekin et al., 2014a](#)). The exotic nuclei display distinct features from those seen in typical stable nuclei, which is attributed partly to the unique characteristics of the nucleon-nucleon interaction. The tensor interaction between nucleons is one such characteristic and is well known to be important in nuclear structure properties ([Lesinski et al., 2007a](#)), e.g., the shell evolution of exotic nuclei ([Otsuka et al., 2006a](#)), spin-orbit splitting ([Colò et al., 2007a](#)), and Gamow-Teller and charge exchange spin-dipole excitations ([Bai et al., 2010a](#)). However, its role in low-energy nuclear reactions is poorly understood as the tensor force has been neglected in most reaction dynamics calculations. In particular, regarding nuclear dynamics, the tensor force changes not only the spin-orbit splitting but also the intrinsic excitations which may give rise to dynamical effects which are more complicated than those arising from simple shell evolution. The study of the effects of the tensor force on heavy-ion fusion dynamics will lead to a better understanding of the effective nucleon-nucleon interaction and of the correlations present in these many-body systems.

The study of heavy-ion interaction potentials is of fundamental importance for above barrier and sub-barrier fusion reactions ([Back et al., 2014a](#)). In general, two categories of theoretical approaches are used for calculating ion-ion potentials. In the first category, phenomenological models such as the Bass model ([Bass, 1974a](#)), the proximity potential ([Ran-](#)

drup and Vaagen, 1978a; Seiwert et al., 1984a), the double-folding potential (Satchler and Love, 1979a; Rhoades-Brown and Oberacker, 1983a), and driven potential from dinuclear system model (Adamian et al., 2004a; Wang et al., 2012a; Zhu et al., 2016a; Bao et al., 2016a; Feng, 2017a) could be mentioned. Although these methods have been successful in explaining particular aspects of reaction data (Randrup, 1978; Fazio et al., 2004), the uncertainty of macroscopic parameters and the lack of microscopic origins restrict their predictive power and may obscure the underlying physical processes. Second category contains the semi- and fully microscopic approaches to obtain potentials by including the interactions of the constituents (Möller et al., 2004a; Guo et al., 2004a, 2005a, 2007b; Lu et al., 2014a). One common assumption used in many of the semi-microscopic calculations is that of the frozen density or sudden approximation (Brueckner et al., 1968a), in which the nuclear densities are unchanged during the computation of the nucleus-nucleus potential as a function of internuclear distance. This approximation may result in an unphysical potential at deep sub-barrier energies, where the inner turning point of the interaction potential corresponds to large nuclear overlap. Various remedies have been developed to address this issue within the confines of the coupled-channels approach (Ş. Mişcu and Esbensen, 2006a; Ichikawa et al., 2007). In other microscopic approaches, such as the constrained mean-field methods, although the nuclear densities are allowed for the rearrangement, the potential energy path is obtained by the static adiabatic approximation, thus ignoring the dynamical effects.

In recent years we have developed the density-constrained time-dependent Hartree-Fock (DC-TDHF) approach for calculating heavy-ion interaction potentials, which naturally incorporate all of the dynamical effects included in the time-dependent Hartree-Fock (TDHF) description of the collision process (Umar and Oberacker, 2006b). These effects include nucleon transfer, couplings between the collective motion and intrinsic degrees of freedom, neck formation, internal excitations, and deformation effects to all orders. The method is based on the TDHF evolution of the nuclear dynamics coupled with density-

constrained (DC) Hartree-Fock (HF) calculations to obtain the ion-ion potential. In contrast to other mean-field based microscopic methods, the DC-TDHF approach doesn't need to introduce external constraining operators which assume that the collective motion is confined to the constrained phase space. That means that the many-body system selects its evolutionary path by itself following the microscopic dynamics. We have applied this method for a wide range of reactions (Umar and Oberacker, 2006c,d, 2008a; Umar et al., 2008a, 2009a; Oberacker et al., 2010a; Keser et al., 2012a; Umar et al., 2012a, 2014a; Godbey et al., 2017a) and found reasonable agreement between the measured fusion cross sections and the DC-TDHF results. To our knowledge, neither the phenomenological nor microscopic methods for calculating ion-ion potential include the tensor force between nucleons, which is an important component of the nuclear force. Our work is the first attempt to investigate the effect induced by the tensor force on heavy-ion interaction potentials.

The TDHF approach is a well-defined framework and provides a useful foundation for a fully microscopic many-body theory. Quantum effects are considered, which is essential for the manifestation of shell effects during the collision dynamics. Recently, the effect of the tensor force in heavy-ion collisions has been studied using direct TDHF calculations (Frassacco et al., 2012a; Dai et al., 2014b; Stevenson et al., 2016a; Shi and Guo, 2017b; Guo et al., 2018b). Furthermore, the TDHF approach provides a deeper understanding of nuclear dynamics, as seen in recent applications to fusion (Simenel et al., 2004; Umar et al., 2009a; Oberacker et al., 2010a; Lu Guo and Takashi Nakatsukasa, 2012a; Keser et al., 2012a; Umar et al., 2012a; Simenel et al., 2013c; Umar et al., 2014a; Washiyama, 2015; Tohyama and Umar, 2016; Godbey et al., 2017a; Simenel et al., 2017a), quasifission (Cédric Golabek and Cédric Simenel, 2009a; Oberacker et al., 2014a; Umar et al., 2015a, 2016a; Chong Yu and Lu Guo, 2017a), transfer reactions (Kouhei Washiyama et al., 2009; Simenel, 2010a, 2011a; Scamps and Lacroix, 2013a; Kazuyuki Sekizawa and Kazuhiro Yabana, 2013a; Wang and Guo, 2016a; Sekizawa and Yabana, 2016a; Sekizawa, 2017a), fission (Simenel and Umar, 2014a; Scamps et al., 2015a; Goddard et al., 2015a, 2016a; Bul-

gac et al., 2016; Tanimura et al., 2017a), and deep inelastic collisions (Maruhn et al., 2006; Guo et al., 2007a, 2008; Iwata and Maruhn, 2011; Dai et al., 2014a,b; Stevenson et al., 2016a; Guo et al., 2017a; Shi and Guo, 2017b; Umar et al., 2017a). For recent reviews see Refs. (Simenel, 2012a; Nakatsukasa et al., 2016; Simenel and Umar, 2018a).

This article is organized as follows. In Sec. 4.2, we summarize the theoretical formalism of Skyrme energy functional with the tensor force included and the TDHF and DC-TDHF approaches. Section 4.3 presents the systematic analysis of the impact of the tensor force on heavy-ion interaction potentials. A summary is given in Sec. 4.4.

4.2 Theoretical framework

Despite the wide application of the TDHF approach, various assumptions and approximations that may affect the TDHF results have been employed in the past. This led to an occasional imperfect or even incorrect reproduction of experimental data. To remedy these problems a considerable theoretical and computational effort has been undertaken for increased numerical accuracy and improved effective interactions. For instance, the inclusion of the spin-orbit interaction solved an early conflict between TDHF predictions and experimental observations (Umar et al., 1986, 1989) and turned out to play an important role in fusion and dissipation dynamics (Maruhn et al., 2006; Dai et al., 2014a). In recent years it has become feasible to perform TDHF calculations on a three-dimensional Cartesian grid without any symmetry restrictions and with accurate numerical methods. In addition, the quality of energy density functional (EDF) has been substantially improved. The time-odd terms in particular have shown to be non-negligible in heavy-ion collisions (Umar and Oberacker, 2006a). However, there are still important components of the basic theory that have not yet been fully implemented, such as the tensor force between nucleons. In order to study the role of tensor force in heavy-ion interaction potential, we incorporate the full tensor force into the microscopic TDHF and DC-TDHF approaches.

4.2.1 Full Skyrme energy functional

Most TDHF calculations employ the Skyrme effective interaction ([Skyrme, 1956a](#)), in which the two-body tensor force was proposed in its original form as

$$\begin{aligned} v_T = & \frac{t_e}{2} \left\{ [3(\sigma_1 \cdot \mathbf{k}')(\sigma_2 \cdot \mathbf{k}') - (\sigma_1 \cdot \sigma_2)\mathbf{k}'^2] \delta(\mathbf{r}_1 - \mathbf{r}_2) \right. \\ & + \delta(\mathbf{r}_1 - \mathbf{r}_2) [3(\sigma_1 \cdot \mathbf{k})(\sigma_2 \cdot \mathbf{k}) - (\sigma_1 \cdot \sigma_2)\mathbf{k}^2] \Big\} \\ & + t_o \left\{ 3(\sigma_1 \cdot \mathbf{k}') \delta(\mathbf{r}_1 - \mathbf{r}_2) (\sigma_2 \cdot \mathbf{k}) - (\sigma_1 \cdot \sigma_2) \mathbf{k}' \delta(\mathbf{r}_1 - \mathbf{r}_2) \mathbf{k} \right\}. \end{aligned} \quad (4.1)$$

The coupling constants t_e and t_o represent the strengths of triplet-even and triplet-odd tensor interactions, respectively. The operator $\mathbf{k} = \frac{1}{2i}(\nabla_1 - \nabla_2)$ acts on the right and $\mathbf{k}' = -\frac{1}{2i}(\nabla'_1 - \nabla'_2)$ acts on the left.

It is natural to represent the total energy of the system

$$E = \int d^3r \mathcal{H}(\rho, \tau, \mathbf{j}, \mathbf{s}, \mathbf{T}, \mathbf{F}, J_{\mu\nu}; \mathbf{r}) \quad (4.2)$$

in terms of the energy functional. The functional is composed by the number density ρ , kinetic density τ , current density \mathbf{j} , spin density \mathbf{s} , spin-kinetic density \mathbf{T} , the tensor-kinetic density \mathbf{F} , and spin-current pseudotensor density J ([Stevenson et al., 2016a](#)). The full version of Skyrme EDF is expressed as

$$\begin{aligned} \mathcal{H} = & \mathcal{H}_0 + \sum_{t=0,1} \left\{ A_t^s s_t^2 + (A_t^{\Delta s} + B_t^{\Delta s}) \mathbf{s}_t \cdot \Delta \mathbf{s}_t + B_t^{\nabla s} (\nabla \cdot \mathbf{s}_t)^2 \right. \\ & + B_t^F (\mathbf{s}_t \cdot \mathbf{F}_t - \frac{1}{2} \left(\sum_{\mu=x}^z J_{t,\mu\mu} \right)^2 - \frac{1}{2} \sum_{\mu,\nu=x}^z J_{t,\mu\nu} J_{t,\nu\mu}) \\ & \left. + (A_t^T + B_t^T) (\mathbf{s}_t \cdot \mathbf{T}_t - \sum_{\mu,\nu=x}^z J_{t,\mu\nu} J_{t,\mu\nu}) \right\}, \end{aligned} \quad (4.3)$$

where \mathcal{H}_0 is the simplified functional used in the Sky3D TDHF code ([Maruhn et al., 2014a](#)) and most TDHF calculations. The terms containing the coupling constants A arise from the Skyrme central force and those with B from the tensor force. The definitions of both A

and B can be found in Refs. (Lesinski et al., 2007a; Davesne et al., 2009a). All the time-even and time-odd terms in Eq. (4.3) have been implemented numerically in the mean-field Hamiltonians of the HF, TDHF and DC-TDHF approaches. As pointed out in Refs. (Lesinski et al., 2007a; Stevenson et al., 2016a), the terms containing the gradient of spin density may cause spin instability in both nuclear structure and reaction studies, hence the terms of $\mathbf{s}_t \cdot \Delta \mathbf{s}_t$ and $(\nabla \cdot \mathbf{s}_t)^2$ have been turned off in all calculations.

4.2.2 TDHF approach

Given a many-body Hamiltonian, the action can be constructed as

$$S = \int_{t_1}^{t_2} dt \langle \Phi(\mathbf{r}, t) | H - i\hbar \partial_t | \Phi(\mathbf{r}, t) \rangle, \quad (4.4)$$

where Φ is the time-dependent many-body wave function. In TDHF approach the many-body wave function $\Phi(\mathbf{r}, t)$ is approximated as a single time-dependent Slater determinant composed of an antisymmetrized product of the single particle states $\phi_\lambda(\mathbf{r}, t)$

$$\Phi(\mathbf{r}, t) = \frac{1}{\sqrt{N!}} \det \{\phi_\lambda(\mathbf{r}, t)\}, \quad (4.5)$$

and this form is kept at all times in the dynamical evolution. By taking the variation of the action with respect to the single-particle wave functions, the set of nonlinear coupled TDHF equations in the multidimensional space-time phase space

$$i\hbar \frac{\partial}{\partial t} \phi_\lambda(\mathbf{r}, t) = h \phi_\lambda(\mathbf{r}, t) \quad (4.6)$$

yields the most probable time-dependent mean-field path, where h is the HF single-particle Hamiltonian. The set of nonlinear TDHF equations has been solved on three-dimensional coordinate space without any symmetry restrictions and with modern, accurate numerical methods (Umar and Oberacker, 2006a; Maruhn et al., 2014a).

4.2.3 Dynamical potential from DC-TDHF approach

Since TDHF theory describes the collective motion of fusion dynamics in terms of semi-classical trajectories, the sub-barrier quantum tunneling of the many-body wave function can not be included. Consequently, direct TDHF calculations can not be used to describe sub-barrier fusion. At present, all sub-barrier fusion calculations assume that there exists an ion-ion potential which depends on the internuclear distance. The microscopic DC-TDHF approach ([Umar and Oberacker, 2006b](#)) is employed to extract the nucleus-nucleus potential from the TDHF time evolution of the dinuclear system. In this approach, at certain time during the evolution, the instantaneous TDHF density is used to perform a static HF energy minimization

$$\delta\langle\Psi_{DC}|H - \int d^3r \lambda(\mathbf{r})\rho(\mathbf{r})|\Psi_{DC}\rangle = 0, \quad (4.7)$$

by constraining the proton and neutron densities to be equal to the instantaneous TDHF densities. Since we are constraining the total density, all moments are simultaneously constrained. DC-TDHF calculations give the adiabatic reference state for a given TDHF state, which is the Slater determinant with the lowest energy for a given density. The minimized energy

$$E_{DC}(\mathbf{R}) = \langle\Psi_{DC}|H|\Psi_{DC}\rangle \quad (4.8)$$

is the density-constrained energy. Since this density-constrained potential still contains the binding energies of individual nuclei which should be subtracted out, the heavy-ion interaction potential is deduced as

$$V(\mathbf{R}) = E_{DC}(\mathbf{R}) - E_{A1} - E_{A2}, \quad (4.9)$$

where E_{A1} and E_{A2} are the binding energies of the two individual nuclei. One should note that this procedure does not affect the TDHF time evolution and contains no free parameters

or normalization.

4.2.4 Bare potential from FHF approach

In previous subsection, the DC-TDHF technique has been introduced to compute the nucleus-nucleus potential in a dynamical microscopic way. All of the dynamical effects included in TDHF is then directly incorporated in the potential. Here we look for a different approach to produce a bare potential which does not include any dynamical contribution, since we aim to disentangle the static and dynamical effects of the tensor force. The bare nucleus-nucleus potential is defined as the interaction potential between the nuclei in their ground states. In addition, to preserve the consistency with microscopic calculations, it is necessary to compute the potential from the same EDF used in HF, TDHF, and DC-TDHF calculations. This is possible using the frozen Hartree-Fock (FHF) technique ([Simenel et al., 2013a](#)), assuming that the densities of the target and projectile remain constant and equal to their respective ground state densities. The potential can then be expressed as

$$V_{\text{FD}}(\mathbf{R}) = E[\rho_1 + \rho_2](\mathbf{R}) - E[\rho_1] - E[\rho_2], \quad (4.10)$$

where ρ_1 and ρ_2 are HF ground state densities of the fragments, and $E[\rho_1 + \rho_2]$ is the same Skyrme EDF as defined in Eqs. (4.2) and (4.3). In the FHF approach, the Pauli principle between pairs of nucleons belonging to different collision partners has been neglected. When the overlap between the density distributions is small, the barrier is almost unaffected by the inclusion of the Pauli principle. However, at larger overlaps of the densities where the Pauli principle is expected to play a more important role, the FHF approximation may not properly account for the potential, particularly the inner part ([Simenel et al., 2017a](#)).

4.3 results

The concept of using density as a constraint for calculating collective states from TDHF time evolution was first introduced in the mid 1980s ([Cusson et al., 1985](#)), and was used for

the microscopic description of nuclear molecular resonances ([Umar et al., 1985](#)). In recent years, the DC-TDHF approach has demonstrated its feasibility and success in explaining sub-barrier fusion dynamics for a wide range of reactions. This is rather remarkable given the fact that the only input in DC-TDHF is the Skyrme effective interaction, and there are no adjustable parameters. In the present work, we focus on how the tensor force affect the nucleus-nucleus potential which is vital for the theoretical analysis of sub-barrier fusion dynamics. We have thus chosen ten representative reactions with proton and neutron numbers of reaction partners corresponding to the magic numbers 8, 20, 28, 50, and 82, in which the spin-saturated shells are 8 and 20.

In the numerical simulation the static HF ground state for the reaction partner has been calculated on the symmetry-unrestricted three-dimensional grid. The resulting Slater determinants for each nucleus comprise the larger Slater determinant describing the colliding system during the dynamical evolution. The TDHF time propagation is performed using a Taylor-series expansion up to the sixth order of the unitary boost operator with a time step of $0.2 \text{ fm}/c$. For the dynamical evolution, we use a numerical box of 48 fm along the collision axis and 24 fm in the other two directions and a grid spacing of 1.0 fm. The initial separation between the two nuclei is 20 fm. The choice of these parameters assures good numerical accuracy in the unrestricted TDHF evolution. We have simultaneously performed the density constraint calculations utilizing the DC-TDHF method at every 10-20 time steps (corresponding to $2\text{-}4 \text{ fm}/c$ interval). The convergence property in DC-TDHF calculations is as good if not better than in the traditional constrained HF with a constraint on a single collective degree of freedom.

We employ the Skyrme interaction in the calculations, in which the tensor force has been constructed in two ways. One is to add the force perturbatively to the existing standard interactions, for instance, the existing Skyrme parameter SLy5 ([Chabanat et al., 1998](#)) plus tensor force, denoted as SLy5t ([Colò et al., 2007b](#)). The comparison between calculations with SLy5 and SLy5t addresses the question on how much of the changes is caused by

tensor force itself. Another approach is to readjust the full set of Skyrme parameters self-consistently. This strategy has been adopted in Ref. ([Lesinski et al., 2007a](#)) and led to the set of *TIJ* parametrizations with a wide range of isoscalar and isovector tensor couplings. Due to its fitting strategy, the contributions from the tensor force and the rearrangement of all other terms could be physically entangled.

For light systems, we choose the spin-unsaturated $^{12}\text{C} + ^{12}\text{C}$ and spin-saturated $^{16}\text{O} + ^{16}\text{O}$ reactions for comparison. As we have reported in Ref. ([Umar et al., 2014a](#)), the potential barriers are sensitive to the colliding energy. Hence, the same initial energy, close to the Coulomb barrier, is used for the reaction with and without tensor forces. In Fig. 4.1, we plot the ion-ion potentials obtained from Eq. (4.9) using the DC-TDHF approach for (a) $^{12}\text{C} + ^{12}\text{C}$ at $E_{\text{c.m.}} = 8$ MeV and (b) $^{16}\text{O} + ^{16}\text{O}$ at $E_{\text{c.m.}} = 12$ MeV with SLy5 (open circle) and SLy5t (solid circle) forces. Both nuclei, ^{12}C and ^{16}O , show spherical ground states with tensor (SLy5t) and without tensor (SLy5) forces, which are in agreement with experimental data and other calculations. The correct description of the initial shape of target and projectile nucleus is important for the dynamical evolution of heavy-ion collisions. We see that for the spin-unsaturated system $^{12}\text{C} + ^{12}\text{C}$, the potential with the tensor force included has an overall higher interaction barrier than without the tensor force, although the difference of the potential barrier peak is small at roughly 0.07 MeV. For the spin-saturated system $^{16}\text{O} + ^{16}\text{O}$, the internuclear potential is close with and without tensor force, having a barrier height of 10.02 MeV and a peak location of 8.66 fm. This indicates that the tensor force has negligible effect on the near-barrier fusion for the spin-saturated system $^{16}\text{O} + ^{16}\text{O}$, which is consistent with the findings in Ref. ([Stevenson et al., 2016a](#)). For these light systems the tensor force shows a small effect on the interaction potential.

For reactions involving two medium mass nuclei, we have chosen five representative reactions $^{40}\text{Ca} + ^{40}\text{Ca}$, $^{40}\text{Ca} + ^{48}\text{Ca}$, $^{48}\text{Ca} + ^{48}\text{Ca}$, $^{48}\text{Ca} + ^{56}\text{Ni}$, and $^{56}\text{Ni} + ^{56}\text{Ni}$, which vary by the total number of spin-unsaturated magic numbers in target and projectile by 0, 1, 2, 3, and 4. In these collisions, the reaction partners are closed-shell corresponding to 20 (spin-

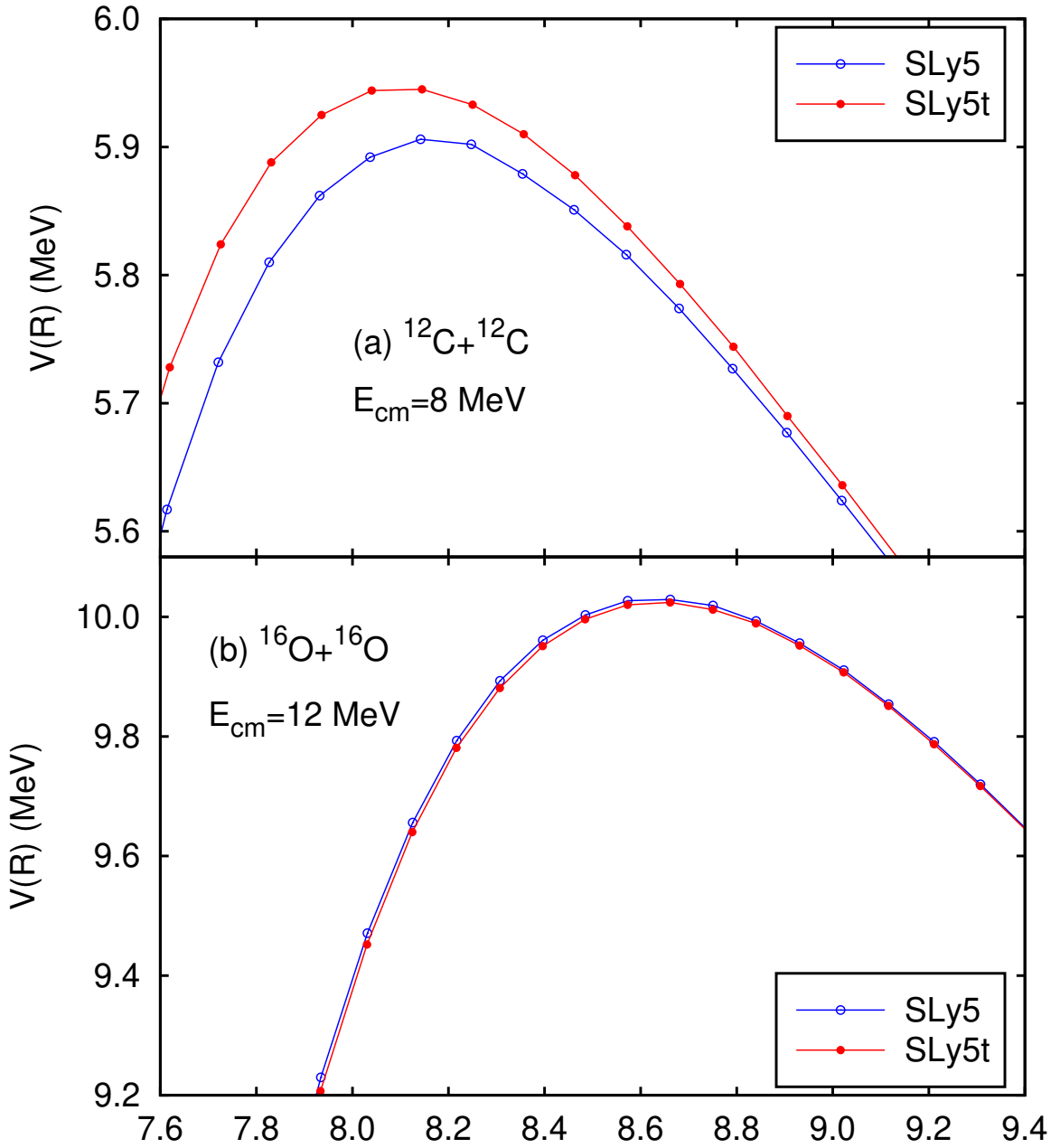


Figure 4.1: Internuclear potential obtained from DC-TDHF approach shown for the evolution of the systems (a) $^{12}\text{C} + ^{12}\text{C}$ at $E_{\text{c.m.}} = 8 \text{ MeV}$ and (b) $^{16}\text{O} + ^{16}\text{O}$ at $E_{\text{c.m.}} = 12 \text{ MeV}$ with SLy5 (open circle) and SLy5t (solid circle) forces.

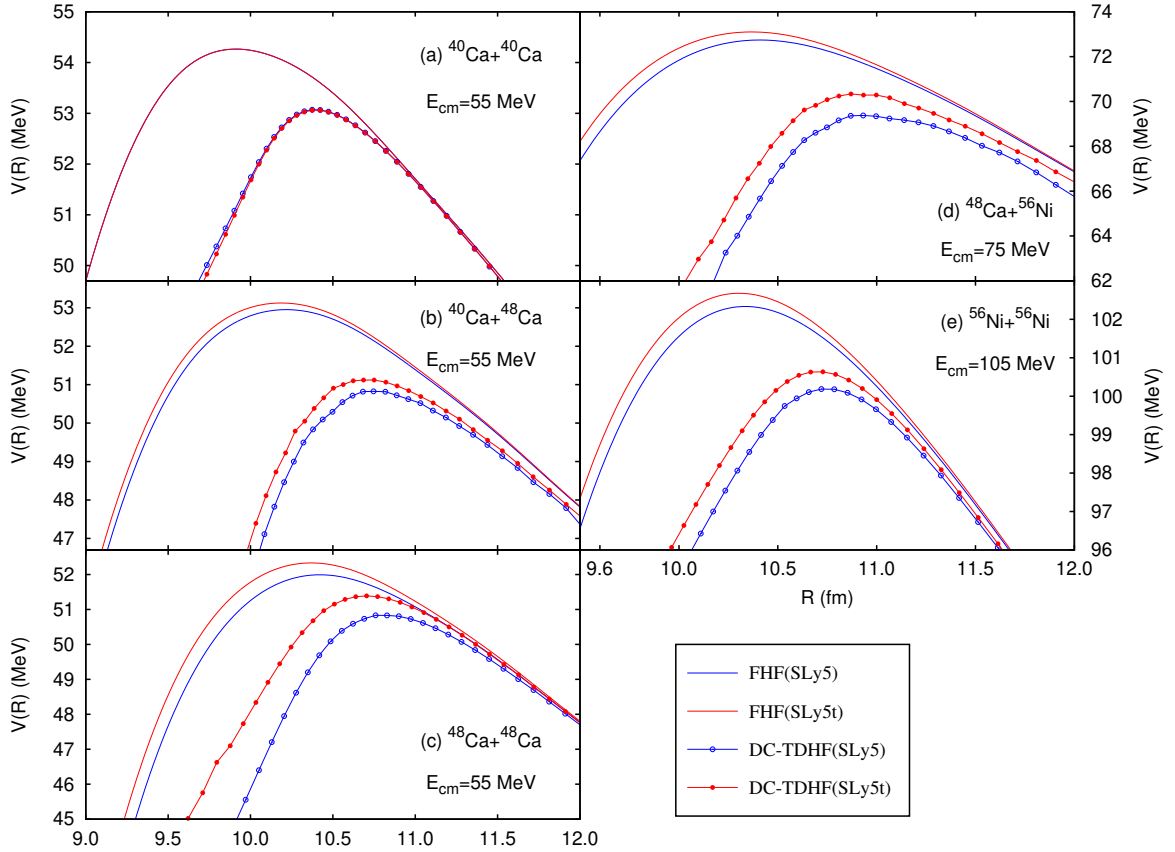


Figure 4.2: Internuclear potential obtained from FHF and DC-TDHF approaches for the Ca+Ca, Ca+Ni, and Ni+Ni reactions with tensor (SLy5t) and without tensor (SLy5) forces.

saturated) and 28 (spin-unsaturated) neutron or proton magic numbers. To disentangle the static (e.g. modification of ground-state density) and dynamical (e.g. modification of couplings, dissipation, and transfer) origins of the tensor force, the nucleus-nucleus potentials obtained both from FHF and DC-TDHF calculations are shown in Fig. 4.2 for all Ca and Ni reactions. In the initial state of the collision dynamics, the deviation of the static FHF potential from the dynamical DC-TDHF result is the order of smaller than 10 keV. For all the Ca and Ni reactions, we observe that the nucleus-nucleus potentials are considerably different for the static FHF and dynamical DC-TDHF results. The static potentials are systematically higher than the dynamical results, and the barrier peaks are located at smaller relative distance with FHF. In particular, the inner part of the potential, having strong effect on the sub-barrier fusion, presents more significant difference for FHF and DC-TDHF results. This behavior is well understood and is a consequence of the absence of Pauli principle and excitations for the frozen density overlaps in FHF potentials ([Simenel et al., 2013a](#); [Guo et al., 2018b](#); [Simenel et al., 2017a](#)), thus the difference between FHF and DC-TDHF is due to dynamical effects. Another interesting observation is that the variation of dynamical barriers due to tensor force is systematically greater than the ones for the static barriers. This indicates that the tensor force influences not only the ground-state single-particle levels, but also the dynamical effects including nucleon transfer, the couplings to low-lying states, and intrinsic excitations. In Ref. ([Guo et al., 2018b](#)), how these dynamical effects affect the fusion barriers heights, computed directly from TDHF, have been investigated to study the role of tensor force on above-barrier fusion dynamics. We note that in Ref. ([Guo et al., 2018b](#)), for the $^{48}\text{Ca} + ^{56}\text{Ni}$ system, the tensor force was observed to decrease the barrier height in direct TDHF calculations, which is the opposite of the trend observed here. This difference might arise from the dynamical energy-dependent effects introduced by the tensor force that are not captured by the DC-TDHF potential.

For the spin-saturated reaction $^{40}\text{Ca} + ^{40}\text{Ca}$, the interaction potential remains nearly unchanged by the inclusion of tensor force for both static and dynamical cases, indicating that

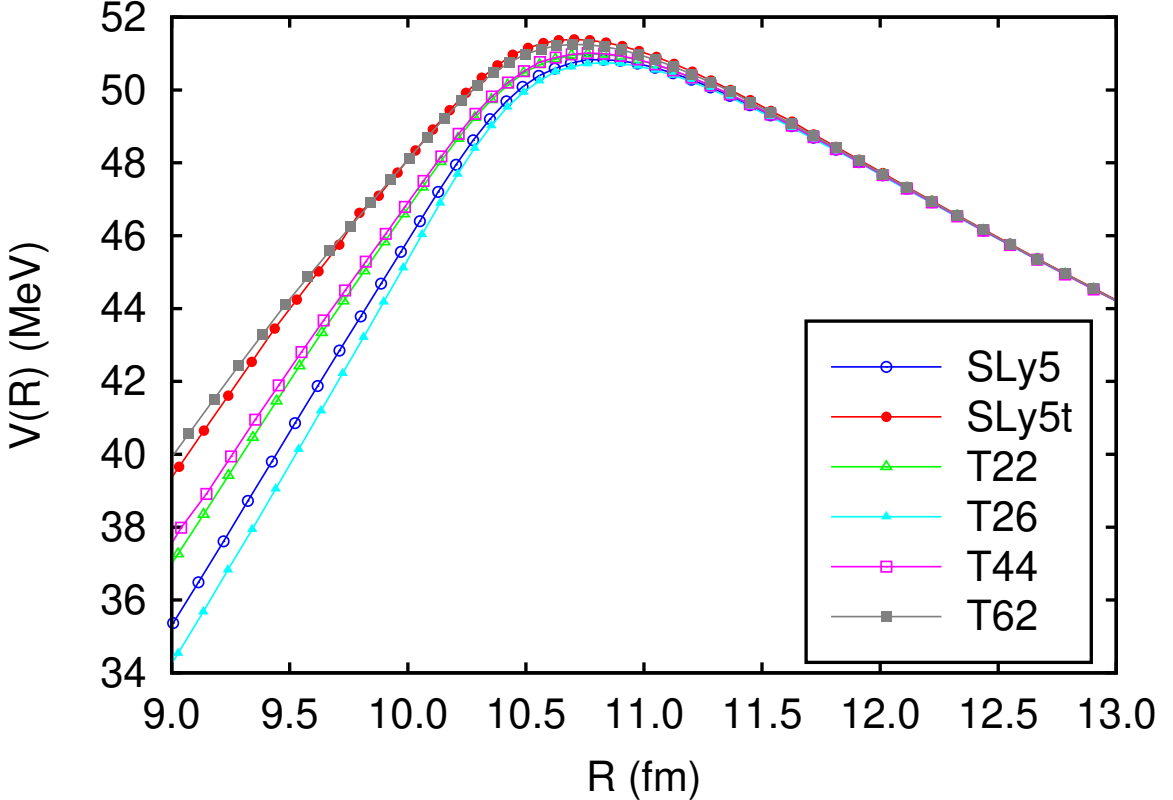


Figure 4.3: Internuclear potential obtained from DC-TDHF approach for the reaction $^{48}\text{Ca} + ^{48}\text{Ca}$ with SLy5, SLy5t, T22, T26, T44, and T62 forces.

the tensor force has almost no impact on the dynamical evolution for spin-saturated systems, since the contribution of tensor force is expected to be nearly zero for the ground state of spin-saturated nuclei. For the spin-unsaturated reactions, the barriers with tensor force SLy5t are systematically higher than those without the tensor force SLy5. This indicates a fusion hindrance effect due to the tensor force in this mass region. Empirically, 1 MeV larger in the inner part of the potential barrier can cause one order lower in the fusion cross section at sub-barrier energies. From the comparison of dynamical potentials for SLy5 and SLy5t, the potential barrier increases from a fraction up to a few MeV due to tensor force, which may result in changes of the sub-barrier fusion cross sections by a few orders of magnitude. For the medium mass systems with proton or neutron magic shells 20 and 28, the tensor force has a significant effect on the nucleus-nucleus potential, particularly in the inner region.

Until now, the studies have utilized the tensor force SLy5t. To obtain a comprehensive and rigorous understanding of the effects of the tensor force in heavy-ion collisions, we now proceed to a comparison among the results of various forces, for which the coupling constants are listed in Tab. 4.1. Taking the reaction $^{48}\text{Ca} + ^{48}\text{Ca}$ as an example, we show

Table 4.1: Isoscalar and isovector spin-current coupling constants in units of MeV fm⁵.

Force	C_0^J	C_1^J
T22	0	0
T26	120	120
T44	120	0
T62	120	-120
SLy5	15.65	64.55
SLy5t	-19.35	-70.45

the nucleus-nucleus potential with the six forces SLy5, SLy5t T22, T26, T44, and T62 in Fig. 4.3. For T22 and T44 the potentials are close to each other, indicating the isoscalar tensor coupling has negligible effect in this reaction. By comparing the results with T26, T44, and T62, the potential increases as the isovector tensor coupling decreases. This clear dependence of isoscalar and isovector tensor coupling may be due to the interplay between tensor terms and rearrangement of mean-field. The effect of the isoscalar tensor with the proton and neutron single particle spectrum moving in the same way seems to be canceled by the refitting of the parameters. However, the refitting does not incorporate the effect of isovector tensor in the same way. Detailed discussions on this can be found in Ref. ([Guo et al., 2018b](#)). The T62 (T26) interaction also leads to similar potentials as SLy5t (SLy5), even though they have quite different tensor coupling constants, because the rearrangement of the mean-field for T62 (T26) produce additional effects which cancel part of the tensor force in SLy5t (SLy5).

To gain a better insight into the tensor force, the dynamical potential is shown in Fig. 4.4 for various Ca+Sn systems which involve one medium and one heavy reaction partner. For ^{48}Ca , ^{100}Sn , and ^{120}Sn , the ground states are found to be spherical for both SLy5 and SLy5t. However, the ^{116}Sn nucleus exhibits small quadrupole deformation β_2 of 0.077

and 0.026 for SLy5 and SLy5t, respectively, for which the deformation difference arises from the tensor force. Since the outcome of collision dynamics strongly depends on the deformation orientation of colliding partners, the deformed nucleus ^{116}Sn is initially set as the tip orientation in both SLy5 and SLy5t with the symmetry axis of ^{116}Sn parallel to the internuclear axis. We find that, for the Ca+Sn systems, the effects of the tensor force show similar trends as in the spin-unsaturated Ca+Ca, Ca+Ni, and Ni+Ni systems presented in Fig. 4.2. The tensor force has the largest effect on the reaction $^{48}\text{Ca} + ^{116}\text{Sn}$ as compared to the reactions with ^{48}Ca colliding ^{100}Sn and ^{120}Sn isotopes, which may be due to the strong effect of the tensor force on the energy difference of single-proton states $1\text{h}_{11/2}$ and $1\text{g}_{9/2}$ along the $Z=50$ isotopes for ^{116}Sn , as shown in Ref. ([Colò et al., 2007a](#)). Another suspected cause for this large effect arising from the tensor force in the $^{48}\text{Ca} + ^{116}\text{Sn}$ reaction is the static deformation effects leading to a vastly different dynamical path for the system.

4.4 Summary

We incorporate the full tensor force into the FHF and DC-TDHF approaches to investigate the impact of the tensor force on heavy-ion internuclear potentials for ten representative systems in different mass regimes. As expected we find that static potentials are systematically higher than the dynamical results, however, the variation of dynamical potential barriers induced by tensor force is larger than those of the static case, which are attributed to the microscopic dynamical effects included in TDHF. For light systems, the tensor force is found to have small effects on the nucleus-nucleus potential, with the barrier height and inner part of the barrier changing by a fraction of an MeV. Even this small change may lead to large effects in cross sections when considering deep sub-barrier collisions at energy scales common in astrophysical systems. For medium and heavy spin-unsaturated reactions the effect is much more pronounced, with changes from a fraction of an MeV to almost 2 MeV for the barrier height. These differences indicate an important impact on sub-barrier fusion dynamics and a substantial fusion hindrance effect arising

from the tensor force.

The fully microscopic TDHF theory has shown itself to be rich in nuclear phenomena and continues to stimulate our understanding of nuclear dynamics. The time-dependent mean-field studies seem to show that the dynamic evolution builds up correlations that are not present in the static theory. While modern Skyrme forces provide a much better description of static nuclear properties in comparison to the earlier parametrizations, there is a need to obtain even better parametrizations that incorporate deformation and reaction data into the fit process. The tensor force should be a part of these investigations.

4.5 Acknowledgments

This work is partly supported by NSF of China (Grants No. 11175252 and 11575189), NSFC-JSPS International Cooperation Program (Grant No. 11711540016), and Presidential Fund of UCAS, and by the U.S. Department of Energy under grant No. DE-SC0013847. The computations in present work have been performed on the High-performance Computing Clusters of SKLTP/ITP-CAS and Tianhe-1A supercomputer located in the Chinese National Supercomputer Center in Tianjin.

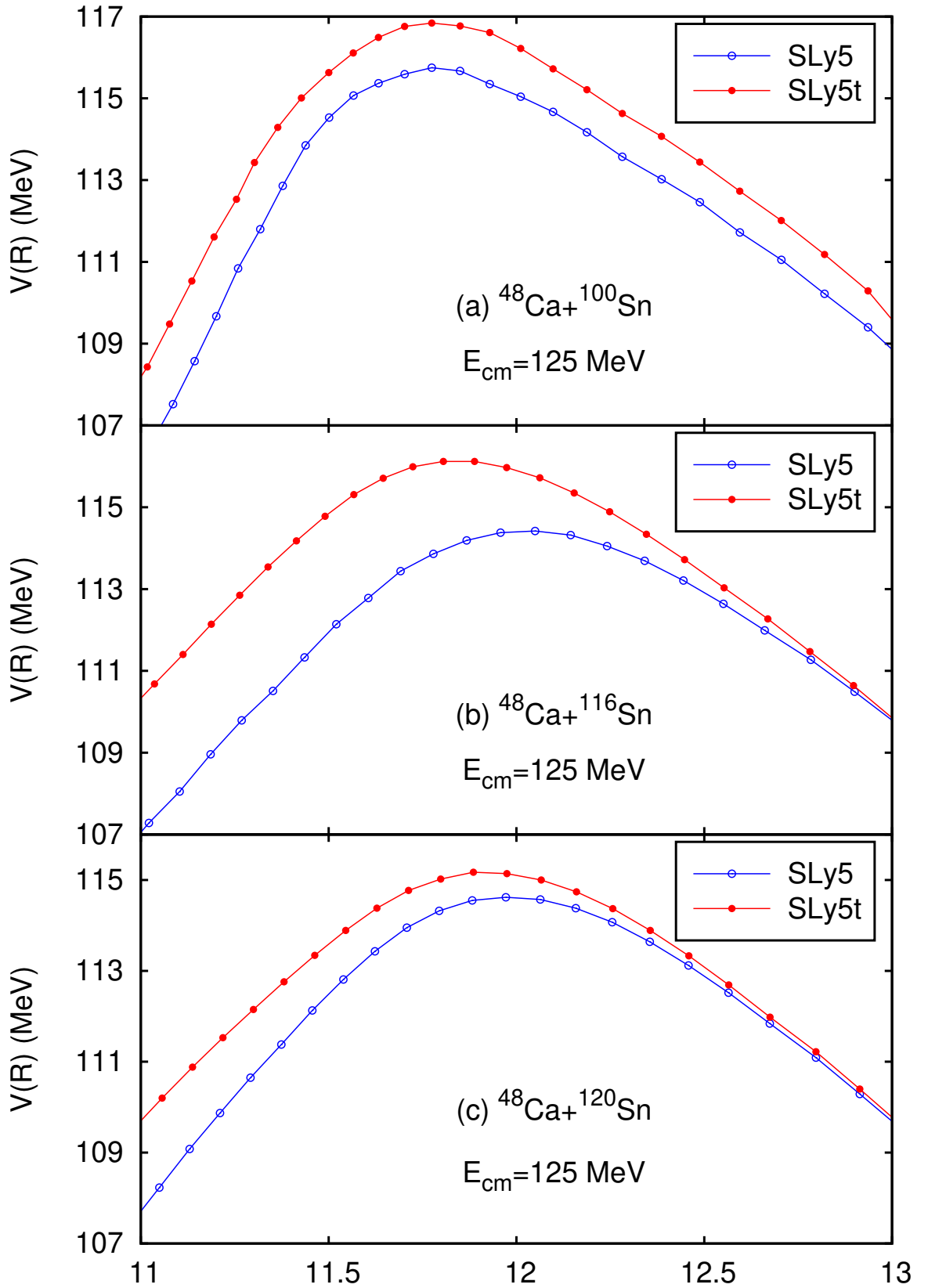


Figure 4.4: Internuclear potential obtained from DC-TDHF approach for the Ca+Sn systems with SLy5 (open circle) and SLy5t (solid circle) forces.

Chapter 5

Influence of the tensor interaction on heavy-ion fusion cross sections

abstract

[Background] While the tensor interaction has been shown to significantly affect the nuclear structure of exotic nuclei, its influence on nuclear reactions has only recently been investigated. The primary reason for this neglect is the fact that most studies of nuclear dynamics do not include the tensor force at all in their models. Indeed, only a few Skyrme parametrizations consider the tensor interaction in parameter determination. With modern research facilities extending our ability to probe exotic nuclei, a correct description of nuclear dynamics and heavy-ion fusion is vital to both supporting and leading experimental efforts.

[Purpose] To investigate the effect of the tensor interaction on fusion cross sections for a variety of nuclear reactions spanning light and heavy nuclei.

[Method] Fusion cross sections are calculated using ion-ion potentials generated by the fully microscopic density-constrained time-dependent Hartree-Fock (DC-TDHF) method with the complete Skyrme tensor interaction.

[Results] For light nuclei, the tensor force only slightly changes the sub-barrier fusion cross sections at very low energies. Heavier nuclei, however, begin to exhibit a substantial hindrance effect in the sub-barrier region. This effect is strongest in spin-unsaturated systems, though can manifest in other configurations as well. Static, ground state deformation effects of the tensor force can also affect cross sections by shifting the fusion barrier.

[Conclusions] The tensor interaction has a measurable effect on the fusion cross sections of nuclei spanning the nuclear chart. The effect comes from both static effects present in the ground state and dynamic processes arising from the time evolution of the system. This motivates the development of a modern Skyrme parameter set that includes all time-odd and tensor terms and that studies moving forward should include the tensor force to

ensure a more robust and complete description of nuclei.

5.1 Introduction

Many applications of nuclear physics rely on our description of both the structure and dynamics of exotic nuclei. From superheavy and neutron rich nuclei formation to modeling the rapid neutron capture process (*r*-process), the fundamental description of static nuclei and how they interact is of great importance to accurately inform emergent theories. In the current era with state-of-the-art radioactive ion beams becoming more available we are presented with excellent opportunities in both the experimental and theoretical study of exotic nuclei and their interactions (Balantekin et al., 2014b).

It is with this motivation that the influence of the tensor interaction on fusion cross sections is being studied. While the importance of the tensor force has been well studied in nuclear structure calculations (Otsuka et al., 2005, 2006b; Lesinski et al., 2007b; Colò et al., 2007b; Bai et al., 2010b; Otsuka et al., 2010; Brink and Stancu, 2018), the impact on nuclear dynamics has only recently been a topic of interest. This relative neglect is primarily due to the tensor interaction not being included in most studies of nuclear reactions, even though the tensor force plays a significant role in intrinsic excitations that may introduce unforeseen dynamical effects. The inclusion of these effects provide a more complete picture into the effective nucleon-nucleon interaction and nuclear reactions in general. A comprehensive review of the various approaches to including the tensor interaction can be found in recent reviews on the subject (Sagawa and Colò, 2014; Stevenson and Barton, 2019).

The study of fusion cross sections both above and below the barrier has been performed for many systems using a number of distinct techniques, though most approaches ultimately require a heavy-ion interaction potential as the starting point (Back et al., 2014b). How one obtains such a potential is also varied, though two main classes can be roughly identified: phenomenological models (Bass, 1974b; Randrup and Vaagen, 1978b; Satchler and Love,

1979b; Rhoades-Brown and Oberacker, 1983b; Seiwert et al., 1984b; Adamian et al., 1996; Chamon et al., 2002; Adamian et al., 2004b; Wang et al., 2012b; Zhu et al., 2016b; Bao et al., 2016b; Feng, 2017b) and (semi-)microscopic models (Brueckner et al., 1968b; Diaz-Torres et al., 1999; Diaz Torres et al., 2001; Möller et al., 2004b; Guo et al., 2004b, 2005b; S. Mišicu and Esbensen, 2006b; Umar and Oberacker, 2006f; Mišicu and Esbensen, 2007; Guo et al., 2007c; Diaz-Torres et al., 2007; Lu et al., 2014b; Simenel et al., 2017b; Diaz-Torres and Wiescher, 2018). Within each class there are myriad methods and assumptions, so we focus on the (semi-)microscopic class of methods which are more germane to the current work. One reason for pursuing a microscopic approach to describe fusion is the desire to have the theoretical description be as close to the underlying physical processes as possible in hopes that this will produce a more predictive technique. It was this desire that led to techniques such as the density-constrained time-dependent Hartree-Fock (DC-TDHF) approach (Umar and Oberacker, 2006f) for calculating heavy-ion interaction potentials which naturally incorporates all dynamical effects coming from the TDHF description of the collision process (Simenel and Umar, 2018b). By using a time evolution of the heavy-ion system as the starting point, you avoid the unphysically large density overlaps seen in simple folding model methods and obtain dynamical effects not seen otherwise. These effects include nucleon transfer, neck formation, internal excitations, and deformation effects and manifest from the time evolution of the initial configuration. That is to say, the dynamic densities evolve self-consistently in a fully microscopic description of two boosted nuclei with no outside constraints. The density-constraint that is performed to the evolved densities is what provides the static collective energy which is then interpreted as the ion-ion interaction potential. The DC-TDHF approach has been applied to many systems spanning the nuclear chart and the fusion cross section results generally agree well with available experimental data (Umar and Oberacker, 2006e,h, 2008b; Umar et al., 2008b; Umar and Oberacker, 2009; Umar et al., 2010a; Oberacker et al., 2010b; Keser et al., 2012b; Umar et al., 2012b, 2014b; Godbey et al., 2017b, 2019a).

By themselves, direct TDHF calculations have been used in recent years to investigate the impact of the tensor force on heavy-ion collisions (Fracasso et al., 2012b; Dai et al., 2014c; Stevenson et al., 2016b; Shi and Guo, 2017a; Guo et al., 2018c), though no studies employing phenomenological nor microscopic methods for obtaining ion-ion potentials have included the tensor interaction until recently (Guo et al., 2018a). To that end, the current work is a follow-up to the initial investigation of fusion barriers for a wide variety of spin saturated and unsaturated nuclear systems and the impact the tensor force has on fusion cross sections at energies above and below the barrier, where in this context spin saturation refers to nuclei where both spin-orbit subshells ($j = l + \frac{1}{2}$ and $j = l - \frac{1}{2}$) are filled. A more detailed description of the methods and theory are in Sec. 5.2, fusion cross section results are presented and discussed in Sec. 5.3, and a brief summary and conclusion comprises Sec. 5.4.

5.2 Theoretical framework

While TDHF has been used for a vast set of problems throughout its history, there is not one standard approach that is universally followed. From the choice of geometric symmetries to the particular EDF employed, there are potential assumptions or omissions that could then lead to an incomplete (or inaccurate) description of nuclear dynamics. The effective interaction in particular is one area which has been a subject of study since the theory's inception. One historical example concerns the time-odd terms of the energy density functional (EDF) which are shown to be non-negligible in heavy-ion collisions (Umar and Oberacker, 2006g). This provides a motivating analogy to the tensor force between nucleons, as it has only recently been included in TDHF investigations as discussed above and may be similarly important.

5.2.1 Full Skyrme energy functional

The bulk of TDHF calculations utilize the Skyrme effective interaction ([Skyrme, 1956b](#)), in which the two-body tensor force was proposed in its original form as

$$v_T = \frac{t_e}{2} \left\{ [3(\sigma_1 \cdot \mathbf{k}')(\sigma_2 \cdot \mathbf{k}') - (\sigma_1 \cdot \sigma_2)\mathbf{k}'^2] \delta(\mathbf{r}_1 - \mathbf{r}_2) + \delta(\mathbf{r}_1 - \mathbf{r}_2) [3(\sigma_1 \cdot \mathbf{k})(\sigma_2 \cdot \mathbf{k}) - (\sigma_1 \cdot \sigma_2)\mathbf{k}^2] \right\} \\ + t_o \left\{ 3(\sigma_1 \cdot \mathbf{k}') \delta(\mathbf{r}_1 - \mathbf{r}_2) (\sigma_2 \cdot \mathbf{k}) - (\sigma_1 \cdot \sigma_2) \mathbf{k}' \delta(\mathbf{r}_1 - \mathbf{r}_2) \mathbf{k} \right\}. \quad (5.1)$$

The coupling constants t_e and t_o represent the strengths of triplet-even and triplet-odd tensor interactions, respectively. The operator $\mathbf{k} = \frac{1}{2i}(\nabla_1 - \nabla_2)$ acts on the right and $\mathbf{k}' = -\frac{1}{2i}(\nabla'_1 - \nabla'_2)$ acts on the left.

The total energy of the system may then be represented as

$$E = \int d^3r \mathcal{H}(\rho, \tau, \mathbf{j}, \mathbf{s}, \mathbf{T}, \mathbf{F}, J_{\mu\nu}; \mathbf{r}) \quad (5.2)$$

in terms of the energy functional. The functional is composed by the number density ρ , kinetic density τ , current density \mathbf{j} , spin density \mathbf{s} , spin-kinetic density \mathbf{T} , the tensor-kinetic density \mathbf{F} , and spin-current pseudotensor density J ([Stevenson et al., 2016b](#)). The full version of Skyrme EDF is expressed as

$$\mathcal{H} = \mathcal{H}_0 + \sum_{t=0,1} \left\{ A_t^s s_t^2 + (A_t^{\Delta s} + B_t^{\Delta s}) \mathbf{s}_t \cdot \Delta \mathbf{s}_t + B_t^{\nabla s} (\nabla \cdot \mathbf{s}_t)^2 \right. \\ \left. + B_t^F (\mathbf{s}_t \cdot \mathbf{F}_t - \frac{1}{2} \left(\sum_{\mu=x}^z J_{t,\mu\mu} \right)^2 - \frac{1}{2} \sum_{\mu,\nu=x}^z J_{t,\mu\nu} J_{t,\nu\mu}) \right. \\ \left. + (A_t^T + B_t^T) (\mathbf{s}_t \cdot \mathbf{T}_t - \sum_{\mu,\nu=x}^z J_{t,\mu\nu} J_{t,\mu\nu}) \right\}, \quad (5.3)$$

where \mathcal{H}_0 is the simplified functional used in the standard Sky3D TDHF code ([Maruhn et al., 2014b](#)). The terms containing the coupling constants A arise from the Skyrme central force and those with B from the tensor force. The definitions of the constants A and B can be

found in Refs. (Lesinski et al., 2007b; Davesne et al., 2009b). All of the time-even and time-odd terms in Eq. (5.3) have been implemented numerically in the mean-field Hamiltonians of the HF, TDHF, and DC-TDHF approaches. As discussed in Refs. (Lesinski et al., 2007b; Stevenson et al., 2016b), the terms containing the gradient of the spin density (the $\mathbf{s}_t \cdot \Delta \mathbf{s}_t$ and $(\nabla \cdot \mathbf{s}_t)^2$ terms) may cause spin instability in both nuclear structure and reaction studies, and are thus turned off in these calculations. This omission of the spin density gradient terms is standard procedure in TDHF studies that include the time-odd terms.

5.2.2 TDHF approach

Given a many-body Hamiltonian, the action can be constructed as

$$S = \int_{t_1}^{t_2} dt \langle \Phi(\mathbf{r}, t) | H - i\hbar \partial_t | \Phi(\mathbf{r}, t) \rangle, \quad (5.4)$$

where Φ is the time-dependent many-body wave function. In TDHF approach the many-body wave function $\Phi(\mathbf{r}, t)$ is approximated as a single time-dependent Slater determinant composed of an antisymmetrized product of the single particle states $\phi_\lambda(\mathbf{r}, t)$

$$\Phi(\mathbf{r}, t) = \frac{1}{\sqrt{N!}} \det \{\phi_\lambda(\mathbf{r}, t)\}, \quad (5.5)$$

and this form is kept at all times in the dynamical evolution. By taking the variation of the action with respect to the single-particle wave functions, the set of nonlinear coupled TDHF equations in the multidimensional space-time phase space

$$i\hbar \frac{\partial}{\partial_t} \phi_\lambda(\mathbf{r}, t) = h \phi_\lambda(\mathbf{r}, t) \quad (5.6)$$

yields the most probable time-dependent mean-field path, where h is the HF single-particle Hamiltonian. For this study, the three-dimensional coordinate space TDHF code Sky3D (Maruhn et al., 2014b) has been extended to include the tensor terms of the interaction. To expand on

the numerical details of the simulations, the static HF ground state for the reaction partner has been calculated on the symmetry-unrestricted three-dimensional grid. The resulting Slater determinants for each nucleus are combined and comprise the larger Slater determinant describing the colliding system. The TDHF time propagation is performed using a Taylor-series expansion up to the sixth order of the unitary boost operator with a time step of $0.2 \text{ fm}/c$. For the dynamical evolution, we use a numerical box of 48 fm along the collision axis and 24 fm in the other two directions and a grid spacing of 1.0 fm. The initial separation between the two nuclei is 20 fm.

5.2.3 Dynamical potential from DC-TDHF approach

The semi-classical nature of TDHF precludes one from fully describing heavy-ion fusion from TDHF calculations alone; while direct TDHF can provide fusion cross sections that agree well above the barrier, sub-barrier calculations result in scattering due to the absence of a many-body description of quantum tunneling. At present, all sub-barrier fusion calculations assume that there exists an ion-ion potential which depends on the internuclear distance. The microscopic DC-TDHF approach ([Umar and Oberacker, 2006f](#)) is employed to extract this heavy-ion potential from the TDHF time evolution of the dinuclear system at above-barrier energies. This approach allows for the determination of an interaction potential that includes all dynamical effects seen in the TDHF evolution. To construct this potential, at certain times during the evolution, the instantaneous TDHF density is used to perform a static HF energy minimization

$$\delta\langle\Psi_{\text{DC}}|H - \int d^3r \lambda(\mathbf{r})\rho(\mathbf{r})|\Psi_{\text{DC}}\rangle = 0, \quad (5.7)$$

by constraining the proton and neutron densities to be equal to the instantaneous TDHF densities. As it is the total density that is being constrained, all moments are simultaneously constrained. DC-TDHF calculations give the adiabatic reference state for a given TDHF state, which is the Slater determinant with the lowest energy for a given density. The

minimized energy

$$E_{DC}(\mathbf{R}) = \langle \Psi_{DC} | H | \Psi_{DC} \rangle \quad (5.8)$$

is the so-called density-constrained energy. Since this density-constrained energy still contains the binding energies of the initial individual nuclei, the heavy-ion interaction potential is deduced as

$$V(\mathbf{R}) = E_{DC}(\mathbf{R}) - E_1 - E_2, \quad (5.9)$$

where E_1 and E_2 are the binding energies of the two individual nuclei. This procedure is performed separately during the time evolution and does not affect the TDHF time evolution in any way. The result is a microscopically determined ion-ion interaction potential that contains no free parameters or normalization. We have performed the density constraint calculations at every 10-20 time steps (corresponding to 2-4 fm/c interval). The choice on how often to perform the density constraint depends entirely on the resolution you want to obtain for the potential and does not affect the evolution in any way. The convergence criteria in DC-TDHF calculations is as good if not better than in the traditional constrained HF with a constraint on a single collective degree of freedom.

5.2.4 Calculation of cross sections from interaction potential

As described above, DC-TDHF provides a way to obtain one dimensional ion-ion fusion potentials, which can then be used to calculate fusion cross sections. The procedure to obtain transmission probabilities $T_l(E_{c.m.})$ (and thus cross sections) from an arbitrary one-dimensional potential can solved by numerical integration of the two-body Schrödinger equation:

$$\left[\frac{-\hbar^2}{2M(R)} \frac{d^2}{dR^2} + \frac{l(l+1)\hbar^2}{2M(R)R^2} + V(R) - E \right] \psi = 0. \quad (5.10)$$

The incoming wave boundary conditions (IWBC) method is used to calculate transmission probabilities which assumes that fusion occurs once the minimum of $V(R)$ is

reached (Rawitscher, 1964). The subtle assumption here is that all transmitted waves (or waves with an energy greater than the barrier) will lead to fusion. This assumption is the primary issue that complicates descriptions of light nuclei systems like $^{12}\text{C}+^{12}\text{C}$ as discussed in (Jiang et al., 2013; Godbey et al., 2019a).

The barrier penetrability $T_l(E_{\text{c.m.}})$ is then the ratio of the incoming flux at the minimum of the potential inside the barrier to the incoming flux at a large distance. Once $T_l(E_{\text{c.m.}})$ is calculated, the fusion cross sections at energies above and below the barrier are calculated as

$$\sigma_f(E_{\text{c.m.}}) = \frac{\pi}{k_0^2} \sum_{l=0}^{\infty} (2l+1) T_l(E_{\text{c.m.}}). \quad (5.11)$$

As DC-TDHF potentials are the result of a TDHF evolution, the coordinate-dependent mass $M(R)$ can be calculated directly from TDHF dynamics (Umar et al., 2009b; Umar and Oberacker, 2009). This mass primarily influences the inner part of the barrier, leading to a broader barrier width thus leading to further hindrance in the sub-barrier region. The effect of the coordinate-dependent mass also plays a role in the energy dependence of the potential (Umar et al., 2014b), as the value of the mass will spike as the nuclei slow down at the point of the barrier. Instead of solving the Schrödinger equation using the coordinate-dependent mass $M(R)$, the potential can be transformed by a scale factor (Umar and Oberacker, 2009; Goeke et al., 1983)

$$d\bar{R} = \left(\frac{M(R)}{\mu} \right)^{\frac{1}{2}} dR. \quad (5.12)$$

Upon making this transformation the coordinate-dependence of $M(R)$ vanishes and is replaced by the reduced mass μ in Eq. (5.10) and the Schrödinger equation is solved using the modified Numerov method as it is formulated in the coupled-channel code CC-FULL (Hagino et al., 1999).

5.3 Results

In choosing representative systems to investigate the effect of the tensor interaction on fusion cross sections, a variety of nuclei were chosen from multiple mass regions and spin structures in an attempt to characterize what effects could be expected from the tensor force's inclusion. One point of interest is in the asymmetry of the interacting fragments, as phenomena like neck formation will take on a more pronounced role for heavily mass asymmetric systems. Additionally, isovector contributions to the potential will be lessened in symmetric collisions (such as $^{48}\text{Ca} + ^{48}\text{Ca}$), and the tensor contribution will be primarily from the isoscalar part of the EDF ([Godbey et al., 2017b](#)).

A note should be made on the Skyrme functionals used in this work, in which the tensor force has been constructed in two ways. One is to add the force perturbatively to an existing standard interaction as was done with the Skyrme parameter set SLy5 ([Chabanat et al., 1998](#)), where the tensor force was added and refit to data, resulting in SLy5t ([Colò et al., 2007b](#)). The comparison between calculations with SLy5 and SLy5t addresses the question on how much of the changes is caused by tensor force itself, as only the tensor parameters were refit. Another approach is to readjust the full set of Skyrme parameters self-consistently. This strategy has been adopted in Ref. ([Lesinski et al., 2007b](#)) and led to the set of TIJ parametrizations with a wide range of isoscalar and isovector tensor couplings. Due to its fitting strategy, the contributions from the tensor force and all other terms cannot so easily be separated. A more detailed analysis of the two fitting approaches is discussed in ([Stevenson and Barton, 2019](#)).

Starting with light systems, fusion cross section results from SLy5 and SLy5t are shown in Fig. 5.1 for the spin-unsaturated $^{12}\text{C} + ^{12}\text{C}$ and $^{12}\text{C} + ^{13}\text{C}$. For both SLy5 and SLy5t spherical ground state solutions were found for both ^{12}C and ^{13}C . In Ref. ([Guo et al., 2018a](#)), a small difference in interaction potentials was found for $^{12}\text{C} + ^{12}\text{C}$, though that difference does not result in an appreciable variation of the cross sections at any energy above or below the barrier at the scales used here.

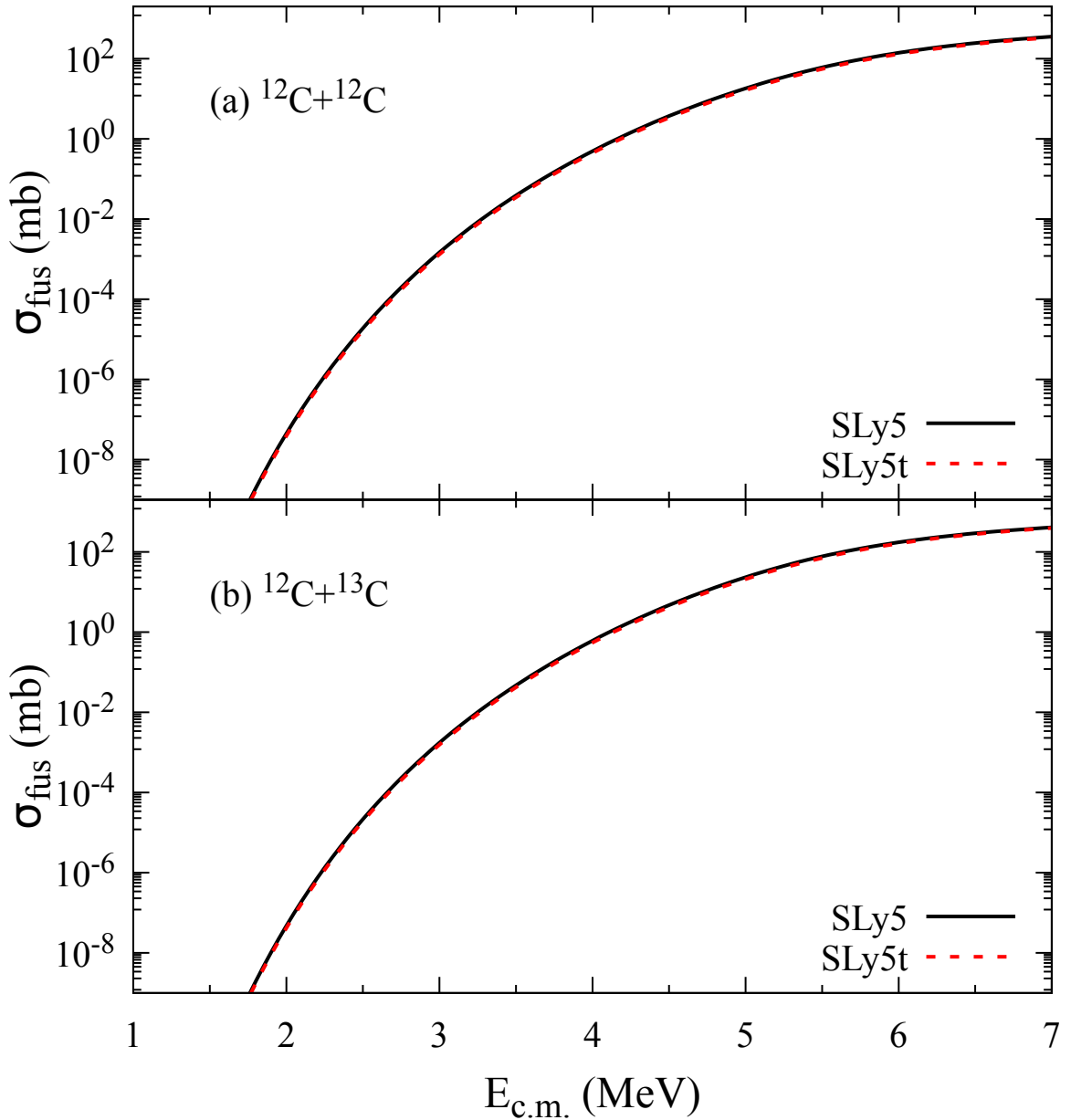


Figure 5.1: Fusion cross sections obtained from the DC-TDHF approach for (a) $^{12}\text{C} + ^{12}\text{C}$ at $E_{\text{c.m.}} = 8$ MeV and (b) $^{12}\text{C} + ^{13}\text{C}$ at $E_{\text{c.m.}} = 8$ MeV with SLy5 (black solid line) and SLy5t (red dashed line) forces.

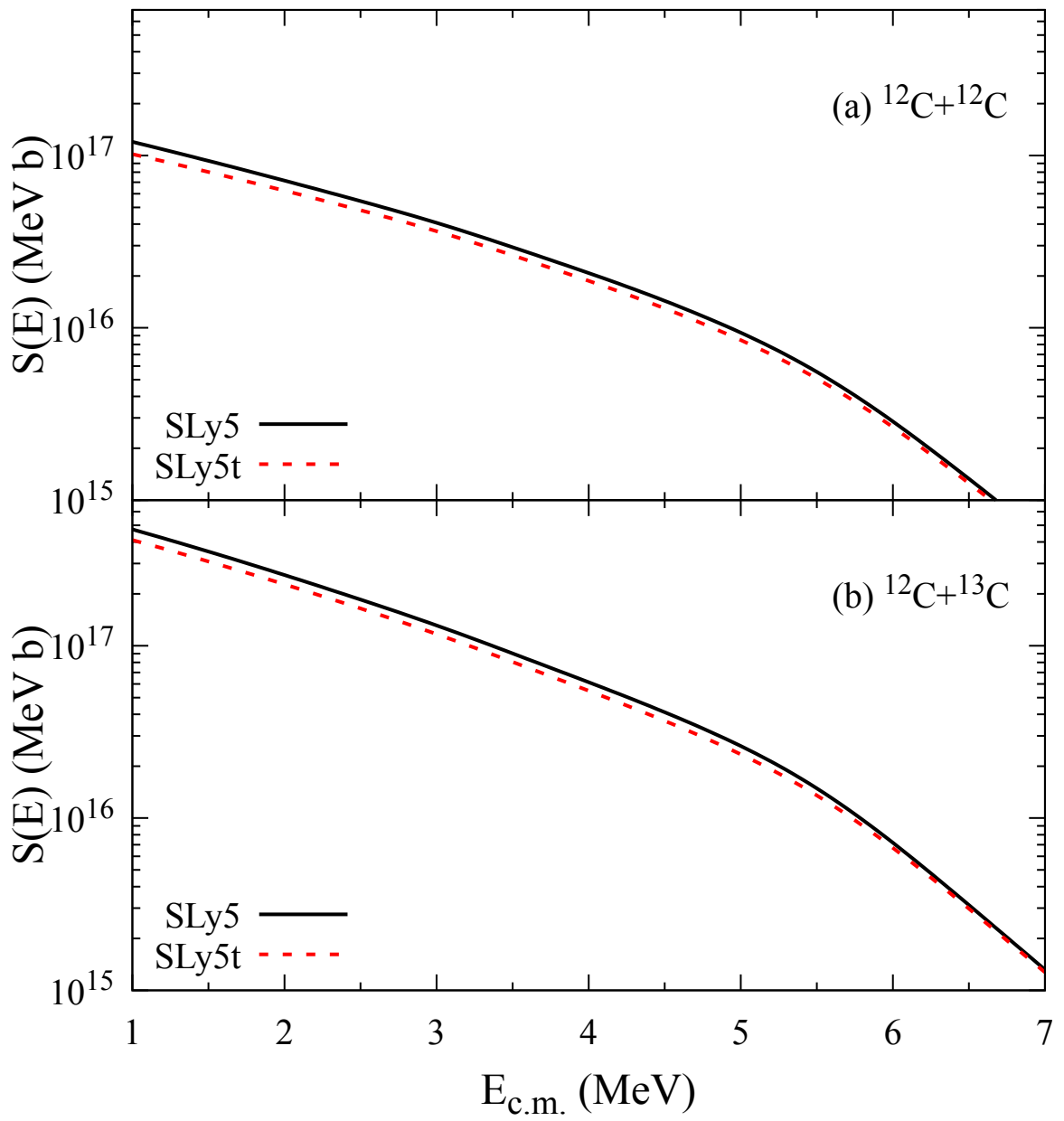


Figure 5.2: S factors obtained from the DC-TDHF approach for (a) $^{12}\text{C} + ^{12}\text{C}$ at $E_{\text{c.m.}} = 8$ MeV and (b) $^{12}\text{C} + ^{13}\text{C}$ at $E_{\text{c.m.}} = 8$ MeV with SLy5 (black solid line) and SLy5t (red dashed line) forces.

$^{12}\text{C} + ^{12}\text{C}$ plays a significant role in nucleosynthesis and the r-process and thus the energies of focus are often in the extreme sub-barrier regime (≈ 1 MeV) (Andrew Cumming and Lars Bildsten, 2001; Strohmayer and Brown, 2002; Hoyle, 1954; Godbey et al., 2019a).

Figure 5.1 spans the entire sub-barrier region, though the large range of values prohibits a close comparison of extreme sub-barrier values. This is a deficiency of logarithmic cross section plots which is addressed in most studies of light systems of astrophysical interest by instead plotting the S factor

$$S(E_{\text{c.m.}}) = \sigma(E_{\text{c.m.}})E_{\text{c.m.}}e^{2\pi\eta}, \quad (5.13)$$

Where $E_{\text{c.m.}}$ is the center of mass energy, $\eta = Z_1Z_2e^2/\hbar v$ is the Sommerfeld parameter, and v is the relative velocity of the nuclei at infinity. The S factor is used primarily due to it removing most of the energy dependence at very low energies, permitting a closer comparison of data and experiment. This quantity is presented in Fig. 5.2 for both $^{12}\text{C} + ^{12}\text{C}$ and $^{12}\text{C} + ^{13}\text{C}$. In contrast to the cross section results, a small difference can be discerned at sub-barrier energies which slightly increases as one descends. The small decrease seen here is of note, though the tensor interaction does not change the overall structure of the S factor at sub-barrier energies via either the manifestation of resonant structures seen in the experimental data or in strong hindrance effects which have been suggested to be present in this system (Jiang et al., 2007).

Moving up in mass, Fig. 5.3 presents cross sections obtained for $^{40}\text{Ca} + ^{40}\text{Ca}$, $^{40}\text{Ca} + ^{48}\text{Ca}$, and $^{48}\text{Ca} + ^{48}\text{Ca}$. These systems are valuable benchmarks as both ^{40}Ca and ^{48}Ca are closed-shell nuclei, though ^{48}Ca has 28 neutrons, corresponding to the spin-unsaturated magic number 28. The symmetric spin-saturated $^{40}\text{Ca} + ^{40}\text{Ca}$ shows almost no difference when comparing the fusion cross sections obtained using the SLy5 and SLy5t forces, though there is a slight variation at low energies. The finding that SLy5 and SLy5t result in nearly identical cross sections at all energy regimes suggests that, even during a dynamic

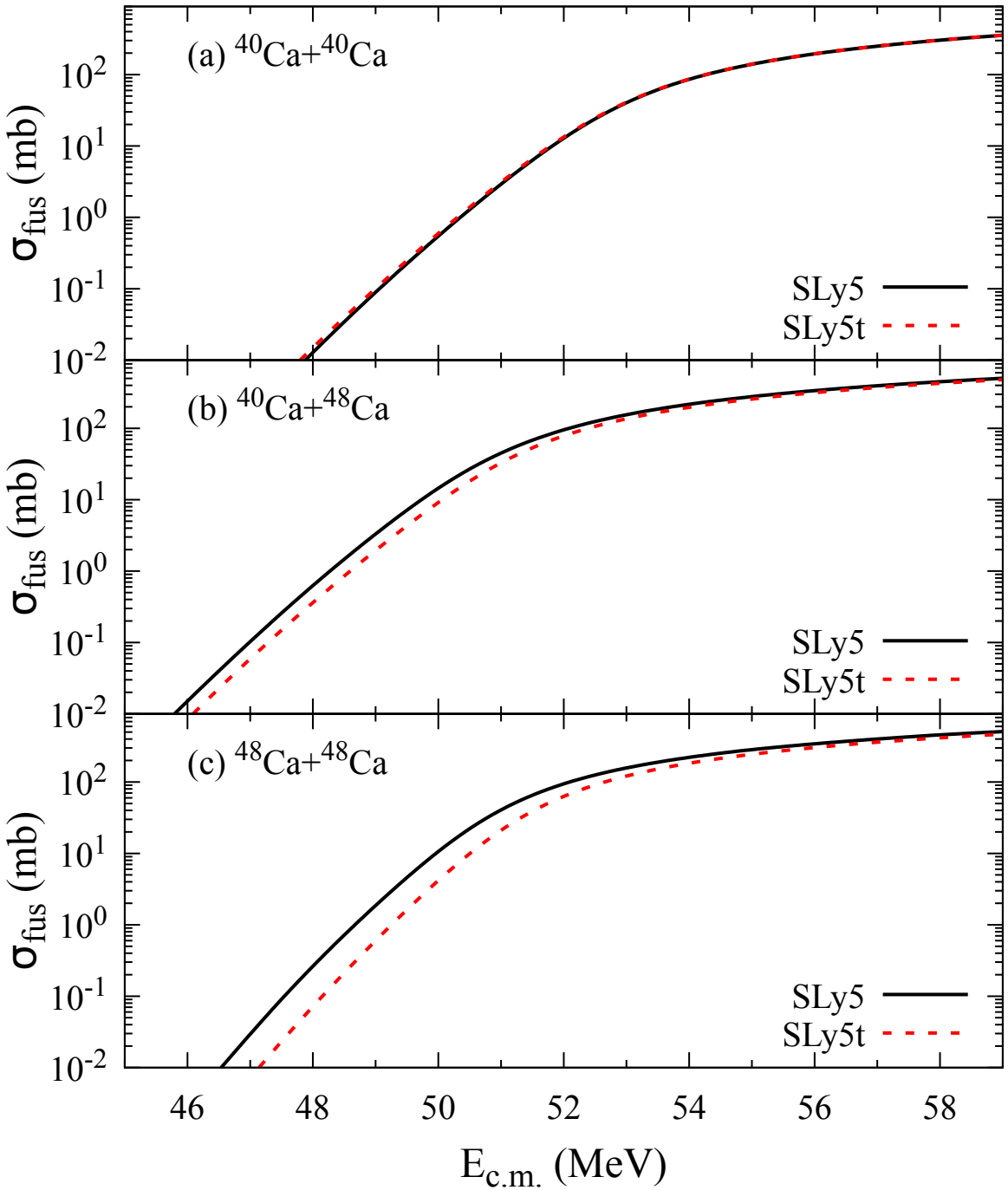


Figure 5.3: Fusion cross sections obtained from the DC-TDHF approach for (a) $^{40}\text{Ca} + ^{40}\text{Ca}$ at $E_{\text{c.m.}} = 55$ MeV, (b) $^{40}\text{Ca} + ^{48}\text{Ca}$ at $E_{\text{c.m.}} = 55$ MeV, and (c) $^{48}\text{Ca} + ^{48}\text{Ca}$ at $E_{\text{c.m.}} = 55$ MeV with SLy5 (black solid line) and SLy5t (red dashed line) forces.

evolution at energies above the barrier, the tensor force does not play a substantial role in collisions between spin-saturated systems. Moving to the asymmetric $^{40}\text{Ca} + ^{48}\text{Ca}$ reaction presents the first example of how the tensor force results in different behavior in the sub-barrier region, with the tensor interaction resulting in a slight fusion hindrance. The difference is small in this case, and it is only substantially different at energies below the barrier. Finally, fusion cross sections of $^{48}\text{Ca} + ^{48}\text{Ca}$ are investigated with and without the inclusion of the tensor interaction. It is in this symmetric system that the largest effect can be seen for the series of calcium reactions. As mentioned above, both fragments have spin-unsaturated neutron shells which is likely the reason for the greater contribution of the tensor force to further fusion hindrance in the sub-barrier region. Additionally, the manifestation of the hindrance phenomenon can be attributed to a substantial shift upwards in energy of the 2_1^+ and 3_1^- vibrational states seen when using SLy5t ([Guo et al., 2018c](#)).

As the $^{48}\text{Ca} + ^{48}\text{Ca}$ results exhibit a large effect when the tensor force is added, it is an excellent candidate system to compare with experimental data for fusion cross sections. Such a comparison is shown in Fig. 5.4 for both SLy5(t) and a selection of the TIJ forces. Starting first in panel (a), it is clear that the inclusion of the tensor interaction corrects the overestimation present when using SLy5 primarily in the sub-barrier region, though the area around the barrier itself is also more in line with what is seen experimentally. To investigate the source of this correction, it is useful to compare different methods of including the tensor interaction as a check for consistency. To this end a selection from the TIJ set of forces was also used; particularly the T22, T26, T44, and T62 forces which each have different isoscalar and isovector couplings. Panel (b) of Fig. 5.4 plots these results from the TIJ set of forces and a similar correction is seen for the T62 interaction. The other predicted cross sections seem to have quite a varied behavior in the sub-barrier region, suggesting that isoscalar and isovector couplings play a role in driving the dynamics for this reaction. The two forces that best reproduced the data were SLy5t and T62 which have very different values for the spin-current coupling constants, though this could perhaps

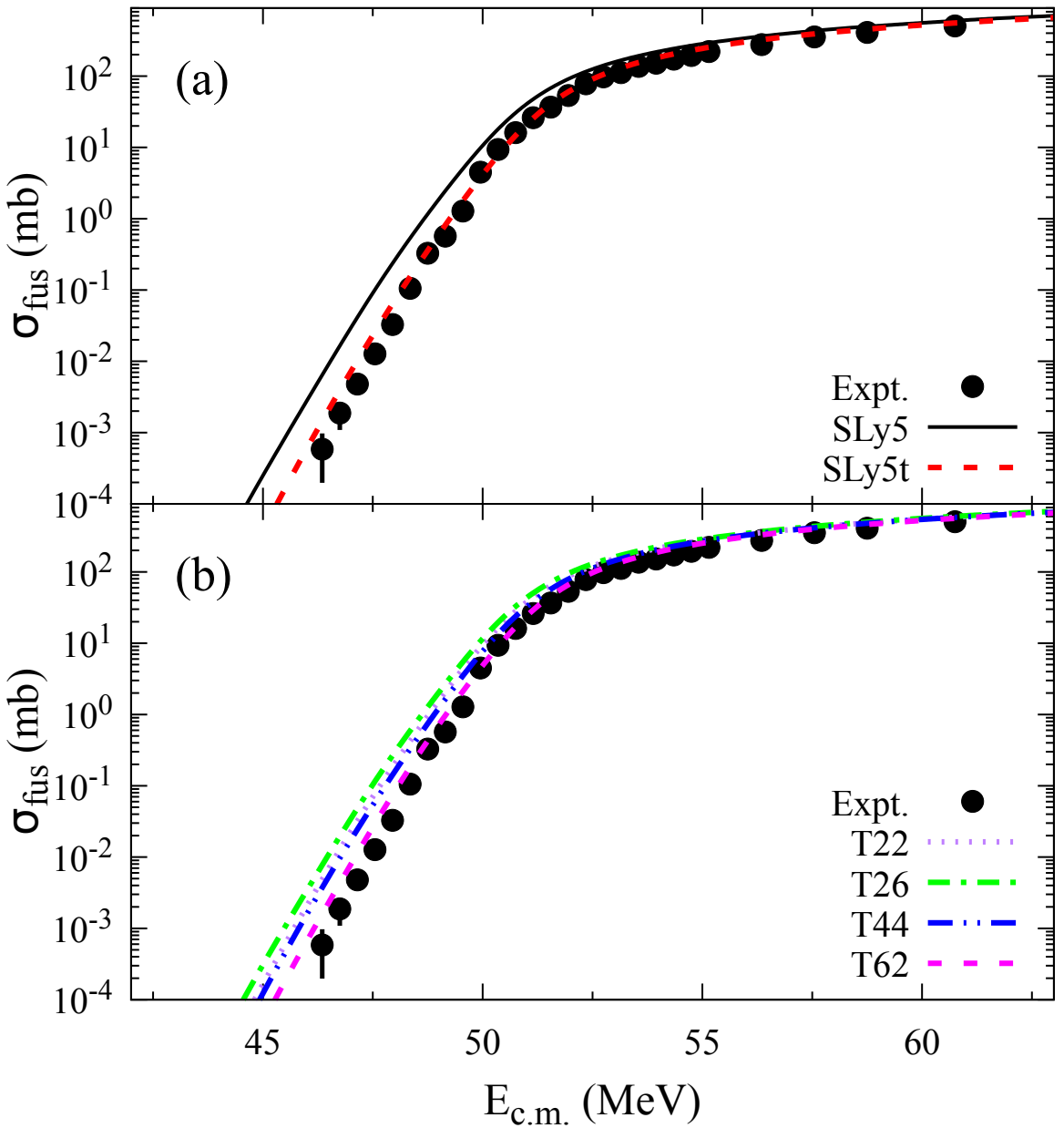


Figure 5.4: Fusion cross sections obtained from the DC-TDHF approach and experimental data from (Stefanini et al., 2009) for $^{48}\text{Ca} + ^{48}\text{Ca}$ at $E_{\text{c.m.}} = 55$ MeV with (a) SLy5 (black solid line) and SLy5t (red dashed line) forces and (b) T22 (purple dotted line), T26 (green dash-dotted line), T44 (blue dash-dot-dotted line), and T62 (orange dashed line) forces.

be explained by the fact that SLy5t had these constants determined as an addition to the unchanged SLy5 functional. Regardless, it is clear that for medium mass, spin-unsaturated systems much is gained by including the tensor interaction in the calculations.

Next we consider the $^{48}\text{Ca} + ^{100,116,120}\text{Sn}$ series which represents a set of mixed-mass systems comprised of a heavy-mass target and a medium-mass projectile. By increasing the mass asymmetry one expects to see larger rearrangement during the reaction resulting in more particle transfer and a more dynamic neck formation around the peak of the barrier, all of which may affect the interaction potential. The results for both SLy5 and SLy5t are presented in Fig. 5.5. For all systems, a deviation from the non-tensor results is observed, though the magnitude varies between them. It should be noted that for ^{48}Ca , ^{100}Sn , and ^{120}Sn the ground state solutions for both forces are found to be spherical, though ^{116}Sn has a slight quadrupole deformation. As the reaction dynamics depend strongly on the initial configuration of the fragments, the symmetry axis of ^{116}Sn is aligned parallel to the collision axis for both SLy5 and SLy5t. The deformation is reduced in SLy5t ($\beta_2 = 0.026$ as opposed to $\beta_2 = 0.077$ seen in SLy5), and thus part of the difference seen for this nucleus could arise from static effects originating in the initial ground state configuration. The reduced deformation is due to the inclusion of the tensor interaction, however, and thus the deviation in cross sections can still be compared.

The final system presented is $^{16}\text{O} + ^{208}\text{Pb}$ which further increases the mass asymmetry of the reaction partners to investigate its effect on fusion cross sections. Both ^{16}O and ^{208}Pb are doubly magic, though only ^{16}O is spin-saturated. As the mass difference between the two fragments is large, substantial density rearrangement will occur over the course of the time evolution, especially at incoming energies close to the fusion barrier. As can be seen in Fig. 5.6, however, it appears that complex dynamical rearrangement alone does not significantly involve the tensor interaction for this system. This also suggests that neck formation and early stage nucleon transfer are not strongly influenced by the inclusion of the tensor force, nor does it introduce hindrance phenomena as is seen in medium-mass

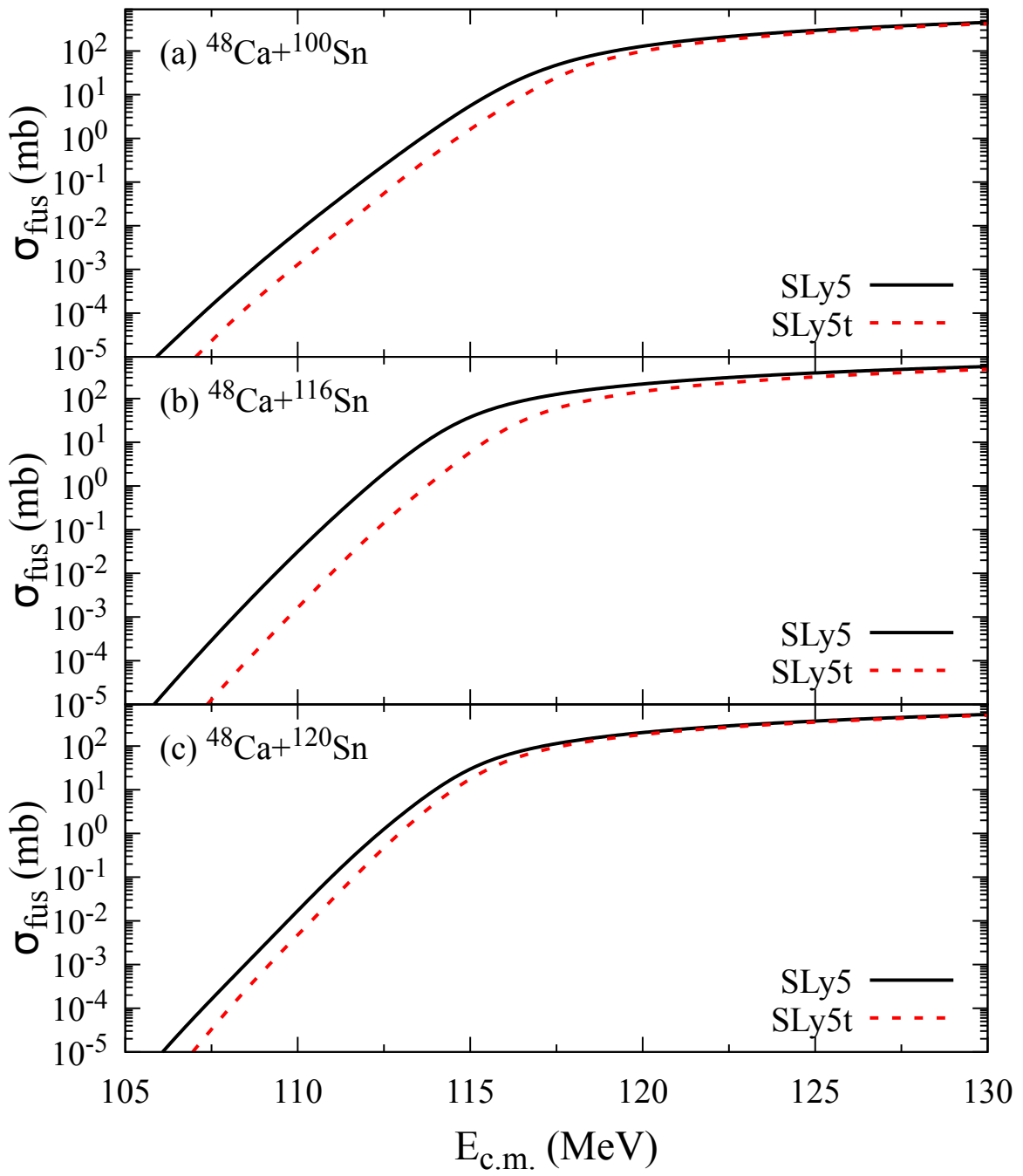


Figure 5.5: Fusion cross sections obtained from the DC-TDHF approach for (a) $^{48}\text{Ca} + ^{100}\text{Sn}$ at $E_{\text{c.m.}} = 125$ MeV, (b) $^{48}\text{Ca} + ^{116}\text{Sn}$ at $E_{\text{c.m.}} = 125$ MeV, and (c) $^{48}\text{Ca} + ^{120}\text{Sn}$ at $E_{\text{c.m.}} = 125$ MeV with SLy5 (black solid line) and SLy5t (red dashed line) forces.

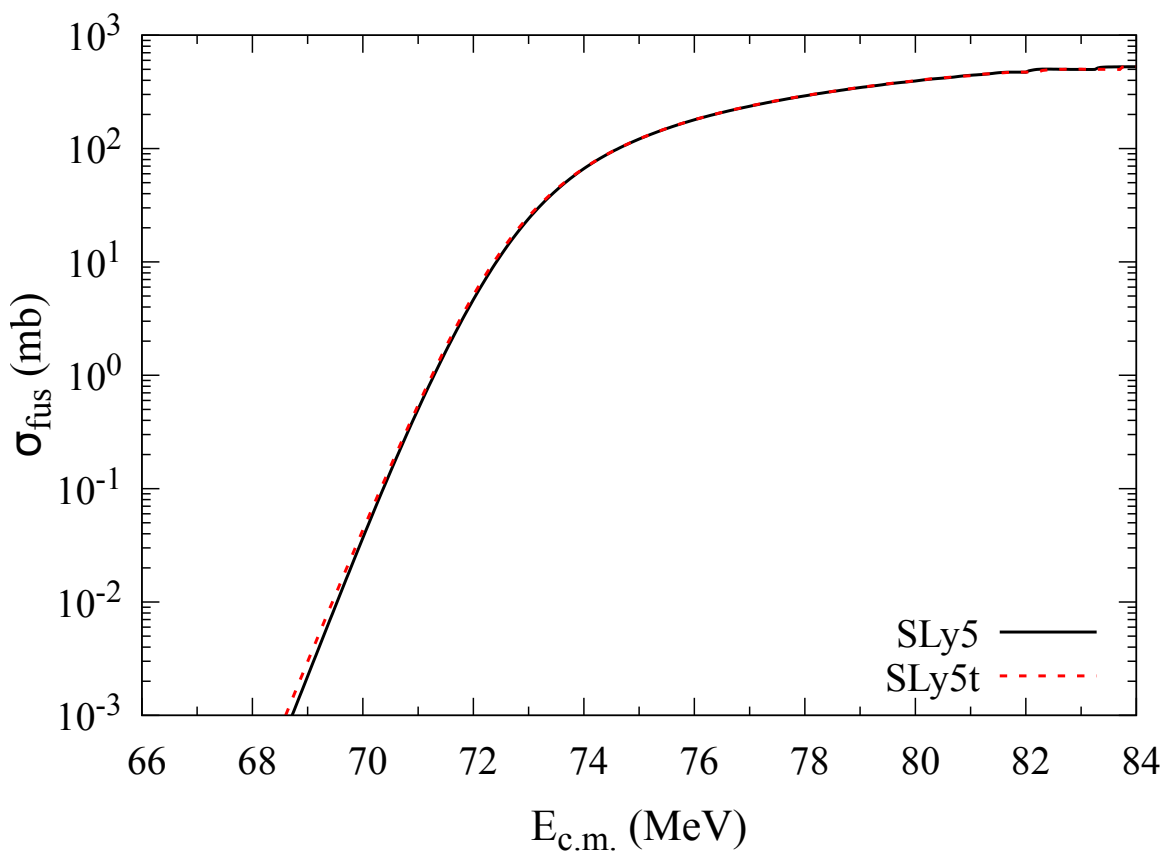


Figure 5.6: Fusion cross sections obtained from the DC-TDHF approach for $^{16}\text{O} + ^{208}\text{Pb}$ at $E_{\text{c.m.}} = 75$ MeV with SLy5 (black solid line) and SLy5t (red dashed line) forces.

systems (Guo et al., 2018c). Further investigation into the effects of particle transfer in systems with large asymmetry are needed, however, to definitively state the role it may play on fusion.

5.4 Conclusions

To conclude, the full tensor interaction has been included in a comprehensive study of fusion cross sections using the DC-TDHF technique. The principal effect of including the tensor force in nuclear reactions is to induce a hindrance effect in the sub-barrier energy regime, though the magnitude of the effect is not uniform for all systems. For example, light systems only see an effect at extreme sub-barrier energies. Even then, the effect is limited to a slight changing of the slope of the cross sections. The move to medium and heavy mass systems on the other hand sees a noted deviation in fusion cross sections when comparing interactions with and without the tensor interaction. Spin-unsaturated systems in particular experience the largest effect and can bring cross sections results more in line with experimental data when the tensor terms are included. As previously explored in (Guo et al., 2018c), the source of hindrance lies primarily in the shifting of low-lying vibrational states for symmetric systems, with particle transfer playing a smaller role in asymmetric collisions of medium-mass nuclei.

It is clear from these results that the tensor interaction has a measurable effect in nuclear reactions and should thus be included if one desires a more complete description of nuclear processes. Including the terms in an ad hoc manner as was done in the case of SLy5t appears to give reasonable results, though a full fitting procedure with all terms should be followed to increase confidence in the forces' representative of nuclei. Parameter sets which have been fit using modern techniques and include all the terms of the Skyrme interaction are well poised to represent the most complete mean-field description of nuclei currently available.

For future studies, further work should of course be done in the investigation of heavy-

ion fusion with the full Skyrme interaction. Heavy systems in particular may be strongly affected by the inclusion of the tensor interaction as well as reactions that lead to super heavy element formation. In addition to fusion, the influence of the tensor force on quasi-fission and fission could be studied using the same TDHF codes that have been utilized for this and previous works.

Acknowledgments

This work is partly supported by NSF of China (Grants No. 11175252 and 11575189), NSFC-JSPS International Cooperation Program (Grant No. 11711540016), and Presidential Fund of UCAS, and by the U.S. Department of Energy under grant No. DE-SC0013847. The computations in present work have been performed on the High-performance Computing Clusters of SKLTP/ITP-CAS and Tianhe-1A supercomputer located in the Chinese National Supercomputer Center in Tianjin.

Chapter 6

Absence of hindrance in microscopic $^{12}\text{C}+^{12}\text{C}$ fusion study

Abstract

[Background] Studies of low-energy fusion of light nuclei are important in astrophysical modeling, with small variations in reaction rates having a large impact on nucleosynthesis yields. Due to the lack of experimental data at astrophysical energies, extrapolation and microscopic methods are needed to model fusion probabilities.

[Purpose] To investigate deep sub-barrier $^{12}\text{C}+^{12}\text{C}$ fusion cross sections and establish trends for the S-factor.

[Method] Microscopic methods based on static Hartree-Fock (HF) and time-dependent Hartree-Fock (TDHF) mean-field theory are used to obtain $^{12}\text{C}+^{12}\text{C}$ ion-ion fusion potentials. Fusion cross sections and astrophysical S-factors are then calculated using the incoming wave boundary condition (IWBC) method.

[Results] Both density-constrained frozen Hartree-Fock (DCFHF) and density-constrained TDHF (DC-TDHF) predict a rising S-factor at low energies, with DC-TDHF predicting a slight damping in the deep sub-barrier region (≈ 1 MeV). Comparison between DC-TDHF calculations and maximum experimental cross-sections in the resonance peaks are good. However the discrepancy in experimental low energy results inhibits interpretation of the trend.

[Conclusions] Using the fully microscopic DCFHF and DC-TDHF methods, no S-factor maximum is observed in the $^{12}\text{C}+^{12}\text{C}$ fusion reaction. In addition, no extreme sub-barrier hindrance is predicted at low energies. The development of a microscopic theory of fusion including resonance effects, as well as further experiments at lower energies must be done before the deep sub-barrier behavior of the reaction can be established.

6.1 Introduction

The study of sub-barrier fusion between light nuclei is of paramount importance to astrophysical applications ranging from element formation to accreting neutron star superbursts. The $^{12}\text{C}+^{12}\text{C}$ fusion reaction in particular stands as a fundamental part of these processes. For example, large type I x-ray bursts (known as superbursts) are suspected to arise from unstable thermonuclear carbon burning in neutron stars accreting material from their partner in binary systems ([Andrew Cumming and Lars Bildsten, 2001](#); [Strohmayer and Brown, 2002](#)). Another example of the importance of this reaction is that it is a vital step on the path to heavier nuclei in the final stages of the helium burning process ([Hoyle, 1954](#)). Reaction rates of $^{12}\text{C}+^{12}\text{C}$ fusion influence both the immediate formation of $A \geq 20$ systems and the creation of larger elements later in the nucleosynthesis processes.

Despite their importance, the $^{12}\text{C}+^{12}\text{C}$ fusion reaction rates at deep sub-barrier energies are poorly known. Experimentally, this is of course due to the extremely low tunneling probabilities at astrophysical energies and the relatively high backgrounds from unwanted reactions ([Spillane et al., 2007](#); [Zickefoose, 2011](#)), motivating for the development of new particle- γ coincidence techniques to reduce this background ([Courtin, S. et al., 2017](#); [Jiang et al., 2018](#)). Resonances in the fusion excitation functions could also be present at deep sub-barrier energies ([Randall L. Cooper et al., 2009](#); [Tumino et al., 2018](#)) and could potentially modify capture rates by orders of magnitudes in this energy range. As a result, with current experimental uncertainties, the bounds of the C-burning reaction rate curves result in a wide range of *s*-process and *p*-process abundances ([Pignatari et al., 2012](#)). New measurements on nearby systems like $^{13}\text{C}+^{12}\text{C}$ ([Zhang and Wang, 2018](#)) have also been performed to establish bounds for the low energy behavior of $^{12}\text{C}+^{12}\text{C}$, as the large resonances and oscillations in the sub-barrier region are absent from the asymmetric systems.

On the theory side, predictions of fusion cross-sections at such low energies vary by orders of magnitude and are thus not able to confidently guide experiments. To assist astrophysical models, attempts have been made to extrapolate $^{12}\text{C}+^{12}\text{C}$ fusion cross sections

to lower energies of astrophysical interest. One common method of extrapolation involves fitting a phenomenological model describing S-factors or cross sections to experimental results and extrapolating the values to lower energies (Fowler et al., 1975; Jiang et al., 2007). The behavior of these models depend on the chosen formula for the fit, resulting in radically different outcomes. Furthermore, these models do not produce the required conditions for superbursts to occur in binary systems (Andrew Cumming et al., 2006), indicating a need for other reactions to provide additional heat, or the presence of resonances (Randall L. Cooper et al., 2009) not accounted for in these extrapolations.

Theoretical developments to improve the description of sub-barrier fusion are based on various strategies. A common approach is to utilize a phenomenological nucleus-nucleus potential and calculating quantum tunneling probabilities for transmission through this potential. One such method utilizes the São Paulo potential, a model that is tuned for astrophysical applications. This model allows for the inclusion of dynamical polarization of the incoming nuclei via an energy dependence of the potential (Gasques et al., 2004, 2005, 2007). Alternatively, polarization effects can be included via the coupled-channels method based on a bare (energy independent) nucleus-nucleus potential, e.g., calculated with a modified double-folding technique (Esbensen et al., 2011; Jiang et al., 2013). Deformation effects of ^{12}C have also been investigated with potential models (Denisov and Pilipenko, 2010), microscopic calculations (Heenen, 1981), and the time-dependent wave-packet method in an attempt to reproduce the resonances that show in $^{12}\text{C}+^{12}\text{C}$ fusion (Diaz-Torres and Wiescher, 2018).

Another strategy is to incorporate dynamical polarization effects via fully microscopic time-dependent approaches such as the time-dependent Hartree-Fock (TDHF) mean-field theory (Negele, 1982; Simenel, 2012b; Simenel and Umar, 2018b). The main motivations for using TDHF as a tool to study ion-ion fusion is that (*i*) it incorporates unrestricted shape evolution of the collision partners induced by coupled-channel effects (Simenel et al., 2013b), and (*ii*) the only parameters of the theory are those of the energy density functional

(usually of the Skyrme type ([Skyrme, 1956b](#)), though results using the quark-meson coupling (QMC) ([Guichon, 1988](#); [Guichon et al., 1996](#); [Stone et al., 2016](#)) approach are also presented here) describing the effective interaction between the nucleons. Direct applications of TDHF to light systems have been performed at and above the fusion barrier ([Bonche et al., 1978](#); [Lebhertz et al., 2012](#); [Simenel et al., 2013d](#)). A drawback of the approach, however, is that it does not incorporate quantum tunneling of the many-body wave-function and thus cannot be used directly to describe sub-barrier fusion.

To overcome this limitation, we predict the nucleus-nucleus potential from TDHF calculations, and then compute transmission probabilities through this potential. The dynamic evolution of the nuclei during the collision leads to an energy dependence of the ion-ion potential as the nuclear densities in near-barrier collisions morph much more than in high energy collisions ([Kouhei Washiyama and Denis Lacroix, 2008](#); [Umar et al., 2014b](#); [Jiang et al., 2014b](#)). Using TDHF to predict nucleus-nucleus potentials has important advantages such as a proper treatment of the Pauli exclusion principle ([Simenel et al., 2017b](#)) and the inclusion of coupling to transfer channels ([Godbey et al., 2017b](#)). Its main limitations, however, are that *(i)* the effect of the couplings are only treated in average (while in coupled-channels calculations the incoming channels are summed coherently) and *(ii)* the energy dependence of the potential is only accounted for at above barrier energies. The second limitation, in particular, is problematic as there is no guarantee that the dynamics of the couplings at the barrier are the same as in deep sub-barrier energies. Nevertheless, predictions of sub-barrier fusion cross-sections based on nucleus-nucleus potentials computed from TDHF trajectories just above the barrier are usually in good agreement with experiments ([Umar et al., 2012b](#); [Umar and Oberacker, 2009](#); [Keser et al., 2012b](#); [Simenel et al., 2013d](#)).

The aim of the present work is to test predictions of $^{12}\text{C}+^{12}\text{C}$ fusion cross-sections at deep-sub-barrier energies with potentials derived microscopically from TDHF trajectories at near-barrier energies. This is achieved with the density-constrained TDHF (DC-TDHF)

method. To consider the separate static and dynamic effects, the density-constrained frozen Hartree-Fock (DCFHF) method has also been used in this study. DCFHF, which is a fully microscopic static approach for studying ion-ion potentials, allows for more direct comparisons to other static approaches and offers a baseline for differences when dynamics is considered ([Simenel et al., 2017b](#)). Our attention is focused on various factors which could impact the theoretical prediction, in order to test the robustness of the predictions. In particular, the effects of numerical approximations, e.g., associated with the grid characteristics, are studied in details. Different energy density functionals are also considered. As the predictions are free of adjustable parameters, our goal is to provide the best possible prediction with existing microscopic tools, with the perspective of identifying limitations of the approach and possible future extensions.

The structure of the paper is as follows. A thorough description of both DCFHF and DC-TDHF approaches is presented in Sec. 6.2 with a general prescription for calculating transmission probabilities presented first. Section 6.3 then presents the results from both methods as they compare to experimental data and recent predictions of the S-factor behavior at low energies of astrophysical interest. Finally a brief summary of the results and a few closing comments are presented in Sec. 6.4.

6.2 Formalism

In this section we introduce the methods used in computing $^{12}\text{C}+^{12}\text{C}$ fusion cross sections.

6.2.1 Density-constrained frozen Hartree-Fock

Following the idea of Brueckner *et al.* ([Brueckner et al., 1968b](#)), we derive the bare ion-ion potential from an energy density functional (EDF) $E[\rho]$ written as an integral of an energy density $\mathcal{H}[\rho(\mathbf{r})]$, i.e.,

$$E[\rho] = \int d\mathbf{r} \mathcal{H}[\rho(\mathbf{r})]. \quad (6.1)$$

The bare potential is obtained by requiring frozen ground-state densities ρ_i of each nucleus ($i = 1, 2$) computed using the Hartree-Fock (HF) mean-field approximation (Hartree, 1928; Fock, 1930). The Skyrme (Skyrme, 1956b) and quark-meson coupling (QMC) (Stone et al., 2016) EDFs are used both to calculate the HF ground state, which are found spherical, and to compute the potential. It accounts for the bulk properties of nuclear matter such as its incompressibility which is crucial at short distances (Brueckner et al., 1968b; Ş. Mişcu and Esbensen, 2006b; Hossain et al., 2015). Overlaying the densities while neglecting the Pauli exclusion principle between nucleons in different nuclei leads to the frozen Hartree-Fock (FHF) potential (Kouhei Washiyama and Denis Lacroix, 2008; Cédric Simenel and Benoit Avez, 2008; Simenel, 2012b)

$$V_{FHF}(R) = \int d\mathbf{r} \mathcal{H}[\rho_1(\mathbf{r}) + \rho_2(\mathbf{r} - R)] - E[\rho_1] - E[\rho_2], \quad (6.2)$$

where R is the distance between the centers of the two nuclei. The resulting FHF potential can then be used to calculate cross sections and related quantities.

The density-constrained FHF (DCFHF) method is the extension of FHF to exactly account for the Pauli exclusion principle between nucleons (Simenel et al., 2017b). This inclusion is obtained by using the same frozen densities ρ_i from the FHF initialization as a constraint for a new HF minimization. This allows the single-particle states to reorganize into a lower energy configuration while maintaining that they are properly antisymmetrized and that the neutron and proton densities remain the same. The potential is defined similarly to FHF, though with the density-constrained wave functions (Simenel et al., 2017b)

$$V_{DCFHF}(R) = \langle \Phi_{DC}(R) | H | \Phi_{DC}(R) \rangle - E[\rho_1] - E[\rho_2]. \quad (6.3)$$

The resulting DCFHF potential has the same barrier height as FHF, though the pressure from the Pauli exclusion principle usually forms a pocket inside the fusion barrier. DCFHF is the static analog to the density-constrained time-dependent Hartree-Fock (DC-TDHF)

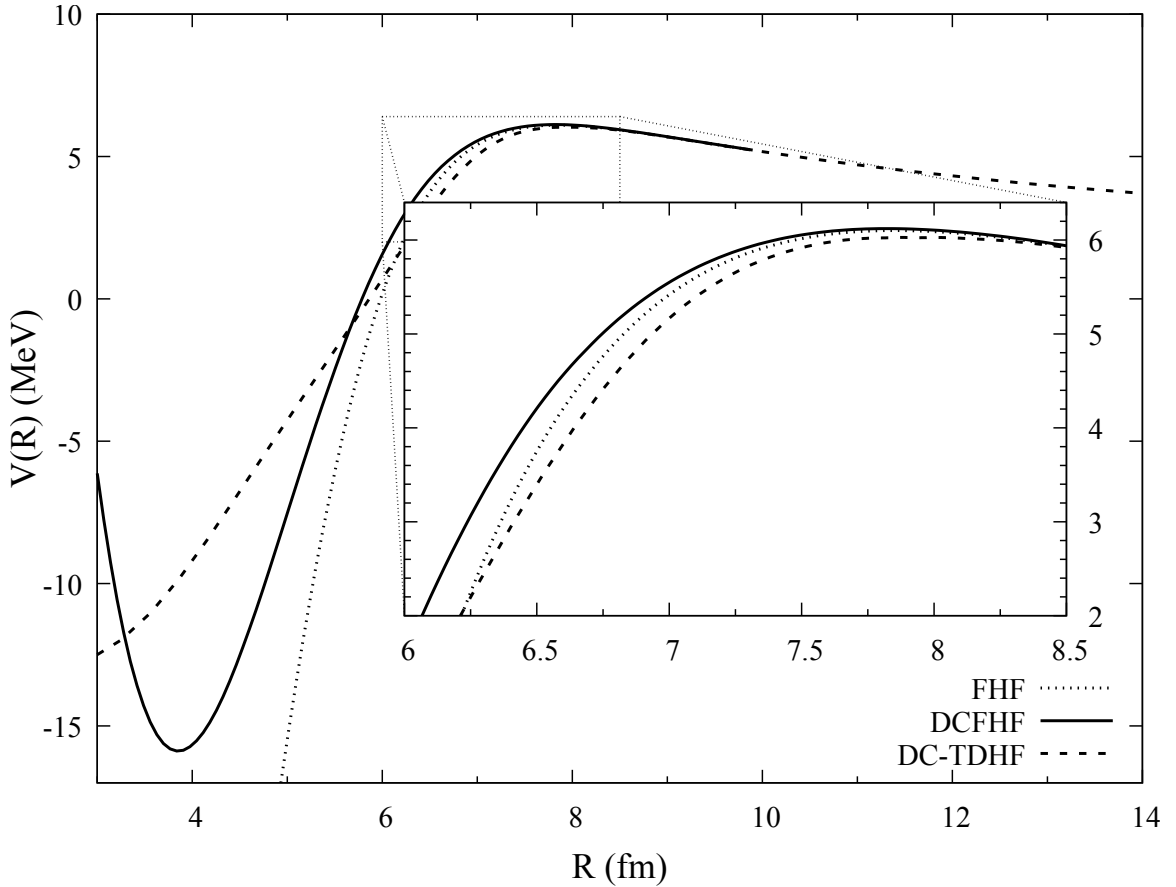


Figure 6.1: Ion-Ion fusion potentials from DC-TDHF, FHF, and DCFHF using the UN-EDF1 force.

approach discussed in Sec. 6.2.2, and thus is particularly useful to separate static and dynamic effects ([Vo-Phuoc et al., 2016](#)).

6.2.2 Density-constrained time-dependent Hartree-Fock

In the TDHF approximation the many-body wave function is taken as a single Slater determinant. In this limit, the variation of the time-dependent action with respect to the single-particle states, ϕ_λ^* , yields the most probable time-dependent path in the multi-dimensional space-time phase space represented as a set of coupled, nonlinear, self-consistent initial value equations for the single-particle states

$$h(\{\phi_\mu\}) \phi_\lambda(r, t) = i\hbar \frac{\partial}{\partial t} \phi_\lambda(r, t) \quad (\lambda = 1, \dots, A), \quad (6.4)$$

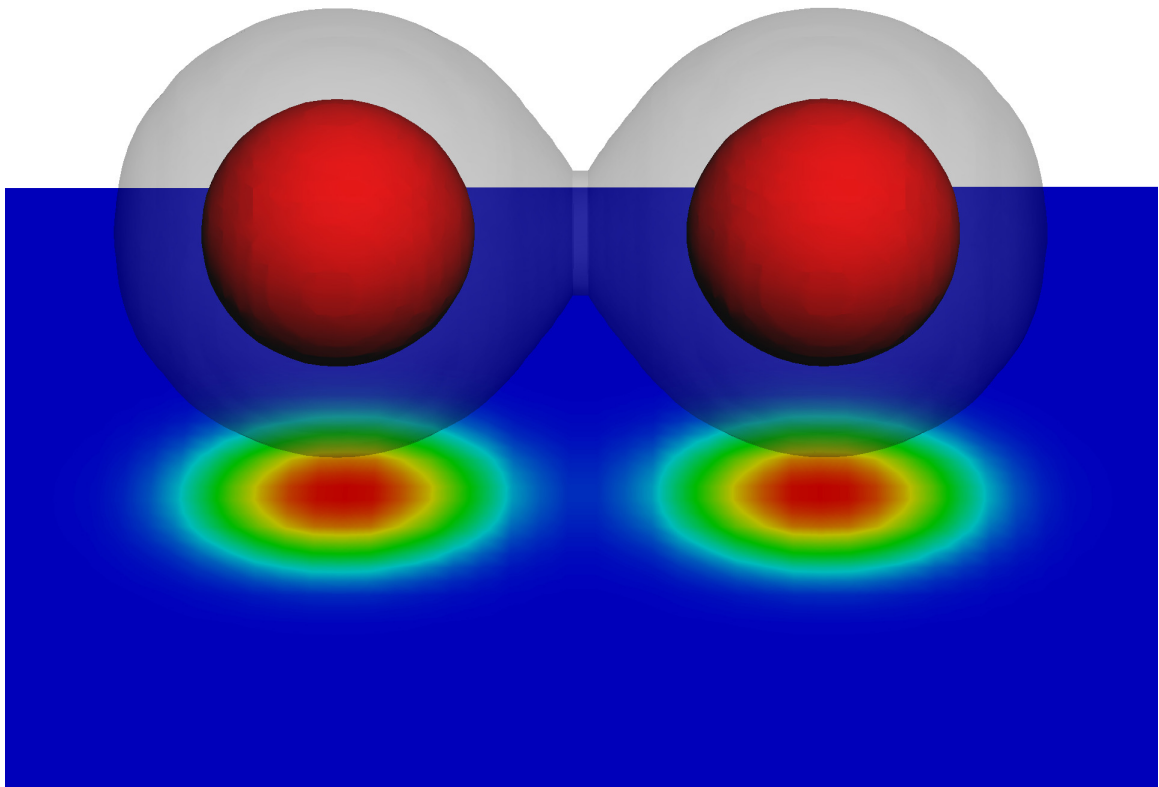


Figure 6.2: 3D contour plot over projected pseudocolor density plot at distance of the barrier peak at $R = 8.06$ fm. Solid red contour surface is drawn for $\rho = 0.08 \text{ fm}^{-3}$ and opaque gray shading is drawn for $\rho = 0.008 \text{ fm}^{-3}$ to show the value and location of interacting densities.

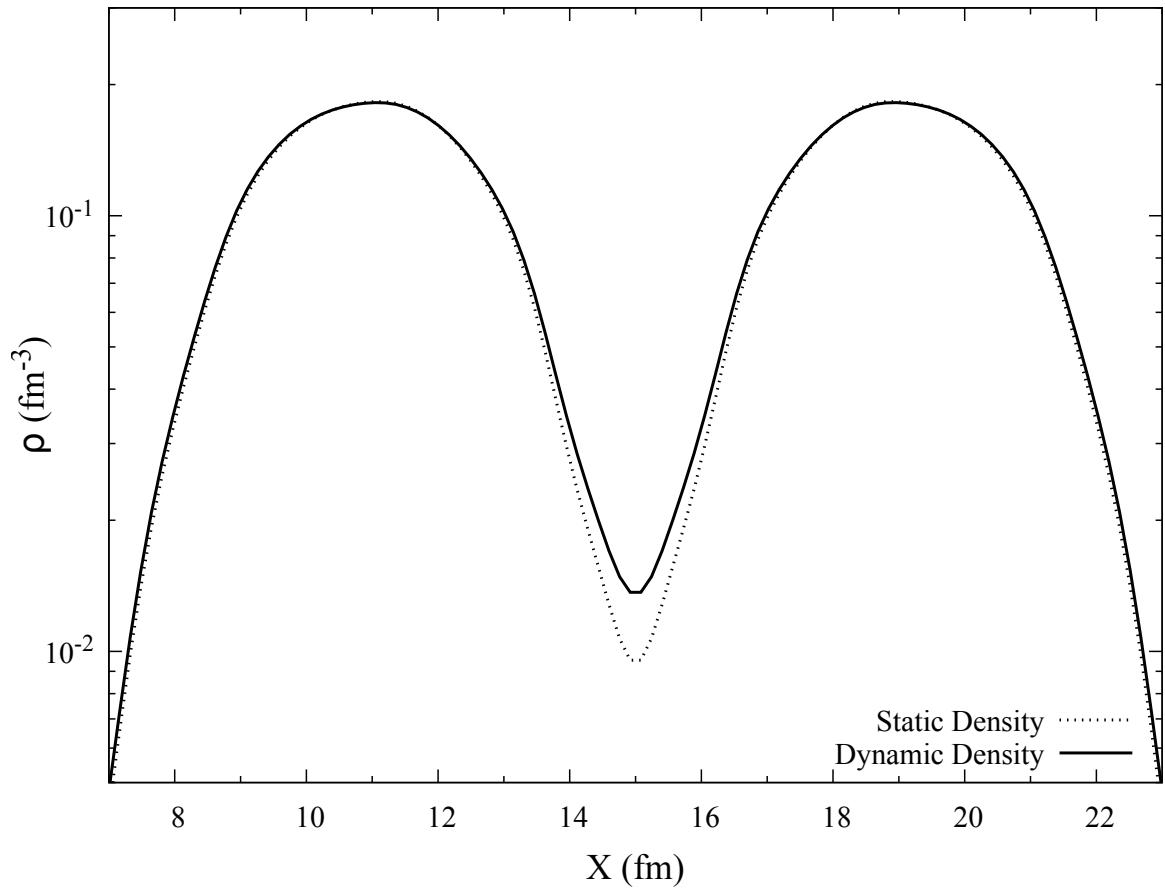


Figure 6.3: Density profile along the collision axis of the $^{12}\text{C} + ^{12}\text{C}$ system at the barrier peak for densities from the static FHF method and dynamic DC-TDHF method.

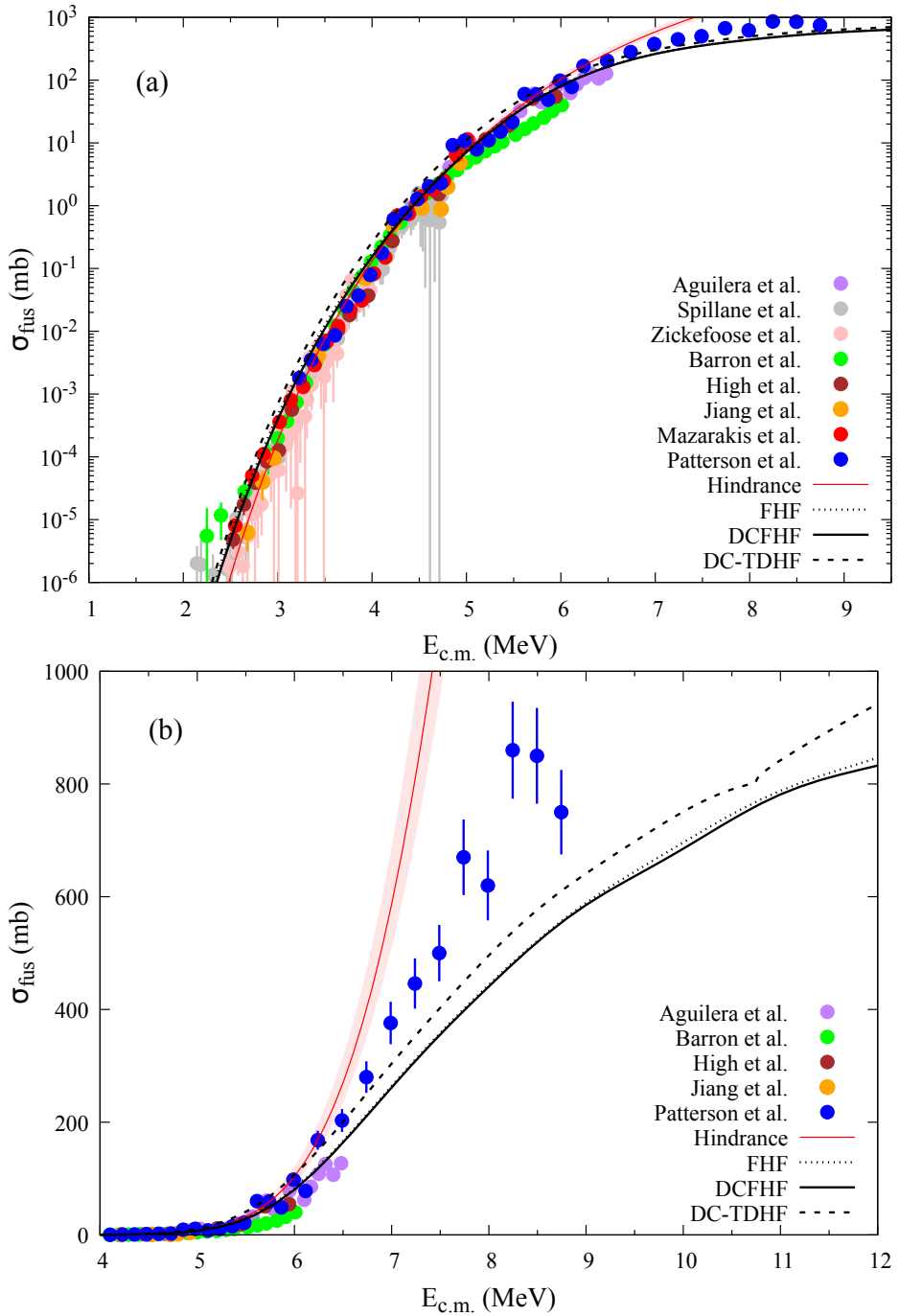


Figure 6.4: Comparison of $^{12}\text{C}+^{12}\text{C}$ fusion cross sections from DC-TDHF, FHF, and DCFHF using the UNEDF1 force and experimental data from (Aguilera et al., 2006; Spillane et al., 2007; Zickefoose, 2011; Barrón-Palos et al., 2006; High and Čujec, 1977; Jiang et al., 2018; Mazarakis and Stephens, 1973; Patterson et al., 1969) in (a) logarithmic and (b) linear scales. The hindrance model is from Ref. (Jiang et al., 2007).

where h is the HF single-particle Hamiltonian. These are the fully microscopic time-dependent Hartree-Fock equations.

The DC-TDHF approach (Umar and Oberacker, 2006f) is then employed to calculate the ion-ion potentials $V_{\text{DC-TDHF}}(R)$ directly from TDHF dynamics and has been used to calculate fusion cross sections for a wide range of reactions (Godbey et al., 2017b; Umar et al., 2014b; Simenel et al., 2013d; Umar et al., 2012b; Umar and Oberacker, 2006e; Oberacker et al., 2010b; Umar et al., 2009b; Jiang et al., 2015b). This approach differs from the DCFHF method in that the nuclear density changes in time following the TDHF evolution. The main steps of this approach are as follows: At certain times t or, equivalently, at certain internuclear distances $R(t)$, a static energy minimization is performed with the same constraint mentioned in Sec. 6.2.1, i.e. constraining the proton and neutron densities to be equal to the instantaneous TDHF densities

$$\delta \langle H - \sum_{q=p,n} \int d\mathbf{r} \lambda_q(\mathbf{r}) \rho_q^{\text{TDHF}}(\mathbf{r}) \rangle = 0. \quad (6.5)$$

We refer to the minimized energy as the “density-constrained energy” $E_{\text{DC}}(R)$. The ion-ion interaction potential $V(R)$ is calculated by subtracting the constant binding energies E_{A_1} and E_{A_2} of the two individual nuclei as obtained by the static HF initialization

$$V(R) = E_{\text{DC}}(R) - E_{A_1} - E_{A_2}. \quad (6.6)$$

The calculated ion-ion fusion barriers incorporate all of dynamical changes in the nuclear density during the TDHF time evolution in a self-consistent manner. As a consequence of this inclusion of dynamical effects the DC-TDHF potential is energy dependent (Umar et al., 2014b). At high collision energies, the densities do not have time to rearrange and the results approach the frozen picture. The features arising from the dynamic collision distinguish DC-TDHF from the fully static DCFHF approach.

6.2.3 Cross sections

Both DCFHF and DC-TDHF provide a way to obtain one dimensional ion-ion fusion potentials, which can then be used to calculate fusion cross sections and related quantities. However, standard implementations of barrier penetration models, i.e., with incoming wave boundary conditions (IWBC) of absorbing imaginary potentials at short distance, cannot account for the sub-barrier resonances observed experimentally (Jiang et al., 2013). Indeed, these boundary conditions are based on the assumption that fusion always occurs when the barrier is overcome, while in reality fusion may not happen if no corresponding states in the compound system are present. This is particularly critical in $^{12}\text{C}+^{12}\text{C}$ at $E < 7$ MeV due to the low level density of positive parity states in ^{24}Mg , hindering fusion off-resonance. DC-TDHF predictions should then be compared with experimental cross-sections on-resonance.

Transmission probabilities $T_l(E_{\text{c.m.}})$ are acquired by numerical integration of the two-body Schrödinger equation:

$$\left[\frac{-\hbar^2}{2M(R)} \frac{d^2}{dR^2} + \frac{l(l+1)\hbar^2}{2M(R)R^2} + V(R) - E \right] \psi = 0. \quad (6.7)$$

The IWBC method is used to calculate transmission probabilities which assumes that fusion occurs once the minimum of $V(R)$ is reached (Rawitscher, 1964). The barrier penetrability $T_l(E_{\text{c.m.}})$ is then the ratio of the incoming flux at the minimum of the potential inside the barrier to the incoming flux at a large distance. Once $T_l(E_{\text{c.m.}})$ is calculated, the fusion cross sections at energies above and below the barrier are calculated as

$$\sigma_f(E_{\text{c.m.}}) = \frac{\pi}{k_0^2} \sum_{l=0}^{\infty} (2l+1) T_l(E_{\text{c.m.}}). \quad (6.8)$$

In the case of DCFHF, the mass is a constant and equal to the reduced mass, $M(R) = \mu$. In the case of DC-TDHF, the coordinate-dependent mass $M(R)$ can be calculated directly from TDHF dynamics (Umar and Oberacker, 2009). This mass primarily influences the

inner part of the barrier, leading to a somewhat broader barrier width thus leading to further hindrance in the sub-barrier region. Instead of solving the Schrödinger equation using the coordinate-dependent mass $M(R)$, the potential can be transformed by a scale factor ([Umar and Oberacker, 2009](#); [Goeke et al., 1983](#))

$$d\bar{R} = \left(\frac{M(R)}{\mu} \right)^{\frac{1}{2}} dR. \quad (6.9)$$

Upon making this transformation $M(R)$ is replaced by the reduced mass μ in Eq. 6.7 and the Schrödinger equation is solved using the modified Numerov method as it is formulated in the coupled-channel code CCFULL ([Hagino et al., 1999](#)).

6.2.4 Energy density functional

Unless otherwise stated, the Skyrme parametrization used was UNEDF1 ([Kortelainen et al., 2012](#)). To investigate the dependence on the choice of the energy density functional we have also performed calculations using the SLy4d functional ([Ka–Hae Kim et al., 1997](#)). Both parametrizations were fitted without the center of mass correction, making them ideal for dynamic calculations.

These parametrizations do not include the tensor terms of the functional. The effects of these terms on heavy-ion fusion have been recently studied ([Dai et al., 2014c](#); [Stevenson et al., 2016b](#); [Guo et al., 2018c](#)). However, a comparison of the nucleus-nucleus potentials calculated with the SLy5 functional (without tensor) ([Chabanat et al., 1998](#)) and with SLy5t (including tensor) ([Colò et al., 2007b](#)) showed that the effect is quite small for $^{12}\text{C} + ^{12}\text{C}$ ([Guo et al., 2018a](#)).

Furthermore, to investigate the behavior of a different density dependence than that of the one used in Skyrme fits, the QMC-I ([Stone et al., 2016](#)) parametrization of the functional based on the quark-meson coupling model ([Guichon, 1988](#); [Guichon et al., 1996](#)) was utilized for the first time in a dynamic fusion study.

6.2.5 Numerical details

All calculations were done using the three dimensional VU-TDHF3D code which contains no symmetry restrictions and implements the full energy-density functional including all time-odd terms ([Umar and Oberacker, 2006g](#)). The numerical box used was 72 fm in length along the collision axis and 24 fm in the other two directions. The basis-spline collocation method used to represent derivative operators on the lattice is robust and allows for a coarser grid spacing (typically 1 fm). However a finer grid spacing of 0.8 fm was used for the current work to ensure very precise calculations. When comparing barrier heights, however, the change between the coarse and fine grid spacings amounts to a difference of about $\Delta V_{\text{peak}} = 0.5 \text{ keV}$.

6.3 Results

In this section we present ion-ion potentials, fusion cross sections, and astrophysical S factors obtained from the methods outlined in Sec. 6.2.

A light system such as $^{12}\text{C} + ^{12}\text{C}$ does not exhibit a strong energy dependence in the DC-TDHF potential, though in practice collision energies close to the fusion barrier are chosen to allow for maximal rearrangement. To this end, the energy chosen for comparison to experiment was $E_{\text{c.m.}} = 6.03 \text{ MeV}$. Figure 6.1 shows a comparison of effective ion-ion potentials as calculated using the methods presented in Sec. 6.2. All three methods result in an effective potential that follows the point Coulomb potential until the nuclear overlap is enough to form the barrier peak. Both FHF and DCFHF potentials form a similar barrier top before diverging in the inner region. For DCFHF, a pocket is formed by the pressure resulting from the Pauli exclusion principle ([Simenel et al., 2017b](#)), whereas FHF decreases rapidly at small distance and has a thinner barrier width overall at sub-barrier energies. The potential that is created from the DC-TDHF method shows that dynamic features of the collision causes the effective potential to deviate from the incoming Coulomb potential earlier than both FHF and DCFHF. Also, DC-TDHF results in a thinner barrier than FHF

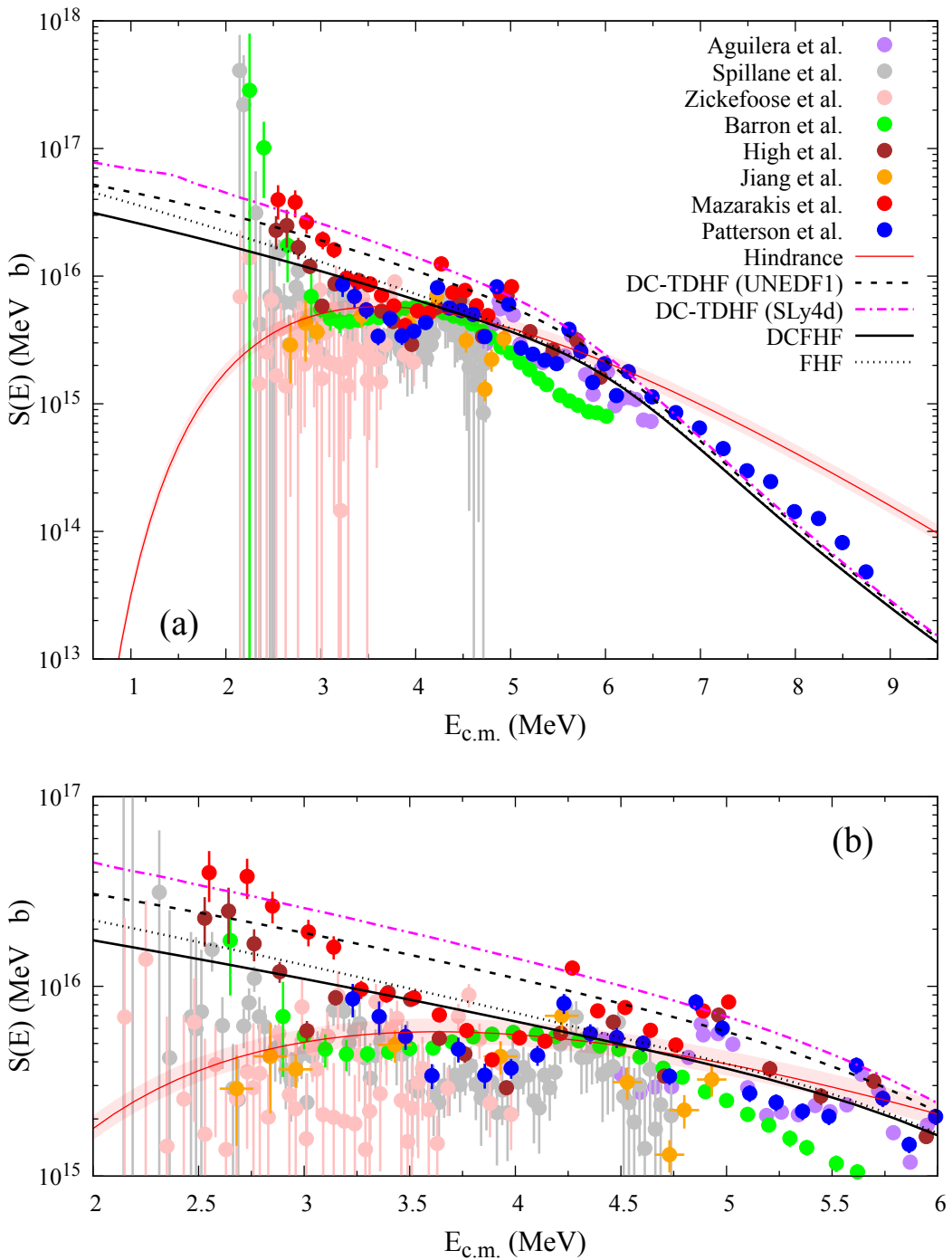


Figure 6.5: Comparison of $^{12}\text{C}+^{12}\text{C}$ fusion S factors from DC-TDHF, FHF, and DCFHF using the UNEDF1 force, DC-TDHF using the SLy4d force, the hindrance model from (Jiang et al., 2007), and experimental data from (Aguilera et al., 2006; Spillane et al., 2007; Zickefoose, 2011; Barrón-Palos et al., 2006; High and Čujec, 1977; Jiang et al., 2018; Mazarakis and Stephens, 1973; Patterson et al., 1969).

and DCFHF, which is expected to enhance sub-barrier cross sections.

In Fig. 6.2, a 3D contour plot resulting from the DC-TDHF calculation is shown over a pseudocolor density plot corresponding to the position of the barrier peak, $R = 8.06$ fm. At this position, the core contours of $\rho = 0.08$ fm $^{-3}$ (solid red contour surface) are well separated at the top of the barrier. The opaque, gray contour is drawn to show the level of the density in the overlapping region, $\rho = 0.008$ fm $^{-3}$. The relatively low density at the barrier peak indicates that Pauli repulsion will play a small role for this system at the barrier radius. Despite being small, this density overlap produces enough attraction to compensate the Coulomb repulsion, leading to fusion.

A more quantitative representation of the density profile at the barrier is shown in Fig. 6.3. Here, the density is plotted along the collision axis. It is interesting to note the higher density in the neck at this separation when dynamics is accounted for (DC-TDHF). This change of neck density, induced by the dynamics, is responsible for the lowering of the barrier in DC-TDHF, as seen in Fig. 6.1. Although this change in barrier energy is relatively small, it can significantly influence tunneling probabilities at deep sub-barrier energies.

The potentials of Fig. 6.1 are used to compute fusion cross sections in Fig. 6.4. At these scales the difference does not appear to be large, though DC-TDHF seems to slightly over predicts cross sections for this system bellow the barrier. However, as discussed in Sec. 6.2.3, the comparison should only be made with the maximum of the cross-section on-resonance ([Jiang et al., 2013](#)), indicating a better agreement.

A standard representation of the sub-barrier fusion cross-section is given by the astrophysical S factor

$$S(E) = \sigma(E)Ee^{2\pi\eta}, \quad (6.10)$$

where E is the center of mass energy, $\eta = Z_1Z_2e^2/\hbar v$ is the Sommerfeld parameter, and v is the relative velocity of the nuclei $v = \sqrt{2E/\mu}$ for a system of reduced mass μ . The S factor is often used to analyze fusion reactions of astrophysical interest as, to some extent, it gets

rid of the strong energy dependence at sub-barrier energies.

Figure 6.5 shows a comparison between theoretical and experimental S factors. Both DCFHF and DC-TDHF predict a similar trend for deep sub-barrier energies. However neither suggest an extreme hindrance effect such as that seen in the power law extrapolation from Jiang et al. ([Jiang et al., 2007](#)). The zoom in the low-energy region in Fig. 6.5(b) shows that DC-TDHF reproduces well the upper bound of the resonances seen in the data, except for the lowest resonance at 2.14 MeV. Note, however, that this resonance is not observed in all channels and is subject to experimental controversy ([Tang, 2018](#)). Similar agreement with experiment was found in earlier extrapolations such as ([Fowler et al., 1975](#); [Gasques et al., 2005](#)), though it should be reiterated that none of the ion-ion potentials presented in this work were fit to experimental data. Note also the role of the Pauli repulsion which can be seen by comparing FHF to DCFHF ([Simenel et al., 2017b](#)). We see that the additional fusion hindrance at sub-barrier energies due to Pauli repulsion is largely negligible at experimental energies.

As mentioned in the introduction, there is no guarantee that the dynamical effects on the potential extracted from a TDHF calculation at an energy near the barrier are the same as in deep sub-barrier energies. To test the validity of this approximation, DC-TDHF calculations have been performed at different TDHF energies, as shown in Fig. 6.6(a). When examining the behavior of the S factors at deep sub-barrier energies, differences in fusion cross sections are greatly magnified. Nevertheless, the difference between the DC-TDHF predictions remains small, indicating that the results are only slightly affected by the energy dependence of the potential. The bulk of this effect arises from the increasing and sharpening peaks of the coordinate dependent mass $M(R)$ at the location of the barrier at lower energies, though as mentioned before, density rearrangement also plays a role.

Finally, let us investigate the sensitivity to the energy density functional. As such, we have plotted the comparison using the resultant S factors in part (b) of Figure 6.6 which shows the astrophysical S factor for three different functionals: the SLy4d ([Ka–Hae Kim](#)

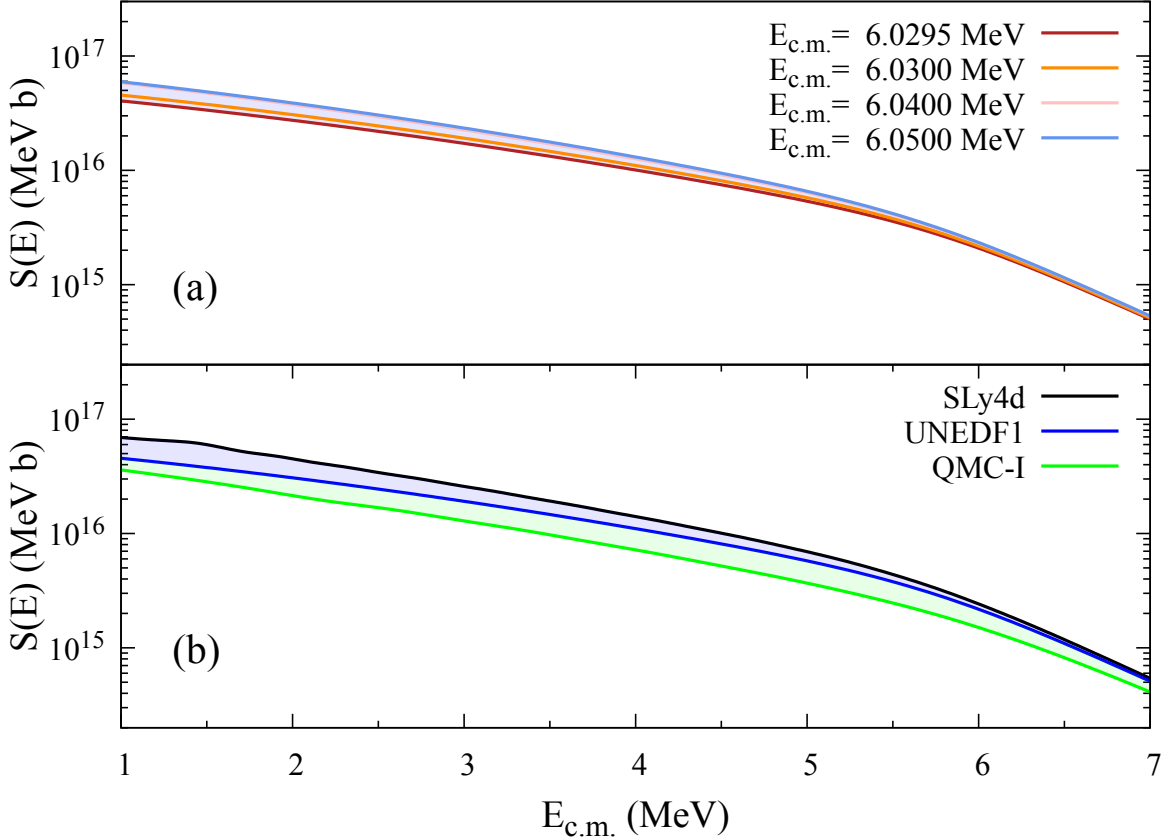


Figure 6.6: Comparison of $^{12}\text{C} + ^{12}\text{C}$ fusion S factors from DC-TDHF at (a) differing TDHF energies and (b) using different functionals.

et al., 1997) and UNEDF1 (Kortelainen et al., 2012) Skyrme functionals and the QMC-I functional which has a different density dependence than the Skyrme one. The main conclusion is that the trends are very similar for these three functionals. In particular, none of them predict a maximum in the S factor. Quantitatively, the QMC results are lower throughout the sub-barrier energy region. Nevertheless, the variations in the experimental data does not allow for the unambiguous identification of what functional best reproduces experimental results.

6.4 Conclusion

A precise study of $^{12}\text{C} + ^{12}\text{C}$ fusion has been performed using multiple parameter-free, microscopic approaches. Various energy density functionals were also explored, includ-

ing the first application to heavy-ion fusion with an energy-density functional based on the quark-meson coupling model. A comparison between FHF and DCFHF approaches shows that Pauli repulsion only plays a minor role in this system, and is not sufficient to induce a maximum in the astrophysical S factor. Dynamical effects described in the DC-TDHF approach exhibit the same trend as static calculations, with slightly higher sub-barrier fusion cross-sections due to a narrowing of the potential barrier. DC-TDHF predictions are in good agreement with the maximum fusion cross-sections on-resonances. The different functionals all lead to the same trends in the astrophysical S factor, with slightly smaller values for the QMC-I functional.

Future studies of other light nuclei should be performed using both DCFHF and DC-TDHF as the effect of dynamic processes may play a larger role in other reactions, e.g. transfer effects in asymmetric systems such as $^{13}\text{C}+^{12}\text{C}$. The separation of static and dynamic effects is an interesting endeavor in itself which may hint at what drives (and hinders) fusion in both light and heavy nuclei.

Finally, to address the limitations inherent in the methods pursued here and to further understand the fusion process for systems like $^{12}\text{C}+^{12}\text{C}$, additional techniques for studying sub-barrier fusion should be explored. One such improvement would be to pursue a fully microscopic description of many-body tunneling, e.g., following Refs. ([Levit et al., 1980](#); [Reinhardt, 1980](#)), to avoid the reduction of the problem to the two-body case as done here. Such a method would be of great use beyond light systems or fusion alone, opening the door for a fully microscopic mean field description of fission and fusion.

Acknowledgments

We thank S. Courtin for useful discussions and for clarifying experimental questions. This work has been supported by the Australian Research Council Grants No. DP180100497 and DP190100256, and by the U.S. Department of Energy under grant No. DE-SC0013847 with Vanderbilt University. Part of this research was undertaken with the assistance of re-

sources from the National Computational Infrastructure (NCI), which is supported by the Australian Government.

Chapter 7

Deformed shell effects in $^{48}\text{Ca} + ^{249}\text{Bk}$ quasifission fragments

Abstract

[Background] Quasifission is the main reaction channel hindering the formation of superheavy nuclei (SHN). Its understanding will help to optimize entrance channels for SHN studies. Quasifission also provides a probe to understand the influence of shell effects in the formation of the fragments.

[Purpose] Investigate the role of shell effects in quasifission and their interplay with the orientation of the deformed target in the entrance channel.

[Methods] $^{48}\text{Ca} + ^{249}\text{Bk}$ collisions are studied with the time-dependent Hartree-Fock approach for a range of angular momenta and orientations.

[Results] Unlike similar reactions with a ^{238}U target, no significant shell effects which could be attributed to ^{208}Pb “doubly-magic” nucleus are found. However, the octupole deformed shell gap at $N = 56$ seems to strongly influence quasifission in the most central collisions.

[Conclusions] Shell effects similar to those observed in fission affect the formation of quasifission fragments. Mass-angle correlations could be used to experimentally isolate the fragments influenced by $N = 56$ octupole shell gaps.

7.1 Introduction

Quasifission occurs when the collision of two heavy nuclei produces two fragments with similar characteristics to fusion-fission fragments, but without the intermediate formation of a fully equilibrated compound nucleus (Heusch et al., 1978; Back et al., 1981, 1983; Bock et al., 1982). It is the main mechanism that hinders fusion of heavy nuclei and consequently the formation of superheavy elements (Sahm et al., 1984; Gäggeler et al., 1984; Schmidt and Morawek, 1991; Back et al., 2014b; Khuyagbaatar et al., 2018; Banerjee et al., 2019). It is thus crucial to achieve a deeper insight of quasifission in order to mini-

imize its impact and maximize the formation of compound nuclei for heavy and superheavy nuclei searches.

Quasifission also provides a unique probe to quantum many-body dynamics of out-of-equilibrium nuclear systems. For instance, quasifission studies bring information on mass equilibration time-scales (Tōke et al., 1985; Shen et al., 1987; du Rietz et al., 2011), on shell effects in the exit channels (Itkis et al., 2004; Nishio et al., 2008; Kozulin et al., 2014; Wakhle et al., 2014; Morjean et al., 2017), as well as on the nuclear equation of state (Veselsky et al., 2016; Zheng et al., 2018). In fusion-fission, the exit channel is essentially determined by the properties of the compound nucleus, and does not depend a priori on the specificity of the entrance channel. This is not the case in quasifission which is known to preserve a strong memory of the entrance channel properties. As a result, understanding the interplay between the entrance and exit channels requires a significant amount of experimental systematic studies. These include investigations of the role of beam energy (Back et al., 1996; Nishio et al., 2008, 2012), dissipation (Williams et al., 2018), fissility of the compound nucleus (Lin et al., 2012; du Rietz et al., 2013), deformation of the target (Hinde et al., 1995, 1996; Knyazheva et al., 2007; Hinde et al., 2008; Nishio et al., 2008), spherical shells of the collision partners (Simenel et al., 2012; Mohanto et al., 2018), and the neutron-to-proton ratio N/Z of the compound nucleus (Hammerton et al., 2015, 2019).

On the theory side, quasifission has been studied with various approaches. This includes classical methods such as a transport model (Diaz-Torres et al., 2001), the dinuclear system model (Adamian et al., 2003; Huang et al., 2010; Bao et al., 2015; Guo et al., 2017b), and models based on the Langevin equation (Zagrebaev and Greiner, 2005; Aritomo, 2009; Aritomo et al., 2012; Karpov and Saiko, 2017; Sekizawa and Hagino, 2019). Microscopic approaches such as quantum molecular dynamics (Wen et al., 2013; Wang and Guo, 2016b; Zhao et al., 2016) and the time-dependent Hartree-Fock (TDHF) theory (Cédric Golabek and Cédric Simenel, 2009b; David J. Kedziora and Cédric Simenel, 2010; Wakhle et al., 2014; Oberacker et al., 2014b; Hammerton et al., 2015; Umar et al., 2015b,

2016b; Sekizawa and Yabana, 2016b; Chong Yu and Lu Guo, 2017b; Ayik et al., 2017, 2018; Sekizawa, 2017c; Wakhle et al., 2018; Morjean et al., 2017; Sekizawa and Hagino, 2019) have also been used. See (Simenel, 2012b; Simenel and Umar, 2018b; Kazuyuki Sekizawa, 2019; Stevenson and Barton, 2019) for recent reviews on TDHF.

An advantage of microscopic calculations is that their only inputs are the parameters of the energy density functional describing the interaction between the nucleons. Since these parameters are usually fitted on nuclear structure properties only, such calculations do not require additional parameters determined from reaction mechanisms, such as nucleus-nucleus potentials. In addition, TDHF calculations treat both reaction mechanisms and structure properties on the same footing. This is important for reactions with actinide targets which exhibit a strong quadrupole deformation.

Indeed, the outcome of the calculations strongly depend on the orientation of the nuclei. For instance, TDHF calculations of $^{40}\text{Ca} + ^{238}\text{U}$ reaction showed that only collisions with the side of the ^{238}U could lead to configurations which are compact enough to enable fusion (Wakhle et al., 2014). This is contrary to the collisions with the tip of ^{238}U which seem to always lead to a fast quasifission (after $\sim 5 - 10$ zeptoseconds (zs) of contact time) as long as contact between collision partners is achieved. A remarkable observation of this work was the systematic production of lead nuclei ($Z = 82$), known to possess a strong spherical proton shell gap, in tip collisions only, showing a strong influence of orientation dependent shell effects in the production of the fragments. Such influence of shell effects was proposed to explain peaks in fragment mass distributions (Itkis et al., 2004; Nishio et al., 2008; Wakhle et al., 2014), but experimental confirmation came only recently with the observation of a peak of quasifission fragments at $Z = 82$ protons from x-ray measurements (Morjean et al., 2017).

Deformed shell effects in the region of ^{100}Zr have also been invoked to interpret the outcome of TDHF simulations of $^{40,48}\text{Ca} + ^{238}\text{U}$, ^{249}Bk collisions (Oberacker et al., 2014b; Umar et al., 2016b). It is then natural to wonder if other shell effects, spherical or deformed,

could be driving the dinuclear system out of its compact shape, into quasifission. Potential candidates are shell effects known to influence the outcome of fission reactions. It has recently been proposed that octupole deformed shell effects, in particular with Z or $N = 52 - 56$, are the main driver to asymmetric fission (Scamps and Simenel, 2018, 2019). The fact that ^{208}Pb can easily acquire an octupole deformation (its first excited state is a 3^- octupole vibration) is compatible with this interpretation. Note also that some superheavy nuclei like ^{294}Og are expected to encounter super-asymmetric fission and produce a heavy fragment around ^{208}Pb (Poenaru and Gherghescu, 2018; Warda et al., 2018; Matheson et al., 2019; Zhang and Wang, 2018), confronting the idea that quasifission valleys could match fission ones.

In this work we study the $^{48}\text{Ca} + ^{249}\text{Bk}$ reaction with the TDHF approach. The choice of this reaction is motivated by its success in forming the element $Z = 117$ (Yu. Ts. Oganessian et al., 2010, 2011; Oganessian et al., 2012, 2013; Khuyagbaatar et al., 2014). Previous TDHF studies of quasifission with actinide targets were restricted to one or two orientations of the target to limit computational time. However, to allow possible comparison with experimental data, it is important to simulate a range of orientations in addition to the usual tip and side configurations. We therefore performed systematic simulations, spanning both a range of orientations and a range of angular momenta. This allows us to study correlations between, e.g., mass, angle, kinetic energy, as well as to predict distributions of neutron and proton numbers at the mean-field level. These distributions are used to identify potential shell gaps driving quasifission. The method is described in Sec. 7.2. The results are discussed in Sec. 7.3. We then conclude in Sec. 7.4.

7.2 Method

The TDHF theory provides a microscopic approach to investigate a large selection of phenomena observed in low energy nuclear physics (Negele, 1982; Simenel, 2012b; Simenel and Umar, 2018b). In particular, TDHF provides a dynamic quantum many-

body description of nuclear reactions in the vicinity of the Coulomb barrier, such as fusion (Bonche et al., 1978; Flocard et al., 1978; Simenel et al., 2001; Umar et al., 2008b; Umar and Oberacker, 2006h; Kouhei Washiyama and Denis Lacroix, 2008; Umar et al., 2010b; Lu Guo and Takashi Nakatsukasa, 2012b; Keser et al., 2012b; Simenel et al., 2013d; Oberacker et al., 2012, 2010b; Umar et al., 2012b; Simenel et al., 2013b; Umar et al., 2014b; Jiang et al., 2014b), deep-inelastic reactions and transfer (Koonin et al., 1977; Simenel, 2010b, 2011b; Umar et al., 2008b; Kazuyuki Sekizawa and Kazuhiro Yabana, 2013b; Scamps and Lacroix, 2013b; Sekizawa and Yabana, 2014; Bourgin et al., 2016; Umar et al., 2017b; Kazuyuki Sekizawa, 2019), and dynamics of (quasi)fission fragments (Umar et al., 2010b; Wakhle et al., 2014; Oberacker et al., 2014b; Simenel and Umar, 2014b; Umar et al., 2015b; Umar and Oberacker, 2015; Scamps et al., 2015b; Goddard et al., 2015b; Aurel Bulgac et al., 2016; Sekizawa and Yabana, 2016b; Umar et al., 2016b). The classification of various reaction types in TDHF is done by calculating the time evolution of expectation values of one-body observables: fragments' centers of masses, mass and charges on each side of the neck, kinetic energy, orbital angular momentum, among others. Quasifission is characterized by two final state fragments that emerge after a long lived composite system (typically longer than 5 zs) and final fragment masses $A_f = A_{\text{CN}}/2 \pm 20$ or more. In addition, final TKEs distinguish quasifission from highly damped deep-inelastic collisions, which have a smaller mass and charge difference between initial and final fragments. In TDHF the mass and charge difference between the initial nuclei and the final fragments measure the number of nucleons transferred. As discussed above fusion corresponds to the case where the final product remains as a single composite for a reasonably long time, chosen here to be 35 zs.

The TDHF equations for the single-particle wave functions

$$h(\{\phi_\mu\}) \phi_\lambda(r, t) = i\hbar \frac{\partial}{\partial t} \phi_\lambda(r, t) \quad (\lambda = 1, \dots, A), \quad (7.1)$$

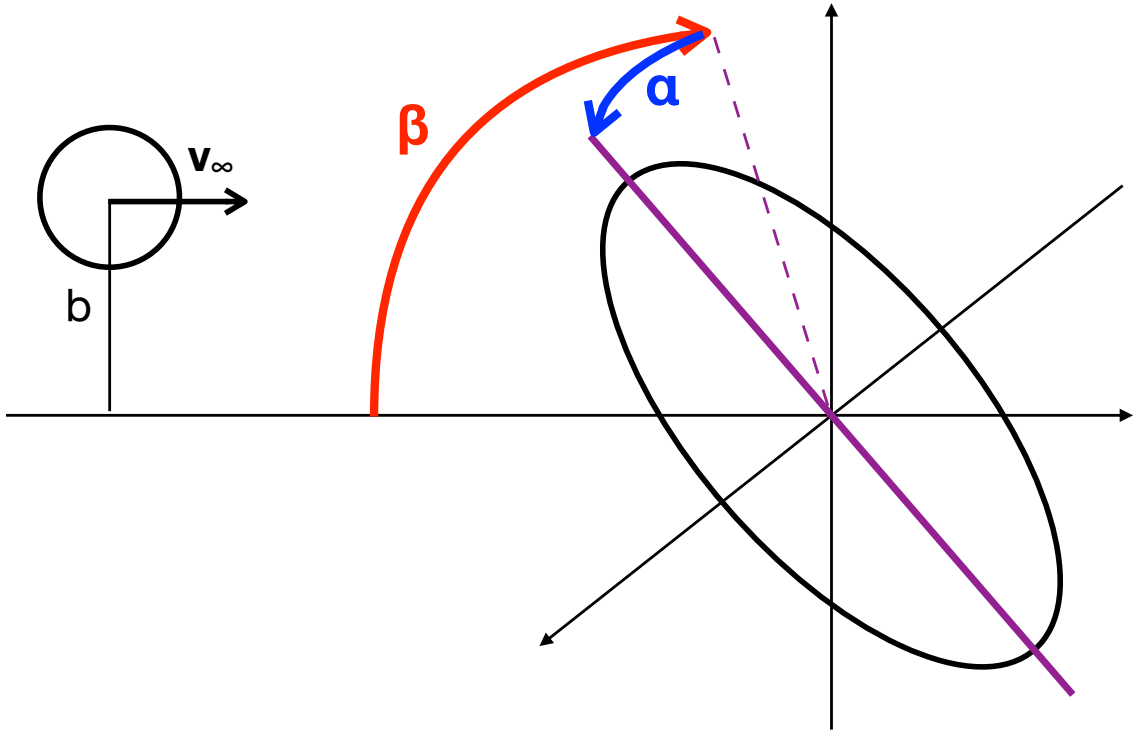


Figure 7.1: Schematic representation of the initial configuration for an impact parameter b and a velocity vector v_∞ defining the collision plane and the collision axis. The orientation of the target is defined by the angles β (rotation around the axis perpendicular to the reaction plane) and α (rotation around the collision axis).

can be derived from a variational principle. The main approximation in TDHF is that the many-body wave function $\Phi(t)$ is assumed to be a single time-dependent Slater determinant at all times. It describes the time-evolution of the single-particle wave functions in a mean-field corresponding to the dominant reaction channel. During the past decade it has become numerically feasible to perform TDHF calculations on a 3D Cartesian grid without any symmetry restrictions and with much more accurate numerical methods ([Bottcher et al., 1989](#); [Umar and Oberacker, 2006g](#); [Kazuyuki Sekizawa and Kazuhiro Yabana, 2013b](#); [Maruhn et al., 2014b](#)).

In this paper, we focus on fusion and quasifission in the reaction $^{48}\text{Ca} + ^{249}\text{Bk}$. In our TDHF calculations we use the Skyrme SLy4d energy density functionals ([Ka-Hae Kim et al., 1997](#)) including all of the relevant time-odd terms in the mean-field Hamil-

tonian. Static Hartree-Fock (HF) calculations without pairing predict a spherical density distribution for ^{48}Ca while ^{249}Bk shows prolate quadrupole and hexadecupole deformation, in agreement with experimental observations. Numerically, we proceed as follows: First we generate very well-converged static HF wave functions for the two nuclei on the 3D grid. Three-dimensional TDHF initialization of the deformed ^{249}Bk nucleus, with a particular alignment of its symmetry axis with respect to the collision axis, can be most easily achieved by evaluating the initial guess for HF calculations on mesh values rotated with respect to the code axes. Subsequent HF iterations do not change this orientation thus resulting in the desired HF solution. This procedure involves no interpolation procedure and is the most straightforward method to implement in TDHF codes ([Pigg et al., 2014](#)). Otherwise, static solutions obtained for extreme angles (0° or 90° with respect to collision axis) can be very accurately interpolated to arbitrary angles ([Pigg et al., 2014](#)) followed by a few additional static iterations for extra accuracy.

The initial separation is chosen to be 30 fm with nuclei in their ground states. The nuclei are assumed to arrive to this separation on a Coulomb trajectory for the purpose of initializing the proper boosts. In the second step, we apply a boost operator to the single-particle wave functions. The calculations end when the fragments are well separated (or after 35 zs if they are still in contact). Outgoing Coulomb trajectories are then assumed to determine the scattering angle.

The time-propagation is carried out using a Taylor series expansion (up to orders 10 – 12) of the unitary mean-field propagator, with a time step $\Delta t = 0.4 \text{ fm/c}$. For reactions leading to superheavy dinuclear systems, the TDHF calculations require very long CPU times: a single TDHF run at fixed $E_{\text{c.m.}}$ energy for a fixed impact parameter b and orientation angle β takes about 2–3 days of CPU time on a 16-processor LINUX workstation.

Assuming the ^{249}Bk nucleus to be axially symmetric with no octupole deformation, the

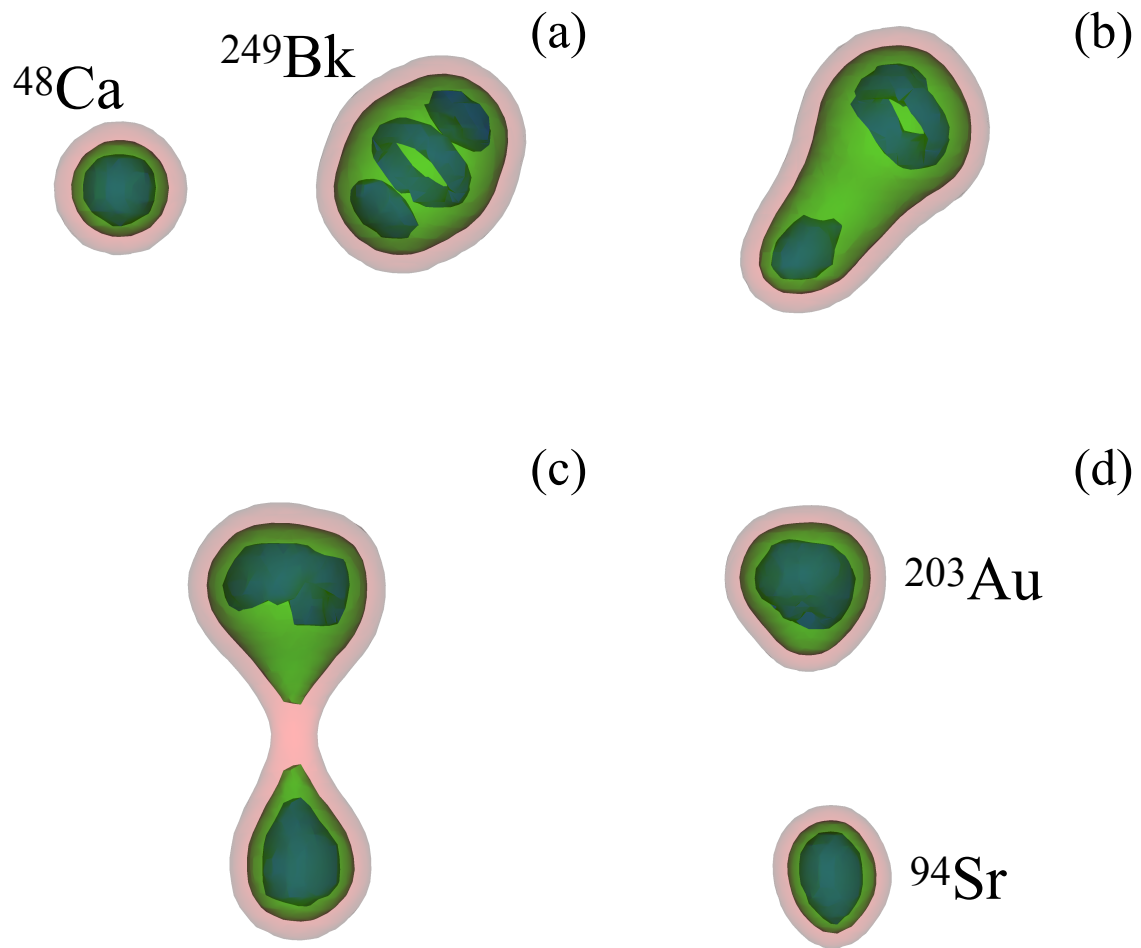


Figure 7.2: Isodensity surfaces at $\rho = 0.145, 0.1$, and 0.02 fm^{-3} in blue, green, and pink, respectively, shown at times $t \approx 0$ (a), 2.1 (b), 5.8 (c), and 6.4 zs (d) for an initial orientation $\beta = 135^\circ$ and an angular momentum $L = 60\hbar$. For visualization purposes, the reaction plane is 37° off the plane of the page.

cross-section or yield for a specific reaction channel ξ is proportional to

$$\sigma_\xi \propto \sum_L (2L+1) \int_0^{\frac{\pi}{2}} d\beta \sin\beta \int_0^\pi d\alpha P_L^{(\xi)}(\beta, \alpha). \quad (7.2)$$

Here, $P_L^{(\xi)}(\beta, \alpha)$ is the probability for the reaction channel ξ and an orientation of the target defined by the rotation angles β and α (see Fig. 7.1). The orientation of the deformation axis is obtained by applying first a rotation of an angle β around the axis perpendicular to the reaction plane, and then a rotation of an angle α around the collision axis.

The TDHF calculations are performed for a range of orbital angular momenta $L_i \hbar$ with $\{L_i\} = \{0, 10, 20 \cdots N_L\}$ and $N_L = 12$ or 13 , depending on the orientation (some orientations lead to quasi-elastic collisions at $L = 120$, in which case $L = 130$ is not computed). The first term is then replaced by

$$\sum_L (2L+1) \rightarrow \sum_{i=1}^{N_L} K_i \text{ with } K_i = \sum_{L=L_i-\Delta_i^-}^{L_i+\Delta_i^+} (2L+1),$$

where $\Delta^+ = 5$, $\Delta_i^- = 0$ and $\Delta_{i \neq 1}^- = 4$.

The double integral in Eq. (7.2) is computationally too demanding. The integral over α is then replaced by a sum over probabilities for $\alpha = 0$ and π . Equivalently, we can ignore α and extend the integral over β up to π . We then define the probability

$$\tilde{P}_{L_i}^{(\xi)}(\beta) = \begin{cases} P_{L_i}^{(\xi)}(\beta, 0) & \text{if } \beta \leq \frac{\pi}{2} \\ P_{L_i}^{(\xi)}(\pi - \beta, \pi) & \text{if } \beta > \frac{\pi}{2} \end{cases}.$$

The remaining integral over β is discretized with $N_\beta = 12$ angles $\{\beta_n\} = \{0^\circ, 15^\circ, 30^\circ, \dots, 165^\circ\}$.

We can finally write the approximate cross-section as

$$\sigma_\xi \simeq \sum_{i=1}^{N_L} K_i \sum_{n=1}^{N_\beta} C_n \tilde{P}_{L_i}^{(\xi)}(\beta_n), \quad (7.3)$$

where we have defined

$$C_n = \begin{cases} 2(1 - \cos \delta) & \text{if } n = 1 \\ \cos(\beta_n - \delta) - \cos(\beta_n + \delta) & \text{if } n > 1, \end{cases}$$

with $\delta = 7.5^\circ$. Note that, because of its semi-classical behavior, the TDHF theory leads to probabilities $\tilde{P}_{L_i}^{(\xi)}(\beta_n) = 0$ or 1 for the reaction channel ξ for a given orientation and angular momentum.

7.3 Results

The $^{48}\text{Ca} + ^{249}\text{Bk}$ at $E_{c.m.} = 234$ MeV has been studied as a function of the orientation β of the target (see Fig. 7.1) and as a function of orbital angular momentum L , given in units of \hbar , totaling 148 collisions.

7.3.1 Quasifission characteristics

Figure 7.2 shows a typical example of density evolution for a non-central collision. Different isodensity surfaces are represented. The rings observed at highest density in panels (a) and (b) are coming from shell structure effects ([Simenel, 2012b](#)). After contact, the nuclei are trapped in a potential pocket, forming a dinuclear system (panel (b)) which, unlike in fusion, does not reach an equilibrated compound nucleus. When the dinuclear system fissions (panel (c)), it forms two fragments (panel (d)) which preserve a memory of the entrance channel.

The outgoing fragments for this reaction are ^{94}Sr and ^{203}Au . Such a significant mass transfer towards a more mass symmetric configuration is one of the characteristics of quasi-

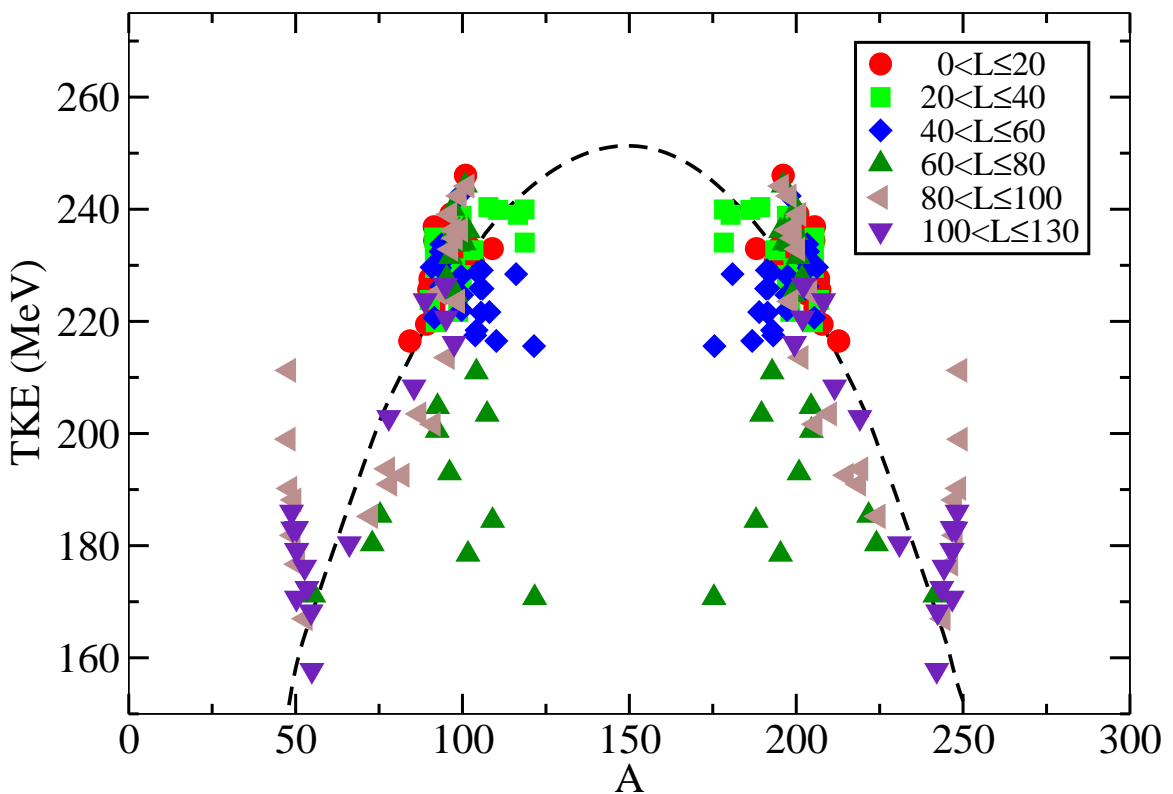


Figure 7.3: Total kinetic energy of the fragments as a function of their mass ratio. The curve corresponds to the Viola systematics ([Viola et al., 1985](#); [Hinde et al., 1987](#)).

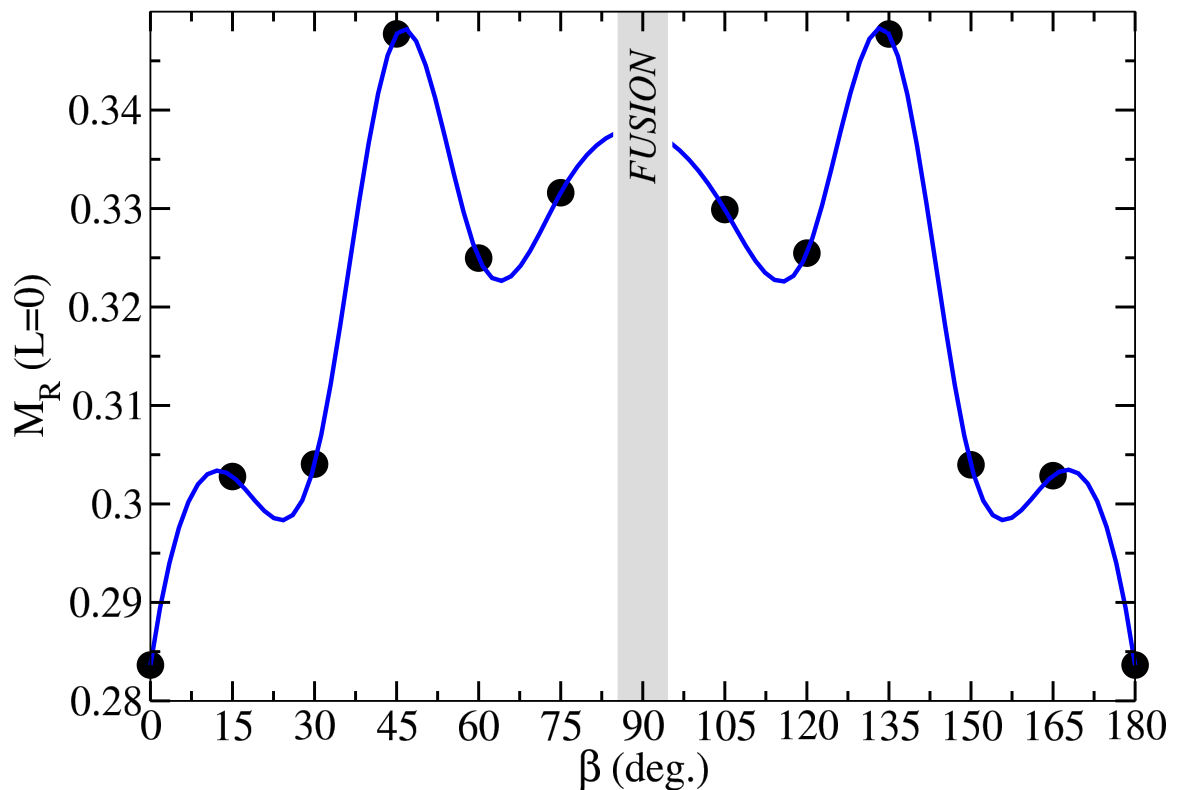


Figure 7.4: Mass ratio M_R as a function of orientation angle β for central collisions. Fusion is indicated by the shaded area.

fission. A second characteristic is the rotation of the dinuclear system before scission. This rotation is due to the initial angular momentum for non-central collisions. For contact times $\tau < 20$ zs, the dinuclear system usually does not undergo a full rotation before scission, resulting in so-called fast quasifission ([du Rietz et al., 2013](#); [Hinde et al., 2018](#)). Such times are also too short for the system to achieve full mass equilibration and form two fragments with similar masses. Fast quasifission then results in correlations between masses and angles which can be used to infer the time scale of the reaction ([Töke et al., 1985](#); [du Rietz et al., 2011](#)). The density evolution represented in Fig. 7.2 is an example of fast quasifission reaction as the fragments are in contact for ~ 6 zs and the dinuclear system rotates by only ~ 90 degrees. In fact, all quasifissions observed in our calculations for this system correspond to fast quasifission, producing fragment mass-angle correlations which will be studied in Section 7.3.3.

Another characteristic of quasifission is that the reaction is fully damped. In quasifission, the outgoing fragments have a total kinetic energy (TKE) essentially determined by their Coulomb repulsion at scission. As a first approximation, this TKE does not depend on the beam energy. Figure 7.3 shows the mass-energy distribution (MED), i.e., the distribution of TKE as a function of the number of nucleons A in the fragments. Except for quasi-elastic reactions in which the masses of the fragments are very close to the projectile and target masses, the TKE are generally distributed around the Viola systematics ([Viola et al., 1985](#); [Hinde et al., 1987](#)) (dashed line) which gives an empirical estimate of fully damped fission fragments.

Each color in Fig. 7.3 shows the location in the MED that is expected for a given range of orbital angular momenta. In each case, two or three values of L and thirteen angles β are included. The more central collisions ($L \leq 80\hbar$) all lead to quasifission, while more peripheral collisions ($L > 80\hbar$) lead to both quasi-elastic and quasifission reactions. This indicates a strong influence of orientation on the reaction outcome.

7.3.2 Effect of target orientation in central collisions

Different orientations of the target lead to different compactness of the dinuclear system. A clear relation between orientation and compactness is obtained in the case of central collisions ($L = 0$) in which case less compact configurations are obtained for $\beta = 0$ and 180 degrees, leading to collisions with the tips of the target, while the most compact configurations are obtained for $\beta = 90$ degrees, leading to collisions with the side. For non-central collisions, the relationship between orientation and compactness is less straightforward and can be estimated assuming Coulomb trajectories until the distance of closest approach ([Wakhle et al., 2014](#)).

Figure 7.4 shows the mass ratio of the fragments, defined as the ratio between the mass of the fragment and the total mass of the system, as a function of the orientation for central collisions. A slight asymmetry between β and $\pi - \beta$ is observed due to a small violation of symmetry under reflection across the plane orthogonal to the main deformation axis of ^{249}Bk HF ground-state.

Fusion is only observed for side collisions, in agreement with previous TDHF studies ([Wakhle et al., 2014](#); [Oberacker et al., 2014b](#); [Umar et al., 2016b](#)). Overall, a small increase of the mass ratio from $M_R \approx 0.28$ to 0.35 is observed when going from tip orientations to more compact configurations. There is, however, no clear transition associated with an eventual critical angle β_{crit} when going from tip to side orientation in this system (except for when fusion is achieved). This shows the importance of considering a full range of intermediate orientations in order to realize quantitative predictions.

7.3.3 Correlations between fragment masses and scattering angles

Experimental studies of correlations between fragment masses and scattering angles have led to considerable insights into quasifission mechanisms in the past ([Tőke et al., 1985](#); [Shen et al., 1987](#); [Hinde et al., 2008](#); [Simenel et al., 2012](#); [du Rietz et al., 2013](#); [Wakhle et al., 2014](#); [Hammerton et al., 2015](#); [Morjean et al., 2017](#); [Mohanto et al., 2018](#);

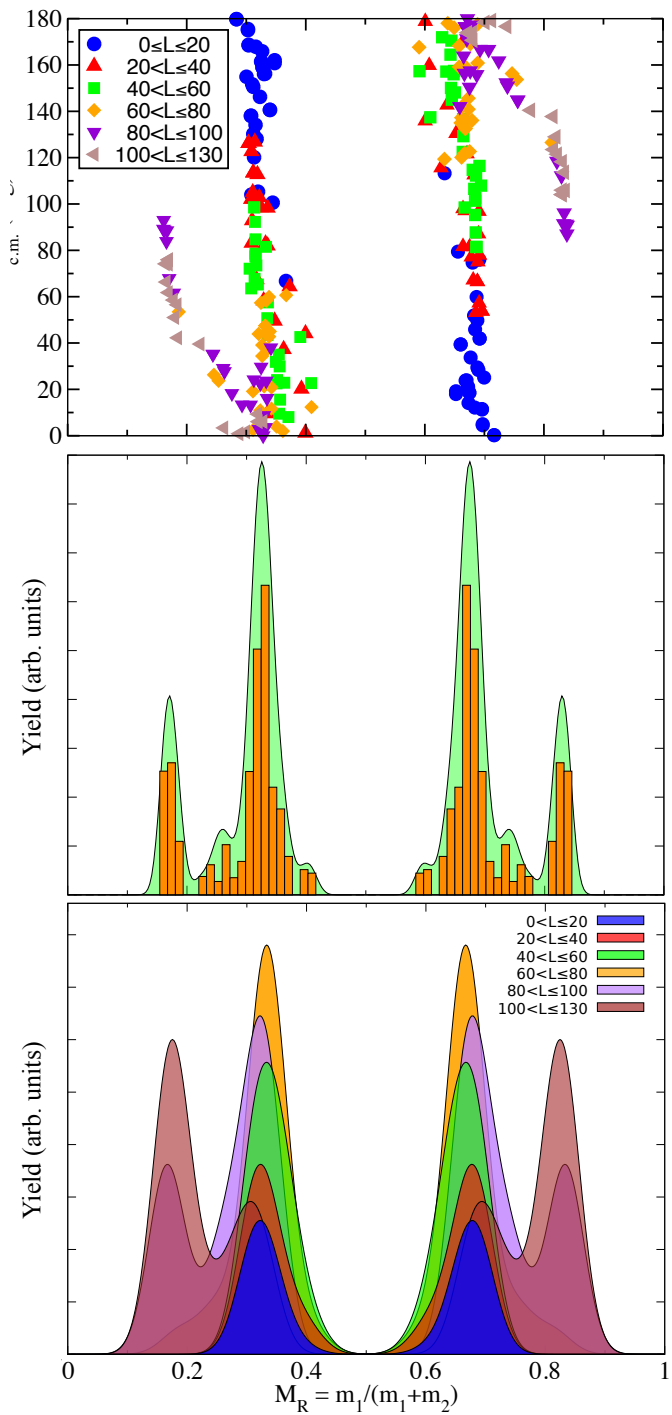


Figure 7.5: (a) Distribution of scattering angle $\theta_{c.m.}$ versus mass ratio M_R (MAD). The colors correspond to different ranges of angular momenta. (b) Fragment mass yield (histogram). The solid line gives a smooth representation of the histogram using the kernel density estimation with bandwidth 0.012. (c) Mass yields obtained for different ranges of angular momenta.

Hinde et al., 2018). TDHF calculations have been used recently to help interpret qualitatively these correlations (Wakhle et al., 2014; Hammerton et al., 2015; Umar et al., 2016b; Sekizawa and Yabana, 2016b). However, these theoretical studies were somewhat limited by the restriction of initial orientations.

The mass-angle distribution (MAD) of the fragments is shown in Fig. 7.5(a). The horizontal axis gives the mass ratio $M_R = \frac{m_1}{m_1+m_2}$ where m_1 and m_2 are the masses of the fragments. These masses are for primary fragments, i.e., before nucleon emission takes place. This is also what is measured experimentally using 2-body kinematics techniques (Tōke et al., 1985; Hinde et al., 1996). The colors represent different angular momentum ranges, as in Fig. 7.3.

Most calculations lead to quasifission with fragment mass ratios $0.28 < M_R < 0.72$, while projectile and target mass ratios are at $M_R \simeq 0.16$ and 0.84 , respectively. This indicates significant mass transfer towards more symmetric mass repartitions. However, full symmetry is never achieved in these TDHF calculations, unlike in $^{40}\text{Ca} + ^{238}\text{U}$ (Wakhle et al., 2014). Most peripheral collisions with $L \geq 70\hbar$ lead to larger mass asymmetries and a transition from quasifission to deep-inelastic and quasi-elastic reactions. Note that fragments from elastic scattering are not shown.

We also see that quasifission fragments are distributed among the full range of scattering angles, from $\theta_{c.m.} = 0$ (forward angles) to 180 degrees (backward angles). This wide angular distribution motivates the development of larger angular acceptance detectors (Khuyagbaatar et al., 2018; Banerjee et al., 2019). Note that each angular momentum range leads itself to a broad distribution of angles. For instance, results from $L \leq 20\hbar$ are found all the way from backward angles to $\theta_{c.m.} \simeq 70$ degrees, while $L \leq 40\hbar$ spans all angles. This is a manifestation of the impact of orientation on the angular distribution: for a given angular momentum, the scattering angle strongly depends on the orientation of the target. However, there is much less dependence of the mass on the orientation, as each orientation leads to approximately similar mass ratio for quasifission outcomes in this system.

Interestingly, the correlation between quasifission fragment masses and angles shows a narrow mass distribution for the light fragment around $M_R \simeq 0.3$ at more backward angles with $\theta_{c.m.} > 70$ degrees. At more forward angles ($\theta_{c.m.} < 70$ degrees), the light fragment mass distribution broadens and slightly shifts towards larger masses ($M_R \sim 0.34$). For symmetry reasons, a similar narrow (respectively broad) mass distribution is found in the heavy fragment at $M_R \simeq 0.7$ (resp. $M_R \sim 0.66$) for $\theta_{c.m.} < 110$ (resp. $\theta_{c.m.} > 110$) degrees. The origin of these features will be discussed using neutron and proton distributions in Sec. 7.3.5.

7.3.4 Fragment mass distributions

The theoretical MAD in Fig. 7.5(a) is useful to investigate correlations between mass and angle. However it is not directly related to yields and cross-sections as it does not account for the $2L + 1$ and $\sin\beta$ terms in Eq. (7.2). Yields are better represented in one-dimensional spectra. Figure 7.5(b) shows a histogram of the mass ratio yield obtained from Eq. (7.2). The solid line curve gives a smooth representation of the histogram. As these are more illustrative, we will only use these smooth representations of yields in later figures.

The quasifission mass yields in Fig. 7.5(b) are strongly peaked at $M_R \sim 0.33$ and 0.67 , with a full width half maximum FWHM $\simeq 0.1$ corresponding to a standard deviation $\sigma_{M_R} \simeq 0.042$. Note that the present TDHF calculations neglect mass distributions associated with each single TDHF calculation outcome. The latter can be computed using particle-number projection techniques (Simenel, 2010b; Kazuyuki Sekizawa and Kazuhiro Yabana, 2013b; Scamps and Lacroix, 2013b; Scamps and Hashimoto, 2017). However, the width of the resulting distributions are known to be underestimated in dissipative collisions (Dasso et al., 1979). Beyond mean-field calculations incorporating one-body fluctuations could also be used (Simenel, 2011b; Williams et al., 2018; Lacroix and Ayik, 2014; Ayik et al., 2015b,a, 2016, 2018; Tanimura et al., 2017b). However, these approaches are not used here as they would significantly increase computing time and would become prohibitive with large ranges of orientations and angular momenta.

We can nevertheless attempt a comparison with typical experimental mass width for quasifission distributions, keeping in mind that our theoretical prediction is a lower bound. Experimental spread σ_{M_R} can roughly be parameterized as a linear function from $\sigma_{M_R}^{(DIC)} \approx 0.025$ typical for deep-inelastic collisions (DIC) at the mass ratio of the projectile and target, to $\sigma_{M_R}^{(FF)} = 0.07$ in fusion-fission at $M_R = 0.5$ (du Rietz et al., 2011). We then get an estimate of $\sigma_{M_R}^{(QF)} \approx 0.047$ at $M_R = 0.33$, which is only $\sim 10\%$ higher than the TDHF prediction. The present calculations, to a large extent, account for the expected fluctuations of the mass of the quasifission fragments. These fluctuations are essentially coming from the various orientations of the deformed target nucleus.

Figure 7.5(c) shows the expected mass ratio yield distributions for various ranges of angular momenta L . The purpose of this figure is to compare quantitatively the relative contributions to the yields when going from central to peripheral collisions. For instance, we see that, because of the $2L + 1$ weighting factor in Eq. (7.2), the most central collisions with $L \leq 20\hbar$, which are found at backward angles in Fig. 7.5(a), have also the smallest contribution to the total yield. In order to understand the transition from $M_R \approx 0.30$ to 0.34 discussed at the end of Sec. 7.3.3, it will then be necessary to fully exploit the correlations between masses and angles of the quasifission fragments.

7.3.5 Identification of shell effects in quasifission fragments

Experimental indications of the role of shell effects in the production of quasifission fragments initially came from mass-yield measurements (Itkis et al., 2004; Nishio et al., 2008; Wakhle et al., 2014). Theoretical predictions from TDHF calculations then supported these views (Wakhle et al., 2014; Oberacker et al., 2014b; Umar et al., 2016b). However, to unambiguously confirm the role of shell effects, proton or neutron numbers distributions have to be measured. Only recently this was done for quasifission for the $^{48}\text{Ti} + ^{238}\text{U}$ reaction using x-ray detectors to identify proton numbers in the fragments (Morjean et al., 2017), thus confirming the role of $Z = 82$ “magic” shell in this reaction.

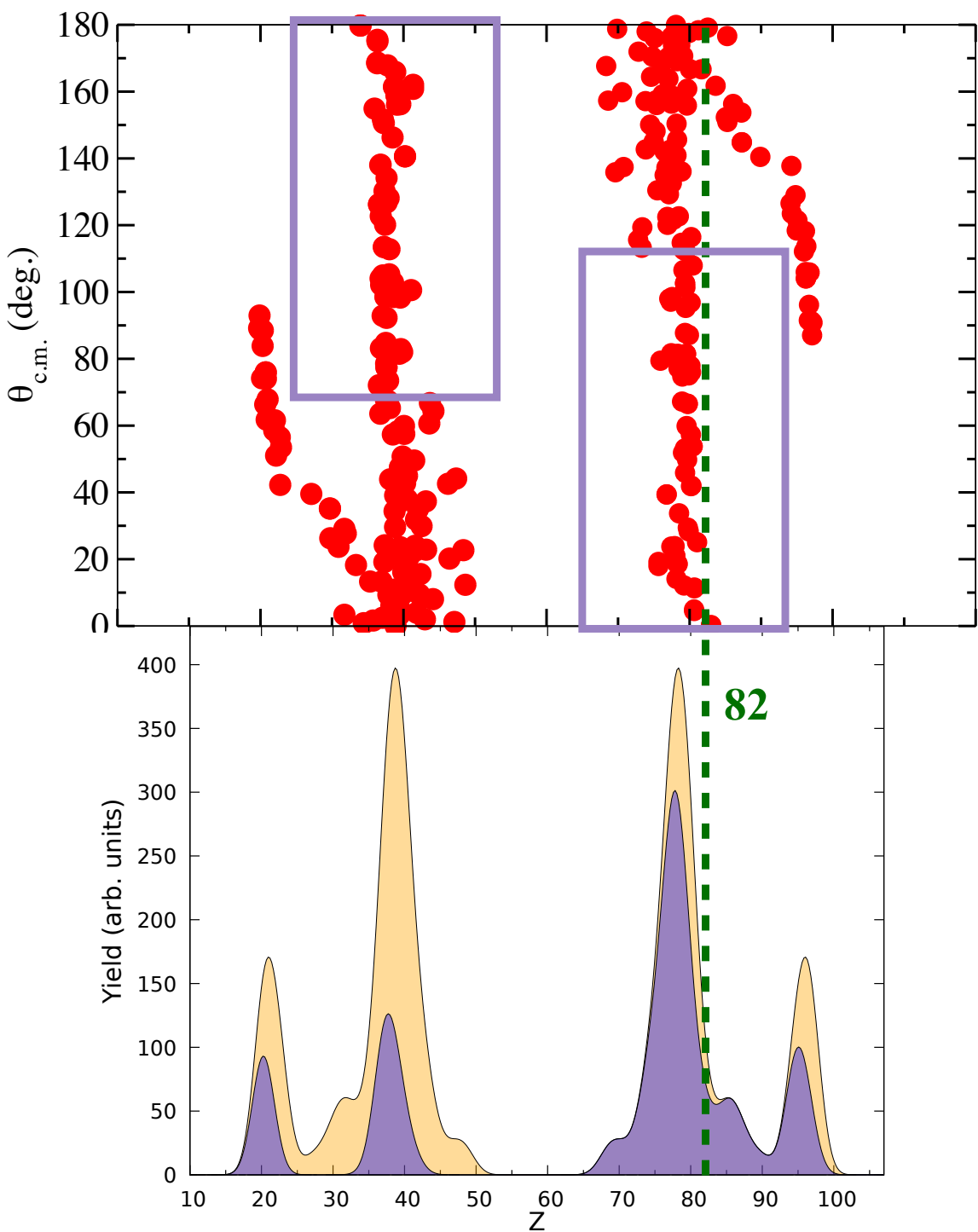


Figure 7.6: (a) Distribution of scattering angle $\theta_{c.m.}$ versus proton number Z (ZAD). (b) Fragment proton number yield without (lighter shade) and with angular cut $\theta_{c.m.} > 70$ degrees (darker shade). The vertical line represents potential proton shell gap.

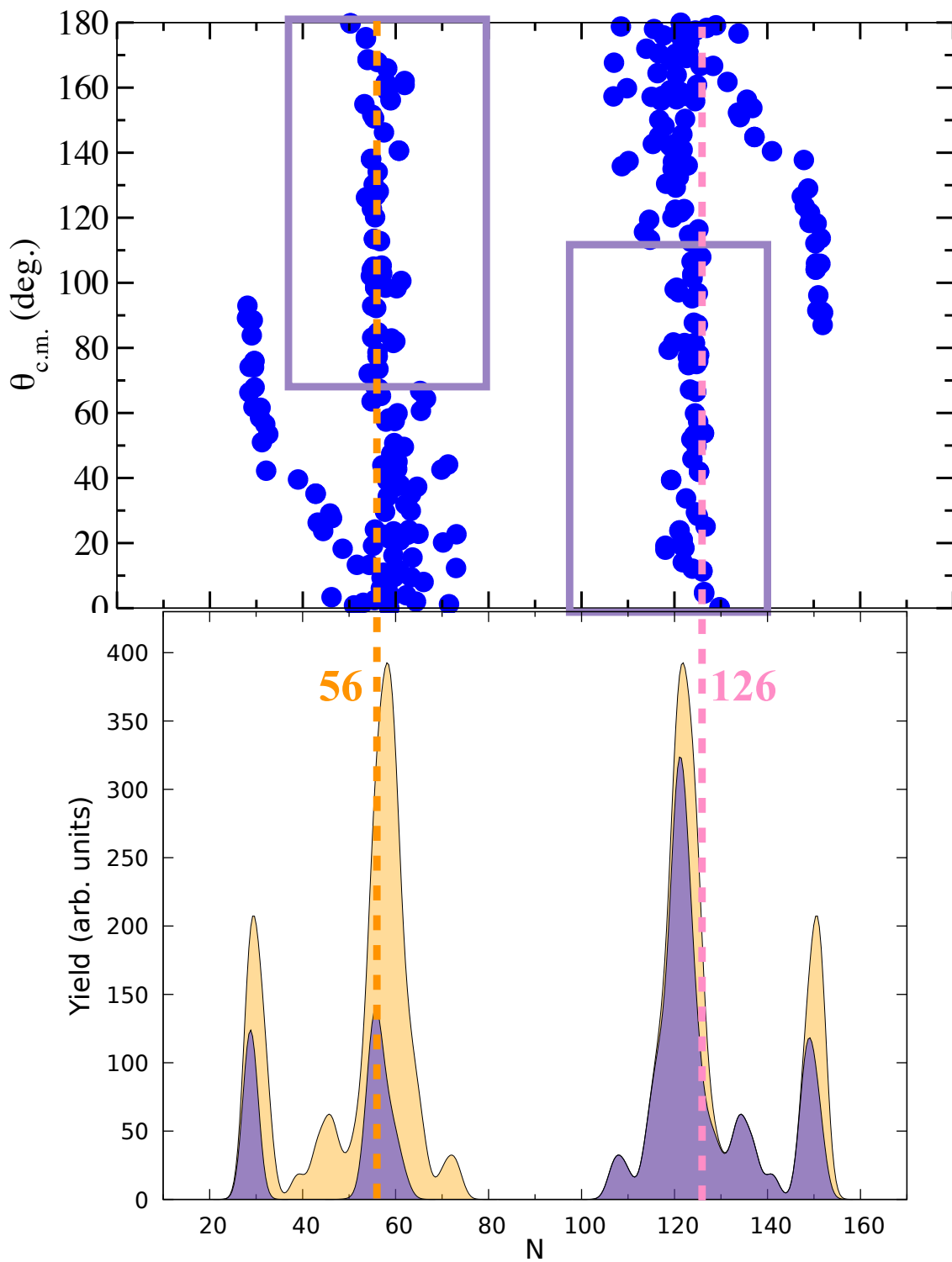


Figure 7.7: (a) Distribution of scattering angle $\theta_{c.m.}$ versus neutron number N (NAD). (b) Fragment neutron number yield without (lighter shade) and with angular cut $\theta_{c.m.} > 70$ degrees (darker shade). The vertical lines represent potential neutron shell gaps.

To investigate the role of potential shell effects in $^{48}\text{Ca}+^{249}\text{Bk}$ quasifission, the correlations between proton and neutron numbers with scattering angles have been plotted in Figs. 7.6(a) and 7.7(a), respectively. Proton and neutron numbers yields are also shown in Figs. 7.6(b) and 7.7(b), respectively. In addition to the total yields obtained without restriction on scattering angles and nucleon numbers (orange spectra), gates on quasifission fragments have also been used (rectangles in Figs. 7.6(a) and 7.7(a)) with $\theta_{c.m.} > 70$ degrees for the light fragments and $\theta_{c.m.} < 110$ degrees for the heavy ones. The resulting gated spectra are shown in purple in Figs. 7.6(b) and 7.7(b).

The vertical dotted line in Fig. 7.6 shows the expected position of fragments affected by $Z = 82$ shell effects. The heavy fragments seem to be systematically lighter, indicating that $Z = 82$ may not play a significant role in this reaction. This is surprising as TDHF studies have shown the importance of this shell gap in quasifission for $^{40,48}\text{Ca}, ^{48}\text{Ti}+^{238}\text{U}$ ([Wakhle et al., 2014](#); [Oberacker et al., 2014b](#); [Morjean et al., 2017](#)).

A similar comparison is made with the “magic” number $N = 126$ in Fig. 7.7. Here, we see that some fragments are indeed formed with $N = 126$. However, both the centroids of the ungated and gated distributions are shifted towards smaller neutron numbers. For the gated spectrum, the shift is relatively small as the peak is centered at $\bar{N}_{gated} \approx 124$. Nevertheless, spherical shell effects are known to be quite localized in the nuclear chart and this “proximity” may as well be coincidental. Other spherical shell effects are also excluded for both protons and neutrons. In particular, the quasifission peaks are far from $Z = 50$ or $N = 50$.

This leaves us with potential deformed shell effects. For instance, the importance of octupole deformed shell gaps at $Z = 52 - 56$ ([Scamps and Simenel, 2018](#)) and $N = 52 - 56$ ([Scamps and Simenel, 2019](#)) have recently been shown to have an important role in driving heavy systems towards asymmetric fission. As a result of these gaps, the nuclei can easily acquire octupole deformations for a small cost (and sometimes even a gain) in energy. This is why their production as fission fragments is naturally favored, as the fissioning system

has no choice but to go through a shape with a neck just before scission, imposing strong octupole deformations in the fragments. Despite its strong spherical shell effects which are expected to energetically favor its production, the formation of ^{132}Sn as a fission fragment is hindered by its strong resistance to octupole deformations. This is not the case, however, of ^{208}Pb which can easily acquire octupole deformations thanks to its low-lying octupole 3^- state.

The orange vertical dotted line in Figure 7.7 indicates the expected location of fragments affected by the $N = 56$ octupole deformed shell gap. It matches very well the position of the gated peak, providing a plausible explanation for the origin of this narrow distribution of quasifission fragments at backward angles, corresponding to more central collisions.

As discussed in Sec. 7.3.3, however, more peripheral collisions ($\theta_{c.m.} < 70$ degrees for the light fragment) lead to the production of slightly more symmetric quasifission fragments. For the light fragment, the Z and N distributions of these more peripheral quasifission events [see Figs. 7.6(a) and 7.7(b)] seem to be centered around $\bar{N}_{periph} \approx 60$ and $\bar{Z}_{periph} \approx 40$, respectively, indicating the production of fragments in the ^{100}Zr region. Similar observations were already made in $^{40,48}\text{Ca} + ^{238}\text{U}$ systems (Oberacker et al., 2014b).

Figure 7.8 shows the distribution of fragments in the N and Z plane. We see that, due to a strong symmetry energy, the fragments have N/Z ratios very close to the one of the compound nucleus. Nevertheless, the light fragments are slightly more proton rich, and the heavy fragments more proton deficient, due to the stronger Coulomb repulsion in the latter. The production of fragments in the ^{100}Zr region is confirmed in the inset of Fig. 7.8. We also see that the fragments with $N = 56$ neutrons correspond essentially to ^{94}Sr , as also illustrated in Fig. 7.2

Shell effects are known to evolve with the deformation of the nucleus. To confirm the presence of shell effects, it is then necessary to verify that the deformation is the one

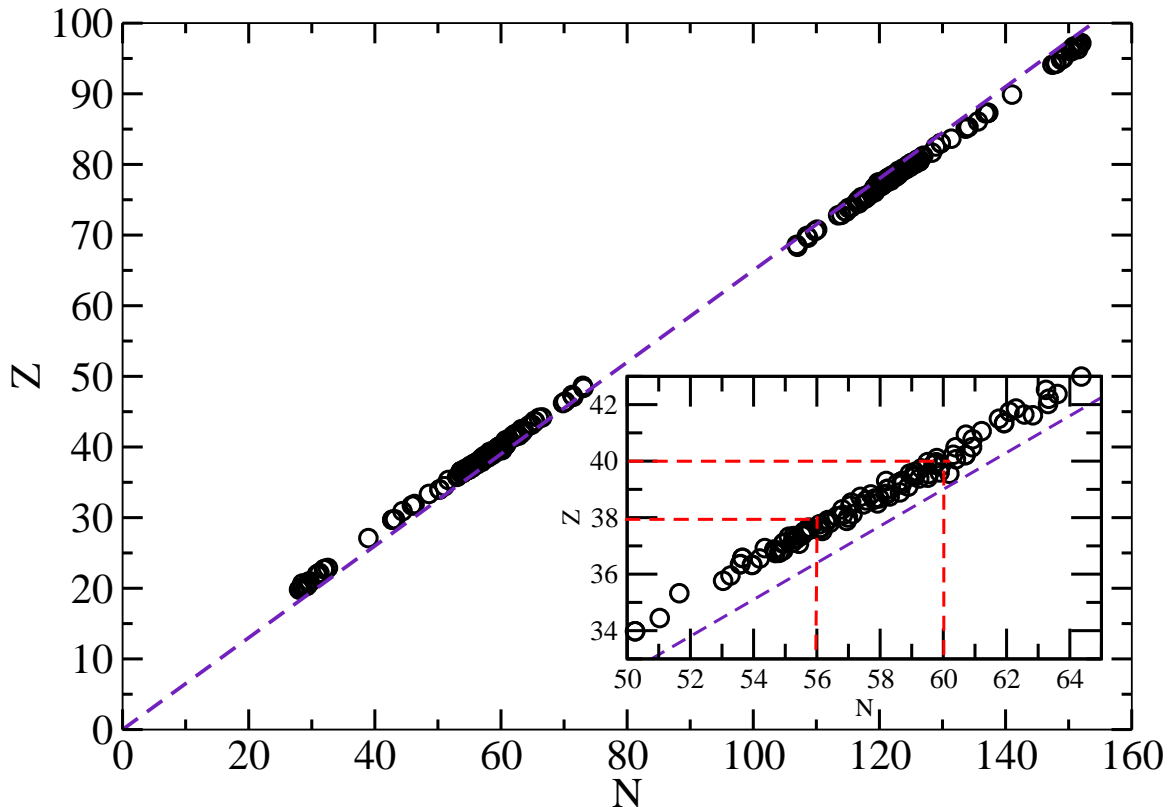


Figure 7.8: Distribution of proton number Z versus neutron number N of the fragments. The dashed line represents the N/Z ratio of the compound nucleus. The inset is a zoom around the light fragment. Thin dashed lines indicate the positions of ^{94}Sr ($Z = 38, N = 56$) and ^{100}Zr ($Z = 40, N = 60$).

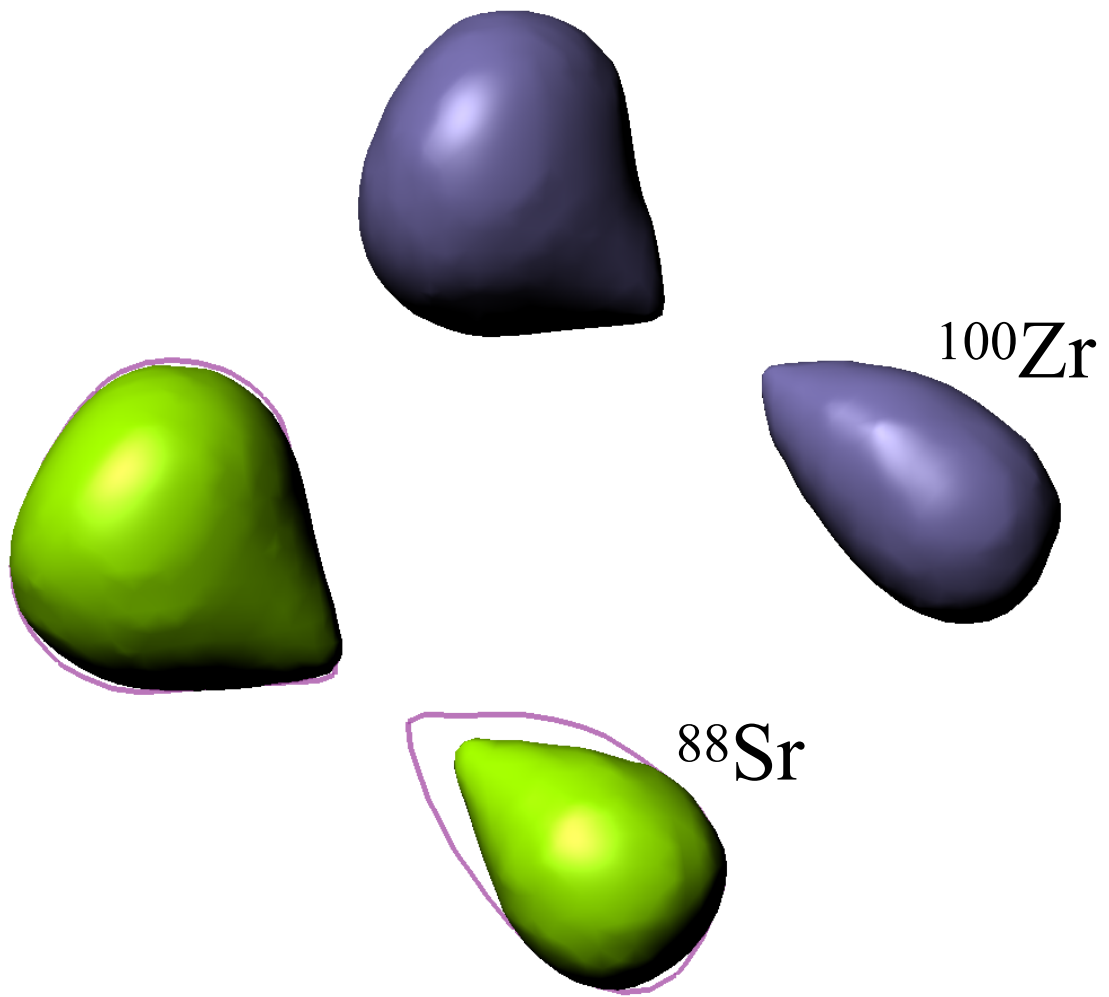


Figure 7.9: Isodensity surfaces at $\rho = 0.1 \text{ fm}^{-3}$ for $L = 90\hbar$ and $\beta = 120^\circ$ (top), and $L = 60\hbar$ and $\beta = 135^\circ$ (bottom), just after the breaking of the neck. The light fragment (right) in the top is a ^{94}Sr ($Z = 38, N = 56$) and a ^{100}Zr ($Z = 40, N = 60$) in the bottom. The contour line in the bottom represents the same density as in the top.

expected to exhibit a shell gap. Typical isosurface densities for reactions just after scission leading to the production of a ^{100}Zr (top) and of a ^{94}Sr (bottom) fragment are shown in Fig. 7.9. In particular, the ^{94}Sr fragment is quite compact with a strong octupole shape, similar to what is observed in fission of mercury isotopes producing $N = 56$ fragments with to octupole shell gaps ([Scamps and Simenel, 2019](#)). The ^{100}Zr fragment is also octupole deformed (as the density is shown just after breaking of the neck) but with a much more elongated shape. Neutron rich zirconium isotopes are indeed expected to exhibit strong quadrupole deformations ([Lalazissis et al., 1999](#); [Blazkiewicz et al., 2005](#); [Hwang et al., 2006](#)).

7.4 Conclusions

The $^{48}\text{Ca} + ^{249}\text{Bk}$ reaction, used experimentally to produce Tennessine ($Z = 117$), has been studied at a center of mass energy of 234 MeV with time-dependent Hartree-Fock simulations. Properties of quasifission fragments, such as mass, numbers of protons and neutrons, kinetic energy, and scattering angles have been studied systematically.

Unlike previous TDHF studies of quasifission, a broad distribution of orientations of the target has been considered for the first time, allowing for the prediction of, e.g., mass yield characteristics that can be directly compared with experiment. Except for a few collisions compatible with fusion or long-time quasifission, the largely dominant outcome is fast quasifission. It is shown that the orientation has also a strong influence on the scattering angle.

Fast quasifission produces peaks in the mass yield distribution for the projectile-like and target-like fragments with a width in good agreement with empirical estimates, despite the fact that the TDHF approach does not account for beyond mean-field fluctuations. Here, the observed fluctuations come mainly from the various orientations of the target in the entrance channel.

The influence of shell effects on the formation of the fragments has been investigated.

Unlike similar reactions with ^{238}U targets, no influence of ^{208}Pb is observed unambiguously. However, elongated fragments in the ^{100}Zr region are produced in the more peripheral quasifission reactions. More central collisions consistently produce fragments with $N = 56$ nucleons for all orientations. This is interpreted as an effect of octupole deformed shells favoring the production of fragments with pear shapes at scission. A similar effect has recently been discussed in the case of fission.

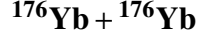
This is the first indication of a potential influence of octupole shell gaps in quasifission. Its experimental confirmation would be particularly interesting as it would point towards strong similarities in how shell effects affect both fission and quasifission. These shell effects in the light fragments will be more easily investigated experimentally at backward angles.

Acknowledgments

We thank D. J. Hinde for useful discussions. This work has been supported by the U.S. Department of Energy under grant No. DE-SC0013847 with Vanderbilt University and by the Australian Research Council Discovery Project (project numbers DP160101254 and DP190100256) funding schemes.

Chapter 8

Microscopic predictions for production of neutron rich nuclei in the reaction



Abstract

[Background] Production of neutron-rich nuclei is of vital importance to both understanding nuclear structure far from stability and to informing astrophysical models of the rapid neutron capture process (r-process). Multinucleon transfer (MNT) in heavy-ion collisions offers a possibility to produce neutron-rich nuclei far from stability.

[Purpose] The $^{176}\text{Yb} + ^{176}\text{Yb}$ reaction has been suggested as a potential candidate to explore the neutron-rich region surrounding the principal fragments. The current study has been conducted with the goal of providing guidance for future experiments wishing to study this (or similar) system.

[Methods] Time-dependent Hartree-Fock (TDHF) and its time-dependent random-phase approximation (TDRPA) extension are used to examine both scattering and MNT characteristics in $^{176}\text{Yb} + ^{176}\text{Yb}$. TDRPA calculations are performed to compute fluctuations and correlations of the neutron and proton numbers, allowing for estimates of primary fragment production probabilities.

[Results] Both scattering results from TDHF and transfer results from the TDRPA are presented for different energies, orientations, and impact parameters. In addition to fragment composition, scattering angles and total kinetic energies, as well as correlations between these observables are presented.

[Conclusions] $^{176}\text{Yb} + ^{176}\text{Yb}$ appears to be an interesting probe for the mid-mass neutron-rich region of the chart of nuclides. The predictions of both TDHF and TDRPA are speculative, and will benefit from future experimental results to test the validity of this approach to studying MNT in heavy, symmetric collisions.

8.1 Introduction

The synthesis of neutron-rich nuclei is one of the most exciting and challenging tasks in both experimental and theoretical nuclear physics. From the lightest systems to the superheavy regime, knowledge about the nuclei at the extremes of the chart of nuclides is vital to understanding physical phenomena at multiple scales. At the foremost, neutron-rich nuclei are at the literal and figurative center of the rapid neutron capture process (r-process). Attempts at modeling the r-process utilize input from nuclear models to inform threshold energies for the reaction types that characterize this process (Cowan et al., 2019). Thus, strong theoretical understanding of both the static and dynamic properties of nuclei far from stability can give vital insight into the formation of stable heavy nuclei.

The production of neutron-rich nuclei is also of interest for studying nuclear structure, where exploring this region of the nuclear landscape clearly probes the edges of our current understanding of how finite nuclei form and are composed (Otsuka et al., 2018). This includes studies of neutron-rich nuclei of all masses, ranging from oxygen (deSouza et al., 2013) up to the superheavy element (SHE) region. SHEs are of particular note, as the formation and static properties of said nuclei have been the focus of many experimental (Hofmann et al., 2002; Münzenberg and Morita, 2015; Morita, 2015; Yu. Ts. Oganessian and Utyonkov, 2015; Roberto et al., 2015) and theoretical (Bender et al., 1999; Nazarewicz et al., 2002; Ćwiok et al., 2005; Pei et al., 2009; Stone et al., 2019) studies.

Over the years, many theoretical approaches to studying neutron-rich nuclei formation have been pursued for various reaction types. One such technique is to use models to study neutron enrichment via multinucleon transfer (MNT) in deep-inelastic collisions (DIC) and quasifission reactions (Adamian et al., 2003; Valery Zagrebaev and Walter Greiner, 2007; Umar et al., 2008b; Cédric Golabek and Cédric Simenel, 2009b; Aritomo, 2009; David J. Kedziora and Cédric Simenel, 2010; Zhao et al., 2016; Sekizawa, 2017c; Wu and Guo, 2019). While quasifission occurs at a much shorter time-scale than fusion-fission (Tōke et al., 1985; du Rietz et al., 2011) and is the primary reaction mechanism that limits the

formation of superheavy nuclei, the fragments produced may still be neutron-rich.

Quasifission reactions are often studied in asymmetric systems with, e.g., an actinide target (Töke et al., 1985; Hinde et al., 1992, 1995; Itkis et al., 2004; Wakhle et al., 2014). However, quasifission can also be present in symmetric systems. In fact, the extreme case of quasifission in actinide-actinide collisions has been suggested as a possible reaction mechanism to obtain neutron-rich isotopes of high Z nuclei in particular as well as a possible means to search for SHE (Majka et al., 2018; Wuenschel et al., 2018). Theoretically, the investigation of actinide-actinide collisions has a rich history with various approaches, including the dinuclear system (DNS) model (Penionzhkevich et al., 2005; Adamian et al., 2008; Feng et al., 2009; Adamian et al., 2010b,a; Feng, 2017b; Zhu et al., 2017; Bao et al., 2018), relativistic mean-field (RMF) and Skyrme HF studies (Gupta et al., 2007), reduced density-matrix formalism (Sargsyan et al., 2009), quantum molecular dynamics (QMD) (Zhao et al., 2009), and improved quantum molecular dynamics (ImQMD) (Julong Tian et al., 2008; Zhao et al., 2016; Wang and Guo, 2016b; Yao and Wang, 2017; Li et al., 2018) calculations, as well as time-dependent Hartree-Fock (TDHF) studies (Cusson et al., 1980; Cédric Golabek and Cédric Simenel, 2009b; David J. Kedziora and Cédric Simenel, 2010). Over recent years, TDHF has proved to be a tool of choice to investigate fragment properties produced in various reactions, such as DIC (Umar et al., 2017b; Wu and Guo, 2019), quasifission (Wakhle et al., 2014; Oberacker et al., 2014b; Hamerton et al., 2015; Umar and Oberacker, 2015; Umar et al., 2016b; Wang and Guo, 2016b; Sekizawa, 2017c; Godbey et al., 2019b; Jiang and Wang, 2020), and fission (Simenel and Umar, 2014b; Scamps et al., 2015b; Goddard et al., 2015b; Tanimura et al., 2015; Goddard et al., 2016b; Aurel Bulgac et al., 2016; Tanimura et al., 2017b; Scamps and Simenel, 2018; Aurel Bulgac et al., 2018; Scamps and Simenel, 2019). Recent reviews (Simenel and Umar, 2018b; Kazuyuki Sekizawa, 2019) succinctly summarize the current state of TDHF (and its extensions) as it has been applied to various MNT reactions.

In this work, we present a study of the $^{176}\text{Yb} + ^{176}\text{Yb}$ system using TDHF and the

time-dependent random phase approximation (TDRPA) extension that considers the effect of one-body fluctuations around the TDHF trajectory. As discussed before, microscopic approaches such as TDHF and its extensions are commonly used in heavy-ion collision studies in different regions of the nuclear chart, positioning TDHF and TDRPA as tools of choice for the current investigation. Symmetric ^{176}Yb reactions were chosen because they are considered as a potential candidate to explore the neutron-rich region around the mass region $A \sim 170 - 180$ of the nuclear chart. Specifically, an experimental investigation of this reaction are being considered in Dubna by Oganessian *et al.* and the work presented here was undertaken at their suggestion ([Yu. Ts. Oganessian, 2018](#)). The base theory (TDHF) and the primary extension (TDRPA) are briefly described in Section 8.2. Results for both scattering characteristics and transfer characteristics are discussed in Section 8.3.1 and Section 8.3.2 respectively. A summary and outlook are then presented in Section 8.4.

8.2 Formalism: TDHF and TDRPA

The TDHF theory provides a microscopic approach with which one may investigate a wide range of phenomena observed in low energy nuclear physics ([Negele, 1982](#); [Simenel, 2012b](#); [Simenel and Umar, 2018b](#); [Kazuyuki Sekizawa, 2019](#)). Specifically, TDHF provides a dynamic quantum many-body description of nuclear reactions in the vicinity of the Coulomb barrier, such as fusion ([Bonche et al., 1978](#); [Flocard et al., 1978](#); [Simenel et al., 2001](#); [Umar and Oberacker, 2006h](#); [Kouhei Washiyama and Denis Lacroix, 2008](#); [Umar et al., 2010b, 2009b](#); [Lu Guo and Takashi Nakatsukasa, 2012b](#); [Keser et al., 2012b](#); [Simenel et al., 2013d](#); [Oberacker et al., 2012, 2010b](#); [Umar et al., 2012b](#); [Simenel et al., 2013b](#); [Umar et al., 2014b](#); [Jiang et al., 2014b](#)) and transfer reactions ([Koonin et al., 1977](#); [Simenel, 2010b, 2011b](#); [Umar et al., 2008b](#); [Kazuyuki Sekizawa and Kazuhiro Yabana, 2013b](#); [Scamps and Lacroix, 2013b](#); [Sekizawa and Yabana, 2014](#); [Bourgin et al., 2016](#); [Umar et al., 2017b](#); [Kazuyuki Sekizawa, 2019](#)).

The TDHF equations for the single-particle wave functions

$$h(\{\phi_\mu\}) \phi_\lambda(r, t) = i\hbar \frac{\partial}{\partial t} \phi_\lambda(r, t) \quad (\lambda = 1, \dots, A), \quad (8.1)$$

can be derived from a variational principle. The principal approximation in TDHF is that the many-body wave function $\Phi(t)$ is assumed to be a single time-dependent Slater determinant at all times. It describes the time-evolution of the single-particle wave functions in a mean-field corresponding to the dominant reaction channel. During the past decade it has become numerically feasible to perform TDHF calculations on a 3D Cartesian grid without any symmetry restrictions and with much more accurate numerical methods ([Bottcher et al., 1989](#); [Umar and Oberacker, 2006g](#); [Kazuyuki Sekizawa and Kazuhiro Yabana, 2013b](#); [Maruhn et al., 2014b](#)).

The main limitation in the TDHF theory when studying features like particle transfer, however, is that it is optimized for the prediction of expectation values of one-body observables ([Roger Balian and Marcel Vénéroni, 1981](#)) and will under-predict fluctuations of those observables ([Dasso et al., 1979](#)). This is due to the fact that the fluctuation of one-body operators (such as the particle number operator) includes the expectation value of the square of a one-body operator,

$$\sigma_{XX} = \sqrt{\langle \hat{X}^2 \rangle - \langle \hat{X} \rangle^2}, \quad (8.2)$$

that is outside the variational space of TDHF ([Roger Balian and Marcel Vénéroni, 1981](#)).

To obtain such quantities one needs to go beyond standard TDHF and consider the fluctuations around the TDHF mean-field trajectory using techniques like the stochastic mean-field theory (SMF) ([Ayik, 2008](#); [Lacroix and Ayik, 2014](#)) or TDRPA ([Roger Balian and Marcel Vénéroni, 1984](#)), both of these approaches have been used to investigate MNT and fragment production ([Ayik et al., 2016, 2017, 2018, 2019a,b](#); [Marston and Koonin, 1985](#); [Bonche and Flocard, 1985](#); [Broomfield and Stevenson, 2008](#); [Broomfield, 2009](#); [Simenel](#),

2011b; Williams et al., 2018). The advantage of these methods compared to others mentioned in the Introduction is that they do not rely on empirical parameters and are fully microscopic. In this work we follow a similar approach as in (Simenel, 2011b; Williams et al., 2018) to obtain particle number fluctuations and distributions about the outgoing fragments.

The foundation of the method is to consider an alternate variational principle for generating the mean-field theory. In particular, the Balian-Vénéróni (BV) variational principle provides a powerful technique that optimizes the evaluation of expectation values for arbitrary operators (Roger Balian and Marcel Vénéroni, 1984; Bonche and Flocard, 1985). When the operator chosen is a one-body operator, the method produces the TDHF equations exactly, suggesting that TDHF is the mean-field theory that is best suited for the calculation of one-body expectation values. However, as mentioned above, the calculation of fluctuations and correlations involves the square of a one-body operator. For TDHF alone, Eq. 8.2 results in the following expression for two generic operators \hat{X} and \hat{Y} ,

$$\sigma_{XY}^2(t_f) = \text{Tr}\left\{ Y\rho(t_f)X[I - \rho(t_f)] \right\}, \quad (8.3)$$

where I is the identity matrix and t_f is the final time. By utilizing the BV variational principle and extending the variational space to optimize for the expectation value of squares of one-body operators, one obtains

$$\sigma_{XY}^2(t_f) = \lim_{\epsilon \rightarrow 0} \frac{\text{Tr}\{[\rho(t_i) - \rho_X(t_i, \epsilon)][\rho(t_i) - \rho_Y(t_i, \epsilon)]\}}{2\epsilon^2} \quad (8.4)$$

which now depends on the one-body density matrices at the initial time t_i . Equation (8.4) also contains the density matrices $\rho_{X,Y}(t_i, \epsilon)$ which have been boosted at t_f and evolved back to t_i .

The procedure to compute Eq. (8.4) involves first transforming the states after the col-

lision as

$$\tilde{\phi}_\alpha^X(r, t_f) = \exp[-i\epsilon N_X \Theta_V(r)] \phi_\alpha(r, t_f), \quad (8.5)$$

where X stands for neutron (N), proton (Z), or total nucleon number (A). The operator N_X ensures that the transformation acts only on nucleons with the correct isospin, with $N_A = 1$, $N_Z = \frac{1-\tau_3}{2}$, and $N_N = \frac{1+\tau_3}{2}$. The operator $\Theta_V(\hat{r})$ is a step function that is either 1 or 0 depending on whether r is within a volume of space, V , delimiting the fragment of interest. Finally, ϵ is a small number that is varied to achieve convergence.

These transformed states are then propagated backwards in time from the final time t_f to the initial time t_i . The trace in Eq. (8.4) can then be calculated, obtaining

$$\sigma_{XY} = \sqrt{\lim_{\epsilon \rightarrow 0} \frac{\eta_{00} + \eta_{XY} - \eta_{0X} - \eta_{0Y}}{2\epsilon^2}}, \quad (8.6)$$

with η_{XY} describing the overlap between the states at time $t = t_i$,

$$\eta_{XY} = \sum_{\alpha\beta} \left| \langle \phi_\alpha^X(t_i) | \phi_\beta^Y(t_i) \rangle \right|^2. \quad (8.7)$$

In the case of $X, Y = 0$, this refers to states obtained with $\epsilon = 0$ in Eq. (8.5). In principle, one should recover exactly the initial state as the evolution is unitary. However, using states that have been evolved forward and then backward in time with $\epsilon = 0$ minimizes systematic errors from numerical inaccuracies ([Bonche and Flocard, 1985](#); [Broomfield, 2009](#)).

The SLy4d parametrization of the Skyrme functional is used ([Ka–Hae Kim et al., 1997](#)) and all calculations were performed in a numerical box with 66×66 points in the reaction plane, and 36 points along the axis perpendicular to the reaction plane. The grid spacing used was a standard 1.0 fm which provides an excellent numerical representation of spatial quantities using the basis spline collocation method ([Umar et al., 1991a](#)). For the TDRPA calculations, each initial orientation, energy, and impact parameter resulted in three additional TDHF evolutions (one for each X) for the time reversed evolution at one value of

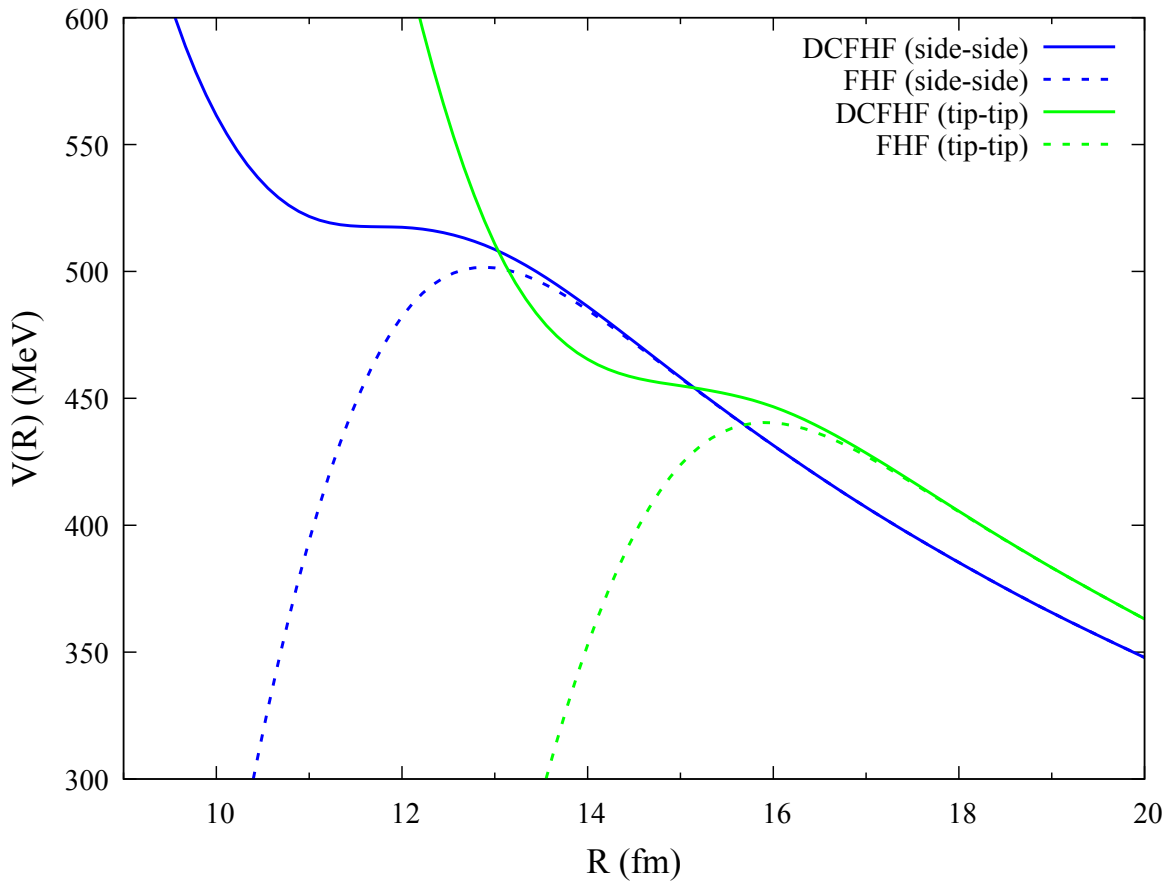


Figure 8.1: Static nuclear potentials for $^{176}\text{Yb} + ^{176}\text{Yb}$ in the side-side (blue (dark) lines) and tip-tip (green (light) lines) orientations from FHF and DCFHF.

$\epsilon = 2 \times 10^{-3}$ in addition to occasionally scanning ϵ to ensure convergence of Eq. (8.6). In total, 200 full TDHF evolutions were required for the results presented in this work with each taking on the order of $10 \sim 55$ hours of wall time due to the large, three-dimensional box size chosen. This corresponds to roughly 250 days of computation time split among multiple nodes for the ^{176}Yb HF ground state configuration with a prolate deformation.

The proton and neutron numbers correlations and fluctuations computed with TDRPA are used to estimate probabilities for the formation of a given nuclide using Gaussian bivariate normal distributions of the form

$$\mathcal{P}(n, z) = \mathcal{P}(0, 0) \exp \left[-\frac{1}{1-\rho^2} \left(\frac{n^2}{\sigma_{NN}^2} + \frac{z^2}{\sigma_{ZZ}^2} - \frac{2\rho n z}{\sigma_{NN}\sigma_{ZZ}} \right) \right], \quad (8.8)$$

where n and z are the number of transferred neutrons and protons, respectively. The correlations between N and Z are quantified by the parameter

$$\rho = \text{sign}(\sigma_{NZ}) \frac{\sigma_{NZ}^2}{\sigma_{NN}\sigma_{ZZ}} = \frac{\langle nz \rangle}{\sqrt{\langle n^2 \rangle \langle z^2 \rangle}}. \quad (8.9)$$

In principle, n and z could be very large and lead to unphysical predictions with fragments having, e.g., a negative number of protons and neutrons, or more nucleons than available. In practice, such spurious results could only happen for the most violent collisions where the fluctuations are large. To avoid such spurious effects, the probabilities are shifted so that \mathcal{P} is zero when one fragment has all (or more) protons or neutrons. The resulting distribution is then normalized.

Although the ^{176}Yb nuclide is in a region where shape coexistence is often found (Fu et al., 2018; Nomura et al., 2011; Robledo et al., 2009; Sarriuguren et al., 2008; Xu et al., 2011), TDHF calculations can only be performed with one well-defined deformation (and orientation) of each collision partners in the entrance channel. In our calculations, the ground state is found to have a prolate deformation with $\beta_2 \simeq 0.33$ in its HF ground state. A higher energy oblate solution is also found with a difference of around 5 MeV in total

binding energy. A set of calculations were also performed for the oblate solution, though the overall transfer behavior was found to be similar for both deformations despite the oblate one resulting in slightly lower fluctuations. In the following, we thus only show results for the prolate ground state.

This deformation allows for possible choices of the orientation of the nuclei. Extreme orientations are called “side” (“tip”) when the deformation axis is initially perpendicular (parallel) to the collision axis. Although various intermediate orientations could be considered ([Godbey et al., 2019b](#)), we limit our study to tip-tip and side-side orientations where the initial orientations of both nuclei are identical. In addition to saving computational time, this restriction is necessary to ensure fully symmetric collisions and to avoid unphysical results in TDRPA ([Williams et al., 2018](#)).

Figure 8.1 shows the nucleus-nucleus potentials computed using the frozen Hartree-Fock (FHF) ([Cédric Simenel and Benoit Avez, 2008](#); [Kouhei Washiyama and Denis Lacroix, 2008](#)) and density-constrained frozen Hartree-Fock (DCFHF) ([Simenel et al., 2017b](#)) methods, respectively neglecting and including the Pauli exclusion principle between the nucleons of different nuclei. Due to Pauli repulsion in DCFHF, the inner pocket potential is very shallow in the side-side configuration, and disappears in the tip-tip one. In this work, the effect of the orientation is studied by comparing tip-tip and side-side configurations at a center of mass energy $E_{\text{c.m.}} = 660$ MeV. In addition, calculations are also performed at $E_{\text{c.m.}} = 880$ MeV for both orientations to investigate the role of the energy on the reaction outcome.

8.3 Results

In this section we present the results of TDHF and TDRPA studies of $^{176}\text{Yb} + ^{176}\text{Yb}$ reactions at different center of mass energies and initial orientations for a range of impact parameters. Both scattering features and particle number fluctuation derived quantities were calculated and are shown below.

8.3.1 Scattering Characteristics

The following section presents scattering results from the standard TDHF calculations of $^{176}\text{Yb} + ^{176}\text{Yb}$ collisions. The TDRPA extension to TDHF is not needed for these results, though this means the points can only be interpreted as the most likely outcome for each initial condition.

Scattering angles for the $^{176}\text{Yb} + ^{176}\text{Yb}$ system for both orientations are presented in Fig. 8.2. A similar deviation from Rutherford scattering is observed at impact parameters $b \leq 8$ fm for both orientations. These deviations are due to nuclear deflection and partial orbiting of the system. Note that no fusion is observed. The relatively flat shape of the curve around $50 - 60^\circ$ at 660 MeV and $20 - 40^\circ$ at 880 MeV implies a large number of events in these particular angular ranges.

The TKE of the outgoing fragments is plotted in Fig. 8.3 as a function of the impact parameter b for side-side collisions at the two center of mass energies. Although dissipation occurs at different impact parameter ranges ($b < 10$ fm at $E_{c.m.} = 660$ MeV and $b < 12$ fm at $E_{c.m.} = 880$ MeV), both curves exhibit similar behavior. In particular, the TKEs saturate at roughly the same energy ($\sim 350 - 400$ MeV) indicating full damping of the initial TKE for the most central collisions.

Among the mechanisms responsible for energy dissipation, nucleon transfer is expected to play an important role. Of course, in symmetric collisions the average number of nucleons in the fragments does not change. Nevertheless, multinucleon transfer is possible thanks to fluctuations, leading to finite widths in the fragment particle number distributions. These fluctuations are explored in the following section.

8.3.2 Transfer Characteristics

This section focuses on the results obtained by extending TDHF to recover particle number fluctuations and correlations with the TDRPA.

Particle number fluctuations (σ_{ZZ} and σ_{NN}) and correlations (σ_{NZ}) calculated from

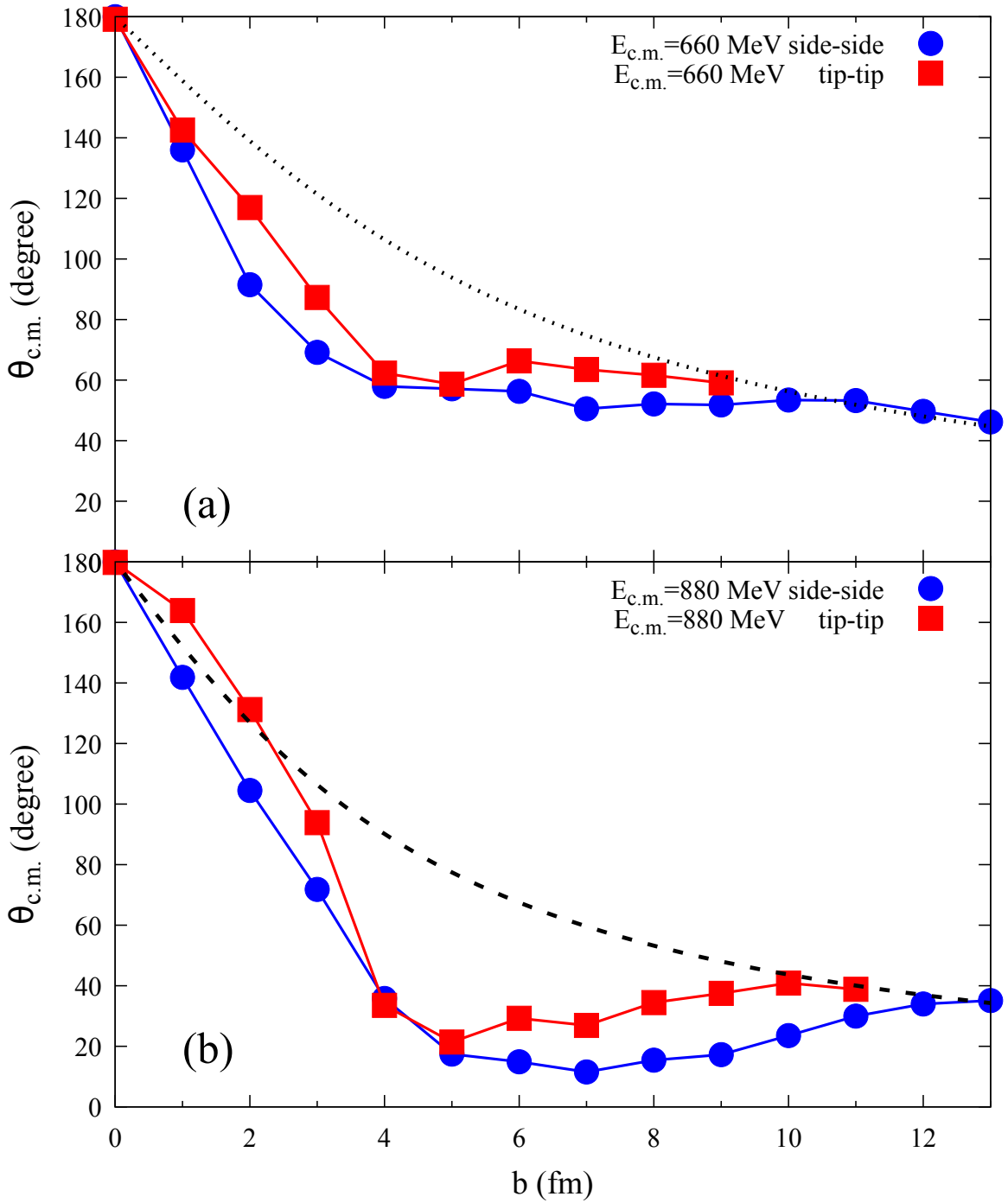


Figure 8.2: Scattering angles for $^{176}\text{Yb} + ^{176}\text{Yb}$ collisions at center of mass energies (a) $E_{c.m.} = 660 \text{ MeV}$ and (b) $E_{c.m.} = 880 \text{ MeV}$ in the side-side (circles) and tip-tip (squares) orientations. The dotted (dashed) line plots the Rutherford scattering angle for $E_{c.m.} = 660 \text{ MeV}$ (880 MeV).

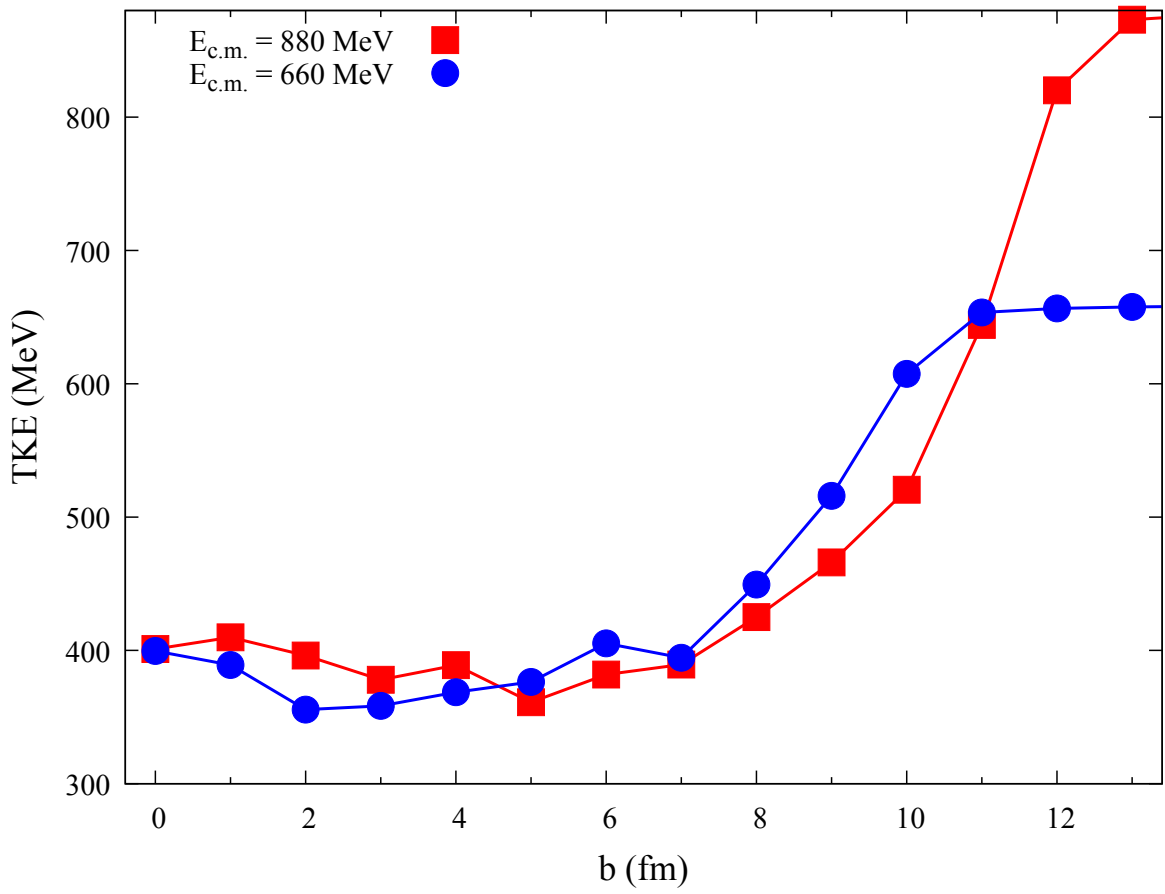


Figure 8.3: Total kinetic energies of the outgoing fragments in $^{176}\text{Yb} + ^{176}\text{Yb}$ collisions at center of mass energies $E_{\text{c.m.}} = 660$ MeV (blue circles) and $E_{\text{c.m.}} = 880$ MeV (red squares) in the side-side orientation.

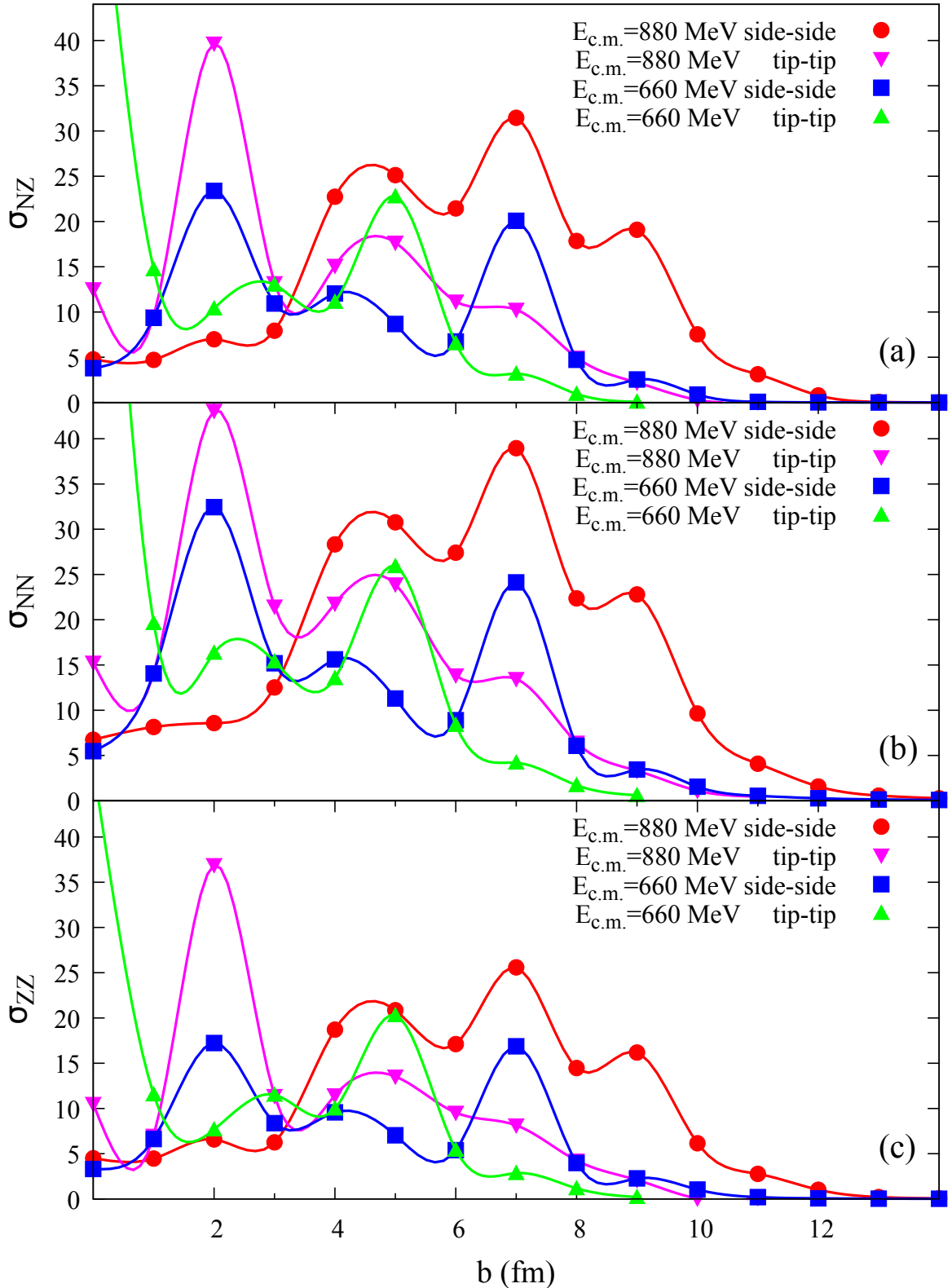


Figure 8.4: TDRPA predictions of correlations σ_{NZ} (a) and fluctuations σ_{NN} (b) and σ_{ZZ} (c) for $^{176}\text{Yb} + ^{176}\text{Yb}$ collisions for four initial configurations over a range of impact parameters.

Eq. (8.6) are shown in Fig. 8.4 as a function of impact parameters for different initial conditions. The fluctuations are greater in general at the smaller impact parameters, though they do not converge to a single value. Similar variations in fluctuations were already observed in earlier TDRPA studies of deep inelastic collisions in lighter systems (Simenel, 2011b; Williams et al., 2018). Particularly large values are sometimes obtained, such as at 660 MeV in tip-tip central ($b = 0$) collisions, indicating approximately flat distributions around the TDHF average.

Fragment mass-angle distributions (MADs) are a standard tool used experimentally to interpret the dynamics of heavy-ion collisions (Tőke et al., 1985; Shen et al., 1987; Hinde et al., 2008; Simenel et al., 2012; du Rietz et al., 2013; Wakhle et al., 2014; Hammerton et al., 2015; Morjean et al., 2017; Mohanto et al., 2018; Hinde et al., 2018). Although TDHF has been used to help interpret theoretically these distributions (Wakhle et al., 2014; Hammerton et al., 2015; Umar et al., 2016b; Sekizawa and Yabana, 2016b), these earlier calculations only incorporate fluctuations coming from the distribution of initial conditions (e.g., different orientations). Here, we go beyond the mean-field prediction by including the fragment mass fluctuations from TDRPA. Note that we only include mass fluctuations, not fluctuations in scattering angle which are still determined solely by TDHF. Calculating quantum fluctuations of scattering angles is beyond the scope of this work, although they might be necessary for a more detailed comparison with experimental MADs.

The resulting MADs for $^{176}\text{Yb} + ^{176}\text{Yb}$ reactions are shown in Fig. 8.5. The mass ratio M_R is defined as the ratio of the fragment mass over the total mass of the system. The distributions of mass ratios are determined assuming Gaussian distributions with standard deviation $\sigma_{M_R} = \sigma_{AA}/A$, limited and normalized to the physical region $0 \leq M_R \leq 1$ (see section 8.2). There is then an M_R distribution per initial condition (defined by $E_{c.m.}$, b , and the orientations), but only a single scattering angle $\theta_{c.m.}$. To obtain a continuous representation of the scattering angle, $\theta_{c.m.}$ is discretized into bins of $\Delta\theta = 1$ degree and interpolated between the values obtained by TDHF.

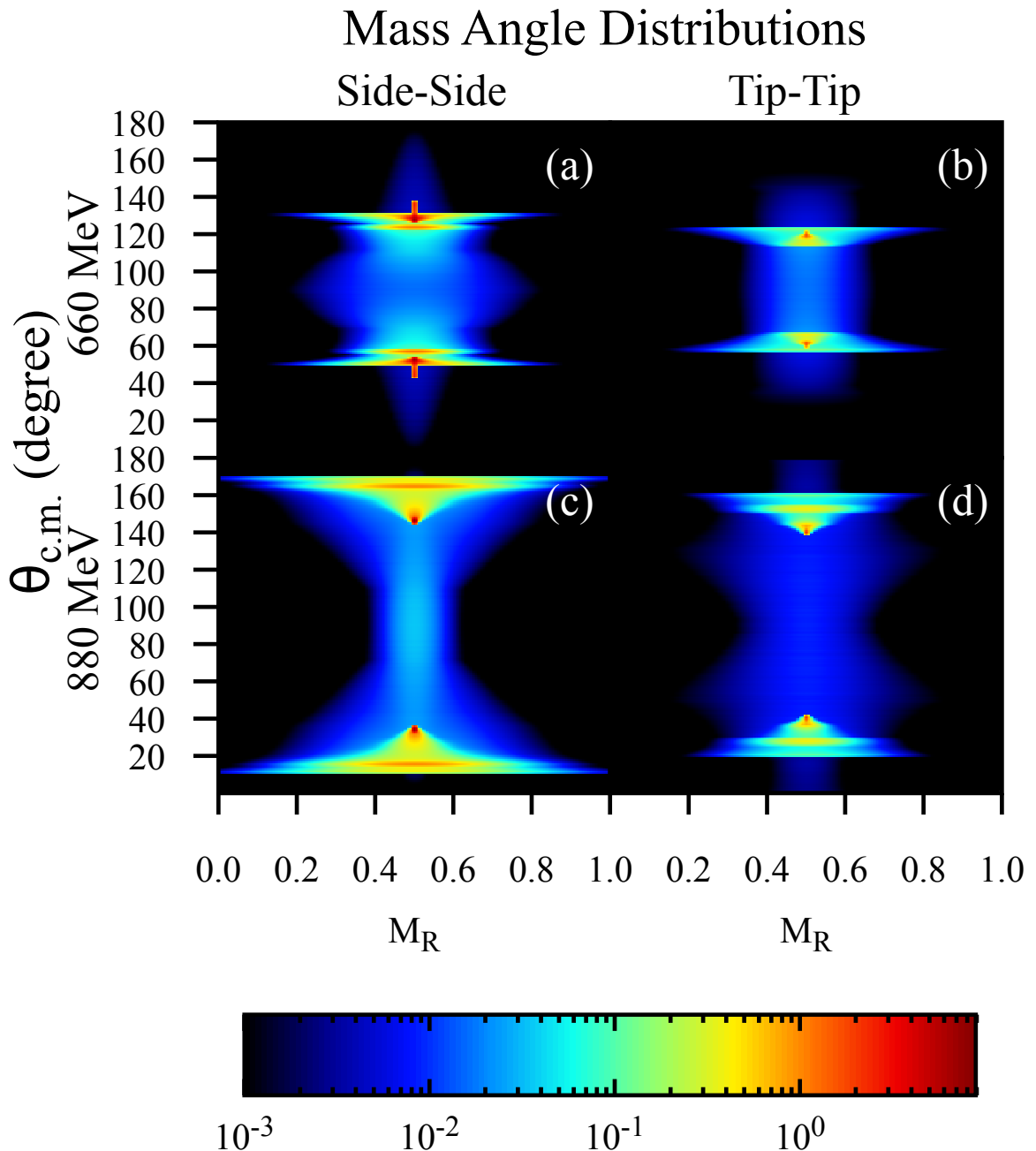


Figure 8.5: Mass angle distributions for $^{176}\text{Yb} + ^{176}\text{Yb}$ collisions at (a) $E_{\text{c.m.}} = 660 \text{ MeV}$ in the side-side orientation, (b) $E_{\text{c.m.}} = 660 \text{ MeV}$ in the tip-tip orientation, (c) $E_{\text{c.m.}} = 880 \text{ MeV}$ in the side-side orientation, and (d) $E_{\text{c.m.}} = 880 \text{ MeV}$ in the tip-tip orientation. The colorbar represents cross sections in millibarns per bin of mass ratio and degree.

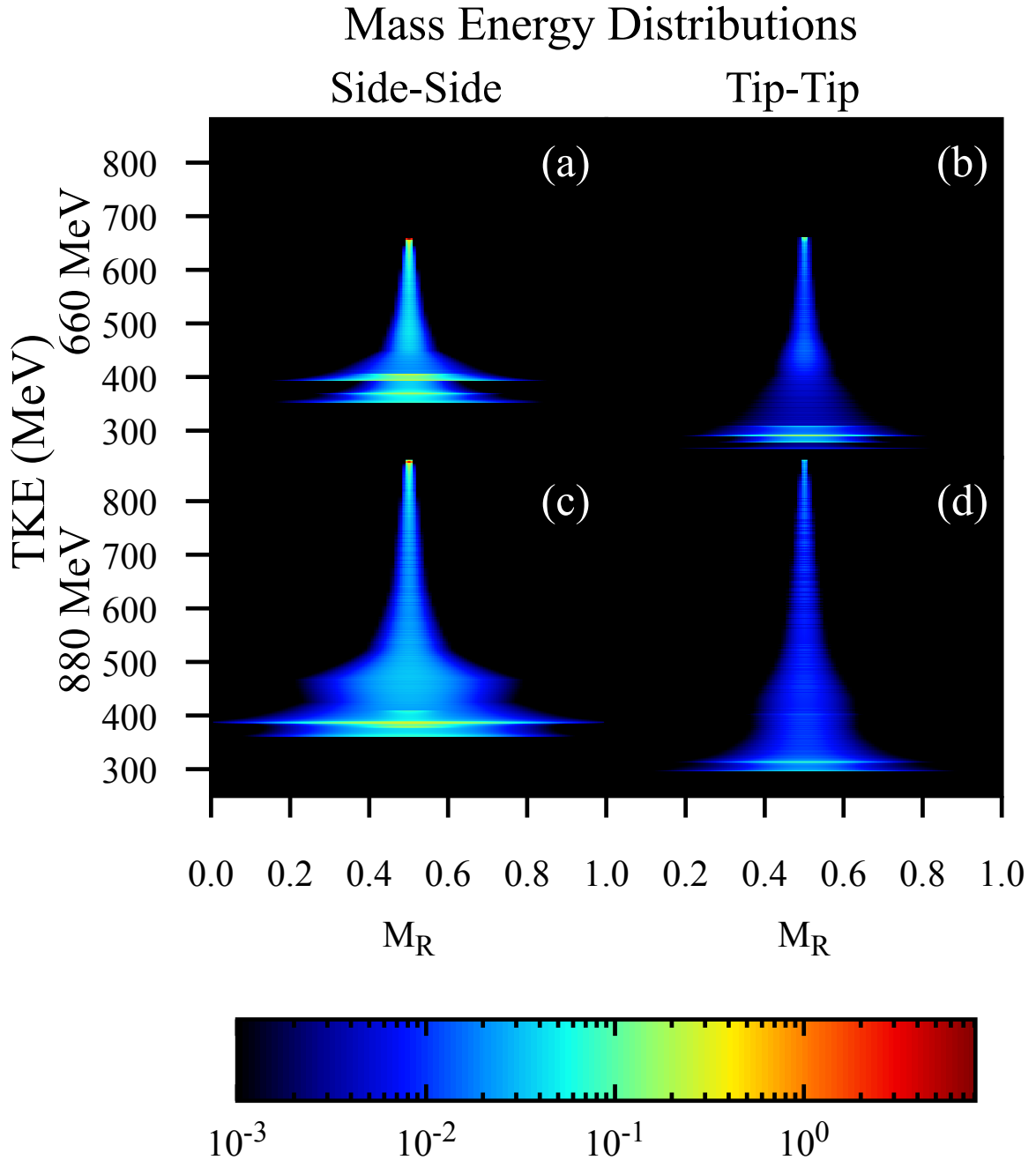


Figure 8.6: Mass energy distributions for $^{176}\text{Yb} + ^{176}\text{Yb}$ collisions at (a) $E_{\text{c.m.}} = 660$ MeV in the side-side orientation, (b) $E_{\text{c.m.}} = 660$ MeV in the tip-tip orientation, (c) $E_{\text{c.m.}} = 880$ MeV in the side-side orientation, and (d) $E_{\text{c.m.}} = 880$ MeV in the tip-tip orientation. The colorbar represents cross sections in millibarns per bin of mass ratio and MeV.

The figures are symmetric about 90° as both outgoing fragments are identically the same and will then travel outwards at complimentary angles. Specific orientations such as side-side and tip-tip will not be accessible in an experimental setting of course. Interestingly, when investigating initial energy dependence of the MAD (compare panels (a) and (c), (b) and (d) in Fig. 8.5), it can be seen that different outgoing angles are preferred depending on the incoming center of mass energy with back (and forward) scattering events being more prevalent in the higher energy regime.

This agrees well with what is seen in Fig. 8.2, where many impact parameters result in scattering angles around $50 - 60$ degrees at $E_{c.m.} = 660$ MeV and around $20 - 40$ degrees at 880 MeV. This is the case for both tip-tip and side-side orientations, though the tip-tip results tend further towards the intermediate angles than side-side at the same energy.

While the predictive capability of this method needs to be compared with experimental results and tested, this suggests a strong energy dependence and that detection of fragment production will greatly benefit from large angle detectors. The energy dependence seen in the MAD is not intuitive, and may prove to be useful for informing experimental setups.

Useful information can also be obtained from the correlations between fragment mass and kinetic energy ([Itkis et al., 2004, 2011, 2015](#); [Kozulin et al., 2019](#); [Banerjee et al., 2019](#)). Figure 8.6 presents mass energy distributions (MED) that detail the predicted TKE of outgoing fragments. It should be noted here that, while the theory provides particle number fluctuations, the values for TKE are single points (as in the case of $\theta_{c.m.}$) as predicted by TDHF alone. That is, widths of the TKE distributions are currently unknown with the method used here. This would make for an excellent extension to the theory, bringing it more in line with what can be experimentally observed.

The MEDs exhibit a continuous broadening of the mass distribution with increasing energy dissipation. The saturation of TKE lies around $350 - 400$ MeV for side-side collisions (see also Fig. 8.3) and around $250 - 300$ MeV for tip-tip. This difference between orientations is interesting as it indicates a larger kinetic energy dissipation with less com-

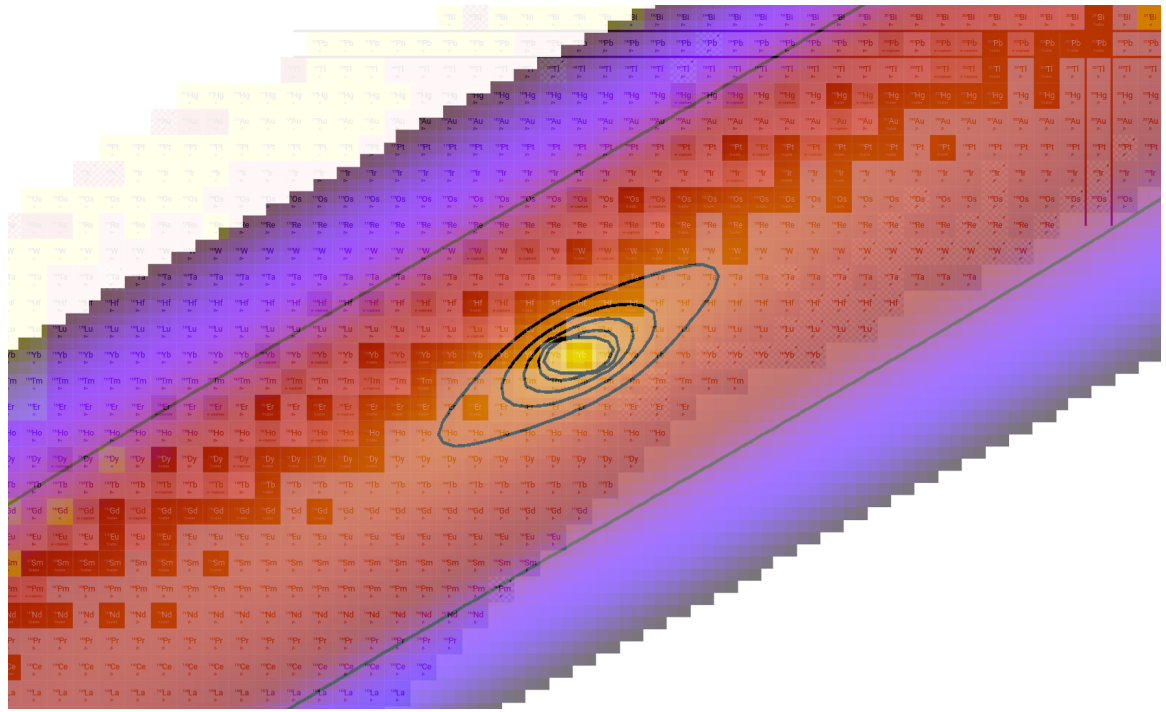


Figure 8.7: Primary fragments production cross sections for $^{176}\text{Yb} + ^{176}\text{Yb}$ collisions at $E_{\text{c.m.}} = 660$ MeV in the side-side orientation overlaid onto the chart of nuclides. The innermost contour corresponds to a cross section of 1 millibarn, with subsequent contours drawn every 0.2 mb. Finally, we also plot a boundary contour drawn at the microbarn level. Chart from ([Edward Simpson, 2019](#)).

pact configurations. A possible explanation is that the nuclei overlap at a larger distance in the tip-tip configuration, thus producing energy dissipation earlier in the collision process than in the side-side orientation.

In general, the MEDs show peaks around the elastic and fully damped regions which results from the large range of impact parameters contributing to both mechanisms.

8.3.3 Primary fragments production

Using the correlations and fluctuations shown in Fig. 8.4, a map of probabilities can be made in the N - Z plane assuming a modified Gaussian bivariate normal distribution (See section 8.2 and Eq. (8.8)). This choice of using a Gaussian is the primary assumption when calculating probabilities and related quantities and may not accurately describe the true distribution far from the center.

These probability distributions at multiple impact parameters can then be integrated over to produce a map of primary fragment production cross sections which is presented in Fig. 8.7 overlaid atop a section of the chart of nuclides in the region surrounding ^{176}Yb ([Edward Simpson, 2019](#)). As the probability distributions for each impact parameter will be centered around the ^{176}Yb ($Z = 70, N = 106$) nuclide, the resulting cross sections are also symmetric about ^{176}Yb . The inclusion of correlations between protons and neutrons via σ_{NZ} more or less aligns the distribution parallel to the valley of stability due to the symmetry energy.

Subsequent decay of the fragments would inevitably bring the final products closer to the valley of stability. Here, our focus is on primary fragment productions and the prediction of evaporation residue cross-sections are beyond the scope of this work. In fact, experimental measurements of mass-angle distributions using time of flight techniques are for primary fragments as they assume two-body kinematics ([Thomas et al., 2008](#)). To estimate the evaporation residue cross-sections would require to first compute the excitation energy of the fragments and then predict their decay with a statistical model ([Umar et al.,](#)

2017b; Sekizawa, 2017b).

One way to minimize evaporation is to consider less violent collisions. In terms of primary fragment productions, 660 and 880 MeV center of mass energies are quite similar (this can be seen by the relatively similar particle number fluctuations in Fig. 8.4). However, the higher energy will lead to more neutron evaporation and thus to less exotic evaporation residues. Use of relatively neutron-rich ^{176}Yb nuclei in symmetric collisions may then allow for this reaction to act as a probe of the neutron-rich region surrounding the principal outgoing fragment.

8.4 Summary and Discussion

Multiple TDHF and TDRPA calculations have been performed for the $^{176}\text{Yb} + ^{176}\text{Yb}$ system with various initial orientations, energies, and impact parameters. Standard TDHF allows for the classification of general scattering characteristics, while the TDRPA technique extends the approach to include correlations and fluctuations of particle numbers of the reaction fragments. This extension provides a theoretical framework that more closely resembles what will be seen in experimental investigations of this (and similar) systems.

In examining figures such as the mass-angle distributions in Fig. 8.5, information regarding the angular distribution of fragments can be gleaned and suggest large acceptance detectors to maximize measurement capability. Mass-energy distributions shown in Fig. 8.6 are also useful to investigate, e.g., the interplay between dissipation and fluctuations. In both cases, however, fluctuations of $\theta_{c.m.}$ and of TKE are not predicted in the present study. The latter would require new implementations of the TDRPA to these observables, or the use of alternative approaches such as the stochastic mean-field theory (Tanimura et al., 2017b) or an extension of the Langevin equation (Bulgac et al., 2019). Both methods have been recently used to investigate kinetic energy distributions in fission fragments. In order to benchmark our theoretical methods as applied to symmetric heavy nuclei, all predictions presented in this study would greatly benefit from experimental verification.

The methods used here provide a very powerful tool for investigating symmetric systems, though an important caveat should be discussed regarding the interpretation of these results. TDRPA produces only correlations and fluctuations, not the actual distributions themselves, which are then taken to be of a Gaussian nature. This assumption may break down when far from the center of the distribution or if the shape at the center itself is too flat and deviates sufficiently from a Gaussian behavior. It is then extremely important to compare with observations made in experimental studies such that we may better understand how to interpret the results coming from these methods.

Regardless, the $^{176}\text{Yb} + ^{176}\text{Yb}$ system presents itself as a viable candidate for studies of MNT processes and production of neutron rich nuclei in the region around $A \sim 176$. The map of possible primary fragments loosely painted in Fig. 8.7 presents an exciting range of previously inaccessible nuclei, with the above caveat applying the further one goes from the center of the distribution. Another caveat is that the predicted distribution is for primary fragments only and that statistical decay should be included in order to predict fragment produced after evaporation, e.g., following ([Sekizawa, 2017b](#); [Umar et al., 2017b](#); [Wu and Guo, 2019](#)).

Acknowledgments

We thank Yu. Ts. Oganessian and D. J. Hinde for stimulating discussions. This work has been supported by the U.S. Department of Energy under grant No. DE-SC0013847 with Vanderbilt University and by the Australian Research Councils Grant No. DP190100256.

Chapter 9

Future Work

9.1 Work in Progress

9.2 Conclusion

REFERENCES

- G. G. Adamian, N. V. Antonenko, R. V. Jolos, S. P. Ivanova, and O. I. Melnikova. Effective nucleus-nucleus potential for calculation of potential energy of a dinuclear system. *Intl. J. Mod. Phys. E*, 05(01):191–216, 1996. doi: 10.1142/S0218301396000098.
- G. G. Adamian, N. V. Antonenko, and W. Scheid. Characteristics of quasifission products within the dinuclear system model. *Phys. Rev. C*, 68:034601, 2003. doi: 10.1103/PhysRevC.68.034601.
- G. G. Adamian, N. V. Antonenko, and W. Scheid. Possibilities of synthesis of new super-heavy nuclei in actinide-based fusion reactions. *Phys. Rev. C*, 69:044601, 2004a. doi: 10.1103/PhysRevC.69.044601.
- G. G. Adamian, N. V. Antonenko, and W. Scheid. Possibilities of synthesis of new super-heavy nuclei in actinide-based fusion reactions. *Phys. Rev. C*, 69:044601, 2004b. doi: 10.1103/PhysRevC.69.044601.
- G. G. Adamian, N. V. Antonenko, S. M. Lukyanov, and Yu. E. Penionzhkevich. Possibility of production of neutron-rich isotopes in transfer-type reactions at intermediate energies. *Phys. Rev. C*, 78:024613, 2008. doi: 10.1103/PhysRevC.78.024613.
- G. G. Adamian, N. V. Antonenko, and D. Lacroix. Production of neutron-rich Ca, Sn, and Xe isotopes in transfer-type reactions with radioactive beams. *Phys. Rev. C*, 82:064611, 2010a. doi: 10.1103/PhysRevC.82.064611.
- G. G. Adamian, N. V. Antonenko, V. V. Sargsyan, and W. Scheid. Possibility of production of neutron-rich Zn and Ge isotopes in multinucleon transfer reactions at low energies. *Phys. Rev. C*, 81:024604, 2010b. doi: 10.1103/PhysRevC.81.024604.
- E. F. Aguilera, P. Rosales, E. Martínez-Quiroz, G. Murillo, M. Fernández, H. Berdejo, D. Lizcano, A. Gómez-Camacho, R. Pollicroniades, A. Varela, E. Moreno, E. Chávez,

M. E. Ortíz, A. Huerta, T. Belyaeva, and M. Wiescher. New γ -ray measurements for $^{12}\text{C} + ^{12}\text{C}$ sub-Coulomb fusion: Toward data unification. *Phys. Rev. C*, 73:064601, 2006. doi: 10.1103/physrevc.73.064601.

Andrew Cumming and Lars Bildsten. Carbon Flashes in the Heavy-Element Ocean on Accreting Neutron Stars. *Astrophys. J.*, 559:L127–L130, 2001. doi: 10.1086/323937.

Andrew Cumming, Jared Macbeth, J. J. M. In 't Zand, and Dany Page. Long type I X-ray bursts and neutron star interior physics. *Astrophys. J.*, 646:429–451, 2006. doi: 10.1086/504698.

Kaoru Aoki and Hisashi Horiuchi. Study of Local Inter–Nucleus Potential on the Basis of the Resonating Group Method. IV: Comparison of Various Approaches to Calculate Inter–Nucleus Potential and Study of the Origins of Deep and Shallow Potentials. *Prog. Theor. Phys.*, 69:1154–1183, 1983. doi: 10.1143/PTP.69.1154.

Y. Aritomo. Analysis of dynamical processes using the mass distribution of fission fragments in heavy-ion reactions. *Phys. Rev. C*, 80:064604, 2009. doi: 10.1103/PhysRevC.80.064604.

Y. Aritomo, K. Hagino, K. Nishio, and S. Chiba. Dynamical approach to heavy-ion induced fission using actinide target nuclei at energies around the Coulomb barrier. *Phys. Rev. C*, 85:044614, 2012. doi: 10.1103/PhysRevC.85.044614.

Aurel Bulgac, Piotr Magierski, Kenneth J. Roche, and Ionel Stetcu. Induced Fission of ^{240}Pu within a Real-Time Microscopic Framework. *Phys. Rev. Lett.*, 116:122504, 2016. doi: 10.1103/physrevlett.116.122504.

Aurel Bulgac, Michael McNeil Forbes, Shi Jin, Rodrigo Navarro Perez, and Nicolas Schunck. Minimal nuclear energy density functional. *Phys. Rev. C*, 97:044313, 2018. doi: 10.1103/PhysRevC.97.044313.

S. Ayik. A stochastic mean-field approach for nuclear dynamics. *Phys. Lett. B*, 658:174, 2008. doi: 10.1016/j.physletb.2007.09.072.

S. Ayik, B. Yilmaz, and O. Yilmaz. Multinucleon exchange in quasifission reactions. *Phys. Rev. C*, 92:064615, 2015a. doi: 10.1103/physrevc.92.064615.

S. Ayik, O. Yilmaz, B. Yilmaz, A. S. Umar, A. Gokalp, G. Turan, and D. Lacroix. Quantal description of nucleon exchange in a stochastic mean-field approach. *Phys. Rev. C*, 91: 054601, 2015b. doi: 10.1103/PhysRevC.91.054601.

S. Ayik, O. Yilmaz, B. Yilmaz, and A. S. Umar. Quantal nucleon diffusion: Central collisions of symmetric nuclei. *Phys. Rev. C*, 94:044624, 2016. doi: 10.1103/PhysRevC.94.044624.

S. Ayik, B. Yilmaz, O. Yilmaz, A. S. Umar, and G. Turan. Multinucleon transfer in central collisions of $^{238}\text{U} + ^{238}\text{U}$. *Phys. Rev. C*, 96:024611, 2017. doi: 10.1103/PhysRevC.96.024611.

S. Ayik, B. Yilmaz, O. Yilmaz, and A. S. Umar. Quantal diffusion description of multinucleon transfers in heavy-ion collisions. *Phys. Rev. C*, 97:054618, 2018. doi: 10.1103/PhysRevC.97.054618.

S. Ayik, B. Yilmaz, O. Yilmaz, and A. S. Umar. Quantal diffusion approach for multinucleon transfers in Xe+Pb collisions. *Phys. Rev. C*, 100:014609, 2019a. doi: 10.1103/PhysRevC.100.014609.

S. Ayik, O. Yilmaz, B. Yilmaz, and A. S. Umar. Heavy-isotope production in $^{136}\text{Xe} + ^{208}\text{Pb}$ collisions at $E_{\text{c.m.}} = 514$ MeV. *Phys. Rev. C*, 100:044614, 2019b. doi: 10.1103/PhysRevC.100.044614.

B. B. Back, H.-G. Clerc, R. R. Betts, B. G. Glagola, and B. D. Wilkins. Observation of

Anisotropy in the Fission Decay of Nuclei with Vanishing Fission Barrier. *Phys. Rev. Lett.*, 46:1068–1071, 1981. doi: 10.1103/PhysRevLett.46.1068.

B. B. Back, R. R. Betts, K. Cassidy, B. G. Glagola, J. E. Gindler, L. E. Glendenin, and B. D. Wilkins. Experimental Signatures of Quasifission Reactions. *Phys. Rev. Lett.*, 50: 818–821, 1983. doi: 10.1103/physrevlett.50.818.

B. B. Back, P. B. Fernandez, B. G. Glagola, D. Henderson, S. Kaufman, J. G. Keller, S. J. Sanders, F. Videbæk, T. F. Wang, and B. D. Wilkins. Entrance-channel effects in quasifission reactions. *Phys. Rev. C*, 53:1734–1744, 1996. doi: 10.1103/physrevc.53.1734.

B. B. Back, H. Esbensen, C. L. Jiang, and K. E. Rehm. Recent developments in heavy-ion fusion reactions. *Rev. Mod. Phys.*, 86:317–360, 2014a. doi: 10.1103/RevModPhys.86.317.

B. B. Back, H. Esbensen, C. L. Jiang, and K. E. Rehm. Recent developments in heavy-ion fusion reactions. *Rev. Mod. Phys.*, 86:317–360, 2014b. doi: 10.1103/RevModPhys.86.317.

C. L. Bai, H. Q. Zhang, H. Sagawa, X. Z. Zhang, G. Colò, and F. R. Xu. Effect of the Tensor Force on the Charge Exchange Spin–Dipole Excitations of ^{208}Pb . *Phys. Rev. Lett.*, 105:072501, 2010a. doi: 10.1103/PhysRevLett.105.072501.

C. L. Bai, H. Q. Zhang, H. Sagawa, X. Z. Zhang, G. Colò, and F. R. Xu. Effect of the Tensor Force on the Charge Exchange Spin–Dipole Excitations of ^{208}Pb . *Phys. Rev. Lett.*, 105:072501, 2010b. doi: 10.1103/PhysRevLett.105.072501.

A. B. Balantekin, J. Carlson, D. J. Dean, G. M. Fuller, R. J. Furnstahl, M. Hjorth-Jensen, R. V. F. Janssens, Bao-An Li, W. Nazarewicz, F. M. Nunes, W. E. Ormand, S. Reddy, and B. M. Sherrill. Nuclear theory and science of the facility for rare isotope beams. *Mod. Phys. Lett. A*, 29:1430010, 2014a. doi: 10.1142/S0217732314300109.

- A. B. Balantekin, J. Carlson, D. J. Dean, G. M. Fuller, R. J. Furnstahl, M. Hjorth-Jensen, R. V. F. Janssens, Bao-An Li, W. Nazarewicz, F. M. Nunes, W. E. Ormand, S. Reddy, and B. M. Sherrill. Nuclear theory and science of the facility for rare isotope beams. *Mod. Phys. Lett. A*, 29:1430010, 2014b. doi: 10.1142/S0217732314300109.
- K. Banerjee, D. J. Hinde, M. Dasgupta, E. C. Simpson, D. Y. Jeung, C. Simenel, B. M. A. Swinton-Bland, E. Williams, I. P. Carter, K. J. Cook, H. M. David, Ch. E. Düllmann, J. Khuyagbaatar, B. Kindler, B. Lommel, E. Prasad, C. Sengupta, J. F. Smith, K. Vo-Phuoc, J. Walshe, and A. Yakushev. Mechanisms Suppressing Superheavy Element Yields in Cold Fusion Reactions. *Phys. Rev. Lett.*, 122:232503, 2019. doi: 10.1103/PhysRevLett.122.232503.
- X. J. Bao, Y. Gao, J. Q. Li, and H. F. Zhang. Theoretical study of the synthesis of superheavy nuclei using radioactive beams. *Phys. Rev. C*, 91:064612, 2015. doi: 10.1103/PhysRevC.91.064612.
- X. J. Bao, Y. Gao, J. Q. Li, and H. F. Zhang. Possibilities for synthesis of new isotopes of superheavy nuclei in cold fusion reactions. *Phys. Rev. C*, 93:044615, 2016a. doi: 10.1103/PhysRevC.93.044615.
- X. J. Bao, Y. Gao, J. Q. Li, and H. F. Zhang. Possibilities for synthesis of new isotopes of superheavy nuclei in cold fusion reactions. *Phys. Rev. C*, 93:044615, 2016b. doi: 10.1103/PhysRevC.93.044615.
- Xiao Jun Bao, Shu Qing Guo, Jun Qing Li, and Hong Fei Zhang. Influence of neutron excess of projectile on multinucleon transfer reactions. *Phys. Lett. B*, 785:221–225, 2018. doi: 10.1016/j.physletb.2018.08.049.
- V. Baran, M. Colonna, M. Di Toro, A. Guarnera, and A. Smerzi. Giant dipole emission as a probe of the entrance channel dynamics. *Nucl. Phys. A*, 600:111–130, 1996. doi: 10.1016/0375-9474(96)00014-0.

- V. Baran, D. M. Brink, M. Colonna, and M. Di Toro. Collective Dipole Bremsstrahlung in Fusion Reactions. *Phys. Rev. Lett.*, 87:182501, 2001. doi: 10.1103/PhysRevLett.87.182501.
- V. Baran, M. Colonna, V. Greco, and M. Di Toro. Reaction dynamics with exotic nuclei. *Phys. Rep.*, 410:335–466, 2005. doi: 10.1016/j.physrep.2004.12.004.
- V. Baran, C. Rizzo, M. Colonna, M. Di Toro, and D. Pierroutsakou. Dynamical dipole mode in fusion reactions with exotic nuclear beams. *Phys. Rev. C*, 79:021603, 2009. doi: 10.1103/PhysRevC.79.021603.
- L. Barrón-Palos, E. F. Aguilera, J. Aspiazu, A. Huerta, E. Martínez-Quiroz, R. Monroy, E. Moreno, G. Murillo, M. E. Ortiz, R. Pollicroniades, A. Varela, and E. Chávez. Absolute cross sections measurement for the $^{12}\text{C} + ^{12}\text{C}$ system at astrophysically relevant energies. *Nucl. Phys. A*, 779:318–332, 2006. doi: 10.1016/j.nuclphysa.2006.09.004.
- R. Bass. Fusion of heavy nuclei in a classical model. *Nucl. Phys. A*, 231:45–63, 1974a. doi: 10.1016/0375-9474(74)90292-9.
- R. Bass. Fusion of heavy nuclei in a classical model. *Nucl. Phys. A*, 231:45–63, 1974b. doi: 10.1016/0375-9474(74)90292-9.
- F. Beck, K.-H. Müller, and H. S. Köhler. Momentum Dependence of the Ion-Ion Potential in a Microscopic Theory. *Phys. Rev. Lett.*, 40:837–840, 1978. doi: 10.1103/physrevlett.40.837.
- M. Bender, K. Rutz, P.-G. Reinhard, J. A. Maruhn, and W. Greiner. Shell structure of superheavy nuclei in self-consistent mean-field models. *Phys. Rev. C*, 60:034304, 1999. doi: 10.1103/PhysRevC.60.034304.
- A. Blazkiewicz, V. E. Oberacker, A. S. Umar, and M. Stoitsov. Coordinate space Hartree-

Fock-Bogoliubov calculations for the zirconium isotope chain up to the two-neutron drip line. *Phys. Rev. C*, 71:054321, 2005. doi: 10.1103/PhysRevC.71.054321.

R. Bock, Y. T. Chu, M. Dakowski, A. Gobbi, E. Grosse, A. Olmi, H. Sann, D. Schwalm, U. Lynen, W. Müller, S. Bjørnholm, H. Esbensen, W. Wölfli, and E. Morenzoni. Dynamics of the fusion process. *Nucl. Phys. A*, 388:334–380, 1982. doi: 10.1016/0375-9474(82)90420-1.

P. Bonche and H. Flocard. Dispersion of one-body operators with the Balian-Veneroni variational principle. *Nucl. Phys. A*, 437:189–207, 1985. doi: 10.1016/0375-9474(85)90232-5.

P. Bonche and D. Vautherin. A mean-field calculation of the equation of state of supernova matter. *Nucl. Phys. A*, 372:496–526, 1981. doi: 10.1016/0375-9474(81)90049-X.

P. Bonche, B. Grammaticos, and S. Koonin. Three-dimensional time-dependent Hartree-Fock calculations of $^{16}\text{O} + ^{16}\text{O}$ and $^{40}\text{Ca} + ^{40}\text{Ca}$ fusion cross sections. *Phys. Rev. C*, 17: 1700–1705, 1978. doi: 10.1103/PhysRevC.17.1700.

C. Bottcher, M. R. Strayer, A. S. Umar, and P.-G. Reinhard. Damped relaxation techniques to calculate relativistic bound-states. *Phys. Rev. A*, 40:4182–4189, 1989. doi: 10.1103/PhysRevA.40.4182.

D. Bourgin, C. Simenel, S. Courtin, and F. Haas. Microscopic study of $^{40}\text{Ca} + ^{58,64}\text{Ni}$ fusion reactions. *Phys. Rev. C*, 93:034604, 2016. doi: 10.1103/PhysRevC.93.034604.

D. M. Brink and FL. Stancu. Interaction potential between two ^{16}O nuclei derived from the Skyrme interaction. *Nucl. Phys. A*, 243:175–188, 1975. doi: 10.1016/0375-9474(75)90027-5.

D. M. Brink and Fl. Stancu. Skyrme density functional description of the double magic ^{78}Ni nucleus. *Phys. Rev. C*, 97:064304, 2018. doi: 10.1103/PhysRevC.97.064304.

J. M. A. Broomfield. *Calculations of Mass Distributions using the Balian-Vénéroni Variational Approach*. PhD thesis, University of Surrey, Guildford, United Kingdom, 2009.

J. M. A. Broomfield and P. D. Stevenson. Mass dispersions from giant dipole resonances using the Balian-Vénéroni variational approach. *J. Phys. G*, 35:095102, 2008. doi: 10.1088/0954-3899/35/9/095102.

Keith A. Brueckner, J. Robert Buchler, and Michael M. Kelly. New Theoretical Approach to Nuclear Heavy-Ion Scattering. *Phys. Rev.*, 173:944–949, 1968a. doi: 10.1103/physrev.173.944.

Keith A. Brueckner, J. Robert Buchler, and Michael M. Kelly. New Theoretical Approach to Nuclear Heavy-Ion Scattering. *Phys. Rev.*, 173:944–949, 1968b. doi: 10.1103/physrev.173.944.

Aurel Bulgac, Piotr Magierski, Kenneth J. Roche, and Ionel Stetcu. Induced Fission of ^{240}Pu within a Real-Time Microscopic Framework. *Phys. Rev. Lett.*, 116:122504, 2016. doi: 10.1103/physrevlett.116.122504.

Aurel Bulgac, Shi Jin, and Ionel Stetcu. Unitary evolution with fluctuations and dissipation. *Phys. Rev. C*, 100:014615, 2019. doi: 10.1103/PhysRevC.100.014615.

Cédric Golabek and Cédric Simenel. Collision Dynamics of Two ^{238}U Atomic Nuclei. *Phys. Rev. Lett.*, 103:042701, 2009a. doi: 10.1103/PhysRevLett.103.042701.

Cédric Golabek and Cédric Simenel. Collision Dynamics of Two ^{238}U Atomic Nuclei. *Phys. Rev. Lett.*, 103:042701, 2009b. doi: 10.1103/PhysRevLett.103.042701.

Cédric Simenel and Benoit Avez. Time-dependent Hartree–Fock description of heavy ions fusion. *Int. J. Mod. Phys. E*, 17:31–40, 2008. doi: 10.1142/S0218301308009525.

E. Chabanat, P. Bonche, P. Haensel, J. Meyer, and R. Schaeffer. A Skyrme parametrization

from subnuclear to neutron star densities Part II. Nuclei far from stabilities. *Nucl. Phys.* A, 635:231–256, 1998. doi: 10.1016/S0375-9474(98)00180-8.

Nicolas Chamel and Paweł Haensel. Physics of Neutron Star Crusts. *Living Rev. Relat.*, 11:10, 2008. doi: 10.12942/lrr-2008-10.

L. C. Chamon, B. V. Carlson, L. R. Gasques, D. Pereira, C. De Conti, M. A. G. Alvarez, M. S. Hussein, M. A. C. Ribeiro, E. S. Rossi, and C. P. Silva. Toward a global description of the nucleus-nucleus interaction. *Phys. Rev. C*, 66:014610, 2002. doi: 10.1103/PhysRevC.66.014610.

Wei-Chia Chen and J. Piekarewicz. Searching for isovector signatures in the neutron-rich oxygen and calcium isotopes. *Phys. Lett. B*, 748:284–288, 2015. doi: 10.1016/j.physletb.2015.07.020.

Chong Yu and Lu Guo. Angular momentum dependence of quasifission dynamics in the reaction $^{48}\text{Ca}+^{244}\text{Pu}$. *Sci. China Phys.*, 60:092011, 2017a. doi: 10.1007/s11433-017-9063-3.

Chong Yu and Lu Guo. Angular momentum dependence of quasifission dynamics in the reaction $^{48}\text{Ca}+^{244}\text{Pu}$. *Sci. China Phys.*, 60:092011, 2017b. doi: 10.1007/s11433-017-9063-3.

G. Colò, H. Sagawa, S. Fracasso, and P. F. Bortignon. Spin-orbit splitting and the tensor component of the Skyrme interaction. *Phys. Lett. B*, 646:227–231, 2007a. doi: <https://doi.org/10.1016/j.physletb.2007.01.033>.

G. Colò, H. Sagawa, S. Fracasso, and P. F. Bortignon. Spin-orbit splitting and the tensor component of the Skyrme interaction. *Phys. Lett. B*, 646:227–231, 2007b. doi: 10.1016/j.physletb.2007.01.033.

Courtin, S., Jiang, C. L., Fruet, G., Heine, M., Jenkins, D. G., Adsley, P., Morris, L. G., Regan, P. H., Rudigier, M., Montanari, D., Della Negra, S., de Séreville, N., Haas, F., Hammache, F., Kirsebom, O. S., Lesrel, J., Meyer, A., Montanari, D., Auranen, K., Avila, M. L., Ayangeakaa, A. D., Back, B. B., Bottoni, S., Carpenter, M., Dickerson, C., DiGiovine, B., Greene, J. P., Henderson, D. J., Hoffman, C. R., Janssens, R. V. F., Kay, B. P., Kuvin, S. A., Lauritsen, T., Pardo, R. C., Rehm, K. E., Santiago-Gonzalez, D., Sethi, J., Seweryniak, D., Talwar, R., Ugalde, C., Zhu, S., Deibel, C. M., Marley, S. T., Bourgin, D., Stodel, C., Lefebvre-Schuhl, A., Almaraz-Calderon, S., Fang, X., Tang, X. D., Alcorta, M., Bucher, B., Albers, M., and Bertone, P. Cross section measurements in the $^{12}\text{C} + ^{12}\text{C}$ system. *EPJ Web Conf.*, 165:01015, 2017. doi: 10.1051/epjconf/201716501015.

John J. Cowan, Christopher Sneden, James E. Lawler, Ani Aprahamian, Michael Wiescher, Karlheinz Langanke, Gabriel Martínez-Pinedo, and Friedrich-Karl Thielemann. Making the Heaviest Elements in the Universe: A Review of the Rapid Neutron Capture Process. *Arxiv:1901.01410*, 2019. URL <https://arxiv.org/abs/1901.01410>.

Ş. Mişcu and H. Esbensen. Hindrance of Heavy-Ion Fusion due to Nuclear Incompressibility. *Phys. Rev. Lett.*, 96:112701, 2006a. doi: 10.1103/PhysRevLett.96.112701.

Ş. Mişcu and H. Esbensen. Hindrance of Heavy-Ion Fusion due to Nuclear Incompressibility. *Phys. Rev. Lett.*, 96:112701, 2006b. doi: 10.1103/PhysRevLett.96.112701.

R. Y. Cusson, J. A. Maruhn, and H. Stöcker. Collision of $^{238}\text{U} + ^{238}\text{U}$ using a three-dimensional TDHF–BCS model. *Z. Phys. A*, 294:257–260, 1980. doi: 10.1007/BF01438163.

R. Y. Cusson, P.-G. Reinhard, M. R. Strayer, J. A. Maruhn, and W. Greiner. Density as a constraint and the separation of internal excitation energy in TDHF. *Z. Phys. A*, 320: 475–482, 1985. doi: 10.1007/BF01415725.

S. Ćwiok, P.-H. Heenen, and W. Nazarewicz. Shape coexistence and triaxiality in the superheavy nuclei. *Nature*, 433:705–709, 2005. doi: 10.1038/nature03336.

Gao-Feng Dai, Lu Guo, En-Guang Zhao, and Shan-Gui Zhou. Dissipation dynamics and spin-orbit force in time-dependent Hartree–Fock theory. *Phys. Rev. C*, 90:044609, 2014a. doi: 10.1103/PhysRevC.90.044609.

GaoFeng Dai, Lu Guo, EnGuang Zhao, and ShanGui Zhou. Effect of tensor force on dissipation dynamics in time-dependent Hartree–Fock theory. *Sci. China Phys.*, 57:1618–1622, 2014b. doi: 10.1007/s11433-014-5536-8.

GaoFeng Dai, Lu Guo, EnGuang Zhao, and ShanGui Zhou. Effect of tensor force on dissipation dynamics in time-dependent Hartree–Fock theory. *Sci. China Phys.*, 57:1618–1622, 2014c. doi: 10.1007/s11433-014-5536-8.

Paweł Danielewicz, Roy Lacey, and William G. Lynch. Determination of the Equation of State of Dense Matter. *Science*, 298:1592–1596, 2002. doi: 10.1126/science.1078070.

M. Dasgupta, D. J. Hinde, A. Diaz-Torres, B. Bouriquet, Catherine I. Low, G. J. Milburn, and J. O. Newton. Beyond the Coherent Coupled Channels Description of Nuclear Fusion. *Phys. Rev. Lett.*, 99:192701, 2007. doi: 10.1103/PhysRevLett.99.192701.

C. H. Dasso and G. Pollarolo. Investigating the nucleus-nucleus potential at very short distances. *Phys. Rev. C*, 68:054604, 2003. doi: 10.1103/physrevc.68.054604.

C. H. Dasso, T. Dossing, and H. C. Pauli. On the mass distribution in Time-Dependent Hartree-Fock calculations of heavy-ion collisions. *Z. Phys. A*, 289:395–398, 1979. doi: 10.1007/BF01409391.

C. H. Dasso, S. Landowne, and A. Winther. Barrier penetration in the presence of coupling to intrinsic degrees of freedom. *Nucl. Phys. A*, 432:495–513, 1985. doi: 10.1016/0375-9474(85)90256-8.

D. Davesne, M. Martini, K. Bennaceur, and J. Meyer. Nuclear response for the Skyrme effective interaction with zero–range tensor terms. *Phys. Rev. C*, 80:024314, 2009a. doi: 10.1103/PhysRevC.80.024314.

D. Davesne, M. Martini, K. Bennaceur, and J. Meyer. Nuclear response for the Skyrme effective interaction with zero–range tensor terms. *Phys. Rev. C*, 80:024314, 2009b. doi: 10.1103/PhysRevC.80.024314.

David J. Kedziora and Cédric Simenel. New inverse quasifission mechanism to produce neutron-rich transfermium nuclei. *Phys. Rev. C*, 81:044613, 2010. doi: 10.1103/PhysRevC.81.044613.

V. Yu. Denisov and N. A. Pilipenko. Fusion of deformed nuclei: $^{12}\text{C} + ^{12}\text{C}$. *Phys. Rev. C*, 81:025805, 2010. doi: 10.1103/PhysRevC.81.025805.

R. T. deSouza, S. Hudan, V. E. Oberacker, and A. S. Umar. Confronting measured near- and sub-barrier fusion cross sections for $^{20}\text{O} + ^{12}\text{C}$ with a microscopic method. *Phys. Rev. C*, 88:014602, 2013. doi: 10.1103/PhysRevC.88.014602.

A. Diaz-Torres, N. V. Antonenko, and W. Scheid. Dinuclear system in diabatic two-center shell model approach. *Nucl. Phys. A*, 652:61–70, 1999. doi: 10.1016/S0375-9474(99)00148-7.

A. Diaz-Torres, G. G. Adamian, N. V. Antonenko, and W. Scheid. Quasifission process in a transport model for a dinuclear system. *Phys. Rev. C*, 64:024604, 2001. doi: 10.1103/PhysRevC.64.024604.

A. Diaz Torres, G. G. Adamian, N. V. Antonenko, and W. Scheid. Potential in mass asymmetry and quasifission in a dinuclear system. *Nucl. Phys. A*, 679:410–426, 2001. doi: 10.1016/s0375-9474(00)00369-9.

A. Diaz-Torres, L. R. Gasques, and M. Wiescher. Effects of nuclear molecular configurations on the astrophysical S-factor for $^{16}\text{O} + ^{16}\text{O}$. *Phys. Lett. B*, 652:255–258, 2007. doi: 10.1016/j.physletb.2007.06.077.

A. Diaz-Torres, D. J. Hinde, M. Dasgupta, G. J. Milburn, and J. A. Tostevin. Dissipative quantum dynamics in low-energy collisions of complex nuclei. *Phys. Rev. C*, 78:064604, 2008. doi: 10.1103/PhysRevC.78.064604.

Alexis Diaz-Torres. Coupled-channels density-matrix approach to low-energy nuclear collision dynamics: A technique for quantifying quantum decoherence effects on reaction observables. *Phys. Rev. C*, 82:054617, 2010. doi: 10.1103/PhysRevC.82.054617.

Alexis Diaz-Torres and Michael Wiescher. Characterizing the astrophysical S factor for $^{12}\text{C} + ^{12}\text{C}$ fusion with wave-packet dynamics. *Phys. Rev. C*, 97:055802, 2018. doi: 10.1103/PhysRevC.97.055802.

J. Dobaczewski and J. Dudek. Time-odd components in the mean field of rotating superdeformed nuclei. *Phys. Rev. C*, 52:1827–1839, 1995. doi: 10.1103/PhysRevC.52.1827.

R. du Rietz, D. J. Hinde, M. Dasgupta, R. G. Thomas, L. R. Gasques, M. Evers, N. Lobanov, and A. Wakhle. Predominant Time Scales in Fission Processes in Reactions of S, Ti and Ni with W: Zeptosecond versus Attosecond. *Phys. Rev. Lett.*, 106: 052701, 2011. doi: 10.1103/PhysRevLett.106.052701.

R. du Rietz, E. Williams, D. J. Hinde, M. Dasgupta, M. Evers, C. J. Lin, D. H. Luong, C. Simenel, and A. Wakhle. Mapping quasifission characteristics and timescales in heavy element formation reactions. *Phys. Rev. C*, 88:054618, 2013. doi: 10.1103/PhysRevC.88.054618.

Edward Simpson. The Colourful Nuclide Chart. Technical report, Australian National University, 2019. URL <https://people.physics.anu.edu.au/~ecs103/chart/>.

Y. M. Engel, D. M. Brink, K. Goeke, S. J. Krieger, and D. Vautherin. Time-dependent Hartree-Fock theory with Skyrme's interaction. *Nucl. Phys. A*, 249:215–238, 1975. doi: 10.1016/0375-9474(75)90184-0.

H. Esbensen and S. Landowne. Higher-order coupling effects in low energy heavy-ion fusion reactions. *Phys. Rev. C*, 35:2090–2096, 1987. doi: 10.1103/PhysRevC.35.2090.

H. Esbensen, C. L. Jiang, and K. E. Rehm. Coupled-channels analysis of $^{58}\text{Ni} + ^{124}\text{Sn}$ reactions. *Phys. Rev. C*, 57:2401–2408, 1998. doi: 10.1103/physrevc.57.2401.

H. Esbensen, X. Tang, and C. L. Jiang. Effects of mutual excitations in the fusion of carbon isotopes. *Phys. Rev. C*, 84:064613, 2011. doi: 10.1103/physrevc.84.064613.

M. Evers, M. Dasgupta, D. J. Hinde, D. H. Luong, R. Rafiei, R. du Rietz, and C. Simenel. Cluster transfer in the reaction $^{16}\text{O} + ^{208}\text{Pb}$ at energies well below the fusion barrier: A possible doorway to energy dissipation. *Phys. Rev. C*, 84:054614, 2011. doi: 10.1103/PhysRevC.84.054614.

G. Fazio, G. Giardina, A. Lamberto, R. Ruggeri, C. Saccá, R. Palamara, A. I. Muminov, A. K. Nasirov, U. T. Yakhshiev, F. Hanappe, T. Materna, and L. Stuttgé. Formation of heavy and superheavy elements by reactions with massive nuclei. *Eur. Phys. J. A*, 19: 89–104, 2004. doi: 10.1140/epja/i2003-10103-6.

Zhao-Qing Feng. Production of neutron-rich isotopes around $N = 126$ in multinucleon transfer reactions. *Phys. Rev. C*, 95:024615, 2017a. doi: 10.1103/PhysRevC.95.024615.

Zhao-Qing Feng. Production of neutron-rich isotopes around $N = 126$ in multinucleon transfer reactions. *Phys. Rev. C*, 95:024615, 2017b. doi: 10.1103/PhysRevC.95.024615.

Zhao-Qing Feng, Gen-Ming Jin, and Jun-Qing Li. Production of heavy isotopes in transfer reactions by collisions of $^{238}\text{U} + ^{238}\text{U}$. *Phys. Rev. C*, 80:067601, 2009. doi: 10.1103/PhysRevC.80.067601.

M. Fierz. Über die relativistische Theorie kräftefreier Teilchen mit beliebigem Spin. *Helv. Phys. Acta*, 12:3, 1939. doi: 10.5169/seals-110930.

Torsten Fliessbach. The optical potential for the elastic heavy ion scattering. *Z. Phys.*, 247: 117–126, 1971. doi: 10.1007/bf01395288.

Torsten Fliessbach. The reduced width amplitude in the reaction theory for composite particles. *Z. Phys. A*, 272:39–46, 1975. doi: 10.1007/bf01408426.

H. Flocard, S. E. Koonin, and M. S. Weiss. Three-dimensional time-dependent Hartree-Fock calculations: Application to $^{16}\text{O} + ^{16}\text{O}$ collisions. *Phys. Rev. C*, 17:1682–1699, 1978. doi: 10.1103/PhysRevC.17.1682.

V. A. Fock. Näherungsmethode zur Lösung des quantenmechanischen Mehrkörperproblems. *Z. Phys.*, 61:126, 1930. doi: 10.1007/BF01340294.

William A. Fowler, Georgeanne R. Caughlan, and Barbara A. Zimmerman. Thermonuclear Reaction Rates, II. *Annu. Rev. Astron. Astrophys.*, 13:69–112, 1975. doi: 10.1146/annurev.aa.13.090175.000441.

S. Fracasso, E. B. Suckling, and P. D. Stevenson. Unrestricted Skyrme-tensor time-dependent Hartree-Fock model and its application to the nuclear response from spherical to triaxial nuclei. *Phys. Rev. C*, 86:044303, 2012a. doi: 10.1103/PhysRevC.86.044303.

S. Fracasso, E. B. Suckling, and P. D. Stevenson. Unrestricted Skyrme-tensor time-dependent Hartree-Fock model and its application to the nuclear response from spherical to triaxial nuclei. *Phys. Rev. C*, 86:044303, 2012b. doi: 10.1103/PhysRevC.86.044303.

Y. Fu, H. Tong, X. F. Wang, H. Wang, D. Q. Wang, X. Y. Wang, and J. M. Yao. Microscopic analysis of shape transition in neutron-deficient Yb isotopes. *Phys. Rev. C*, 97:014311, 2018. doi: 10.1103/PhysRevC.97.014311.

- H. Gäggeler, T. Sikkeland, G. Wirth, W. Brüchle, W. Bögl, G. Franz, G. Herrmann, J. V. Kratz, M. Schädel, K. Sümmerer, and W. Weber. Probing sub-barrier fusion and extra-push by measuring fermium evaporation residues in different heavy ion reactions. *Z. Phys. A*, 316:291–307, 1984. doi: 10.1007/BF01439902.
- L. R. Gasques, L. C. Chamon, D. Pereira, M. A. G. Alvarez, E. S. Rossi, C. P. Silva, and B. V. Carlson. Global and consistent analysis of the heavy-ion elastic scattering and fusion processes. *Phys. Rev. C*, 69:034603, 2004. doi: 10.1103/PhysRevC.69.034603.
- L. R. Gasques, A. V. Afanasjev, E. F. Aguilera, M. Beard, L. C. Chamon, P. Ring, M. Wiescher, and D. G. Yakovlev. Nuclear fusion in dense matter: Reaction rate and carbon burning. *Phys. Rev. C*, 72:025806, 2005. doi: 10.1103/PhysRevC.72.025806.
- L. R. Gasques, A. V. Afanasjev, M. Beard, J. Lubian, T. Neff, M. Wiescher, and D. G. Yakovlev. São Paulo potential as a tool for calculating S factors of fusion reactions in dense stellar matter. *Phys. Rev. C*, 76:045802, 2007. doi: 10.1103/PhysRevC.76.045802.
- K. Godbey, A. S. Umar, and C. Simenel. Dependence of fusion on isospin dynamics. *Phys. Rev. C*, 95:011601(R), 2017a. doi: 10.1103/PhysRevC.95.011601.
- K. Godbey, A. S. Umar, and C. Simenel. Dependence of fusion on isospin dynamics. *Phys. Rev. C*, 95:011601(R), 2017b. doi: 10.1103/PhysRevC.95.011601.
- K. Godbey, C Simenel, and A. S. Umar. Absence of hindrance in microscopic $^{12}\text{C} + ^{12}\text{C}$ fusion study. *Phys. Rev. C*, 100:024619, 2019a. doi: 10.1103/PhysRevC.100.024619.
- K. Godbey, A. S. Umar, and C Simenel. Deformed shell effects in $^{48}\text{Ca} + ^{249}\text{Bk}$ quasifission fragments. *Phys. Rev. C*, 100:024610, 2019b. doi: 10.1103/PhysRevC.100.024610.
- P. M. Goddard, P. D. Stevenson, and A. Rios. Fission dynamics within time-dependent Hartree-Fock: deformation-induced fission. *Phys. Rev. C*, 92:054610, 2015a. doi: 10.1103/PhysRevC.92.054610.

P. M. Goddard, P. D. Stevenson, and A. Rios. Fission dynamics within time-dependent Hartree-Fock: deformation-induced fission. *Phys. Rev. C*, 92:054610, 2015b. doi: 10.1103/PhysRevC.92.054610.

P. M. Goddard, P. D. Stevenson, and A. Rios. Fission dynamics within time-dependent Hartree–Fock. II. Boost-induced fission. *Phys. Rev. C*, 93:014620, 2016a. doi: 10.1103/PhysRevC.93.014620.

P. M. Goddard, P. D. Stevenson, and A. Rios. Fission dynamics within time–dependent Hartree–Fock. II. Boost-induced fission. *Phys. Rev. C*, 93:014620, 2016b. doi: 10.1103/PhysRevC.93.014620.

K. Goeke, F. Grümmer, and P.-G Reinhard. Three-dimensional nuclear dynamics in the quantized ATDHF approach. *Ann. Phys.*, 150:504–551, 1983. doi: 10.1016/0003-4916(83)90025-8.

G.-H. Göritz and U. Mosel. Optical potentials for elastic heavy ion scattering. *Z. Phys. A*, 277:243–248, 1976. doi: 10.1007/bf01415599.

P. A. M. Guichon. A possible quark mechanism for the saturation of nuclear matter. *Phys. Lett. B*, 200:235 – 240, 1988. doi: 10.1016/0370-2693(88)90762-9.

Pierre A. M. Guichon, Koichi Saito, Evguenii Rodionov, and Anthony W. Thomas. The role of nucleon structure in finite nuclei. *Nucl. Phys. A*, 601:349–379, 1996. doi: 10.1016/0375-9474(96)00033-4.

Lu Guo, Fumihiko Sakata, and En-Guang Zhao. Characteristic feature of self–consistent mean–field in level crossing region. *Nucl. Phys. A*, 740:59–76, 2004a. doi: <https://doi.org/10.1016/j.nuclphysa.2004.04.117>.

Lu Guo, Fumihiko Sakata, and En-Guang Zhao. Characteristic feature of self–consistent

mean-field in level crossing region. *Nucl. Phys. A*, 740:59–76, 2004b. doi: 10.1016/j.nuclphysa.2004.04.117.

Lu Guo, Fumihiko Sakata, and En-guang Zhao. Applicability of self-consistent mean-field theory. *Phys. Rev. C*, 71:024315, 2005a. doi: 10.1103/PhysRevC.71.024315.

Lu Guo, Fumihiko Sakata, and En-guang Zhao. Applicability of self-consistent mean-field theory. *Phys. Rev. C*, 71:024315, 2005b. doi: 10.1103/PhysRevC.71.024315.

Lu Guo, J. A. Maruhn, and P.-G. Reinhard. Boost-invariant mean field approximation and the nuclear Landau-Zener effect. *Phys. Rev. C*, 76:014601, 2007a. doi: 10.1103/PhysRevC.76.014601.

Lu Guo, J. A. Maruhn, and P.-G. Reinhard. Triaxiality and shape coexistence in germanium isotopes. *Phys. Rev. C*, 76:034317, 2007b. doi: 10.1103/PhysRevC.76.034317.

Lu Guo, J. A. Maruhn, and P.-G. Reinhard. Triaxiality and shape coexistence in germanium isotopes. *Phys. Rev. C*, 76:034317, 2007c. doi: 10.1103/PhysRevC.76.034317.

Lu Guo, J. A. Maruhn, P.-G. Reinhard, and Y. Hashimoto. Conservation properties in the time-dependent Hartree Fock theory. *Phys. Rev. C*, 77:041301, 2008. doi: 10.1103/PhysRevC.77.041301.

Lu Guo, Chong Yu, Long Shi, and Cédric Simenel. Skyrme tensor force in the collision $^{16}\text{O} + ^{40}\text{Ca}$. *Eur. Phys. J. Web Conf.*, 163:00021, 2017a. doi: <https://doi.org/10.1051/epjconf/201716300021>.

Lu Guo, K. Godbey, and A. S. Umar. Influence of the tensor force on the microscopic heavy-ion interaction potential. *Phys. Rev. C*, 98:064607, 2018a. doi: 10.1103/PhysRevC.98.064607.

Lu Guo, Cédric Simenel, Long Shi, and Chong Yu. The role of tensor force in heavy-ion

fusion dynamics. *Phys. Lett. B*, 782:401–405, 2018b. doi: 10.1016/j.physletb.2018.05.066.

Lu Guo, Cédric Simenel, Long Shi, and Chong Yu. The role of tensor force in heavy-ion fusion dynamics. *Phys. Lett. B*, 782:401–405, 2018c. doi: 10.1016/j.physletb.2018.05.066.

S. Q. Guo, Y. Gao, J. Q. Li, and H. F. Zhang. Dynamical deformation in heavy ion reactions and the characteristics of quasifission products. *Phys. Rev. C*, 96:044622, 2017b. doi: 10.1103/PhysRevC.96.044622.

Raj K. Gupta, S. K. Patra, P. D. Stevenson, and Walter Greiner. A highly neutron-rich cluster and/or a superheavy nucleus in the compound nucleus $^{238}\text{U} + ^{238}\text{U}$: A mean field study. *Intl. J. Mod. Phys. E*, 16:1721–1732, 2007. doi: 10.1142/S0218301307006137.

P. Haensel and J. L. Zdunik. Equation of state and structure of the crust of an accreting neutron star. *Astron. Astrophys.*, 229:117–122, 1990. URL http://articles.adsabs.harvard.edu/cgi-bin/nph-iarticle_query?1990A&26A...229..117H&data_type=PDF_HIGH&whole_paper=YES&type=PRINTER&filetype=.pdf.

K. Hagino, N. Rowley, and A. T. Kruppa. A program for coupled-channel calculations with all order couplings for heavy-ion fusion reactions. *Comput. Phys. Commun.*, 123:143–152, 1999. doi: 10.1016/s0010-4655(99)00243-x.

K. Hammerton, Z. Kohley, D. J. Hinde, M. Dasgupta, A. Wakhle, E. Williams, V. E. Oberacker, A. S. Umar, I. P. Carter, K. J. Cook, J. Greene, D. Y. Jeung, D. H. Luong, S. D. McNeil, C. S. Palshetkar, D. C. Rafferty, C. Simenel, and K. Stiefel. Reduced quasifission competition in fusion reactions forming neutron-rich heavy elements. *Phys. Rev. C*, 91:041602(R), 2015. doi: 10.1103/PhysRevC.91.041602.

K. Hammerton, D. J. Morrissey, Z. Kohley, D. J. Hinde, M. Dasgupta, A. Wakhle, E. Williams, I. P. Carter, K. J. Cook, J. Greene, D. Y. Jeung, D. H. Luong, S. D. Mc-

Neil, C. Palshetkar, D. C. Rafferty, C. Simenel, and K. Stiefel. Entrance channel effects on the quasifission reaction channel in Cr+W systems. *Phys. Rev. C*, 99:054621, 2019. doi: 10.1103/PhysRevC.99.054621.

D. R. Hartree. The Wave Mechanics of an Atom with a Non-Coulomb Central Field. Part I. Theory and Methods. *Math. Proc. Camb. Phil. Soc.*, 24:89, 1928. doi: 10.1017/S0305004100011919.

P.-H. Heenen. Low energy fusion of $^{12}\text{C} + ^{12}\text{C}$ and $^{16}\text{O} + ^{16}\text{O}$ systems. *Phys. Lett. B*, 99: 298 – 300, 1981. doi: 10.1016/0370-2693(81)91129-1.

Henning Esbensen and Şerban Mişicu. Hindrance of $^{16}\text{O} + ^{208}\text{Pb}$ fusion at extreme sub-barrier energies. *Phys. Rev. C*, 76:054609, 2007. doi: 10.1103/PhysRevC.76.054609.

B. Heusch, C. Volant, H. Freiesleben, R. P. Chestnut, K. D. Hildenbrand, F. Pühlhofer, W. F. W. Schneider, B. Kohlmeyer, and W. Pfeffer. The reaction mechanism in the system $^{132}\text{Xe} + ^{56}\text{Fe}$ at 5.73 MeV/u: Evidence for a new type of strongly damped collisions. *Z. Phys. A*, 288:391–400, 1978. doi: 10.1007/BF01417723.

M. D. High and B. Čujec. The $^{12}\text{C} + ^{12}\text{C}$ sub-Coulomb fusion cross section. *Nucl. Phys. A*, 282:181–188, 1977. doi: 10.1016/0375-9474(77)90179-8.

D. J. Hinde, J. R. Leigh, J. J. M. Bokhorst, J. O. Newton, R. L. Walsh, and J. W. Boldeman. Mass-split dependence of the pre- and post-scission neutron multiplicities for fission of ^{251}Es . *Nucl. Phys. A*, 472:318–332, 1987. doi: 10.1016/0375-9474(87)90213-2.

D. J. Hinde, D. Hilscher, H. Rossner, B. Gebauer, M. Lehmann, and M. Wilpert. Neutron emission as a probe of fusion-fission and quasi-fission dynamics. *Phys. Rev. C*, 45:1229–1259, 1992. doi: 10.1103/PhysRevC.45.1229.

D. J. Hinde, M. Dasgupta, J. R. Leigh, J. P. Lestone, J. C. Mein, C. R. Morton, J. O. Newton,

and H. Timmers. Fusion-Fission versus Quasifission: Effect of Nuclear Orientation. *Phys. Rev. Lett.*, 74:1295–1298, 1995. doi: 10.1103/PhysRevLett.74.1295.

D. J. Hinde, M. Dasgupta, J. R. Leigh, J. C. Mein, C. R. Morton, J. O. Newton, and H. Timmers. Conclusive evidence for the influence of nuclear orientation on quasifission. *Phys. Rev. C*, 53:1290–1300, 1996. doi: 10.1103/PhysRevC.53.1290.

D. J. Hinde, R. G. Thomas, R. du Rietz, A. Diaz-Torres, M. Dasgupta, M. L. Brown, M. Evers, L. R. Gasques, R. Rafiei, and M. D. Rodriguez. Disentangling Effects of Nuclear Structure in Heavy Element Formation. *Phys. Rev. Lett.*, 100:202701, 2008. doi: 10.1103/PhysRevLett.100.202701.

D. J. Hinde, D. Y. Jeung, E. Prasad, A. Wakhle, M. Dasgupta, M. Evers, D. H. Luong, R. du Rietz, C. Simenel, E. C. Simpson, and E. Williams. Sub-barrier quasifission in heavy element formation reactions with deformed actinide target nuclei. *Phys. Rev. C*, 97:024616, 2018. doi: 10.1103/PhysRevC.97.024616.

S. Hofmann, F. P. Heßberger, D. Ackermann, G. Münzenberg, S. Antalic, P. Cagarda, B. Kindler, J. Kojouharova, M. Leino, B. Lommel, R. Mann, A. G. Popeko, S. Reshitko, S. Šaro, J. Uusitalo, and A. V. Yeremin. New results on elements 111 and 112. *Eur. Phys. J. A*, 14:147–157, 2002. doi: 10.1140/epja/i2001-10119-x.

C. J. Horowitz, M. A. Pérez-García, and J. Piekarewicz. Neutrino–pasta scattering: The opacity of nonuniform neutron-rich matter. *Phys. Rev. C*, 69:045804, 2004. doi: 10.1103/PhysRevC.69.045804.

S. Hossain, A. S. B. Tariq, Athoy Nilima, M. Sujan Islam, R. Majumder, M. A. Sayed, M. M. Billah, M. M. B. Azad, M. A. Uddin, I. Reichstein, F. B. Malik, and A. K. Basak. Dependence of the $^{16}\text{O} + ^{16}\text{O}$ nuclear potential on nuclear incompressibility. *Phys. Rev. C*, 91:064613, 2015. doi: 10.1103/PhysRevC.91.064613.

F. Hoyle. On Nuclear Reactions Occuring in Very Hot STARS.I. the Synthesis of Elements from Carbon to Nickel. *Astrophys. J. Suppl. Ser.*, 1:121, 1954. doi: 10.1086/190005.

Minghui Huang, Zaiguo Gan, Xiaohong Zhou, Junqing Li, and W. Scheid. Competing fusion and quasifission reaction mechanisms in the production of superheavy nuclei. *Phys. Rev. C*, 82:044614, 2010. doi: 10.1103/PhysRevC.82.044614.

J. K. Hwang, A. V. Ramayya, J. H. Hamilton, Y. X. Luo, A. V. Daniel, G. M. Ter-Akopian, J. D. Cole, and S. J. Zhu. Half-life measurements of several states in $^{95,97}\text{Sr}$, $^{97,100,104}\text{Zr}$, ^{106}Mo , and ^{148}Ce . *Phys. Rev. C*, 73:044316, 2006. doi: 10.1103/PhysRevC.73.044316.

Takatoshi Ichikawa. Systematic investigations of deep sub-barrier fusion reactions using an adiabatic approach. *Phys. Rev. C*, 92:064604, 2015. doi: 10.1103/PhysRevC.92.064604.

Takatoshi Ichikawa, Kouichi Hagino, and Akira Iwamoto. Existence of a one-body barrier revealed in deep subbarrier fusion. *Phys. Rev. C*, 75:057603, 2007. doi: 10.1103/physrevc.75.057603.

I. M. Itkis, E. M. Kozulin, M. G. Itkis, G. N. Knyazheva, A. A. Bogachev, E. V. Chernysheva, L. Krupa, Yu. Ts. Oganessian, V. I. Zagrebaev, A. Ya. Rusanov, F. Goennenwein, O. Dorvaux, L. Stuttgé, F. Hanappe, E. Vardaci, and E. Goés de Brennand. Fission and quasifission modes in heavy-ion-induced reactions leading to the formation of Hs*. *Phys. Rev. C*, 83:064613, 2011. doi: 10.1103/PhysRevC.83.064613.

M. G. Itkis, J. Äystö, S. Beghini, A. A. Bogachev, L. Corradi, O. Dorvaux, A. Gadea, G. Giardina, F. Hanappe, I. M. Itkis, M. Jandel, J. Kliman, S. V. Khlebnikov, G. N. Kniyeva, N. A. Kondratiev, E. M. Kozulin, L. Krupa, A. Latina, T. Materna, G. Montagnoli, Yu. Ts. Oganessian, I. V. Pokrovsky, E. V. Prokhorova, N. Rowley, V. A. Rubchenya, A. Ya. Rusanov, R. N. Sagaidak, F. Scarlassara, A. M. Stefanini, L. Stuttge, S. Szilner, M. Trotta, W. H. Trzaska, D. N. Vakhtin, A. M. Vinodkumar, V. M. Voskressenski, and

V. I. Zagrebaev. Shell effects in fission and quasi-fission of heavy and superheavy nuclei. *Nucl. Phys. A*, 734:136–147, 2004. doi: 10.1016/j.nuclphysa.2004.01.022.

M. G. Itkis, E. Vardaci, I. M. Itkis, G. N. Knyazheva, and E. M. Kozulin. Fusion and fission of heavy and superheavy nuclei (experiment). *Nucl. Phys. A*, 944:204–237, 2015. doi: 10.1016/j.nuclphysa.2015.09.007.

Y. Iwata and J. A. Maruhn. Enhanced spin-current tensor contribution in collision dynamics. *Phys. Rev. C*, 84:014616, 2011. doi: 10.1103/PhysRevC.84.014616.

C. L. Jiang, H. Esbensen, K. E. Rehm, B. B. Back, R. V. F. Janssens, J. A. Caggiano, P. Collon, J. Greene, A. M. Heinz, D. J. Henderson, I. Nishinaka, T. O. Pennington, and D. Seweryniak. Unexpected Behavior of Heavy-Ion Fusion Cross Sections at Extreme Sub-Barrier Energies. *Phys. Rev. Lett.*, 89:052701, 2002. doi: 10.1103/physrevlett.89.052701.

C. L. Jiang, K. E. Rehm, B. B. Back, and R. V. F. Janssens. Expectations for ^{12}C and ^{16}O induced fusion cross sections at energies of astrophysical interest. *Phys. Rev. C*, 75: 015803, 2007. doi: 10.1103/PhysRevC.75.015803.

C. L. Jiang, A. M. Stefanini, H. Esbensen, K. E. Rehm, L. Corradi, E. Fioretto, P. Mason, G. Montagnoli, F. Scarlassara, R. Silvestri, P. P. Singh, S. Szilner, X. D. Tang, and C. A. Ur. Fusion hindrance for Ca+Ca systems: Influence of neutron excess. *Phys. Rev. C*, 82: 041601, 2010. doi: 10.1103/PhysRevC.82.041601.

C. L. Jiang, B. B. Back, H. Esbensen, R. V. F. Janssens, K. E. Rehm, and R. J. Charity. Origin and Consequences of $^{12}\text{C} + ^{12}\text{C}$ Fusion Resonances at Deep Sub-barrier Energies. *Phys. Rev. Lett.*, 110:072701, 2013. doi: 10.1103/physrevlett.110.072701.

C. L. Jiang, K. E. Rehm, B. B. Back, H. Esbensen, R. V. F. Janssens, A. M. Stefanini, and G. Montagnoli. Influence of heavy-ion transfer on fusion reactions. *Phys. Rev. C*, 89: 051603(R), 2014a. doi: 10.1103/physrevc.89.051603.

C. L. Jiang, A. M. Stefanini, H. Esbensen, K. E. Rehm, S. Almaraz-Calderon, M. L. Avila, B. B. Back, D. Bourgin, L. Corradi, S. Courtin, E. Fioretto, F. Galtarossa, A. Goasduff, F. Haas, M. M. Mazzocco, D. Montanari, G. Montagnoli, T. Mijatovic, R. Sagaidak, D. Santiago-Gonzalez, F. Scarlassara, E. E. Strano, and S. Szilner. Fusion reactions of $^{58,64}\text{Ni} + ^{124}\text{Sn}$. *Phys. Rev. C*, 91:044602, 2015a. doi: 10.1103/physrevc.91.044602.

C. L. Jiang, D. Santiago-Gonzalez, S. Almaraz-Calderon, K. E. Rehm, B. B. Back, K. Au- ranen, M. L. Avila, A. D. Ayangeakaa, S. Bottoni, M. P. Carpenter, C. Dickerson, B. Di- Giovine, J. P. Greene, C. R. Hoffman, R. V. F. Janssens, B. P. Kay, S. A. Kuvin, T. Lau- ritzen, R. C. Pardo, J. Sethi, D. Seweryniak, R. Talwar, C. Ugalde, S. Zhu, D. Bour- gin, S. Courtin, F. Haas, M. Heine, G. Fruet, D. Montanari, D. G. Jenkins, L. Morris, A. Lefebvre-Schuhl, M. Alcorta, X. Fang, X. D. Tang, B. Bucher, C. M. Deibel, and S. T. Marley. Reaction rate for carbon burning in massive stars. *Phys. Rev. C*, 97: 012801, 2018. doi: 10.1103/PhysRevC.97.012801.

X. Jiang, J. A. Maruhn, and S. W. Yan. Configuration transition effect in heavy-ion fusion reactions with deformed nuclei. *EPL*, 112:12001, 2015b. doi: 10.1209/0295-5075/112/12001.

Xiang Jiang and Nan Wang. Probing the production mechanism of neutron-rich nuclei in multinucleon transfer reactions. *Phys. Rev. C*, 101:014604, 2020. doi: 10.1103/ PhysRevC.101.014604.

Xiang Jiang, Joachim A. Maruhn, and Shiwei Yan. Microscopic study of noncentral effects in heavy-ion fusion reactions with spherical nuclei. *Phys. Rev. C*, 90:064618, 2014b. doi: 10.1103/PhysRevC.90.064618.

Junlong Tian, Xizhen Wu, Kai Zhao, Yingxun Zhang, and Zhuxia Li. Properties of the composite systems formed in the reactions $^{238}\text{U} + ^{238}\text{U}$ and $^{232}\text{Th} + ^{250}\text{Cf}$. *Phys. Rev. C*, 77:064603, 2008. doi: 10.1103/PhysRevC.77.064603.

Ka-Hae Kim, Takaharu Otsuka, and Paul Bonche. Three-dimensional TDHF calculations for reactions of unstable nuclei. *J. Phys. G*, 23:1267, 1997. doi: 10.1088/0954-3899/23/10/014.

A. V. Karpov and V. V. Saiko. Modeling near-barrier collisions of heavy ions based on a Langevin-type approach. *Phys. Rev. C*, 96:024618, 2017. doi: 10.1103/PhysRevC.96.024618.

A. V. Karpov, V. A. Rachkov, and V. V. Samarin. Quantum coupled-channels model of nuclear fusion with a semiclassical consideration of neutron rearrangement. *Phys. Rev. C*, 92:064603, 2015. doi: 10.1103/PhysRevC.92.064603.

Kazuyuki Sekizawa. TDHF Theory and Its Extensions for the Multinucleon Transfer Reaction: A Mini Review. *Front. Phys.*, 7:20, 2019. doi: 10.3389/fphy.2019.00020.

Kazuyuki Sekizawa and Kazuhiro Yabana. Time-dependent Hartree-Fock calculations for multinucleon transfer processes in $^{40,48}\text{Ca} + ^{124}\text{Sn}$, $^{40}\text{Ca} + ^{208}\text{Pb}$, and $^{58}\text{Ni} + ^{208}\text{Pb}$ reactions. *Phys. Rev. C*, 88:014614, 2013a. doi: 10.1103/PhysRevC.88.014614.

Kazuyuki Sekizawa and Kazuhiro Yabana. Time-dependent Hartree-Fock calculations for multinucleon transfer processes in $^{40,48}\text{Ca} + ^{124}\text{Sn}$, $^{40}\text{Ca} + ^{208}\text{Pb}$, and $^{58}\text{Ni} + ^{208}\text{Pb}$ reactions. *Phys. Rev. C*, 88:014614, 2013b. doi: 10.1103/PhysRevC.88.014614.

R. Keser, A. S. Umar, and V. E. Oberacker. Microscopic study of Ca+Ca fusion. *Phys. Rev. C*, 85:044606, 2012a. doi: 10.1103/PhysRevC.85.044606.

R. Keser, A. S. Umar, and V. E. Oberacker. Microscopic study of Ca+Ca fusion. *Phys. Rev. C*, 85:044606, 2012b. doi: 10.1103/PhysRevC.85.044606.

J. Khuyagbaatar, A. Yakushev, Ch. E. Düllmann, D. Ackermann, L.-L. Andersson, M. Asai, M. Block, R. A. Boll, H. Brand, D. M. Cox, M. Dasgupta, X. Derkx, A. Di Nitto, K. Eberhardt, J. Even, M. Evers, C. Fahlander, U. Forsberg, J. M. Gates, N. Gharibyan,

P. Golubev, K. E. Gregorich, J. H. Hamilton, W. Hartmann, R.-D. Herzberg, F. P. Heßberger, D. J. Hinde, J. Hoffmann, R. Hollinger, A. Hübner, E. Jäger, B. Kindler, J. V. Kratz, J. Krier, N. Kurz, M. Laatiaoui, S. Lahiri, R. Lang, B. Lommel, M. Maiti, K. Miernik, S. Minami, A. Mistry, C. Mokry, H. Nitsche, J. P. Omtvedt, G. K. Pang, P. Papadakis, D. Renisch, J. Roberto, D. Rudolph, J. Runke, K. P. Rykaczewski, L. G. Sarmiento, M. Schädel, B. Schausten, A. Semchenkov, D. A. Shaughnessy, P. Steinegger, J. Steiner, E. E. Tereshatov, P. Thörle-Pospiech, K. Tinschert, T. Torres De Heidenreich, N. Trautmann, A. Türler, J. Uusitalo, D. E. Ward, M. Wegrzecki, N. Wiehl, S. M. Van Cleve, and V. Yakusheva. $^{48}\text{Ca} + ^{249}\text{Bk}$ Fusion Reaction Leading to Element $Z = 117$: Long-Lived α -Decaying ^{270}Db and Discovery of ^{266}Lr . *Phys. Rev. Lett.*, 112: 172501, 2014. doi: 10.1103/PhysRevLett.112.172501.

J. Khuyagbaatar, H. M. David, D. J. Hinde, I. P. Carter, K. J. Cook, M. Dasgupta, Ch. E. Düllmann, D. Y. Jeung, B. Kindler, B. Lommel, D. H. Luong, E. Prasad, D. C. Rafferty, C. Sengupta, C. Simenel, E. C. Simpson, J. F. Smith, K. Vo-Phuoc, J. Walsh, A. Wakhle, E. Williams, and A. Yakushev. Nuclear structure dependence of fusion hindrance in heavy element synthesis. *Phys. Rev. C*, 97:064618, 2018. doi: 10.1103/PhysRevC.97.064618.

G. N. Knyazheva, E. M. Kozulin, R. N. Sagaidak, A. Yu. Chizhov, M. G. Itkis, N. A. Kondratiev, V. M. Voskressensky, A. M. Stefanini, B. R. Behera, L. Corradi, E. Fioretto, A. Gadea, A. Latina, S. Szilner, M. Trotta, S. Beghini, G. Montagnoli, F. Scarlassara, F. Haas, N. Rowley, P. R. S. Gomes, and A. Szanto de Toledo. Quasifission processes in $^{40,48}\text{Ca} + ^{144,154}\text{Sm}$ reactions. *Phys. Rev. C*, 75:064602, 2007. doi: 10.1103/PhysRevC.75.064602.

Z. Kohley, J. F. Liang, D. Shapira, R. L. Varner, C. J. Gross, J. M. Allmond, A. L. Caraley, E. A. Coello, F. Favela, K. Lagergren, and P. E. Mueller. Near-Barrier Fusion of Sn + Ni and Te + Ni Systems: Examining the Correlation between Nu-

cleon Transfer and Fusion Enhancement. *Phys. Rev. Lett.*, 107:202701, 2011. doi: 10.1103/PhysRevLett.107.202701.

Z. Kohley, J. F. Liang, D. Shapira, C. J. Gross, R. L. Varner, J. M. Allmond, J. J. Kolata, P. E. Mueller, and A. Roberts. Sub-barrier fusion enhancement with radioactive ^{134}Te . *Phys. Rev. C*, 87:064612, 2013. doi: 10.1103/physrevc.87.064612.

J. J. Kolata, A. Roberts, A. M. Howard, D. Shapira, J. F. Liang, C. J. Gross, R. L. Varner, Z. Kohley, A. N. Villano, H. Amro, W. Loveland, and E. Chavez. Fusion of $^{124,132}\text{Sn}$ with $^{40,48}\text{Ca}$. *Phys. Rev. C*, 85:054603, 2012. doi: 10.1103/PhysRevC.85.054603.

S. E. Koonin, K. T. R. Davies, V. Maruhn-Rezwani, H. Feldmeier, S. J. Krieger, and J. W. Negele. Time-dependent Hartree-Fock calculations for $^{16}\text{O} + ^{16}\text{O}$ and $^{40}\text{Ca} + ^{40}\text{Ca}$ reactions. *Phys. Rev. C*, 15:1359–1374, 1977. doi: 10.1103/PhysRevC.15.1359.

M. Kortelainen, J. McDonnell, W. Nazarewicz, P.-G. Reinhard, J. Sarich, N. Schunck, M. V. Stoitsov, and S. M. Wild. Nuclear energy density optimization: Large deformations. *Phys. Rev. C*, 85:024304, 2012. doi: 10.1103/PhysRevC.85.024304.

Kouhei Washiyama and Denis Lacroix. Energy dependence of the nucleus-nucleus potential close to the Coulomb barrier. *Phys. Rev. C*, 78:024610, 2008. doi: 10.1103/PhysRevC.78.024610.

Kouhei Washiyama, Sakir Ayik, and Denis Lacroix. Mass dispersion in transfer reactions with a stochastic mean-field theory. *Phys. Rev. C*, 80:031602, 2009. doi: 10.1103/PhysRevC.80.031602.

Kouichi Hagino and Noboru Takigawa. Subbarrier Fusion Reactions and Many-Particle Quantum Tunneling. *Prog. Theor. Phys.*, 128:1001–1060, 2012. doi: 10.1143/PTP.128.1061.

E. M. Kozulin, G. N. Knyazheva, S. N. Dmitriev, I. M. Itkis, M. G. Itkis, T. A. Loktev, K. V. Novikov, A. N. Baranov, W. H. Trzaska, E. Vardaci, S. Heinz, O. Beliuskina, and S. V. Khlebnikov. Shell effects in damped collisions of ^{88}Sr with ^{176}Yb at the Coulomb barrier energy. *Phys. Rev. C*, 89:014614, 2014. doi: 10.1103/PhysRevC.89.014614.

E. M. Kozulin, G. N. Knyazheva, T. K. Ghosh, A. Sen, I. M. Itkis, M. G. Itkis, K. V. Novikov, I. N. Diatlov, I. V. Pchelintsev, C. Bhattacharya, S. Bhattacharya, K. Banerjee, E. O. Saveleva, and I. V. Vorobiev. Fission and quasifission of the composite system $Z = 114$ formed in heavy-ion reactions at energies near the coulomb barrier. *Phys. Rev. C*, 99:014616, 2019. doi: 10.1103/PhysRevC.99.014616.

Denis Lacroix and Sakir Ayik. Stochastic quantum dynamics beyond mean field. *Eur. Phys. J. A*, 50:95, 2014. doi: 10.1140/epja/i2014-14095-8.

G. A. Lalazissis, S. Raman, and P. Ring. Ground-state properties of even-even nuclei in the relativistic mean-field theory. *At. Data Nucl. Data Tables*, 71:1–40, 1999. doi: 10.1006/adnd.1998.0795.

D. Lebhertz, S. Courtin, F. Haas, D. G. Jenkins, C. Simenel, M.-D. Salsac, D. A. Hutcheon, C. Beck, J. Cseh, J. Darai, C. Davis, R. G. Glover, A. Goasduff, P. E. Kent, G. Levai, P. L. Marley, A. Michalon, J. E. Pearson, M. Rousseau, N. Rowley, and C. Ruiz. $^{12}\text{C}(^{16}\text{O},\gamma)^{28}\text{Si}$ radiative capture: Structural and statistical aspects of the γ decay. *Phys. Rev. C*, 85:034333, 2012. doi: 10.1103/PhysRevC.85.034333.

T. Lesinski, M. Bender, K. Bennaceur, T. Duguet, and J. Meyer. Tensor part of the Skyrme energy density functional: Spherical nuclei. *Phys. Rev. C*, 76:014312, 2007a. doi: 10.1103/PhysRevC.76.014312.

T. Lesinski, M. Bender, K. Bennaceur, T. Duguet, and J. Meyer. Tensor part of the Skyrme energy density functional: Spherical nuclei. *Phys. Rev. C*, 76:014312, 2007b. doi: 10.1103/PhysRevC.76.014312.

S. Levit, J. W. Negele, and Z. Paltiel. Barrier penetration and spontaneous fission in the time-dependent mean-field approximation. *Phys. Rev. C*, 22:1979–1995, 1980. doi: 10.1103/PhysRevC.22.1979.

Bao-An Li, Àngels Ramos, Giuseppe Verde, and Isaac Vidaña. Topical issue on Nuclear Symmetry Energy. *Eur. Phys. J. A*, 50:1, 2014. URL <http://epja.epj.org/component/toc/?task=topic&id=260>.

Cheng Li, Peiwei Wen, Jingjing Li, Gen Zhang, Bing Li, Xinxin Xu, Zhong Liu, Shaofei Zhu, and Feng-Shou Zhang. Production mechanism of new neutron-rich heavy nuclei in the $^{136}\text{Xe} + ^{198}\text{Pt}$ reaction. *Phys. Lett. B*, 776:278–283, 2018. doi: 10.1016/j.physletb.2017.11.060.

J. F. Liang, J. M. Allmond, C. J. Gross, P. E. Mueller, D. Shapira, R. L. Varner, M. Dasgupta, D. J. Hinde, C. Simenel, E. Williams, K. Vo-Phuoc, M. L. Brown, I. P. Carter, M. Evers, D. H. Luong, T. Ebadi, and A. Wakhle. Examining the role of transfer coupling in sub-barrier fusion of $^{46,50}\text{Ti} + ^{124}\text{Sn}$. *Phys. Rev. C*, 94:024616, 2016. doi: 10.1103/physrevc.94.024616.

C. J. Lin, R. du Rietz, D. J. Hinde, M. Dasgupta, R. G. Thomas, M. L. Brown, M. Evers, L. R. Gasques, and M. D. Rodriguez. Systematic behavior of mass distributions in ^{48}Ti -induced fission at near-barrier energies. *Phys. Rev. C*, 85:014611, 2012. doi: 10.1103/PhysRevC.85.014611.

W. Loveland. Synthesis of transactinide nuclei using radioactive beams. *Phys. Rev. C*, 76:014612, 2007. doi: 10.1103/PhysRevC.76.014612.

Bing-Nan Lu, Jie Zhao, En-Guang Zhao, and Shan-Gui Zhou. Multidimensionally-constrained relativistic mean-field models and potential-energy surfaces of actinide nuclei. *Phys. Rev. C*, 89:014323, 2014a. doi: 10.1103/PhysRevC.89.014323.

Bing-Nan Lu, Jie Zhao, En-Guang Zhao, and Shan-Gui Zhou. Multidimensionally-constrained relativistic mean-field models and potential-energy surfaces of actinide nuclei. *Phys. Rev. C*, 89:014323, 2014b. doi: 10.1103/PhysRevC.89.014323.

Lu Guo and Takashi Nakatsukasa. Time-dependent Hartree-Fock studies of the dynamical fusion threshold. *EPJ Web Conf.*, 38:09003, 2012a. doi: 10.1051/epjconf/20123809003.

Lu Guo and Takashi Nakatsukasa. Time-dependent Hartree-Fock studies of the dynamical fusion threshold. *EPJ Web Conf.*, 38:09003, 2012b. doi: 10.1051/epjconf/20123809003.

Z. Majka, R. Płaneta, Z. Sosin, A. Wieloch, K. Zelga, M. Adamczyk, K. Pelczar, M. Barbui, S. Wuenschel, K. Hagel, X. Cao, E.-J. Kim, J. Natowitz, R. Wada, H. Zheng, G. Giuliani, and S. Kowalski. A novel experimental setup for rare events selection and its potential application to super-heavy elements search. *Acta Phys. Pol. B*, 49:1801, 2018. doi: 10.5506/APhysPolB.49.1801.

J. B. Marston and S. E. Koonin. Mean-Field Calculations of Fluctuations in Nuclear Collisions. *Phys. Rev. Lett.*, 54:1139–1141, 1985. doi: 10.1103/PhysRevLett.54.1139.

J. A. Maruhn, P.-G. Reinhard, P. D. Stevenson, and M. R. Strayer. Spin-excitation mechanisms in Skyrme-force time-dependent Hartree-Fock calculations. *Phys. Rev. C*, 74: 027601, 2006. doi: 10.1103/PhysRevC.74.027601.

J. A. Maruhn, P.-G. Reinhard, P. D. Stevenson, and A. S. Umar. The TDHF Code Sky3D. *Comput. Phys. Commun.*, 185:2195–2216, 2014a. doi: 10.1016/j.cpc.2014.04.008.

J. A. Maruhn, P.-G. Reinhard, P. D. Stevenson, and A. S. Umar. The TDHF Code Sky3D. *Comput. Phys. Commun.*, 185:2195–2216, 2014b. doi: 10.1016/j.cpc.2014.04.008.

Zachary Matheson, Samuel A. Giuliani, Witold Nazarewicz, Jhilam Sadhukhan, and Nicolas Schunck. Cluster radioactivity of $^{294}_{118}\text{Og}_{176}$. *Phys. Rev. C*, 99:041304, 2019. doi: 10.1103/PhysRevC.99.041304.

Michael G. Mazarakis and William E. Stephens. Experimental Measurements of the ^{12}C + ^{12}C Nuclear Reactions at Low Energies. *Phys. Rev. C*, 7:1280–1287, 1973. doi: 10.1103/physrevc.7.1280.

Ş. Mişcu and H. Esbensen. Signature of shallow potentials in deep sub-barrier fusion reactions. *Phys. Rev. C*, 75:034606, 2007. doi: 10.1103/physrevc.75.034606.

G. Mohanto, D. J. Hinde, K. Banerjee, M. Dasgupta, D. Y. Jeung, C. Simenel, E. C. Simpson, A. Wakhle, E. Williams, I. P. Carter, K. J. Cook, D. H. Luong, C. S. Palshetkar, and D. C. Rafferty. Interplay of spherical closed shells and N/Z asymmetry in quasifission dynamics. *Phys. Rev. C*, 97:054603, 2018. doi: 10.1103/PhysRevC.97.054603.

Peter Möller, Arnold J. Sierk, and Akira Iwamoto. Five-Dimensional Fission–Barrier Calculations from ^{70}Se to ^{252}Cf . *Phys. Rev. Lett.*, 92:072501, 2004a. doi: 10.1103/PhysRevLett.92.072501.

Peter Möller, Arnold J. Sierk, and Akira Iwamoto. Five-Dimensional Fission–Barrier Calculations from ^{70}Se to ^{252}Cf . *Phys. Rev. Lett.*, 92:072501, 2004b. doi: 10.1103/PhysRevLett.92.072501.

G. Montagnoli, A. M. Stefanini, C. L. Jiang, H. Esbensen, L. Corradi, S. Courtin, E. Fioretto, A. Goasduff, F. Haas, A. F. Kifle, C. Michelagnoli, D. Montanari, T. Mijatović, K. E. Rehm, R. Silvestri, Pushpendra P. Singh, F. Scarlassara, S. Szilner, X. D. Tang, and C. A. Ur. Fusion of $^{40}\text{Ca} + ^{40}\text{Ca}$ and other Ca + Ca systems near and below the barrier. *Phys. Rev. C*, 85:024607, 2012. doi: 10.1103/PhysRevC.85.024607.

Kosuke Morita. SHE research at RIKEN/GARIS. *Nucl. Phys. A*, 944:30–61, 2015. doi: 10.1016/j.nuclphysa.2015.10.007.

M. Morjean, D. J. Hinde, C. Simenel, D. Y. Jeung, M. Airiau, K. J. Cook, M. Dasgupta, A. Drouart, D. Jacquet, S. Kalkal, C. S. Palshetkar, E. Prasad, D. Rafferty, E. C. Simpson, L. Tassan-Got, K. Vo-Phuoc, and E. Williams. Evidence for the Role of Proton

Shell Closure in Quasifission Reactions from X-Ray Fluorescence of Mass–Identified Fragments. *Phys. Rev. Lett.*, 119:222502, 2017. doi: 10.1103/PhysRevLett.119.222502.

C. R. Morton, A. C. Berrian, M. Dasgupta, D. J. Hinde, J. O. Newton, K. Hagino, and I. J. Thompson. Coupled-channels analysis of the $^{16}\text{O} + ^{208}\text{Pb}$ fusion barrier distribution. *Phys. Rev. C*, 60:044608, 1999. doi: 10.1103/PhysRevC.60.044608.

G. Münzenberg and K. Morita. Synthesis of the heaviest nuclei in cold fusion reactions. *Nucl. Phys. A*, 944:3–4, 2015. doi: 10.1016/j.nuclphysa.2015.06.007.

Takashi Nakatsukasa, Kenichi Matsuyanagi, Masayuki Matsuo, and Kazuhiro Yabana. Time-dependent density-functional description of nuclear dynamics. *Rev. Mod. Phys.*, 88:045004, 2016. doi: 10.1103/RevModPhys.88.045004.

W. Nazarewicz, M. Bender, S. Ćwiok, P. H. Heenen, A. T. Kruppa, P.-G. Reinhard, and T. Vertse. Theoretical description of superheavy nuclei. *Nucl. Phys. A*, 701:165–171, 2002. doi: 10.1016/S0375-9474(01)01567-6.

J. W. Negele. The mean-field theory of nuclear-structure and dynamics. *Rev. Mod. Phys.*, 54:913–1015, 1982. doi: 10.1103/RevModPhys.54.913.

V. A. Nesterov. Effect of the Pauli exclusion principle and the polarization of nuclei on the potential of their interaction for the example of the $^{16}\text{O} + ^{16}\text{O}$ system. *Phys. At. Nucl.*, 76: 577–584, 2013. doi: 10.1134/s106377881304008x.

K. Nishio, H. Ikezoe, S. Mitsuoka, I. Nishinaka, Y. Nagame, Y. Watanabe, T. Ohtsuki, K. Hirose, and S. Hofmann. Effects of nuclear orientation on the mass distribution of fission fragments in the reaction of $^{36}\text{S} + ^{238}\text{U}$. *Phys. Rev. C*, 77:064607, 2008. doi: 10.1103/PhysRevC.77.064607.

K. Nishio, S. Mitsuoka, I. Nishinaka, H. Makii, Y. Wakabayashi, H. Ikezoe, K. Hirose, T. Ohtsuki, Y. Aritomo, and S. Hofmann. Fusion probabilities in the reactions $^{40,48}\text{Ca}$

+ ^{238}U at energies around the Coulomb barrier. *Phys. Rev. C*, 86:034608, 2012. doi: 10.1103/PhysRevC.86.034608.

K. Nomura, T. Otsuka, R. Rodríguez-Guzmán, L. M. Robledo, and P. Sarriguren. Collective structural evolution in neutron-rich Yb, Hf, W, Os, and Pt isotopes. *Phys. Rev. C*, 84: 054316, 2011. doi: 10.1103/PhysRevC.84.054316.

V. E. Oberacker and A. S. Umar. Microscopic analysis of sub-barrier fusion enhancement in $^{132}\text{Sn} + ^{40}\text{Ca}$ versus $^{132}\text{Sn} + ^{48}\text{Ca}$. *Phys. Rev. C*, 87:034611, 2013. doi: 10.1103/PhysRevC.87.034611.

V. E. Oberacker, A. S. Umar, J. A. Maruhn, and P.-G. Reinhard. Microscopic study of the $^{132,124}\text{Sn} + ^{96}\text{Zr}$ reactions: Dynamic excitation energy, energy-dependent heavy-ion potential, and capture cross section. *Phys. Rev. C*, 82:034603, 2010a. doi: 10.1103/PhysRevC.82.034603.

V. E. Oberacker, A. S. Umar, J. A. Maruhn, and P.-G. Reinhard. Microscopic study of the $^{132,124}\text{Sn} + ^{96}\text{Zr}$ reactions: Dynamic excitation energy, energy-dependent heavy-ion potential, and capture cross section. *Phys. Rev. C*, 82:034603, 2010b. doi: 10.1103/PhysRevC.82.034603.

V. E. Oberacker, A. S. Umar, J. A. Maruhn, and P.-G. Reinhard. Dynamic microscopic study of pre-equilibrium giant resonance excitation and fusion in the reactions $^{132}\text{Sn} + ^{48}\text{Ca}$ and $^{124}\text{Sn} + ^{40}\text{Ca}$. *Phys. Rev. C*, 85:034609, 2012. doi: 10.1103/PhysRevC.85.034609.

V. E. Oberacker, A. S. Umar, and C. Simenel. Dissipative dynamics in quasifission. *Phys. Rev. C*, 90:054605, 2014a. doi: 10.1103/PhysRevC.90.054605.

V. E. Oberacker, A. S. Umar, and C. Simenel. Dissipative dynamics in quasifission. *Phys. Rev. C*, 90:054605, 2014b. doi: 10.1103/PhysRevC.90.054605.

Yu. Ts. Oganessian, F. Sh. Abdullin, C. Alexander, J. Binder, R. A. Boll, S. N. Dmitriev, J. Ezold, K. Felker, J. M. Gostic, R. K. Grzywacz, J. H. Hamilton, R. A. Henderson, M. G. Itkis, K. Miernik, D. Miller, K. J. Moody, A. N. Polyakov, A. V. Ramayya, J. B. Roberto, M. A. Ryabinin, K. P. Rykaczewski, R. N. Sagaidak, D. A. Shaughnessy, I. V. Shirokovsky, M. V. Shumeiko, M. A. Stoyer, N. J. Stoyer, V. G. Subbotin, A. M. Sukhov, Yu. S. Tsyanov, V. K. Utyonkov, A. A. Voinov, and G. K. Vostokin. Production and Decay of the Heaviest Nuclei $^{293,294}117$ and $^{294}118$. *Phys. Rev. Lett.*, 109:162501, 2012. doi: 10.1103/PhysRevLett.109.162501.

Yu. Ts. Oganessian, F. Sh. Abdullin, C. Alexander, J. Binder, R. A. Boll, S. N. Dmitriev, J. Ezold, K. Felker, J. M. Gostic, R. K. Grzywacz, J. H. Hamilton, R. A. Henderson, M. G. Itkis, K. Miernik, D. Miller, K. J. Moody, A. N. Polyakov, A. V. Ramayya, J. B. Roberto, M. A. Ryabinin, K. P. Rykaczewski, R. N. Sagaidak, D. A. Shaughnessy, I. V. Shirokovsky, M. V. Shumeiko, M. A. Stoyer, N. J. Stoyer, V. G. Subbotin, A. M. Sukhov, Yu. S. Tsyanov, V. K. Utyonkov, A. A. Voinov, and G. K. Vostokin. Experimental studies of the $^{249}\text{Bk} + ^{48}\text{Ca}$ reaction including decay properties and excitation function for isotopes of element 117, and discovery of the new isotope ^{277}Mt . *Phys. Rev. C*, 87: 054621, 2013. doi: 10.1103/PhysRevC.87.054621.

Takaharu Otsuka, Toshio Suzuki, Rintaro Fujimoto, Hubert Grawe, and Yoshinori Akaishi. Evolution of Nuclear Shells due to the Tensor Force. *Phys. Rev. Lett.*, 95:232502, 2005. doi: 10.1103/PhysRevLett.95.232502.

Takaharu Otsuka, Toshiaki Matsuo, and Daisuke Abe. Mean Field with Tensor Force and Shell Structure of Exotic Nuclei. *Phys. Rev. Lett.*, 97:162501, 2006a. doi: 10.1103/PhysRevLett.97.162501.

Takaharu Otsuka, Toshiaki Matsuo, and Daisuke Abe. Mean Field with Tensor Force and Shell Structure of Exotic Nuclei. *Phys. Rev. Lett.*, 97:162501, 2006b. doi: 10.1103/PhysRevLett.97.162501.

Takaharu Otsuka, Toshio Suzuki, Michio Honma, Yutaka Utsuno, Naofumi Tsunoda, Koshiroh Tsukiyama, and Morten Hjorth-Jensen. Novel Features of Nuclear Forces and Shell Evolution in Exotic Nuclei. *Phys. Rev. Lett.*, 104:012501, 2010. doi: 10.1103/PhysRevLett.104.012501.

Takaharu Otsuka, Alexandra Gade, Olivier Sorlin, Toshio Suzuki, and Yutaka Utsuno. Evolution of nuclear structure in exotic nuclei driven by nuclear forces. *Arxiv:1805.06501*, 2018. URL <https://arxiv.org/abs/1805.06501>. Accepted in Rev. Mod. Phys.

J. R. Patterson, H. Winkler, and C. S. Zaidins. Experimental Investigation of the Stellar Nuclear Reaction $^{12}\text{C} + ^{12}\text{C}$ at Low Energies. *Astrophys. J.*, 157:367, 1969. doi: 10.1086/150073.

W. Pauli. Über den Zusammenhang des Abschlusses der Elektronengruppen im Atom mit der Komplexstruktur der Spektren. *Z. Phys.*, 31:765, 1925. doi: 10.1007/BF02980631.

W. Pauli. The Connection Between Spin and Statistics. *Phys. Rev.*, 58:716–722, 1940. doi: 10.1103/PhysRev.58.716.

J. C. Pei, W. Nazarewicz, J. A. Sheikh, and A. K. Kerman. Fission Barriers of Compound Superheavy Nuclei. *Phys. Rev. Lett.*, 102:192501, 2009. doi: 10.1103/PhysRevLett.102.192501.

Yu. E. Penionzhkevich, G. G. Adamian, and N. V. Antonenko. Towards neutron drip line via transfer-type reactions. *Phys. Lett. B*, 621:119–125, 2005. doi: 10.1016/j.physletb.2005.05.085.

Ph. Chomaz, M. Di Toro, and A. Smerzi. Pre-equilibrium effects on properties of hot giant-dipole resonances. *Nucl. Phys. A*, 563:509–524, 1993. doi: 10.1016/0375-9474(93)90126-I.

D. A. Pigg, A. S. Umar, and V. E. Oberacker. Eulerian rotations of deformed nuclei for TDDFT calculations. *Comput. Phys. Commun.*, 185:1410–1414, 2014. doi: 10.1016/j.cpc.2014.02.004.

M. Pignatari, R. Hirschi, M. Wiescher, R. Gallino, M. Bennett, M. Beard, C. Fryer, F. Herwig, G. Rockefeller, and F. X. Timmes. The $^{12}\text{C} + ^{12}\text{C}$ reaction and the impact on nucleosynthesis in massive stars. *Astrophys. J.*, 762:31, 2012. doi: 10.1088/0004-637x/762/1/31.

D. N. Poenaru and R. A. Gherghescu. α decay and cluster radioactivity of nuclei of interest to the synthesis of $Z = 119, 120$ isotopes. *Phys. Rev. C*, 97:044621, 2018. doi: 10.1103/PhysRevC.97.044621.

D. C. Rafferty, M. Dasgupta, D. J. Hinde, C. Simenel, E. C. Simpson, E. Williams, I. P. Carter, K. J. Cook, D. H. Luong, S. D. McNeil, K. Ramachandran, K. Vo-Phuoc, and A. Wakhle. Multinucleon transfer in $^{16,18}\text{O}$, $^{19}\text{F}+^{208}\text{Pb}$ reactions at energies near the fusion barrier. *Phys. Rev. C*, 94:024607, 2016. doi: 10.1103/physrevc.94.024607.

Randall L. Cooper, Andrew W. Steiner, and Edward F. Brown. Possible resonances in the $^{12}\text{C} + ^{12}\text{C}$ fusion rate and superburst ignition. *Astrophys. J.*, 702:660–671, 2009. doi: 10.1088/0004-637X/702/1/660.

J. Randrup. Mass transport in nuclear collisions. *Nucl. Phys. A*, 307:319–348, 1978. doi: 10.1016/0375-9474(78)90621-8.

J. Randrup and J. S. Vaagen. On the proximity treatment of the interaction between deformed nuclei. *Phys. Lett. B*, 77:170–173, 1978a. doi: 10.1016/0370-2693(78)90613-5.

J. Randrup and J. S. Vaagen. On the proximity treatment of the interaction between deformed nuclei. *Phys. Lett. B*, 77:170–173, 1978b. doi: 10.1016/0370-2693(78)90613-5.

George H. Rawitscher. Approximate Independence of Optical-Model Elastic Scattering Calculations on the Potential at Small Distances. *Phys. Rev.*, 135:B605–B612, 1964. doi: 10.1103/PhysRev.135.B605.

H. Reinhardt. Semiclassical theory of large amplitude collective excitations. *Nucl. Phys. A*, 346:1–69, 1980. doi: 10.1016/0375-9474(80)90488-1.

M. J. Rhoades-Brown and V. E. Oberacker. Strong Enhancement of Subbarrier Fusion due to Negative Hexadecapole Deformation. *Phys. Rev. Lett.*, 50:1435–1438, 1983a. doi: 10.1103/PhysRevLett.50.1435.

M. J. Rhoades-Brown and V. E. Oberacker. Strong Enhancement of Subbarrier Fusion due to Negative Hexadecapole Deformation. *Phys. Rev. Lett.*, 50:1435–1438, 1983b. doi: 10.1103/PhysRevLett.50.1435.

J. B. Roberto, C. W. Alexander, R. A. Boll, J. D. Burns, J. G. Ezold, L. K. Felker, S. L. Hogle, and K. P. Rykaczewski. Actinide targets for the synthesis of super-heavy elements. *Nucl. Phys. A*, 944:99–116, 2015. doi: 10.1016/j.nuclphysa.2015.06.009.

L M Robledo, R Rodríguez-Guzmán, and P Sarriuguren. Role of triaxiality in the ground-state shape of neutron-rich Yb, Hf, W, Os and Pt isotopes. *J. Phys. G*, 36:115104, 2009. doi: 10.1088/0954-3899/36/11/115104.

Roger Balian and Marcel Vénéroni. Time-Dependent Variational Principle for Predicting the Expectation Value of an Observable. *Phys. Rev. Lett.*, 47:1353, 1981. doi: 10.1103/PhysRevLett.47.1353.

Roger Balian and Marcel Vénéroni. Fluctuations in a time-dependent mean-field approach. *Phys. Lett. B*, 136:301–306, 1984. doi: 10.1016/0370-2693(84)92008-2.

N. Rowley and K. Hagino. Entrance-channel effects in heavy-ion capture: role of octupole phonons. *Nucl. Phys. A*, 834:110c–116c, 2010. doi: 10.1016/j.nuclphysa.2009.12.018.

N. Rowley, I. J. Thompson, and M. A. Nagarajan. Neutron flow and necking in heavy-ion fusion reactions. *Phys. Lett. B*, 282:276–280, 1992. doi: 10.1016/0370-2693(92)90638-k.

Hiroyuki Sagawa and Gianluca Colò. Tensor interaction in mean-field and density functional theory approaches to nuclear structure. *Prog. Part. Nucl. Phys.*, 76:76–115, 2014. doi: 10.1016/j.ppnp.2014.01.006.

C.-C. Sahm, H.-G. Clerc, K.-H. Schmidt, W. Reisdorf, P. Armbruster, F. P. Heßberger, J. G. Keller, G. Münzenberg, and D. Vermeulen. Hindrance of fusion in central collisions of heavy symmetric nuclear systems. *Z. Phys. A*, 319:113–118, 1984. doi: 10.1007/BF01415623.

V. V. Sargsyan, Z. Kanokov, G. G. Adamian, N. V. Antonenko, and W. Scheid. Interaction times in the $^{136}\text{Xe} + ^{136}\text{Xe}$ and $^{238}\text{U} + ^{238}\text{U}$ reactions with a quantum master equation. *Phys. Rev. C*, 80:047603, 2009. doi: 10.1103/PhysRevC.80.047603.

P. Sarriuguren, R. Rodríguez-Guzmán, and L. M. Robledo. Shape transitions in neutron-rich Yb, Hf, W, Os, and Pt isotopes within a Skyrme Hartree-Fock + BCS approach. *Phys. Rev. C*, 77:064322, 2008. doi: 10.1103/PhysRevC.77.064322.

G. R. Satchler and W. G. Love. Folding model potentials from realistic interactions for heavy-ion scattering. *Phys. Rep.*, 55:183–254, 1979a. doi: 10.1016/0370-1573(79)90081-4.

G. R. Satchler and W. G. Love. Folding model potentials from realistic interactions for heavy-ion scattering. *Phys. Rep.*, 55:183–254, 1979b. doi: 10.1016/0370-1573(79)90081-4.

Guillaume Scamps and Yukio Hashimoto. Transfer probabilities for the reactions $^{14,20}\text{O} + ^{20}\text{O}$ in terms of multiple time-dependent Hartree-Fock-Bogoliubov trajectories. *Phys. Rev. C*, 96:031602, 2017. doi: 10.1103/PhysRevC.96.031602.

Guillaume Scamps and Denis Lacroix. Effect of pairing on one- and two-nucleon transfer below the Coulomb barrier: A time-dependent microscopic description. *Phys. Rev. C*, 87:014605, 2013a. doi: 10.1103/PhysRevC.87.014605.

Guillaume Scamps and Denis Lacroix. Effect of pairing on one- and two-nucleon transfer below the Coulomb barrier: A time-dependent microscopic description. *Phys. Rev. C*, 87:014605, 2013b. doi: 10.1103/PhysRevC.87.014605.

Guillaume Scamps and Cédric Simenel. Impact of pear-shaped fission fragments on mass-asymmetric fission in actinides. *Nature*, 564(7736):382–385, 2018. doi: 10.1038/s41586-018-0780-0.

Guillaume Scamps and Cédric Simenel. Effect of shell structure on the fission of sub-lead nuclei. *Phys. Rev. C*, 100:041602, 2019. doi: 10.1103/PhysRevC.100.041602.

Guillaume Scamps, Cédric Simenel, and Denis Lacroix. Superfluid dynamics of ^{258}Fm fission. *Phys. Rev. C*, 92:011602(R), 2015a. doi: 10.1103/PhysRevC.92.011602.

Guillaume Scamps, Cédric Simenel, and Denis Lacroix. Superfluid dynamics of ^{258}Fm fission. *Phys. Rev. C*, 92:011602, 2015b. doi: 10.1103/PhysRevC.92.011602.

E. W. Schmid, S. Saito, and H. Fiedeldey. The concept of a Pauli barrier in nucleus-nucleus scattering. *Z. Phys. A*, 306:37–42, 1982. doi: 10.1007/BF01413405.

K.-H. Schmidt and W. Morawek. The conditions for the synthesis of heavy nuclei. *Rep. Prog. Phys.*, 54:949, 1991. doi: 10.1088/0034-4885/54/7/002.

M. Seiwert, W. Greiner, V. Oberacker, and M. J. Rhoades-Brown. Test of the proximity theorem for deformed nuclei. *Phys. Rev. C*, 29:477–485, 1984a. doi: 10.1103/PhysRevC.29.477.

M. Seiwert, W. Greiner, V. Oberacker, and M. J. Rhoades-Brown. Test of the proximity

theorem for deformed nuclei. *Phys. Rev. C*, 29:477–485, 1984b. doi: 10.1103/PhysRevC.29.477.

K. Sekizawa and K. Hagino. Time-dependent Hartree-Fock plus Langevin approach for hot fusion reactions to synthesize the $Z = 120$ superheavy element. *Phys. Rev. C*, 99:051602, 2019. doi: 10.1103/PhysRevC.99.051602.

Kazuyuki Sekizawa. Enhanced nucleon transfer in tip collisions of $^{238}\text{U} + ^{124}\text{Sn}$. *Phys. Rev. C*, 96:041601(R), 2017a. doi: 10.1103/PhysRevC.96.041601.

Kazuyuki Sekizawa. Microscopic description of production cross sections including deexcitation effects. *Phys. Rev. C*, 96:014615, 2017b. doi: 10.1103/physrevc.96.014615.

Kazuyuki Sekizawa. Enhanced nucleon transfer in tip collisions of $^{238}\text{U} + ^{124}\text{Sn}$. *Phys. Rev. C*, 96:041601(R), 2017c. doi: 10.1103/PhysRevC.96.041601.

Kazuyuki Sekizawa and Kazuhiro Yabana. Particle-number projection method in time-dependent Hartree-Fock theory: Properties of reaction products. *Phys. Rev. C*, 90:064614, 2014. doi: 10.1103/PhysRevC.90.064614.

Kazuyuki Sekizawa and Kazuhiro Yabana. Time-dependent Hartree-Fock calculations for multinucleon transfer and quasifission processes in the $^{64}\text{Ni} + ^{238}\text{U}$ reaction. *Phys. Rev. C*, 93:054616, 2016a. doi: 10.1103/PhysRevC.93.054616.

Kazuyuki Sekizawa and Kazuhiro Yabana. Time-dependent Hartree-Fock calculations for multinucleon transfer and quasifission processes in the $^{64}\text{Ni} + ^{238}\text{U}$ reaction. *Phys. Rev. C*, 93:054616, 2016b. doi: 10.1103/PhysRevC.93.054616.

G. Shen, C. J. Horowitz, and S. Teige. New equation of state for astrophysical simulations. *Phys. Rev. C*, 83:035802, 2011. doi: 10.1103/PhysRevC.83.035802.

W. Q. Shen, J. Albinski, A. Gobbi, S. Gralla, K. D. Hildenbrand, N. Herrmann, J. Kuzminski, W. F. J. Müller, H. Stelzer, J. Töke, B. B. Back, S. Bjørnholm, and S. P. Sørensen.

Fission and quasifission in U-induced reactions. *Phys. Rev. C*, 36:115–142, 1987. doi: 10.1103/PhysRevC.36.115.

L. Shi and Lu Guo. Skyrme Tensor Force in $^{16}\text{O} + ^{16}\text{O}$ Fusion Dynamics. *Nucl. Phys. Rev.*, 34(1):41, 2017a. doi: 10.11804/NuclPhysRev.34.01.041.

Long Shi and Lu Guo. Skyrme Tensor Force in $^{16}\text{O} + ^{16}\text{O}$ Fusion Dynamics. *Nucl. Phys. Rev.*, 34:41, 2017b. doi: 10.11804/NuclPhysRev.34.01.041.

C. Simenel and A. S. Umar. Formation and dynamics of fission fragments. *Phys. Rev. C*, 89:031601(R), 2014a. doi: 10.1103/PhysRevC.89.031601.

C. Simenel and A. S. Umar. Formation and dynamics of fission fragments. *Phys. Rev. C*, 89:031601(R), 2014b. doi: 10.1103/PhysRevC.89.031601.

C. Simenel and A. S. Umar. Heavy-ion collisions and fission dynamics with the time-dependent Hartree-Fock theory and its extensions. *Prog. Part. Nucl. Phys.*, 103:19–66, 2018a. doi: 10.1016/j.ppnp.2018.07.002.

C. Simenel and A. S. Umar. Heavy-ion collisions and fission dynamics with the time-dependent Hartree-Fock theory and its extensions. *Prog. Part. Nucl. Phys.*, 103:19–66, 2018b. doi: 10.1016/j.ppnp.2018.07.002.

C. Simenel, Ph. Chomaz, and G. de France. Quantum Calculation of the Dipole Excitation in Fusion Reactions. *Phys. Rev. Lett.*, 86:2971–2974, 2001. doi: 10.1103/PhysRevLett.86.2971.

C. Simenel, Ph. Chomaz, and G. de France. Quantum Calculations of Coulomb Reorientation for Sub-Barrier Fusion. *Phys. Rev. Lett.*, 93:102701, 2004. doi: 10.1103/PhysRevLett.93.102701.

C. Simenel, Ph. Chomaz, and G. de France. Fusion process studied with a preequilibrium

giant dipole resonance in time-dependent Hartree-Fock theory. *Phys. Rev. C*, 76:024609, 2007. doi: 10.1103/PhysRevC.76.024609.

C. Simenel, D. J. Hinde, R. du Rietz, M. Dasgupta, M. Evers, C. J. Lin, D. H. Luong, and A. Wakhle. Influence of entrance-channel magicity and isospin on quasi-fission. *Phys. Lett. B*, 710:607–611, 2012. doi: 10.1016/j.physletb.2012.03.063.

C. Simenel, M. Dasgupta, D. J. Hinde, and E. Williams. Microscopic approach to coupled-channels effects on fusion. *Phys. Rev. C*, 88:064604, 2013a. doi: 10.1103/PhysRevC.88.064604.

C. Simenel, M. Dasgupta, D. J. Hinde, and E. Williams. Microscopic approach to coupled-channels effects on fusion. *Phys. Rev. C*, 88:064604, 2013b. doi: 10.1103/PhysRevC.88.064604.

C. Simenel, R. Keser, A. S. Umar, and V. E. Oberacker. Microscopic study of $^{16}\text{O} + ^{16}\text{O}$ fusion. *Phys. Rev. C*, 88:024617, 2013c. doi: 10.1103/PhysRevC.88.024617.

C. Simenel, R. Keser, A. S. Umar, and V. E. Oberacker. Microscopic study of $^{16}\text{O} + ^{16}\text{O}$ fusion. *Phys. Rev. C*, 88:024617, 2013d. doi: 10.1103/PhysRevC.88.024617.

C. Simenel, A. S. Umar, K. Godbey, M. Dasgupta, and D. J. Hinde. How the Pauli exclusion principle affects fusion of atomic nuclei. *Phys. Rev. C*, 95:031601, 2017a. doi: 10.1103/physrevc.95.031601.

C. Simenel, A. S. Umar, K. Godbey, M. Dasgupta, and D. J. Hinde. How the Pauli exclusion principle affects fusion of atomic nuclei. *Phys. Rev. C*, 95:031601, 2017b. doi: 10.1103/physrevc.95.031601.

Cédric Simenel. Particle Transfer Reactions with the Time-Dependent Hartree-Fock Theory Using a Particle Number Projection Technique. *Phys. Rev. Lett.*, 105:192701, 2010a. doi: 10.1103/PhysRevLett.105.192701.

Cédric Simenel. Particle Transfer Reactions with the Time-Dependent Hartree-Fock Theory Using a Particle Number Projection Technique. *Phys. Rev. Lett.*, 105:192701, 2010b. doi: 10.1103/PhysRevLett.105.192701.

Cédric Simenel. Particle-Number Fluctuations and Correlations in Transfer Reactions Obtained Using the Balian-Vénéroni Variational Principle. *Phys. Rev. Lett.*, 106:112502, 2011a. doi: 10.1103/PhysRevLett.106.112502.

Cédric Simenel. Particle-Number Fluctuations and Correlations in Transfer Reactions Obtained Using the Balian-Vénéroni Variational Principle. *Phys. Rev. Lett.*, 106:112502, 2011b. doi: 10.1103/PhysRevLett.106.112502.

Cédric Simenel. Nuclear quantum many-body dynamics. *Eur. Phys. J. A*, 48:152, 2012a. doi: 10.1140/epja/i2012-12152-0.

Cédric Simenel. Nuclear quantum many-body dynamics. *Eur. Phys. J. A*, 48:152, 2012b. doi: 10.1140/epja/i2012-12152-0.

Bikash Sinha and Steven A. Moszkowski. The nucleus-nucleus interaction potential using density-dependent delta interaction. *Phys. Lett. B*, 81:289–294, 1979. doi: 10.1016/0370-2693(79)90337-X.

T. H. R. Skyrme. CVII. The nuclear surface. *Phil. Mag.*, 1:1043–1054, 1956a. doi: 10.1080/14786435608238186.

T. H. R. Skyrme. CVII. The nuclear surface. *Phil. Mag.*, 1:1043–1054, 1956b. doi: 10.1080/14786435608238186.

T. Spillane, F. Raiola, C. Rolfs, D. Schürmann, F. Strieder, S. Zeng, H.-W. Becker, C. Bordeanu, L. Gialanella, M. Romano, and J. Schweitzer. $^{12}\text{C} + ^{12}\text{C}$ fusion Reactions near the Gamow Energy. *Phys. Rev. Lett.*, 98:122501, 2007. doi: 10.1103/physrevlett.98.122501.

- A. M. Stefanini, G. Montagnoli, R. Silvestri, L. Corradi, S. Courtin, E. Fioretto, B. Guiot, F. Haas, D. Lebhertz, P. Mason, F. Scarlassara, and S. Szilner. How does fusion hindrance show up in medium-light systems? The case of $^{48}\text{Ca} + ^{48}\text{Ca}$. *Phys. Lett. B*, 679:95–99, 2009. doi: 10.1016/j.physletb.2009.07.017.
- A. M. Stefanini, G. Montagnoli, L. Corradi, S. Courtin, E. Fioretto, A. Goasduff, F. Haas, P. Mason, R. Silvestri, Pushpendra P. Singh, F. Scarlassara, and S. Szilner. Fusion hindrance for $^{58}\text{Ni} + ^{54}\text{Fe}$. *Phys. Rev. C*, 82:014614, 2010. doi: 10.1103/physrevc.82.014614.
- P. D. Stevenson and M. C. Barton. Low-energy heavy-ion reactions and the Skyrme effective interaction. *Prog. Part. Nucl. Phys.*, 104:142–164, 2019. doi: 10.1016/j.ppnp.2018.09.002.
- P. D. Stevenson, E. B. Suckling, S. Fracasso, M. C. Barton, and A. S. Umar. Skyrme tensor force in heavy ion collisions. *Phys. Rev. C*, 93:054617, 2016a. doi: 10.1103/physrevc.93.054617.
- P. D. Stevenson, E. B. Suckling, S. Fracasso, M. C. Barton, and A. S. Umar. Skyrme tensor force in heavy ion collisions. *Phys. Rev. C*, 93:054617, 2016b. doi: 10.1103/physrevc.93.054617.
- J. R. Stone, P. A. M. Guichon, P.-G. Reinhard, and A. W. Thomas. Finite Nuclei in the Quark-Meson Coupling Model. *Phys. Rev. Lett.*, 116:092501, 2016. doi: 10.1103/physrevlett.116.092501.
- J. R. Stone, K. Morita, P. A. M. Guichon, and A. W. Thomas. Physics of even-even super-heavy nuclei with $96 < Z < 110$ in the quark-meson-coupling model. *Phys. Rev. C*, 100:044302, 2019. doi: 10.1103/PhysRevC.100.044302.
- E. C. Stoner. The distribution of electrons among atomic levels. *Phil. Mag.*, 48:719, 1924.

T. E. Strohmayer and E. F. Brown. A remarkable 3 hour thermonuclear burst from 4U 1820 – 30. *Astrophys. J.*, 566:1045–1059, 2002. doi: 10.1086/338337.

Takatoshi Ichikawa, Kouichi Hagino, and Akira Iwamoto. Signature of Smooth Transition from Sudden to Adiabatic States in Heavy-Ion Fusion Reactions at Deep Sub-Barrier Energies. *Phys. Rev. Lett.*, 103:202701, 2009. doi: 10.1103/PhysRevLett.103.202701.

X. D. Tang. Heavy ion fusion reactions in stars. *AIP Conf. Proc.*, 1947:020024, 2018. doi: 10.1063/1.5030828.

Y. C. Tang, M. LeMere, and D. R. Thompson. Resonating-group method for nuclear many-body problems. *Phys. Rep.*, 47:167–223, 1978. doi: 10.1016/0370-1573(78)90175-8.

Yusuke Tanimura, Denis Lacroix, and Guillaume Scamps. Collective aspects deduced from time-dependent microscopic mean-field with pairing: Application to the fission process. *Phys. Rev. C*, 92:034601, 2015. doi: 10.1103/PhysRevC.92.034601.

Yusuke Tanimura, Denis Lacroix, and Sakir Ayik. Microscopic Phase-Space Exploration Modeling of ^{258}Fm Spontaneous Fission. *Phys. Rev. Lett.*, 118:152501, 2017a. doi: 10.1103/PhysRevLett.118.152501.

Yusuke Tanimura, Denis Lacroix, and Sakir Ayik. Microscopic Phase-Space Exploration Modeling of ^{258}Fm Spontaneous Fission. *Phys. Rev. Lett.*, 118:152501, 2017b. doi: 10.1103/PhysRevLett.118.152501.

R. G. Thomas, D. J. Hinde, D. Duniec, F. Zenke, M. Dasgupta, M. L. Brown, M. Evers, L. R. Gasques, M. D. Rodriguez, and A. Diaz-Torres. Entrance channel dependence of quasifission in reactions forming ^{220}Th . *Phys. Rev. C*, 77:034610, 2008. doi: 10.1103/PhysRevC.77.034610.

Akihiro Tohsaki, Fumiya Tanabe, and Ryozo Tamagaki. Microscopic Study of ^{16}O - ^{16}O Interaction by the Resonating Group Method. *Prog. Theor. Phys.*, 53:1022–1041, 1975. doi: 10.1143/PTP.53.1022.

M. Tohyama and A. S. Umar. Two-body dissipation effects on the synthesis of superheavy elements. *Phys. Rev. C*, 93:034607, 2016. doi: 10.1103/PhysRevC.93.034607.

J. Tōke, R. Bock, G. X. Dai, A. Gobbi, S. Gralla, K. D. Hildenbrand, J. Kuzminski, W. F. J. Müller, A. Olmi, H. Stelzer, B. B. Back, and S. Bjørnholm. Quasi-fission: The mass-drift mode in heavy-ion reactions. *Nucl. Phys. A*, 440:327–365, 1985. doi: 10.1016/0375-9474(85)90344-6.

M. B. Tsang, Yingxun Zhang, P. Danielewicz, M. Famiano, Zhuxia Li, W. G. Lynch, and A. W. Steiner. Constraints on the Density Dependence of the Symmetry Energy. *Phys. Rev. Lett.*, 102:122701, 2009. doi: 10.1103/PhysRevLett.102.122701.

A. Tumino, C. Spitaleri, M. La Cognata, S. Cherubini, G. L. Guardo, M. Gulino, S. Hayakawa, I. Indelicato, L. Lamia, H. Petrascu, R. G. Pizzone, S. M. R. Puglia, G. G. Rapisarda, S. Romano, M. L. Sergi, R. Spartá, and L. Trache. An increase in the $^{12}\text{C} + ^{12}\text{C}$ fusion rate from resonances at astrophysical energies. *Nature*, 557(7707): 687–690, 2018. doi: 10.1038/s41586-018-0149-4.

A. S. Umar and V. E. Oberacker. Three-dimensional unrestricted time-dependent Hartree-Fock fusion calculations using the full Skyrme interaction. *Phys. Rev. C*, 73:054607, 2006a. doi: 10.1103/PhysRevC.73.054607.

A. S. Umar and V. E. Oberacker. Heavy-ion interaction potential deduced from density-constrained time-dependent Hartree-Fock calculation. *Phys. Rev. C*, 74:021601, 2006b. doi: 10.1103/PhysRevC.74.021601.

A. S. Umar and V. E. Oberacker. Time dependent Hartree-Fock fusion calculations for

spherical, deformed systems. *Phys. Rev. C*, 74:024606, 2006c. doi: 10.1103/PhysRevC.74.024606.

A. S. Umar and V. E. Oberacker. Dynamical deformation effects in subbarrier fusion of $^{64}\text{Ni} + ^{132}\text{Sn}$. *Phys. Rev. C*, 74:061601, 2006d. doi: 10.1103/PhysRevC.74.061601.

A. S. Umar and V. E. Oberacker. Dynamical deformation effects in subbarrier fusion of $^{64}\text{Ni} + ^{132}\text{Sn}$. *Phys. Rev. C*, 74:061601, 2006e. doi: 10.1103/PhysRevC.74.061601.

A. S. Umar and V. E. Oberacker. Heavy-ion interaction potential deduced from density-constrained time-dependent Hartree-Fock calculation. *Phys. Rev. C*, 74:021601, 2006f. doi: 10.1103/PhysRevC.74.021601.

A. S. Umar and V. E. Oberacker. Three-dimensional unrestricted time-dependent Hartree-Fock fusion calculations using the full Skyrme interaction. *Phys. Rev. C*, 73:054607, 2006g. doi: 10.1103/PhysRevC.73.054607.

A. S. Umar and V. E. Oberacker. Time dependent Hartree-Fock fusion calculations for spherical, deformed systems. *Phys. Rev. C*, 74:024606, 2006h. doi: 10.1103/PhysRevC.74.024606.

A. S. Umar and V. E. Oberacker. $^{64}\text{Ni} + ^{64}\text{Ni}$ fusion reaction calculated with the density-constrained time-dependent Hartree-Fock formalism. *Phys. Rev. C*, 77:064605, 2008a. doi: 10.1103/PhysRevC.77.064605.

A. S. Umar and V. E. Oberacker. $^{64}\text{Ni} + ^{64}\text{Ni}$ fusion reaction calculated with the density-constrained time-dependent Hartree-Fock formalism. *Phys. Rev. C*, 77:064605, 2008b. doi: 10.1103/PhysRevC.77.064605.

A. S. Umar and V. E. Oberacker. Density-constrained time-dependent Hartree-Fock calculation of $^{16}\text{O} + ^{208}\text{Pb}$ fusion cross-sections. *Eur. Phys. J. A*, 39:243–247, 2009. doi: 10.1140/epja/i2008-10712-5.

A. S. Umar and V. E. Oberacker. Time-dependent HF approach to SHE dynamics. *Nucl. Phys. A*, 944:238–256, 2015. doi: 10.1016/j.nuclphysa.2015.02.011.

A. S. Umar, M. R. Strayer, R. Y. Cusson, P.-G. Reinhard, and D. A. Bromley. Time-dependent Hartree-Fock calculations of $^4\text{He} + ^{14}\text{C}$, $^{12}\text{C} + ^{12}\text{C}(0^+)$, and $^4\text{He} + ^{20}\text{Ne}$ molecular formations. *Phys. Rev. C*, 32:172–183, 1985. doi: 10.1103/PhysRevC.32.172.

A. S. Umar, M. R. Strayer, and P.-G. Reinhard. Resolution of the Fusion Window Anomaly in Heavy-Ion Collisions. *Phys. Rev. Lett.*, 56:2793–2796, 1986. doi: 10.1103/PhysRevLett.56.2793.

A. S. Umar, M. R. Strayer, P.-G. Reinhard, K. T. R. Davies, and S.-J. Lee. Spin-orbit force in time-dependent Hartree-Fock calculations of heavy-ion collisions. *Phys. Rev. C*, 40: 706–714, 1989. doi: 10.1103/PhysRevC.40.706.

A. S. Umar, M. R. Strayer, J. S. Wu, D. J. Dean, and M. C. Güçlü. Nuclear Hartree-Fock calculations with splines. *Phys. Rev. C*, 44:2512–2521, 1991a. doi: 10.1103/PhysRevC.44.2512.

A. S. Umar, J. Wu, M. R. Strayer, and C. Bottcher. Basis-spline collocation method for the lattice solution of boundary-value-problems. *J. Comp. Phys.*, 93:426–448, 1991b. doi: 10.1016/0021-9991(91)90193-O.

A. S. Umar, V. E. Oberacker, and J. A. Maruhn. Neutron transfer dynamics and doorway to fusion in time-dependent Hartree-Fock theory. *Eur. Phys. J. A*, 37:245–250, 2008a. doi: 10.1140/epja/i2008-10614-6.

A. S. Umar, V. E. Oberacker, and J. A. Maruhn. Neutron transfer dynamics and doorway to fusion in time-dependent Hartree-Fock theory. *Eur. Phys. J. A*, 37:245–250, 2008b. doi: 10.1140/epja/i2008-10614-6.

A. S. Umar, V. E. Oberacker, J. A. Maruhn, and P.-G. Reinhard. Microscopic calculation of precompound excitation energies for heavy-ion collisions. *Phys. Rev. C*, 80:041601, 2009a. doi: 10.1103/PhysRevC.80.041601.

A. S. Umar, V. E. Oberacker, J. A. Maruhn, and P.-G. Reinhard. Microscopic calculation of precompound excitation energies for heavy-ion collisions. *Phys. Rev. C*, 80:041601, 2009b. doi: 10.1103/PhysRevC.80.041601.

A. S. Umar, J. A. Maruhn, N. Itagaki, and V. E. Oberacker. Microscopic Study of the Triple- α Reaction. *Phys. Rev. Lett.*, 104:212503, 2010a. doi: 10.1103/PhysRevLett.104.212503.

A. S. Umar, V. E. Oberacker, J. A. Maruhn, and P.-G. Reinhard. Entrance channel dynamics of hot and cold fusion reactions leading to superheavy elements. *Phys. Rev. C*, 81: 064607, 2010b. doi: 10.1103/PhysRevC.81.064607.

A. S. Umar, V. E. Oberacker, and C. J. Horowitz. Microscopic sub-barrier fusion calculations for the neutron star crust. *Phys. Rev. C*, 85:055801, 2012a. doi: 10.1103/PhysRevC.85.055801.

A. S. Umar, V. E. Oberacker, and C. J. Horowitz. Microscopic sub-barrier fusion calculations for the neutron star crust. *Phys. Rev. C*, 85:055801, 2012b. doi: 10.1103/PhysRevC.85.055801.

A. S. Umar, V. E. Oberacker, J. A. Maruhn, and P.-G. Reinhard. Microscopic composition of ion-ion interaction potentials. *Phys. Rev. C*, 85:017602, 2012c. doi: 10.1103/PhysRevC.85.017602.

A. S. Umar, C. Simenel, and V. E. Oberacker. Energy dependence of potential barriers and its effect on fusion cross sections. *Phys. Rev. C*, 89:034611, 2014a. doi: 10.1103/PhysRevC.89.034611.

A. S. Umar, C. Simenel, and V. E. Oberacker. Energy dependence of potential barriers and its effect on fusion cross sections. *Phys. Rev. C*, 89:034611, 2014b. doi: 10.1103/PhysRevC.89.034611.

A. S. Umar, V. E. Oberacker, and C. Simenel. Shape evolution and collective dynamics of quasifission in the time-dependent Hartree-Fock approach. *Phys. Rev. C*, 92:024621, 2015a. doi: 10.1103/PhysRevC.92.024621.

A. S. Umar, V. E. Oberacker, and C. Simenel. Shape evolution and collective dynamics of quasifission in the time-dependent Hartree-Fock approach. *Phys. Rev. C*, 92:024621, 2015b. doi: 10.1103/PhysRevC.92.024621.

A. S. Umar, V. E. Oberacker, and C. Simenel. Fusion and quasifission dynamics in the reactions $^{48}\text{Ca} + ^{249}\text{Bk}$ and $^{50}\text{Ti} + ^{249}\text{Bk}$ using a time-dependent Hartree-Fock approach. *Phys. Rev. C*, 94:024605, 2016a. doi: 10.1103/PhysRevC.94.024605.

A. S. Umar, V. E. Oberacker, and C. Simenel. Fusion and quasifission dynamics in the reactions $^{48}\text{Ca} + ^{249}\text{Bk}$ and $^{50}\text{Ti} + ^{249}\text{Bk}$ using a time-dependent Hartree-Fock approach. *Phys. Rev. C*, 94:024605, 2016b. doi: 10.1103/PhysRevC.94.024605.

A. S. Umar, C. Simenel, and W. Ye. Transport properties of isospin asymmetric nuclear matter using the time-dependent Hartree–Fock method. *Phys. Rev. C*, 96:024625, 2017a. doi: 10.1103/PhysRevC.96.024625.

A. S. Umar, C. Simenel, and W. Ye. Transport properties of isospin asymmetric nuclear matter using the time-dependent Hartree–Fock method. *Phys. Rev. C*, 96:024625, 2017b. doi: 10.1103/PhysRevC.96.024625.

R. Utama, J. Piekarewicz, and H. B. Prosper. Nuclear mass predictions for the crustal composition of neutron stars: A Bayesian neural network approach. *Phys. Rev. C*, 93: 014311, 2016. doi: 10.1103/PhysRevC.93.014311.

V. Yu. Denisov and V. A. Nesterov. Effect of the Pauli exclusion principle on the potential of nucleus-nucleus interaction. *Phys. At. Nucl.*, 73:1142–1151, 2010. doi: 10.1134/s1063778810070070.

V. Yu. Denisov and W. Nörenberg. Entrance channel potentials in the synthesis of the heaviest nuclei. *Eur. Phys. J. A*, 15:375–388, 2002. doi: 10.1140/epja/i2002-10039-3.

Valery Zagrebaev and Walter Greiner. Shell effects in damped collisions: a new way to superheavies. *J. Phys. G*, 34:2265, 2007. doi: 10.1088/0954-3899/34/11/004.

M. Veselsky, J. Klimo, Yu-Gang Ma, and G. A. Soulard. Constraining the equation of state of nuclear matter from fusion hindrance in reactions leading to the production of superheavy elements. *Phys. Rev. C*, 94:064608, 2016. doi: 10.1103/PhysRevC.94.064608.

V. E. Viola, K. Kwiatkowski, and M. Walker. Systematics of fission fragment total kinetic-energy release. *Phys. Rev. C*, 31:1550–1552, 1985. doi: 10.1103/PhysRevC.31.1550.

K. Vo-Phuoc, C. Simenel, and E. C. Simpson. Dynamical effects in fusion with exotic nuclei. *Phys. Rev. C*, 94:024612, 2016. doi: 10.1103/physrevc.94.024612.

T. Wada and H. Horiuchi. Comparison of the Microscopic Potential with the Optical Potential in the $\alpha+^{16}\text{O}$ System. *Phys. Rev. Lett.*, 58:2190–2193, 1987. doi: 10.1103/PhysRevLett.58.2190.

A. Wakhle, C. Simenel, D. J. Hinde, M. Dasgupta, M. Evers, D. H. Luong, R. du Rietz, and E. Williams. Interplay between Quantum Shells and Orientation in Quasifission. *Phys. Rev. Lett.*, 113:182502, 2014. doi: 10.1103/PhysRevLett.113.182502.

A. Wakhle, K. Hammerton, Z. Kohley, D. J. Morrissey, K. Stiefel, J. Yurkon, J. Walshe, K. J. Cook, M. Dasgupta, D. J. Hinde, D. J. Jeung, E. Prasad, D. C. Rafferty, C. Simenel, E. C. Simpson, K. Vo-Phuoc, J. King, W. Loveland, and R. Yanez. Capture cross sections

for the synthesis of new heavy nuclei using radioactive beams. *Phys. Rev. C*, 97:021602, 2018. doi: 10.1103/PhysRevC.97.021602.

Nan Wang, En-Guang Zhao, Werner Scheid, and Shan-Gui Zhou. Theoretical study of the synthesis of superheavy nuclei with $Z = 119$ and 120 in heavy-ion reactions with transuranium targets. *Phys. Rev. C*, 85:041601, 2012a. doi: 10.1103/PhysRevC.85.041601.

Nan Wang, En-Guang Zhao, Werner Scheid, and Shan-Gui Zhou. Theoretical study of the synthesis of superheavy nuclei with $Z = 119$ and 120 in heavy-ion reactions with transuranium targets. *Phys. Rev. C*, 85:041601, 2012b. doi: 10.1103/PhysRevC.85.041601.

Ning Wang and Lu Guo. New neutron-rich isotope production in $^{154}\text{Sm} + ^{160}\text{Gd}$. *Phys. Lett. B*, 760:236–241, 2016a. doi: 10.1016/j.physletb.2016.06.073.

Ning Wang and Lu Guo. New neutron-rich isotope production in $^{154}\text{Sm} + ^{160}\text{Gd}$. *Phys. Lett. B*, 760:236–241, 2016b. doi: 10.1016/j.physletb.2016.06.073.

M. Warda, A. Zdeb, and L. M. Robledo. Cluster radioactivity in superheavy nuclei. *Phys. Rev. C*, 98:041602, 2018. doi: 10.1103/PhysRevC.98.041602.

Kouhei Washiyama. Microscopic analysis of fusion hindrance in heavy nuclear systems. *Phys. Rev. C*, 91:064607, 2015. doi: 10.1103/PhysRevC.91.064607.

Gentaro Watanabe, Hidetaka Sonoda, Toshiki Maruyama, Katsuhiko Sato, Kenji Yasuoka, and Toshikazu Ebisuzaki. Formation of Nuclear Pasta in Supernovae. *Phys. Rev. Lett.*, 103:121101, 2009. doi: 10.1103/PhysRevLett.103.121101.

Kai Wen, Fumihiko Sakata, Zhu-Xia Li, Xi-Zhen Wu, Ying-Xun Zhang, and Shan-Gui Zhou. Non-Gaussian Fluctuations and Non-Markovian Effects in the Nuclear Fusion Process: Langevin Dynamics Emerging from Quantum Molecular Dynamics Simulations. *Phys. Rev. Lett.*, 111:012501, 2013. doi: 10.1103/PhysRevLett.111.012501.

E. Williams, K. Sekizawa, D. J. Hinde, C. Simenel, M. Dasgupta, I. P. Carter, K. J. Cook, D. Y. Jeung, S. D. McNeil, C. S. Palshetkar, D. C. Rafferty, K. Ramachandran, and A. Wakhle. Exploring Zeptosecond Quantum Equilibration Dynamics: From Deep-Inelastic to Fusion-Fission Outcomes in $^{58}\text{Ni} + ^{60}\text{Ni}$ Reactions. *Phys. Rev. Lett.*, 120: 022501, 2018. doi: 10.1103/PhysRevLett.120.022501.

F. L. H. Wolfs. Fission and deep-inelastic scattering yields for $^{58}\text{Ni} + ^{112,124}\text{Sn}$ at energies around the barrier. *Phys. Rev. C*, 36:1379–1386, 1987. doi: 10.1103/physrevc.36.1379.

Zhenji Wu and Lu Guo. Microscopic studies of production cross sections in multinucleon transfer reaction $^{58}\text{Ni} + ^{124}\text{Sn}$. *Phys. Rev. C*, 100:014612, 2019. doi: 10.1103/PhysRevC.100.014612.

S. Wuenschel, K. Hagel, M. Barbui, J. Gauthier, X. G. Cao, R. Wada, E. J. Kim, Z. Majka, R. Płaneta, Z. Sosin, A. Wieloch, K. Zelga, S. Kowalski, K. Schmidt, C. Ma, G. Zhang, and J. B. Natowitz. Experimental survey of the production of α -decaying heavy elements in $^{238}\text{U} + ^{232}\text{Th}$ reactions at 7.5–6.1 MeV/nucleon. *Phys. Rev. C*, 97:064602, 2018. doi: 10.1103/PhysRevC.97.064602.

C. Xu, H. Hua, X. Q. Li, J. Meng, Z. H. Li, F. R. Xu, Y. Shi, H. L. Liu, S. Q. Zhang, Z. Y. Li, L. H. Zhu, X. G. Wu, G. S. Li, C. Y. He, S. G. Zhou, S. Y. Wang, Y. L. Ye, D. X. Jiang, T. Zheng, J. L. Lou, L. Y. Ma, E. H. Wang, Y. Y. Cheng, and C. He. New insight into the shape coexistence and shape evolution of ^{157}Yb . *Phys. Rev. C*, 83:014318, 2011. doi: 10.1103/PhysRevC.83.014318.

Hong Yao and Ning Wang. Microscopic dynamics simulations of multinucleon transfer in $^{86}\text{Kr} + ^{64}\text{Ni}$ at 25 MeV/nucleon. *Phys. Rev. C*, 95:014607, 2017. doi: 10.1103/PhysRevC.95.014607.

J. M. Yao and K. Hagino. Anharmonicity of multi-octupole-phonon excitations in ^{208}Pb :

Analysis with multireference covariant density functional theory and subbarrier fusion of $^{16}\text{O} + ^{208}\text{Pb}$. *Phys. Rev. C*, 94:011303, 2016. doi: 10.1103/PhysRevC.94.011303.

Yu. Ts. Oganessian. Private Communication, 2018.

Yu. Ts. Oganessian and V. K. Utyonkov. Superheavy nuclei from ^{48}Ca -induced reactions. *Nucl. Phys. A*, 944:62–98, 2015. doi: 10.1016/j.nuclphysa.2015.07.003.

Yu. Ts. Oganessian, F. Sh. Abdullin, P. D. Bailey, D. E. Benker, M. E. Bennett, S. N. Dmitriev, J. G. Ezold, J. H. Hamilton, R. A. Henderson, M. G. Itkis, Yu. V. Lobanov, A. N. Mezentsev, K. J. Moody, S. L. Nelson, A. N. Polyakov, C. E. Porter, A. V. Ramayya, F. D. Riley, J. B. Roberto, M. A. Ryabinin, K. P. Rykaczewski, R. N. Sagaidak, D. A. Shaughnessy, I. V. Shirokovsky, M. A. Stoyer, V. G. Subbotin, R. Sudowe, A. M. Sukhov, Yu. S. Tsyganov, V. K. Utyonkov, A. A. Voinov, G. K. Vostokin, and P. A. Wilk. Synthesis of a New Element with Atomic Number $Z = 117$. *Phys. Rev. Lett.*, 104:142502, 2010. doi: 10.1103/PhysRevLett.104.142502.

Yu. Ts. Oganessian, F. Sh. Abdullin, P. D. Bailey, D. E. Benker, M. E. Bennett, S. N. Dmitriev, J. G. Ezold, J. H. Hamilton, R. A. Henderson, M. G. Itkis, Yu. V. Lobanov, A. N. Mezentsev, K. J. Moody, S. L. Nelson, A. N. Polyakov, C. E. Porter, A. V. Ramayya, F. D. Riley, J. B. Roberto, M. A. Ryabinin, K. P. Rykaczewski, R. N. Sagaidak, D. A. Shaughnessy, I. V. Shirokovsky, M. A. Stoyer, V. G. Subbotin, R. Sudowe, A. M. Sukhov, R. Taylor, Yu. S. Tsyganov, V. K. Utyonkov, A. A. Voinov, G. K. Vostokin, and P. A. Wilk. Eleven new heaviest isotopes of elements $Z = 105$ to $Z = 117$ identified among the products of $^{249}\text{Bk} + ^{48}\text{Ca}$ reactions. *Phys. Rev. C*, 83:054315, 2011. doi: 10.1103/physrevc.83.054315.

V. I. Zagrebaev. Sub-barrier fusion enhancement due to neutron transfer. *Phys. Rev. C*, 67: 061601, 2003. doi: 10.1103/physrevc.67.061601.

V. I. Zagrebaev, V. V. Samarin, and Walter Greiner. Sub-barrier fusion of neutron-rich

nuclei and its astrophysical consequences. *Phys. Rev. C*, 75:035809, 2007. doi: 10.1103/PhysRevC.75.035809.

Valery Zagrebaev and Walter Greiner. Unified consideration of deep inelastic, quasi-fission and fusion-fission phenomena. *J. Phys. G*, 31:825, 2005. doi: 10.1088/0954-3899/31/7/024.

Y. L. Zhang and Y. Z. Wang. Systematic study of cluster radioactivity of superheavy nuclei. *Phys. Rev. C*, 97:014318, 2018. doi: 10.1103/PhysRevC.97.014318.

Kai Zhao, Xizhen Wu, and Zhuxia Li. Quantum molecular dynamics study of the mass distribution of products in 7.0A MeV $^{238}\text{U} + ^{238}\text{U}$ collisions. *Phys. Rev. C*, 80:054607, 2009. doi: 10.1103/PhysRevC.80.054607.

Kai Zhao, Zhuxia Li, Yingxun Zhang, Ning Wang, Qingfeng Li, Caiwan Shen, Yongjia Wang, and Xizhen Wu. Production of unknown neutron-rich isotopes in $^{238}\text{U} + ^{238}\text{U}$ collisions at near-barrier energy. *Phys. Rev. C*, 94:024601, 2016. doi: 10.1103/PhysRevC.94.024601.

H. Zheng, S. Burrello, M. Colonna, D. Lacroix, and G. Scamps. Connecting the nuclear equation of state to the interplay between fusion and quasifission processes in low-energy nuclear reactions. *Phys. Rev. C*, 98:024622, 2018. doi: 10.1103/PhysRevC.98.024622.

Long Zhu, Jun Su, and Feng-Shou Zhang. Influence of the neutron numbers of projectile and target on the evaporation residue cross sections in hot fusion reactions. *Phys. Rev. C*, 93:064610, 2016a. doi: 10.1103/PhysRevC.93.064610.

Long Zhu, Jun Su, and Feng-Shou Zhang. Influence of the neutron numbers of projectile and target on the evaporation residue cross sections in hot fusion reactions. *Phys. Rev. C*, 93:064610, 2016b. doi: 10.1103/PhysRevC.93.064610.

Long Zhu, Jun Su, Wen-Jie Xie, and Feng-Shou Zhang. Theoretical study on production of heavy neutron-rich isotopes around the N=126 shell closure in radioactive beam induced transfer reactions. *Phys. Lett. B*, 767:437–442, 2017. doi: 10.1016/j.physletb.2017.01.082.

James Zickefoose. $^{12}\text{C} + ^{12}\text{C}$ Fusion: Measurement and Advances Toward the Gamow Energy. PhD thesis, University of Connecticut, 2011. URL <https://opencommons.uconn.edu/dissertations/AAI3485448>.

P. G. Zint and U. Mosel. Kinetic energy contributions to heavy ion potentials. *Phys. Lett. B*, 56:424–426, 1975. doi: 10.1016/0370-2693(75)90402-5.

Appendix A

Appendix A